

# Feedback and Adjoint Based Control of Boundary Layer Flows

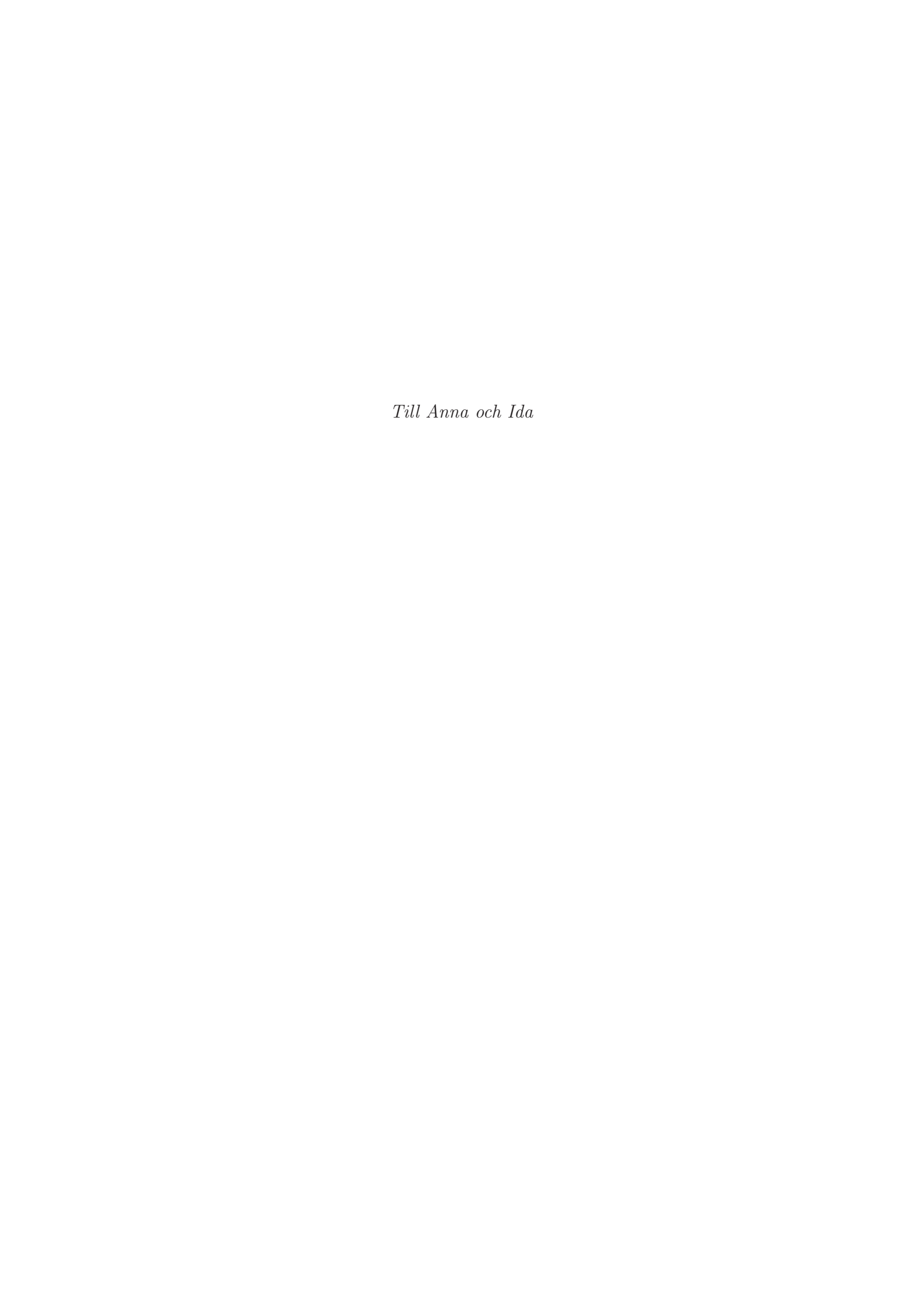
by

Mattias Chevalier



December 2004 Technical Reports from Royal Institute of Technology Department of Mechanics SE-100 44 Stockholm, Sweden

Typsatt i  $\mathcal{A}_{\mathcal{M}}\mathcal{S}$ - $\mathbb{A}^{T}_{\mathbf{E}}X$ . Akademisk avhandling som med tillstånd av Kungliga Tekniska Högskolan i Stockholm framlägges till offentlig granskning för avläggande av teknologie doktorsexamen tisdagen den 7:e december 2004 kl. 10.15 i Kollegiesalen, Administrationsbyggnaden, Kungliga Tekniska Högskolan, Valhallavägen 79, Stockholm. © Mattias Chevalier 2004 Edita Norstedts Tryckeri, Stockholm 2004



### Feedback and Adjoint Based Control of Boundary Layer Flows

#### **Mattias Chevalier**

Department of Mechanics, Royal Institute of Technology S-100 44 Stockholm, Sweden

#### Abstract

Linear and nonlinear optimal control have been investigated in transitional channel and boundary layer flows. The flow phenomena that we study are governed by the incompressible Navier–Stokes equations and the main aim with the control is to prevent transition from laminar to turbulent flows. A linear model-based feedback control approach, that minimizes an objective function which measures the perturbation energy, can be formulated where the Orr–Sommerfeld/Squire equations model the flow dynamics. A limitation with the formulation is that it requires complete state information. However, the control problem can be combined with a state estimator to relax this requirement. The estimator requires only wall measurements to reconstruct the flow in an optimal manner.

Physically relevant stochastic models are suggested for the estimation problem which turns out to be crucial for fast convergence. Based on these models the estimator is shown to work for both infinitesimal as well as finite amplitude perturbations in direct numerical simulations of a channel flow at  $Re_{cl} = 3000$ .

A stochastic model for external disturbances is also constructed based on statistical data from a turbulent channel flow at  $Re_{\tau}=100$ . The model is successfully applied to estimate a turbulent channel flow at the same Reynolds number.

The combined control and estimation problem, also known as a compensator, is applied to spatially developing boundary layers. The compensator is shown to successfully reduce the perturbation energy for Tollmien–Schlichting waves and optimal perturbations in the Blasius boundary layer. In a Falkner–Skan–Cooke boundary layer the perturbation energy of traveling and stationary cross-flow disturbances are also reduced.

A nonlinear control approach using the Navier–Stokes equations and the associated adjoint equations are derived and implemented in the context of direct numerical simulations of spatially-developing three-dimensional boundary layer flows and the gradient computation is verified with finite-differences. The nonlinear optimal control is shown to be more efficient in reducing the disturbance energy than feedback control when nonlinear interactions are becoming significant in the boundary layer. For weaker disturbances the two methods are almost indistinguishable.

**Descriptors:** transition control, flow control, feedback control, optimal control, objective function, Orr–Sommerfeld/Squire equations, boundary layer flow, Falkner–Skan–Cooke flow, Navier–Stokes equations, Riccati equation, adjoint equations, DNS, estimation, LQG.

# Preface

This thesis considers the study of feedback and adjoint based control in different boundary layer flows. The thesis is divided in two parts where the first part is an introduction to the research topic and an overview and summary of the present contribution to the field of fluid mechanics. The second part consists of five papers. A guide to the papers and the contributions of different authors is included in the last chapter of part one.

The five papers in part two are adjusted to comply with the present thesis format for consistency, but their content have not been altered compared to published versions except for minor refinements and corrections.

Stockholm, November 2004

Mattias Chevalier

# Contents

Preface		vi
Part 1.	Overview and summary	1
Chapter 1. Overview		2
1.1. Introduction		2
1.2. Optimal control		3
1.3. Outline		5
Chapter 2	2. Linear control	6
2.1. Co	ontroller	7
2.2. Es	timator	9
2.2.1.	Measurements	10
2.2.2.	Stochastic framework	10
2.2.3.	Modeling of the initial condition	10
2.2.4.	Modeling of external disturbances in transitional flows	11
2.2.5.	Modeling of external disturbances in turbulent flows	12
2.2.6.	Modeling of sensor noise	14
2.2.7.	Kalman filter	17
2.2.8.	Extended Kalman filter	18
2.3. Co	ompensator	18
2.4. Nu	nmerics	19
2.4.1.	Spatial discretization	20
2.4.2.	Temporal discretization	20
2.5. Tr	ansitional channel flow estimation	21
2.6. Turbulent channel flow estimation		21
2.7. Co	ompensator results	23
2.7.1.	Parallel Falkner–Skan–Cooke boundary layer	23
2.7.2.	Spatially developing Falkner–Skan–Cooke boundary layer	24
2.7.3.	Tollmien–Schlichting waves in a Blasius boundary layer	25

# viii CONTENTS

2.7.4. S	treamwise streaks in a Blasius boundary layer	27
Chapter 3.	Nonlinear control	29
3.1. Gover	rning equations	29
3.1.1. E	Blowing and suction control	29
3.1.2. In	nitial condition control	30
3.2. Nonlin	near optimization problem and the gradient	30
3.3. Computational issues		32
3.4. Resul	ts	33
3.4.1. E	Blowing and suction control	33
3.4.2. In	nitial value control	34
Chapter 4.	Direct numerical simulations	36
4.1. Pseud	lo-spectral collocation algorithm	36
4.2. Pseud	lo-spectral finite difference algorithm	38
Chapter 5.	Conclusion and summary	39
Chapter 6.	Papers and authors contributions	41
Acknowledgment		44
Bibliography		45
Part 2. Papers		49
Paper 1.	State estimation in wall-bounded flow systems. Part 1. Laminar flows	53
Paper 2.	State estimation in wall-bounded flow systems. Part 2. Turbulent flows	93
Paper 3.	Linear compensator control of a pointsource induced perturbation in a Falkner–Skan–Cooke boundary layer	121
Paper 4.	Linear feedback control and estimation applied to instabilities in spatially developing boundary layers	131
Paper 5.	Adjoint based control in channel and boundary layer flows	161

# Part 1 Overview and summary

#### CHAPTER 1

# Overview

#### 1.1. Introduction

The interest in controlling complex physical phenomena has grown as the need for and the possible benefits from this knowledge have become clearer, both economically but also environmentally. The field of aerodynamics is no exception. For example, large amounts of money could be saved if one could lower the fuel consumption of an airplane by just a fraction. Controlling the flow around the aircraft might be one way to achieve that.

A fluid motion over any surface includes a thin region, called a boundary layer, in which the flow is accelerated from rest to the freestream velocity a short distance above the surface. If disturbances are introduced in the boundary layer, for example through wall roughness, acoustic waves, or freestream turbulence, these disturbances can lead to transition from laminar to turbulent flows. A flow is laminar when the fluid motion is smooth and regular. The turbulent state on the other hand is characterized by rapidly varying velocities in both time and space. The transition phase that occurs between the laminar and turbulent flow has been and still is an area of intensive research. Through a better physical understanding of transition to turbulence it is also easier to understand how to control the different phases.

In many aerodynamic applications it is preferable to have a laminar flow since the friction drag gets lower. For example by extending the laminar flow regions on wings the drag can be reduced and the fuel consumption would decrease as a consequence. In other applications a turbulent flow state is preferable, for example in combustion engines where optimal mixing is desirable.

The transition phase is especially interesting, in terms of control, because we have the prospect of preventing or delaying transition to turbulence by controlling strong inherent instabilities using only minute control efforts.

Flow control, as a concept, covers all kinds of efforts to control flow phenomena. Interest in different aspects of flow control goes back hundreds of years and this interest has now grown into a well-established research area. The notion of flow control includes a wide variety of both methods and applications and a classification of those methods is useful. The first distinction is whether energy is fed into the flow or not. In passive control methods the flow field is altered without any energy addition. One classical example is the golf ball that would fly shorter if it had no dimples. The dimples trigger turbulence

which in turn delay separation and drag is reduced. In *active* control methods, an energy input to the flow is required. This can be done in two ways, either in a predetermined manner, open loop, or in a closed loop form, where some measurements are input to the control loop. The latter method is also known as *feedback control*, which emanates from the fact that measurements of the state is fed back to the controller that *reacts* on the basis of that information.

To construct effective control algorithms a thorough understanding of the underlying physics is needed. However since flow phenomena can be complex and non-intuitive the optimal control can be difficult to find solely based on intuition and knowledge. Therefore we would like to construct the control algorithm in such a way that as little as possible a priori knowledge about the flow is needed. This can be achieved by incorporating modern control theories that more systematically approach the design of the controller. This has been done during the last decade, however, to be able to apply these more advanced feedback flow control algorithms, appropriate sensors and actuators that can sense and act on sufficiently small scales in the flow, are needed. A rapid development in Micro-electro-mechanical systems (MEMS) technology has lead to laboratory experiments with promising devices.

In this thesis different methods of optimal control have been investigated by means of numerical experiments. The main aim has been to prevent transition to turbulence in boundary layer flows by applying blowing and suction control on the boundary. The final goal is to be able to apply the control algorithms to engineering applications but more work has to be done before active optimal control algorithms have reached that state.

Due to the fact that we study flow control through numerical simulations we are limited to low Reynolds numbers and simple geometries. On the other hand, as opposed to an experiment, we can get complete information about the flow state at all times which makes it easier to evaluate and understand different control strategies.

# 1.2. Optimal control

During the last decade, new approaches to solve flow control problems have emerged. By formulating the flow control problems as optimization problems where one wants to minimize or maximize some flow properties, one obtains a problem similar to what is studied in *optimal control* theory. The early publications regarding optimal flow control problems, such as Abergel & Temam (1990), Glowinski (1991), Gunzburger et al. (1989), Sritharan (1991a), Sritharan (1991b), and Gunzburger et al. (1992) are mostly concerned with theoretical aspects of the optimal control problem. Once the theoretical foundation was built, subsequent publications present results from numerical simulations where the optimal control for different flow configurations was computed.

When formulating an optimal control problem we need to have a model that describes the dynamics of the flow. We also need an objective function

#### 4 1. OVERVIEW

that determines what we want to target with the control. Finally we also need to decide the means of control.

A major distinction is whether the governing equations are linear or nonlinear. The nonlinear optimization problems are computationally expensive to solve and the control works only for the very conditions it is designed for. This condition can be relaxed however through a robust control formulation, see e.g. Bewley et al. (2000). Examples of nonlinear control are given Joslin et al. (1997) where the optimal control of spatially growing two-dimensional disturbances in a boundary layer over a flat plate is computed. In Berggren (1998) the vorticity is minimized in an internal unsteady flow using blowing and suction on a part of the boundary and in Bewley et al. (2001) a turbulent flow at  $Re_{\tau} = 180$  is completely relaminarized also using blowing and suction control which was shown in a direct numerical simulations. Other examples of successful application of nonlinear optimal control are given in Collis et al. (2000) where the flow dynamics is modeled in large eddy simulations and in He et al. (2000) where two different control approaches are successfully tested to reduce the drag resulting from the flow around a cylinder. The first approach is to use cylinder rotations to control the flow and the other is to use blowing and suction on parts of the cylinder wall.

The first linear feedback control schemes based on modern control theory are reported in Hu & Bau (1994) and Joshi et al. (1995). In these works closed loop control is achieved by stabilizing unstable eigenvalues. In Joshi et al. (1995) also model reduction is applied. In Bewley & Liu (1998) the control and estimation problem were studied separately for single wavenumber pairs. Transfer functions were used to evaluate the performance. The linear controller was then applied to larger problems. In Högberg et al. (2003b) relaminarization of a turbulent channel flow at  $Re_{\tau}=100$  was demonstrated and in Högberg & Henningson (2002) different transition scenarios were controlled in spatially developing boundary layer flows. Non-parallel flows were also targeted in Cathalifaud & Bewley (2004a) Cathalifaud & Bewley (2004b) where the flow dynamics were modeled by the Parabolized stability equations (PSE).

The state feedback controller has showed to work well even for flows where nonlinear interactions take place we. However in real application the complete state information is seldom available. The full state information requirement can be relaxed through the use of a state estimator. The state estimator reconstructs the flow state based on wall measurements. The controller and estimator was combined into a compensator and tried in direct numerical simulations in Högberg  $et\ al.\ (2003\ a)$  but room for improvement in terms of the estimator efficiency.

The key to successful implementation of optimal control algorithms to engineering applications in the future is that appropriate sensors and actuators can be manufactured small and fast enough to target the small scales of turbulent

flows and to a low cost. The MEMS technology has been shown promising results but much work remains to be done, see e.g. Ho & Tai (1998) and Yoshino  $et\ al.\ (2003)$ .

An overview of much of the most recent progress in the field of flow control is given in Kim (2003). Other recent reviews are given in e.g. Hinze & Kunish (2000), Bewley (2001), Högberg (2001).

#### 1.3. Outline

In chapter 2 a linear optimal control problem is stated and the state feedback control and state estimation approaches used in order to solve the problem are discussed. Chapter 3 introduces the nonlinear optimization problem and presents a standard solution procedure that has been used in the present work. In both chapter 2 and chapter 3 some related results are shown. Chapter 4 gives a short description of the different flow solvers that have been used for the direct numerical simulations presented in this thesis. A summary and conclusions are given in chapter 5 which is followed by chapter 6 describing the different authors contributions to the papers presented in part two of the thesis.

#### CHAPTER 2

# Linear control

The problem of linear model-based feedback control based on noisy measurements can be decomposed into two independent subproblems: first, the state feedback control problem also referred to as full information control, in which full state information is used to determine effective control feedback, and, second, the state estimation problem. In the state estimation problem wall measurements are continuously used to force a real-time calculation of the flow system in an optimal sense such that the calculated estimated flow state eventually approximates the actual flow state.

Once both subproblems are solved, one can combine them to control a flow based on noisy wall measurements of the flow system. The overall performance of the resulting linear feedback control scheme is limited by the individual performance of the two subproblems upon which it is based. For the application of linear control theory to wall-bounded flows, though encouraging results have been obtained previously on the state feedback control problem (see, for example, Bewley & Liu (1998) and Högberg  $et\ al.\ (2003\ a)$ ), more effective state estimation strategies are needed.

In order to apply linear feedback control theory we need a linear system of equations describing the flow, an objective function which determines what the control should target, means of control, and models for the unknown disturbances acting on the flow.

The starting point when designing the state-feedback controller is the Orr–Sommerfeld/Squire equations which govern the evolution of small perturbations of the wall-normal velocity and wall-normal verticity  $(v,\eta)$  in a laminar flow with the streamwise velocity component U=U(y) and the spanwise velocity component W=W(y). Control will be applied through blowing and suction distributed over the complete wall or on parts of the wall. Furthermore, only zero-mass flux control will be allowed since we primarily target the strong instabilities already in the flow with minute energy expenditure and not to adjust the mean flow. The Orr–Sommerfeld/Squire equations are

$$\begin{pmatrix} \dot{\hat{v}} \\ \dot{\hat{\eta}} \end{pmatrix} = \underbrace{\begin{pmatrix} \mathcal{L}_{OS} & 0 \\ \mathcal{L}_{C} & \mathcal{L}_{SQ} \end{pmatrix}}_{\mathcal{L}_{OSS}} \begin{pmatrix} \hat{v} \\ \hat{\eta} \end{pmatrix},$$
(2.1)

where the Orr-Sommerfeld  $(\mathcal{L}_{OS})$ , the Squire  $(\mathcal{L}_{SQ})$ , and the coupling  $(\mathcal{L}_{C})$  operators are

$$\mathcal{L}_{OS} = \hat{\Delta}^{-1} [-i(k_x U + k_z W)\hat{\Delta} + ik_x U'' + ik_z W'' + \hat{\Delta}^2/Re],$$

$$\mathcal{L}_{SQ} = -i(k_x U + k_z W) + \hat{\Delta}/Re,$$

$$\mathcal{L}_C = i(k_x W' - k_z U'),$$
(2.2)

and where  $\{k_x, k_z\}$  is the wavenumber vector,  $\hat{\Delta}$  denotes the horizontally Fourier transformed Laplacian and the wall-normal derivatives are indicated by ('). This system is accompanied by the following boundary conditions for the boundary layer flow

$$\hat{v}(0,t) = \varphi, \quad D\hat{v}(0,t) = 0, \quad \hat{\eta}(0,t) = 0,$$

$$\hat{v}(y,t) = 0, \quad D\hat{v}(y,t) = 0, \quad \hat{\eta}(y,t) = 0, \quad \text{as} \quad y \to \infty.$$
(2.3)

The control enters the system through the boundary condition on the wall-normal velocity  $\varphi$ . The Reynolds number  $Re_{\delta_0^*}$  is based on the freestream velocity and the displacement thickness at x=0 denoted  $\delta_0^*$ . For the channel flow configuration the freestream boundary condition is replaced by a no-slip condition identical to the lower wall boundary condition. In the channel flow the Reynolds number  $Re_{cl}$  is based in the centerline velocity and half-channel width h. Details regarding the linearization for the channel flow can be found in paper 1 and paper 2 and linearization in boundary layer flows can be found in paper 4.

#### 2.1. Controller

In order to apply linear control theory to a dynamical system we need to put it on  $state\ space\ form$ 

$$\dot{q} = Aq + Bu + B_1 f, \quad q(0) = q_0,$$
  
 $r = Cq + q.$  (2.4)

where q is the state. The external disturbances, denoted by f, force the state through the input operator  $B_1$ , and  $q_0$  is the initial condition. The operator  $B_1$  transforms a forcing on (u, v, w) to a forcing on  $(v, \eta)$ . The control signal u affects the system through the input operator B. Operator C extracts the measurements from the state variable, and g adds a stochastic measurement noise with given statistical properties. The noisy measurement is then r. Once we have the physical model on this form, we can apply the tools from control theory, see for example Lewis & Syrmos (1995).

To fit the Orr–Sommerfeld/Squire equations with the accompanying boundary conditions we transform the blowing and suction boundary condition to a volume forcing. Since the system of equations is linear we can use the superposition principle and divide the flow in a homogeneous and a particular part. One valid solution to the particular problem is a stationary solution where the boundary condition is unity. This gives a system where the state q is defined

$$q = \begin{pmatrix} \hat{v}(y,t) \\ \hat{\eta}(y,t) \\ \varphi(t) \end{pmatrix}, \tag{2.5}$$

and operator A and B as

$$A = \begin{pmatrix} \mathcal{L}_{OSS} & 0\\ 0 & 0 \end{pmatrix}, \quad B = \begin{pmatrix} -q_p\\ 1 \end{pmatrix}, \quad u = \dot{\varphi}$$
 (2.6)

. We also define

$$\begin{pmatrix} \hat{v} \\ \hat{\eta} \end{pmatrix} = \begin{pmatrix} \hat{v}_h \\ \hat{\eta}_h \end{pmatrix} + \varphi \begin{pmatrix} \hat{v}_p \\ \hat{\eta}_p \end{pmatrix} = q_h + \varphi q_p. \tag{2.7}$$

Furthermore we are free to choose  $\mathcal{L}_{OSS}q_p=0$  which simplifies the system to solve.

The next step toward defining the optimization problem is to choose the objective function we want to minimize. In this study we have chosen to minimize the perturbation energy

$$J = \int_{0}^{\infty} (q^* \mathcal{Q}q + l^2 u^* u) dt$$
 (2.8)

where  $l^2$  is included to penalize the time derivative of the control  $\dot{\varphi}$ 

$$Q = \begin{pmatrix} Q & Qq_p \\ q_p^* & (1+r^2)q_p^*Qq_p \end{pmatrix}, \tag{2.9}$$

where the term  $r^2$  is an extra penalty on the control signal  $\hat{\varphi}$ , itself and where

$$(\hat{v}^* \quad \hat{\eta}^*) Q \begin{pmatrix} \hat{v} \\ \hat{\eta} \end{pmatrix} = ||q||_E = \langle q, q \rangle_E = \frac{1}{8k^2} \int_{-1}^1 \left( k^2 |\hat{v}|^2 + \left| \frac{\partial \hat{v}}{\partial y} \right|^2 + |\hat{\eta}|^2 \right) dy,$$

$$(2.10)$$

(2.10) is the kinetic energy of the flow perturbation where  $k^2 = k_x^2 + k_z^2$ . We now want to find the optimal K(t) that feeds back the control based on the state q

$$u = K(t)q. (2.11)$$

A detailed derivation of the optimal feedback can be found in Lewis & Syrmos (1995). The lifting procedure as well as the complete derivation of the optimal controller can also be found in, for example, Högberg  $et\ al.\ (2003a)$  and Högberg (2001). The optimal feedback is given through the non-negative self-adjoint solution of a differential Riccati equation (DRE)

$$\frac{\partial X}{\partial t} + A^*X + XA - \frac{1}{\varepsilon}XBB^*X + Q = 0. \tag{2.12}$$

However to simplify the control problem we assume that  $T\to\infty$  which means that the optimal feedback gain is computed for an infinite time horizon of the objective function. This gives us the algebraic Riccati equation (ARE)

$$A^*X + XA - \frac{1}{\varepsilon}XBB^*X + Q = 0 (2.13)$$

as

where X again is the non-negative and self-adjoint solution. Note that the linear feedback law is the same regardless of what kind of disturbances that are present in the flow and is thus computed once and for all for a given base flow. From linear control theory it follows that the optimal choice of control gain K with respect to the chosen objective function is

$$K = -\frac{1}{l^2}B^*X. (2.14)$$

The feedback gain K computed for a sufficient range of wavenumber pairs are then Fourier transformed in the horizontal directions gives us a physical space control law which was first reported in Högberg *et al.* (2003*a*).

#### 2.2. Estimator

One of the primary challenges of the state estimation problem is that its framing is based centrally on quantities which are difficult to model, namely the expected statistics of the initial conditions, the sensor noise, and the external disturbances acting on the system. The state estimation problem may be thought of as a *filtering* problem; that is, the estimator uses the governing equation as a filter to extract, from the available noisy measurements of a small portion of the dynamic system, that component of the measurements which is most consistent with the dynamic equation itself. In other words, the estimator uses the governing equation to extract the signal from the noise, and in the process builds an estimate of the entire state of the system.

We now construct an estimator, analogous to system (2.4), of the form

$$\dot{\hat{q}} = A\hat{q} + Bu - v, \quad \hat{q}(0) = 0,$$
  
 $\hat{r} = C\hat{q}.$  (2.15)

The dynamic operator A and operator B are the same as in system (2.4). Added to this system is also a feedback forcing term v defined as

$$v = L\tilde{r} = L(r - \hat{r}), \tag{2.16}$$

proportional to the difference between the measurements of the flow and estimated flow. The feedback operator L is left to be specified and the choice is crucial for fast convergence of the estimator toward the actual flow.

Once we have supplied models for the statistical quantities of the initial condition  $q_0$ , the unknown external forcing f, and the unknown sensor noise g we can apply linear control theory to formulate and solve an optimization problem which gives an optimal L such that the estimator converges to a good approximation of q. The different statistical models we have chosen are briefly described in the following sections. More detailed descriptions of all the models are found paper 1. Paper 2 contains a detailed modeling of the external disturbances in a turbulent channel flow.

#### 2.2.1. Measurements

The present work attempts to develop the best possible estimate of the state based on measurements of the flow on the wall(s). As discussed in paper 1, and in greater detail in Bewley & Protas (2004), the three measurements assumed to be available at the walls are the distributions of the streamwise and spanwise skin friction and pressure fluctuations.

$$\begin{cases} \tau_x = \tau_{xy}|_{\text{wall}} = \frac{1}{Re} \frac{\partial u}{\partial y}\Big|_{\text{wall}} = \frac{1}{Re} \frac{i}{k^2} (k_x D^2 v - k_z D \eta)|_{\text{wall}}, \\ \tau_z = \tau_{zy}|_{\text{wall}} = \frac{1}{Re} \frac{\partial w}{\partial y}\Big|_{\text{wall}} = \frac{1}{Re} \frac{i}{k^2} (k_z D^2 v + k_x D \eta)|_{\text{wall}}, \\ p = p|_{\text{wall}} = \frac{1}{Re} \frac{1}{k^2} D^3 v|_{\text{wall}}. \end{cases}$$

# 2.2.2. Stochastic framework

The flow system that we want to estimate is affected by an unknown initial condition, the unknown external disturbances that disturb the evolution of the state, and the unknown sensor noise that corrupts the measurements. Since the estimator is intended to converge effectively over a large number of possible realizations, a statistical description (mean and covariance) of these unknown quantities may be used to tune the feedback in the estimator design. The estimator which we will design, also known as a Kalman filter, will be optimal in the sense of obtaining the most accurate estimate possible over a large set of realizations of the system in which the initial conditions, external disturbances, and sensor noise have the assumed statistical properties.

In order to express the stochastic quantities we define the expectation operator  $E[\cdot]$  as the average over all possible realizations of the stochastic input in question. In the present formulation it is the *covariance* that needs to be modeled carefully.

## 2.2.3. Modeling of the initial condition

The aim is to construct an estimator that works well for a range of possible initial conditions. We know however from flow physics that some initial conditions are more likely to appear. We thus construct a covariance model for the initial condition so that we can combine random modes with flow structures that we expect to appear, as for example Tollmien–Schlichting waves, streamwise vortices, or streaks depending on the specific flow conditions. The covariance of the initial condition is denoted  $S_0$ .

Note that the specific initial condition for each wavenumber pair  $\{k_x, k_z\}$  is given only through its shape (of the coherent structures of the forcing) whereas amplitude and phase are random. Furthermore we assume that the mean of the initial condition is zero which means that there is no preferred structure. Due to the fact that the initial condition is always zero in the estimator  $S_0$  also

represents the covariance of the state estimation error. Details on the modeling of the initial condition can be found in paper 1.

# 2.2.4. Modeling of external disturbances in transitional flows

We assume that the external disturbances  $f = (f_1, f_2, f_3)^T$  in equation (2.4) is a zero-mean  $(E[f_j(x, y, z, t)] = 0)$  stationary white Gaussian process with auto-correlation

$$E[f_j(x, y, z, t)f_k(x + r_x, y', z + r_z, t')] = \underbrace{\delta(t - t')}_{\text{Temporal}} \underbrace{Q_{f_j f_k}(y, y', r_x, r_z)}_{\text{Spatial}}, \quad (2.17)$$

where  $\delta(\cdot)$  denotes the Dirac  $\delta$ -function. The derivation for the equations for the covariance of the state is simplified by the assumption of a white random process in time. This assumption is valid when the characteristic time scales of the external disturbances are short compared with the time scales of the flow system. When this is not the case an additional filter can be added that colors the external disturbances (see e.g. Lewis (1986)).

The corresponding quantity in Fourier space is the covariance operator  $R_{f_if_j}$  that we choose to model as

$$R_{f_j f_k}(y, y', k_x, k_z) = \delta_{jk} d(k_x, k_z) \mathcal{M}^y(y, y').$$

To formulate a useful model of  $d=d(k_x,k_z)$  we want to parameterize it in such a way that the expected energy of the disturbances can easily be changed to fit different transition scenarios. For the boundary layer estimation presented in paper 4 the expected energy is assumed to decay exponentially in wavenumber space with the peak located at  $\{k_x^0,k_z^0\}$ 

$$d(k_x, k_z) = \exp\left[-\left(\frac{k_x^0 - k_x}{d_x}\right)^2 - \left(\frac{k_z^0 - k_z}{d_z}\right)^2\right],$$

with the additional design parameters  $d_x$ , and  $d_z$ . The design parameter  $d_y$  determines the width of the two-point correlation of the disturbance in the wall-normal direction according to

$$\mathcal{M}^{y}(y, y') = \exp\left[-\frac{(y - y')^{2}}{2d_{y}}\right],$$

which means that we have localized structures in space.

In figure 2.1 examples of covariance models for both channel and boundary layer flows are presented. Figure 2.1(a) and 2.1(c) show examples on how  $\delta_{jk}\mathcal{M}^y(y,y')$  varies with y and y' for j=1,2,3 and k=1,2,3 for channel and boundary layer flows respectively. The corresponding amplitude distribution as a function of wavenumber pair  $\{k_x,k_z\}$  are shown in 2.1(b) and 2.1(d) for channel and boundary layer flows. The covariance model in Figure 2.1(d) is constructed to account for inflectional instabilities in a Falkner–Skan–Cooke boundary layer, see section 2.7.2. Note that other choices of d and  $\mathcal{M}^y$  can be made which might be experimented with in future work.

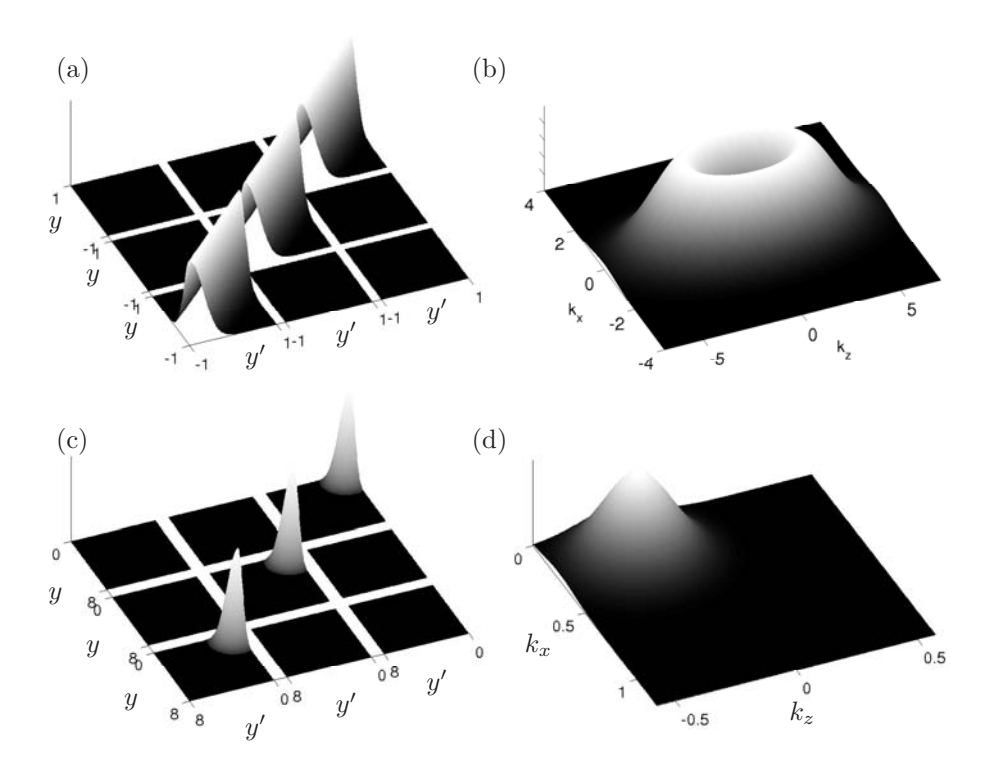


FIGURE 2.1. Statistical model for the external disturbances  $R_{f_jf_k}(y,y',k_x,k_z) = \delta_{jk}d(k_x,k_z)\mathcal{M}^y(y,y')$  acting on system (2.4). (a) Example of the y-variation of  $R_{f_jf_k}$  for channel flow. (b) Example of the amplitude d as a function of the wavenumber pair  $\{k_x,k_z\}$  for channel flow. (c) The y-variation of  $R_{f_jf_k}$  used for the estimation of cross-flow vortices in a FSC boundary layer flow. (d) The amplitude function for the same case as in (c). Note that the peak is translated to wavenumber pair  $\{0.25, -0.25\}$  in order to sense the dominant eigenmode for this particular setup in an efficient manner.

## 2.2.5. Modeling of external disturbances in turbulent flows

A turbulent flow that has reached statistically steady state can be naturally fit into the framework of state feedback with time-independent feedback gains L. In the stochastic forcing vector f in equation (2.4) we now include the statistics of the nonlinear terms of the Navier–Stokes equations that are missing in the linear dynamic operator A. Jovanović & Bamieh (2001) proposed a stochastic disturbance model which, when used to force the linearized open-loop Navier–Stokes equation, led to a simulated flow state with certain second-order statistics (specifically,  $u_{rms}$ ,  $v_{rms}$ ,  $w_{rms}$ , and the Reynolds stress  $-\overline{uv}$ )

which to a certain degree matched statistics from DNS of a turbulent flow at

The system model considered in this work is the Navier-Stokes equation for the three velocity components  $\{U, V, W\}$  and pressure P of an incompressible channel flow, written as a (nonlinear) perturbation about a base flow profile  $\bar{u}(y)$  and bulk pressure variation  $\bar{p}(x)$  such that, defining

$$\begin{pmatrix} U \\ V \\ W \\ P \end{pmatrix} = \begin{pmatrix} u \\ v \\ w \\ p \end{pmatrix} + \begin{pmatrix} \bar{u}(y) \\ 0 \\ 0 \\ \bar{p}(x) \end{pmatrix},$$

where  $\{u, v, w, p\}$  denote the fluctuating components of the flow, we have

$$\frac{\partial u}{\partial t} + \bar{u}\frac{\partial u}{\partial x} + v\frac{\partial \bar{u}}{\partial y} = -\frac{\partial p}{\partial x} + \frac{1}{Re}\Delta u + f_1, \qquad (2.18a)$$

$$\frac{\partial v}{\partial t} + \bar{u}\frac{\partial v}{\partial x} = -\frac{\partial p}{\partial y} + \frac{1}{Re}\Delta v + f_2, \qquad (2.18b)$$

$$\frac{\partial v}{\partial t} + \bar{u}\frac{\partial v}{\partial x} = -\frac{\partial p}{\partial y} + \frac{1}{Re}\Delta v + f_2, \qquad (2.18b)$$

$$\frac{\partial w}{\partial t} + \bar{u}\frac{\partial w}{\partial x} = -\frac{\partial p}{\partial z} + \frac{1}{Re}\Delta w + f_3, \qquad (2.18c)$$

$$\frac{\partial u}{\partial x} + \frac{\partial v}{\partial y} + \frac{\partial w}{\partial z} = 0, \tag{2.19}$$

where

$$f_{1} = -u\frac{\partial u}{\partial x} - v\frac{\partial u}{\partial y} - w\frac{\partial u}{\partial z} - \frac{\partial \bar{p}}{\partial x} + \frac{1}{Re}\frac{\partial^{2}\bar{u}}{\partial y^{2}},$$

$$f_{2} = -u\frac{\partial v}{\partial x} - v\frac{\partial v}{\partial y} - w\frac{\partial v}{\partial z},$$

$$f_{3} = -u\frac{\partial w}{\partial x} - v\frac{\partial w}{\partial y} - w\frac{\partial w}{\partial z}.$$

$$(2.20)$$

The base flow profile  $\bar{u}(y)$  is defined as the mean flow,

$$\bar{u}(y) = \lim_{T \to \infty} \frac{1}{T L_x L_z} \int_0^T \int_0^{L_x} \int_0^{L_z} U dz dx dt,$$

and  $\bar{p}(x)$  is selected to account for the mean pressure gradient sustaining the

We will assume that  $f = (f_1, f_2, f_3)^T$  is essentially uncorrelated from one time step to the next (that is, we assume that f is "white" in time) in order to simplify the design of the estimator. We proceed by developing an accurate model for the assumed spatial correlations of f. As the system under consideration is statistically homogeneous in the x- and z-directions, the covariance of the stochastic forcing f may be parameterized in physical space as in (2.17).

The statistics of f is gathered in direct numerical simulations of turbulent channel flow at Reynolds number  $Re_{\tau}=100$ . As the system under consideration is statistically homogeneous, or "spatially invariant", in the x- and z-directions, it is more convenient to work with the Fourier transform of the two-point correlation  $Q_{f_if_j}$  rather than working with  $Q_{f_if_j}$  itself, as the calculation of  $Q_{f_if_j}$  in physical space involves a convolution sum, which reduces to a simple multiplication in Fourier space. The Fourier transform of  $Q_{f_if_j}$ , which we identify as the spectral density function  $R_{f_if_i}$ , is defined as

$$R_{f_i f_j}(y, y', k_x, k_z) = \frac{1}{4\pi^2} \int_{-L_x/2}^{L_x/2} \int_{-L_z/2}^{L_z/2} Q_{f_i f_j}(y, y', r_x, r_z) \exp[-ik_x r_x - ik_z r_z] dr_x dr_z.$$
(2.21)

Note that we neglect correlations between different wavenumber pairs as this is not needed the way we build the estimator. The spectral density function can thus be written

$$R_{f_i f_j}(y, y', k_x, k_z) = \lim_{T \to \infty} \frac{1}{T} \int_0^T f_i(k_x, y, k_z) f_j^*(k_x, y', k_z) dt.$$
 (2.22)

For each wavenumber pair  $\{k_x, k_z\}$  we now have a matrix of covariance data  $R_{f_if_j} = R_{f_if_j}(y,y',k_x,k_z)$  which can be seen for different wavenumber pairs in figure 2.2. The data is then used in the optimization problem when computing the feedback gains. The resulting estimation gains are well resolved for the range of wavenumber pairs used in the DNS. The gains transformed to physical space convolution kernels are shown in figure 2.3 for the v (left column) and  $\eta$  (right column) components of the flow and for the three measurements  $\tau_x$ ,  $\tau_z$ , and p. The maximum amplitude as a function of wavenumber pair  $\{k_x, k_z\}$  is shown in figure 2.4.

All turbulent direct numerical simulations are performed with the code briefly described in chapter 4 and more thoroughly in paper 2.

## 2.2.6. Modeling of sensor noise

All three wall measurements described in section 2.2.1 are assumed to be corrupted by sensor noise. The noise for each sensor is modeled as a random process, white in both space and time, and where the amplitude determines the quality of each sensor. The measurements are also assumed to be independent of each other. The covariance of the noise vector g, appearing in system (2.4), can thus be described in Fourier space by a diagonal  $3 \times 3$  matrix G whose diagonal elements  $\alpha_t^2$  are the variances of the individual sensor noise.

When the signal-to-noise ratio is low the measured signal should be fed back gently into the estimator. If the signal-to-noise ratio is high we trust the signal and thus it can be fed back with more strength.

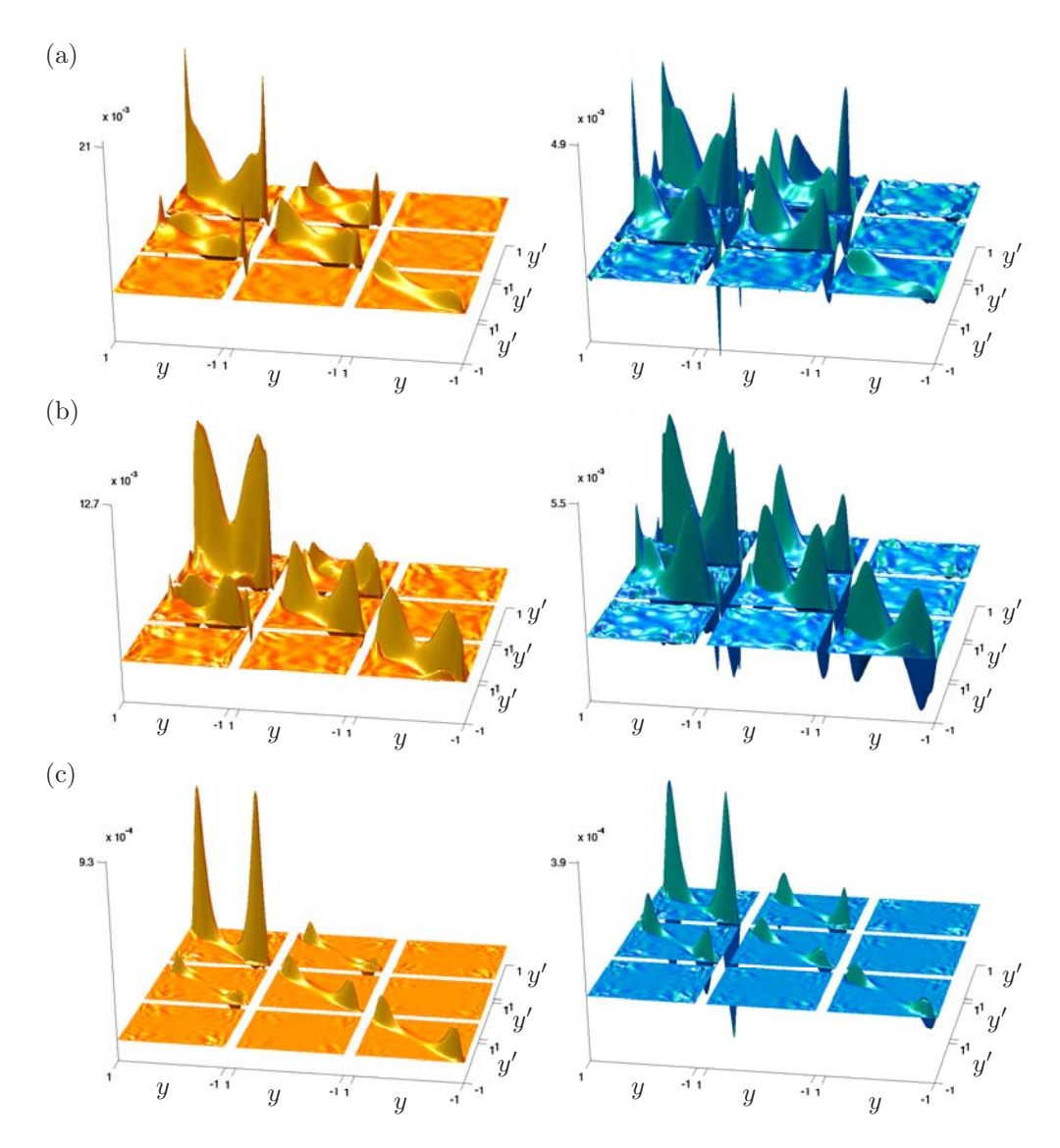


FIGURE 2.2. The covariance of  $\hat{f}$ , taken from DNS, at wavenumber pair  $\{0.5, 1.5\}$ ,  $\{3, 1.5\}$ , and  $\{10, 30\}$  in figure (a), (b), and (c) respectively. The nine "squares" correspond to the correlation between the different components of the forcing vector. From top to bottom and left to right the components are  $f_1$ ,  $f_2$ , and  $f_3$  on each axis. The width of each side of each square represents the width of the channel, [-1,1]. The variance is seen along the diagonal of each square. The left column contains the real part and the right column represents the imaginary part.



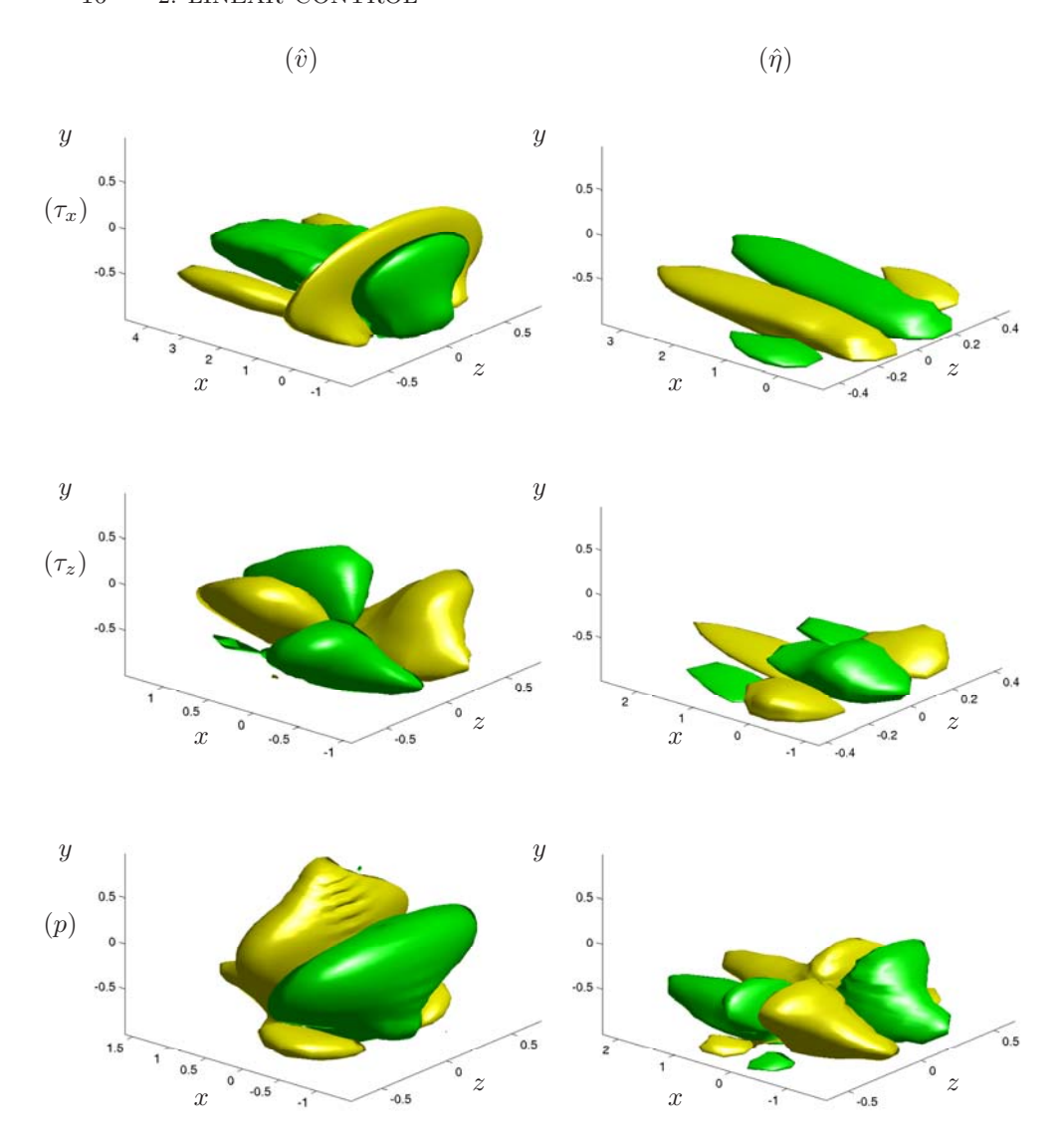


Figure 2.3. Isosurface plots of steady-state estimation convolution kernels relating the measurements  $\tau_x$ ,  $\tau_z$ , and p at the point  $\{x=0,\ y=0,\ z=0\}$  on the wall to the estimator forcing on the interior of the domain for the evolution equation for the estimate of (left)  $\hat{v}$  and (right)  $\hat{\eta}$ . Positive (green) and negative (yellow) isosurfaces with isovalues of  $\pm 5\%$  of the maximum amplitude for each kernel are illustrated. The kernels are based on statistical data gathered from turbulent direct numerical simulations.

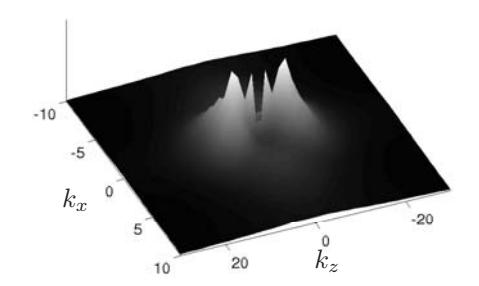


FIGURE 2.4. Maximum amplitude of turbulent covariance data as a function of wavenumber pair  $\{k_x, k_z\}$ . The corresponding two-point correlations along the wall-normal coordinate are shown in figure 2.2.

For transitional flows an intermediate level of feedback is desired in the estimator design due to the fact that if the feedback becomes too strong it may knock the estimated flow out of the small perturbation neighborhood assumed in the linear model used in the design process. On the other hand if it becomes to weak the convergence in the estimator may be both slow and inaccurate. For given covariances of the initial conditions and external disturbances we thus have the means, through the sensor noise, to tune the feedback strength into the estimator.

#### 2.2.7. Kalman filter

Kalman filter theory, combined with the models outlined in sections 2.2.3, 2.2.4, and 2.2.6 for the statistics of the unknown initial conditions  $q_0$ , the unknown external forcing f, and the unknown sensor noise g respectively, provides a convenient and mathematically-rigorous tool for computing the feedback operator L in the estimator described above such that  $\hat{q}$  converges to an accurate approximation of q. Note that the volume forcing v used to apply corrections to the estimator is proportional to the measurement error  $\tilde{r} = r - \hat{r}$ .

The solution of the Kalman filter problem in the classical, finite-dimensional setting is well known (see, e.g., Lewis & Syrmos (1995) p. 463–470). The corresponding operator equations applicable here, though more involved to derive, are completely analogous (see Balakrishnan 1976).

From linear control theory is follows that the covariance  $S(t) = R_{qq}(t)$  of the flow state q(t) is governed by the Lyapunov equation

$$\dot{S}(t) = AS(t) + S(t)A^* + BRB^*, \quad S(0) = S_0. \tag{2.23}$$

The covariance  $P(t) = R_{\tilde{q}\tilde{q}}(t)$  of the state estimation error  $\tilde{q}(t) = q(t) - \hat{q}(t)$ , for a given L(t), is governed by the Lyapunov equation

$$\dot{P}(t) = A_0(t)P(t) + P(t)A_0^*(t) + BRB^* + L(t)GL^*(t), \quad P(0) = S_0, \quad (2.24)$$

where  $A_0(t) = A + L(t)C$ . The optimal L(t) that minimizes the expected energy of the state estimation error at all times (that is, which minimizes the trace of P(t)) is given by the solution of the differential Riccati equation (DRE)

$$\dot{P}(t) = AP(t) + P(t)A^* + BRB^* - P(t)C^*G^{-1}CP(t), \quad P(0) = S_0, \quad (2.25)$$
 where

$$L(t) = -P(t)C^*G^{-1}. (2.26)$$

Note that the expressions in equations (2.23), (2.24), and (2.25) are identical in both the finite-dimensional and infinite-dimensional settings.

Note also that, for a linear, time-invariant (LTI) system (that is, for A, B, C, R, G independent of time), the covariance of the estimation error, P(t), and the corresponding feedback which minimizes its trace, L(t), follow a transient near t=0 due to the effect of the initial condition  $S_0$ , eventually reaching a steady state for large t in which  $\dot{P}(t)=0$  and  $\dot{L}(t)=0$ . In order to minimize the magnitude of the transient of the trace of P(t), it is necessary to solve the differential Riccati equation given above. If one is only interested in minimizing the trace of P(t) at statistical steady state, it is sufficient to compute time-independent feedback L by solving the algebraic Riccati equation (ARE) formed by setting  $\dot{P}(t)=0$  in (2.25).

# 2.2.8. Extended Kalman filter

The Kalman filter is an "optimal" estimator (in several rigorous respects—see Anderson & Moore (1979) for a detailed discussion) in the linear setting. When a Kalman filter is applied to a nonlinear system, its performance is typically degraded, due to the fact that the linear model upon which the Kalman filter is based does not include all the terms of the (nonlinear) equation governing the actual system. A common approach to partially account for this deficiency is to reintroduce the system nonlinearity to the estimator model after the Kalman filter is designed. This approach is called an extended Kalman filter, see e.g. Gelb (1974). This type of estimator is identical to the Kalman filter except that the nonlinearity in the system is also present in the estimator model when marching in time. The extension makes some sense: if the estimate of the state happens to match the actual state, no feedback from measurements is required for the extended Kalman filter to track the subsequent flow state. This is not the case for the standard (linear) Kalman filter.

#### 2.3. Compensator

The compensator combines the full information controller described in section 2.1 with the state estimator described in section 2.2 in the sense that the estimated flow state in the estimator is fed into the controller. Since the estimator

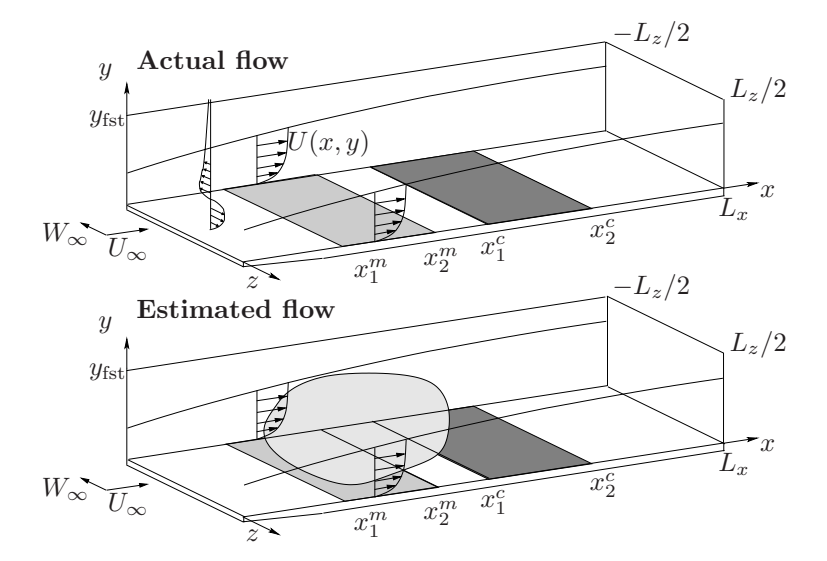


FIGURE 2.5. Compensator configuration. The upper box represents the "real" flow where the light grey rectangle along the wall is the measurement region and the corresponding dark grey rectangle is the control area. In the beginning of the box a perturbation is indicated as a function of the wall-normal coordinate. This perturbation will evolve as we integrate the system in time. The estimated flow system is depicted in the lower box. Here the volume force that is based on the wall measurements and the estimation gains is shown as a grey cloud in the computational domain.

only relies on different measurements of flow quantities at the wall the requirement of complete flow information to compute a control is relaxed which closes the gap to experimental realization of the control algorithm. Note however that instead a real-time calculation of the estimator flow system has to be done.

The compensator algorithm is depicted in figure 2.5. The "real" flow could be an experimental setup where only wall information is extracted. However, so far in our studies the "real" flow has always been a computer simulation. The algorithm can be summarized in the following steps:

- 1. Extract wall measurements in both "real" and estimated flow
- 2. Compute the estimator volume forcing based on precomputed estimation gains and the difference of the wall measurements from the "real" and estimated flow
- 3. Apply the volume forcing to the estimator flow to make it converge to the "real" flow
- 4. Compute control signal based on the reconstructed state in the estimator
- 5. Apply the control signal in both the "real" and estimated flow

#### 2.4. Numerics

In order to compute the optimal control and feedback gains from the ARE or the DRE, it is necessary to discretize the operator form of the equations (2.13) and (2.25) and solve them in the finite-dimensional setting. However, in order to be relevant for the PDE problem of interest, the resulting feedback gains must converge to continuous functions as the numerical grid is refined.

#### 2.4.1. Spatial discretization

We need to build discrete system operators for A, B,  $B_1$ , C, their respective adjoints as well as the energy measure Q in the objective function and the disturbance covariances R, G, and  $S_0$ . In all our studies, the discrete operators are obtained through enforcement of the Orr–Sommerfeld/Squire equations at each point of a Gauss–Lobatto grid using a Chebyshev collocation scheme, taking

$$f_i = f(y_i), \quad y_i = \cos \frac{i\pi}{N}, \quad i = 0, \dots, N,$$

where N+1 is the number of grid points in the wall-normal direction. The discrete operators and differentiation matrices are determined using the spectral Matlab Differentiation Matrix Suite of Weideman & Reddy (2000). This suite provides differentiation matrices invoking clamped boundary conditions  $(f(\pm 1) = f'(\pm 1) = 0)$ , using the procedure suggested by Huang & Sloan (1993), to give an Orr–Sommerfeld/Squire matrix with satisfactory numerical properties, avoiding unstable or lightly-damped spurious eigenmodes. The first-order, second-order, and third-order differentiation matrices so obtained, denoted  $D^1$ ,  $D^2$ , and  $D^3$  respectively, are combined according to the equations given previously to compute the discrete matrices A, B, and C in a straightforward fashion.

Necessary adjoint operators are defined in a discrete sense meaning that they are the conjugate transpose of the operator itself. The integration weights  $W(y_j)$  for the Chebyshev grid with the Gauss–Lobatto collocation points are computed using the algorithm from Hanifi *et al.* (1996). These weights provide spectral accuracy in the numerical integration used to assemble the energy measure matrix Q.

#### 2.4.2. Temporal discretization

When searching for the infinite time horizon control feedback or the estimation feedback for statistically steady state we only solve the ARE defined in equation (2.13). However, in paper 1 we also solve the time evolution of the estimation feedback gains which requires the solution of the DRE defined as in equation (2.25). One could directly march the DRE in time with, for example, a Runge–Kutta method but instead we choose to march in time the Chandrasekhar equation, see Kailath (1973), which solves for the time derivative of the estimation error covariance matrix,  $\dot{P}(t)$ . More details about the algorithm are found in paper 1.

#### 2.5. Transitional channel flow estimation

The stochastic models that are developed in paper 1, and briefly discussed in section 2.2, are used to estimate infinitesimal as well as finite amplitude perturbations in direct numerical simulations of a channel flow at  $Re_{cl} = 3000$  based on the centerline velocity and channel half width. The localized flow perturbations studied in Henningson *et al.* (1993) are used to test the convergence of the estimator.

The evolution of the energy of the state and estimation error for both the moderate-amplitude and the small-amplitude perturbations are plotted in figure 2.6. All curves have been normalized to unity at t=0 to ease the comparison. The difference in normalized energy between the two cases is due to nonlinear interactions that take place in the moderate-amplitude case (compare the thick solid line and the thick dashed line). For both cases, the initial stage of the evolution (during which nonlinear effects are fairly small) is well estimated (thin lines). As the moderate-amplitude perturbation evolves and its amplitude grows, nonlinear effects become significant, and the performance of the linear estimator (thin solid line) is degraded as compared with the performance of the linear estimator in the small-amplitude case (thin dashed line), but still it is relatively good when compared to the flow energy.

By using an extended Kalman filter, as described in section 2.2.8, the performance of estimator is improved when nonlinear interactions are present in the flow to be estimated. This can be clearly seen in figure 2.6 where the extended Kalman filter (thin dot-dashed line) is performing better than its standard Kalman filter counterpart (the thin solid line).

For these cases nine different set of estimation gains have been applied which are the optimal gains at the times given in the following sequence  $\{1, 2, 3, 4, 5, 10, 15, 20, 60\}$ . This sequence captures the fast initial transient in the gains and converges to the steady state gains.

#### 2.6. Turbulent channel flow estimation

By using statistics of nonlinear terms in the Navier–Stokes equations, as outlined in paper 2, into the state feedback optimization problem we can compute well-resolved estimation gains for all three wall-measurements defined defined in section 2.2.1. Here we have chosen to define the measurement vector r to contain scaled versions of the wall values of the wall-normal derivative of the wall-normal vorticity,  $\eta_y/Re$ , the second wall-normal derivative of the wall-normal velocity,  $v_{yy}/Re$ , and the pressure, p. Note that we can easily relate this transformed measurement vector to the raw measurements of  $\tau_x = u_y/Re$ ,  $\tau_z = w_y/Re$ , and p on the walls, which might be available from an experiment.

The resulting physical-space convolution kernels, shown in section 2.2.5, are then used to estimate a turbulent channel flow at  $Re_{\tau}=100$  with both Kalman and extended Kalman filters. In order to tune the available estimator parameters the Reynolds number was kept low to ease the resolution requirements and hence the computational effort for the simulations.

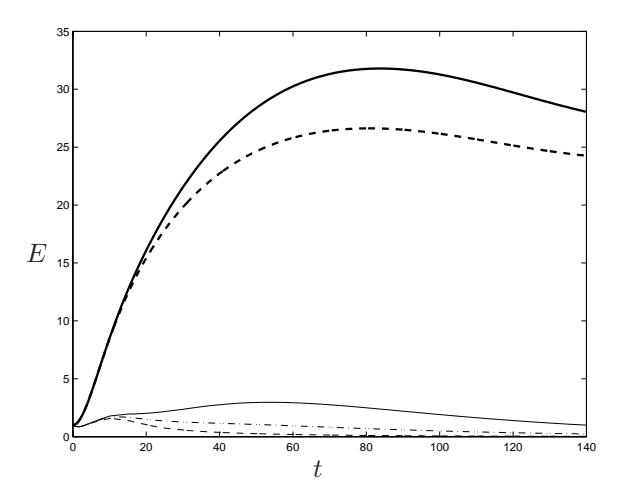


FIGURE 2.6. Evolution of the normalized flow energy (thick lines) and normalized estimation error energy (thin lines) for the case with moderate-amplitude initial conditions (solid) and low-amplitude initial conditions (dashed). The evolution of the normalized estimation error energy for the extended Kalman filter in the case with moderate-amplitude initial conditions is also plotted (thin dot-dashed line), illustrating a significant improvement as compared with the performance of the corresponding Kalman filter (thin solid line) when nonlinearities are significant.

In figure 2.4 the total energy of the estimation error, defined as

$$\operatorname{errn}_{y}^{\text{tot}}(q,\hat{q}) = \frac{\left(\int_{0}^{L_{x}} \int_{0}^{L_{z}} (\hat{q} - q)^{*} Q(\hat{q} - q) \, \mathrm{d}x \mathrm{d}z\right)^{1/2}}{\left(\int_{0}^{L_{x}} \int_{0}^{L_{z}} q^{*} Q q \, \mathrm{d}x \mathrm{d}z\right)^{1/2}},$$
(2.27)

is plotted versus the wall-normal coordinate. The actual and estimated state are denoted by q and  $\hat{q}$  respectively. This is the quantity that we, in an average sense, are minimizing for in the construction of the optimal estimation gains which makes it a relevant measure when evaluating the performance of the estimator. Note that operator Q represent the energy inner-product in  $(v,\eta)$  coordinates as defined in (2.10). Close to the wall the error is small but it increases as we go further into the channel. The thin and thick lines are from Kalman and extended Kalman filter simulations respectively. To further investigate the impact of using estimation gains based on the statistics from the present study or based on simpler models such as assuming spatially uncorrelated stochastic forcing we also test the estimator performance (shown as dashed lines) for only one measurement. Based on a spatially uncorrelated stochastic model and the numerical approach presented in section 2.4.1 it is not

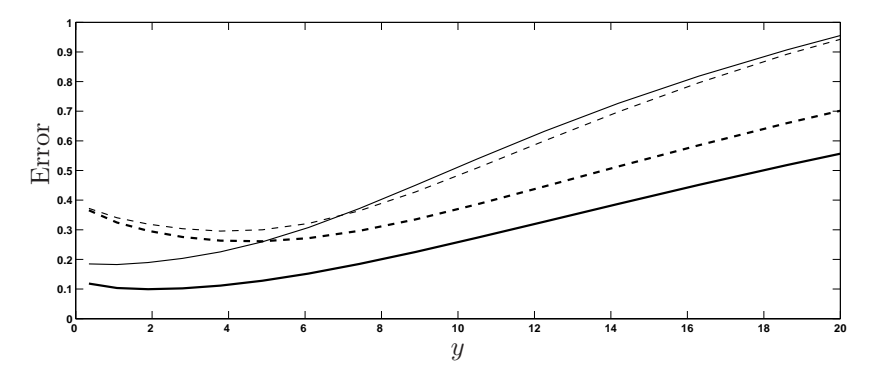


FIGURE 2.7. The total energy of the estimation error is shown as a function of the wall-normal distance. The solid line denotes the error when all three measurements are applied in the estimator. The dashed line represents the estimator performance when using only the  $\eta_y$  measurement respectively. The thick lines show the extended Kalman filter and the thin lines the Kalman filter data.

possible to retrieve well-resolved gains for more than one measurement. The major difference however comes from the fact that we now have estimation gains for all three measurements which can be seen as the solid lines in figure 2.7. Despite the strong nonlinear interactions in the turbulent flow the Kalman filter is performing surprisingly well compared to the extended Kalman filter.

# 2.7. Compensator results

A summary of the compensator results from paper 4 are discussed in the following section. For details about box sizes and resolutions and the numerical parameters for the different disturbances see paper 4. The code used for the compensator simulations are described in chapter 4.

Note, that in the work with compensators in spatially developing boundary layers so far we let the estimator run for a while before we turn on the controller. Once the estimator has converged we turn on the controller and we thereby close the loop in figure 1 2.5. This is done to give the controller better initial state information. Note also that we let all perturbation types evolve long enough so that they have propagated through the computational box before we turn in the control. In future studies we will explore the limits of the compensator in terms of how much information the controller needs in the initial transient phase.

#### 2.7.1. Parallel Falkner-Skan-Cooke boundary layer

To verify the compensator algorithm in the DNS code we tested it in a parallel Falkner–Skan–Cooke (FSC) boundary layer flow with low-amplitude disturbances. The base flow considered has a Reynolds number  $Re_{\delta_0^*} = 337.9$  based on

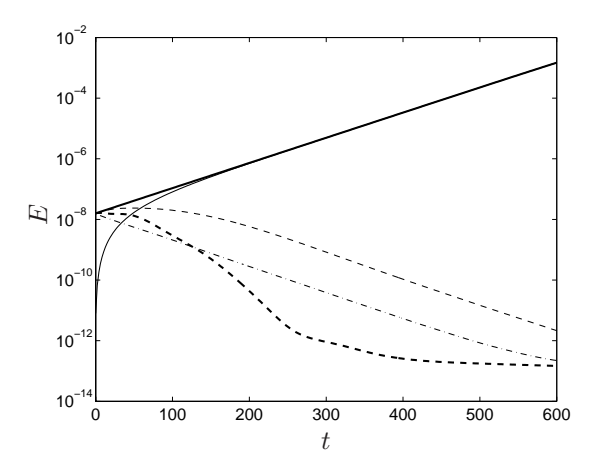


FIGURE 2.8. Time evolution of the perturbation energy of the uncontrolled unstable eigenmode at  $\alpha=0.25, \beta=-0.25$  in a Falkner–Skan–Cooke boundary layer and the corresponding controlled system. Solid: uncontrolled energy growth. Dashed: full information control is applied. Solid-thin: energy growth in the estimator when no control is applied. Dash-dotted-thin: the estimation error when no control is applied. Dashed-thin: compensator control is applied.

the displacement thickness,  $\delta_0^*$ , and chordwise freestream at the beginning of the computational box. There is also a spanwise velocity component  $W_{\infty} = 1.442$  of the base flow normalized with the chordwise freestream velocity. The initial condition is perturbed with an unstable eigenmode at wavenumber pair  $\{k_x = 0.25, k_z = -0.25\}$ . Due to an inflection point in the base flow this eigenmode grows exponentially in time as can be seen in figure 2.8. Both the full information controller and the compensator control are able to switch the exponential disturbance growth into decay. Since the initial condition in the estimator is the base flow without any perturbations the compensator performance is not as good as the full-state information in the beginning. Once the estimate gets closer to the real flow the disturbance is decaying exponentially when compensator control is applied.

# 2.7.2. Spatially developing Falkner-Skan-Cooke boundary layer

The same base flow setup as described in section 2.7.1 is used here with the only difference that the flow is now developing downstream. A perturbation with random spanwise distribution and randomly varying amplitudes develop into traveling cross-flow vortices downstream.

The measurement region is located in  $x \in [40, 150]$  and the control is applied in the strip  $x \in [175, 325]$ . In figure 2.9 the time averaged perturbation energy as a function of the chordwise coordinate and integrated in the spanwise

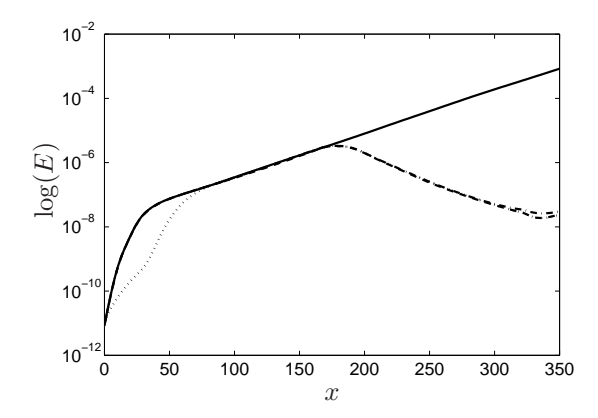


FIGURE 2.9. Time averaged perturbation energy for cross-flow vortices in a spatial Falkner–Skan–Cooke boundary layer. Solid: uncontrolled energy growth. Dashed: full information control. Dash-dotted: energy growth and decay when compensator control is applied.

direction is plotted for uncontrolled flow (solid) and full information control (dashed) and compensator control (dash-dotted).

The perturbation energy in the estimator is shown as a dotted line. As can be seen in the figure the performance of the two controllers are similar. The compensator control is only slightly less efficient in reducing the perturbation energy than the full information controller and they both turn exponential growth in to decay. In figure 2.10(a) and (b) the wall-normal velocity component is shown in a x-z plane at y=0.5 for uncontrolled and compensator controlled flow respectively. At the beginning of the control region, the control is of opposition type since the light and dark regions are shifted over the control domain.

Figure 2.11 shows the evolution of disturbance energy integrated in space. During the first 2000 time units the "real" flow is run in parallel with the estimator to let the estimator catch up. After about 500 time units the estimated state has converged to the actual flow downstream of the measurement region. At t=2000 the compensator control is turned on and the disturbance energy starts to decay.

#### 2.7.3. Tollmien-Schlichting waves in a Blasius boundary layer

The Tollmien–Schlichting (TS) wave perturbation is applied and studied in a Blasius boundary layer with zero streamwise pressure gradient. We also assume no mean-flow component in the z-direction. The wave is introduced by applying an oscillating volume force localized in the x- and z-direction in the far upstream part of the computational box. The dimensionless oscillating frequency is F=200 where  $F=10^62\pi f\nu/U_\infty^2$  and where f is the frequency

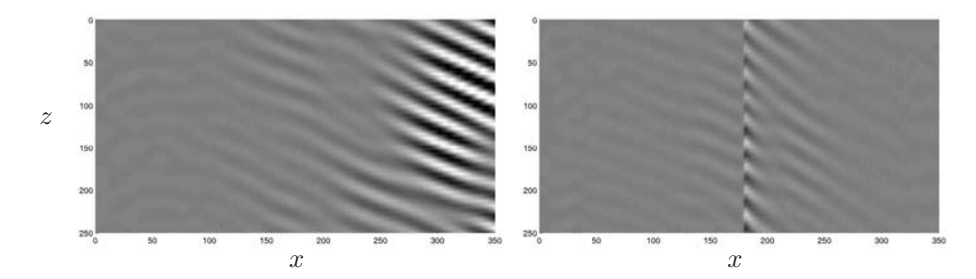


FIGURE 2.10. Snapshots of the wall-normal velocity component at y=0.5. The flow state is depicted in part (a). In (b) the effect of the compensator control is shown. In the controlled flow the control has been applied for 2000 time units i.e. all the transient effects that occur due to the startup of the control with the perturbations present have settled down. The control is applied in  $x \in [175, 325]$ . The black to white scale lies in the interval  $v \in (-0.00045, 0.00045)$ .

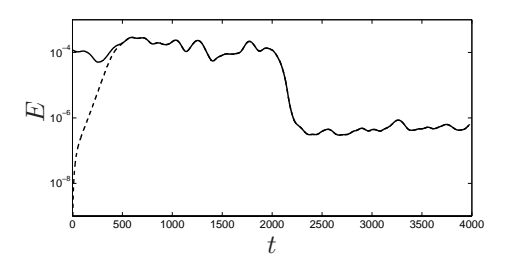


FIGURE 2.11. Time evolution of the disturbance energy integrated throughout the computational box. During the first 2000 time units the flow is uncontrolled. At time t=2000 the compensator control is turned on. Solid: energy in the "real" flow. Dashed: energy in the estimator.

and  $\nu$  is the kinematic viscosity. Branch I for this TS-wave is located at x=27 and extends to branch II at x=219. The measurement region is  $x\in[40,150]$  and the control region is  $x\in[175,325]$  which means that they both overlap the exponential growth region between branch I and branch II.

In figure 2.12 the uncontrolled energy growth and decay is plotted as a solid line. The volume forcing does not impose a clean TS-wave from the beginning which explains the initial transient and but further downstream a TS-wave is emerging and we get the expected exponential growth. The dashed and dash-dotted lines show the energy growth which is soon turned into decay in the beginning of the control region when the full information and compensator control are applied. The difference between the full information control and compensator control is due to the approximative flow state from the estimator the compensator control is based on. However, despite the approximative flow

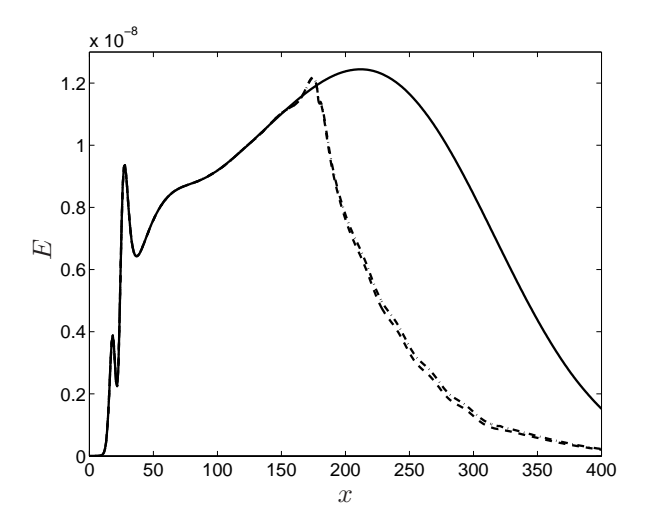


FIGURE 2.12. Spatial evolution of the perturbation energy of a TS-wave in a spatially growing boundary layer. Solid: uncontrolled energy growth. Dashed: energy growth and decay when full information control is applied. Dash-dotted: energy growth and decay with compensator control.

state information the compensator is are able to turn the exponential growth into exponential decay.

### 2.7.4. Streamwise streaks in a Blasius boundary layer

A transient growth scenario is studied where optimal perturbations are developing downstream to form streamwise streaks. The spatial optimal perturbation (see Andersson *et al.* (1999) and Luchini (2000)) with maximum growth at x=237 is introduced in the fringe region.

The measurement region is located in  $x \in [0,300]$  and the control is applied in two different simulations at  $x \in [300,450]$  and  $x \in [300,750]$  respectively. In figure 2.13 the disturbance energy integrated in time and spanwise direction, is shown. Both the full information control (dashed) and the compensator control (dash-dotted) equally well manage to lower the disturbance amplitude over the control strip. The longer interval is shown with thin lines and the short interval is represented with thick lines. Right behind both the control strips however there is a stronger dip for the full information controller. Eventually the disturbance energy starts to increase again but without reaching the amplitude levels for the uncontrolled flow. Note that the gains are computed for a flow linearized around the same streamwise position at x = 375.

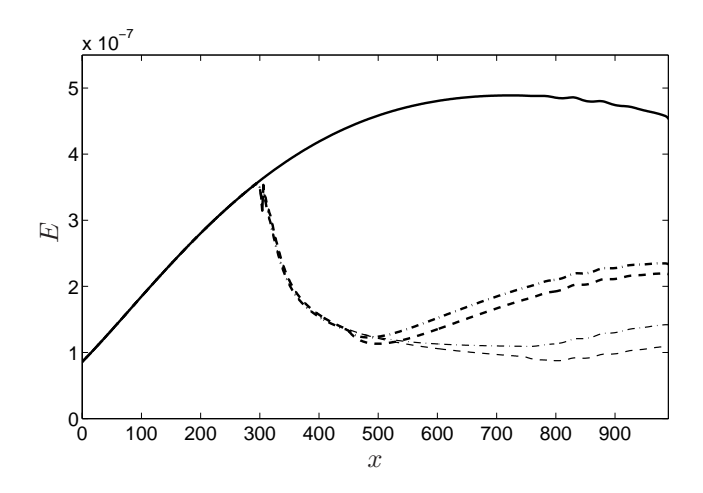


FIGURE 2.13. The energy of the optimal spatial perturbation at x=237.24 as a function of downstream position. Solid: uncontrolled energy growth. Dashed: full information control applied in region  $x \in [300,450]$ . Dash-dotted: compensator control with the measurement region  $x \in [0,300]$  and the control region  $x \in [300,450]$ . Thin-solid: estimator energy. Thin-dashed: full information control applied in region  $x \in [300,725]$ . Thin dash-dotted: compensator control with the measurement region  $x \in [0,300]$  and the control region  $x \in [300,725]$ .

#### CHAPTER 3

# Nonlinear control

The goal of an optimal controller is to minimize or maximize an objective function. When formulating such a problem, three important decisions are needed, governing equations, an objective function to determine what we want to control, and means of control. For a particular flow geometry with given fluid properties, each choice has to be made with care. The state equation should of course model the appropriate physics. This choice also indirectly affects the choice of methods to use when solving the optimal control problem. If we are working with nonlinear governing equations, such as the Navier-Stokes equations, we have to use an iterative procedure to solve the optimization problem and retrieve the optimal control, as opposed to the linear controller which can be applied online in a feedback loop. This is further described in chapter 2. In this chapter two different nonlinear optimization problems are stated, solution strategies are described and some results are presented. In terms of nonlinear control the main effort has been directed toward finding optimal blowing and suction profiles in boundary layer flows. An initial study to find optimal initial conditions is also described. The complete descriptions of the nonlinear optimization studies are found in paper 5.

# 3.1. Governing equations

3.1.1. Blowing and suction control

The governing equations are the incompressible Navier–Stokes equations, here written on dimensionless form,

$$\begin{cases}
\frac{\partial u}{\partial t} + (u \cdot \nabla)u = -\nabla \pi + \frac{1}{Re} \Delta u, \\
\nabla \cdot u = 0, \\
u|_{t=0} = u_0,
\end{cases}$$
(3.1)

where  $u = (u_1, v, w)$  is the velocity vector and  $\pi$  is the pressure. Periodic boundary conditions in x- and z-directions, and control through blowing and suction together with a no-slip condition for the directions parallel to the wall gives the complete set of boundary conditions. The numerical scheme is further described in chapter 4.

To get the desired effect out of the control one needs to choose what properties of the flow to target. This choice is formulated as an *objective function* 

which in this particular case has the form

$$J(\varphi) = \frac{\varepsilon}{2} \int_{T_1^c}^{T_2^c} \int_{\Gamma} |v|^2 d\Gamma dt + \frac{1}{2} \int_{T_1^o}^{T_2^o} \int_{\Omega} |u - u_T|^2 dQ,$$
 (3.2)

where  $(T_1^c, T_2^c)$  is the control time period and  $(T_1^o, T_2^o)$  is the observation time period. The target velocity profile is denoted by  $u_T$  and the control, which is the wall-normal velocity on the wall, is denoted by v. A regularization term with penalty parameter  $\varepsilon$  is also added to put a limit on the control strength. The choice of objective function is usually a non-trivial matter due to the complicated physics present in aerodynamic flows.

#### 3.1.2. Initial condition control

The derivation and implementation of finding the optimal initial condition that gives the highest energy amplification is done for channel flows. The non-dimensional, incompressible Navier–Stokes equations with Reynolds number, Re, based on the centerline velocity and half the channel height are,

$$\begin{cases}
\frac{\partial u}{\partial t} + (u \cdot \nabla)u - \frac{1}{Re}\Delta u + \nabla \pi = -\nabla P, \\
\nabla \cdot u = 0, \\
u|_{t=0} = \varphi + u_T(0),
\end{cases}$$
(3.3)

where  $u=(u_1,v,w)$  is the velocity vector,  $\pi$  is the pressure and  $\nabla P$  represents the pressure gradient driving the flow and can either be constant or used to ensure constant mass flux. The control  $\varphi$  is entering the equations through the initial condition as a disturbance on top of a laminar flow. Periodic boundary conditions are assumed in the x- and z-directions and no-slip conditions for the directions parallel to the walls.

The objective function J measures the ratio in disturbance energy at final and initial time

$$J(\varphi) = -\frac{\int_{\Omega} |u(T) - u_T(T)|^2 d\Omega}{\int_{\Omega} |\varphi|^2 d\Omega}.$$
 (3.4)

Time T denotes the final simulation time. The target velocity profile denoted  $u_T$  represents the laminar flow field.

# 3.2. Nonlinear optimization problem and the gradient

Once the objective functions (3.2) and (3.4) are defined we can formulate the nonlinear optimization problem as: find  $\varphi^*$  which satisfies

$$J(\varphi^*) \le J(\varphi) \quad \forall \ \varphi \in \mathcal{U}_{ad}$$
 (3.5)

where  $\mathcal{U}_{ad}$  has been used to denote the set of admissible controls.

To solve the nonlinear optimization problem (3.5) we use a gradient based approach. The gradient of the objective function,  $\nabla J$ , is defined by

$$\delta J(\varphi) = \lim_{s \to 0} \frac{J(\varphi + s \,\delta\varphi) - J(\varphi)}{s} = \langle \nabla J, \delta\varphi \rangle$$

$$= \left\langle \frac{\partial J}{\partial \varphi_L}, \delta\varphi \right\rangle + \left\langle \frac{\partial J}{\partial \varphi_U}, \delta\varphi \right\rangle, \tag{3.6}$$

where  $\delta\varphi$  is the first variation of the control. The functional  $\delta J$  is the first variation of J with respect to  $\delta\varphi$ . The gradient may be expressed in terms of the solution of an *adjoint equation*. The complete derivation of the adjoint equations and the corresponding gradients are given in paper 5 in this thesis. Here we only state the final gradient expressions that rely on the adjoint state p and adjoint pressure denoted  $\sigma$ .

For the blowing and suction control the gradient becomes

$$\frac{\partial J}{\partial \varphi} = \int_{\Gamma_c} \psi \left( \varepsilon \varphi^T \psi - \sigma \right) d\Gamma, \tag{3.7}$$

where  $\psi$  denotes the base functions for the control and  $\Gamma_c$  denotes the control interval.

For the initial condition control we can identify the gradient of the objective function (3.4) to be

$$\frac{\partial J}{\partial \varphi} = \frac{1}{c} \left[ a \varphi - b p(0) \right],$$

where the constants  $a,\,b,\,{\rm and},\,c$  are defined as

$$a = \int_{\Omega} |u(T) - u_T(T)|^2 d\Omega, \quad b = \int_{\Omega} |\varphi|^2 d\Omega, \quad \text{and} \quad c = \left[\int_{\Omega} |\varphi|^2 d\Omega\right]^2.$$

The first term of the gradient is due to the normalization of the objective function. Note that when we have reached optimum and the gradient is zero the initial condition is equal to the adjoint field times a scaling factor. Thus the optimality condition reads

$$\frac{\varphi}{E'(0)} = \frac{p(0)}{E'(T)},$$
 (3.8)

where E' denotes the disturbance energy.

Note that we discretize the expressions for the adjoint equations and the gradient that have been derived on the "continuous" level.

As mentioned the non-linearity in the state equation prohibits direct solution of the nonlinear optimization problem. Instead an iterative procedure is needed to find the optimal control. The general procedure is described in Figure 3.1. First, the governing equations (GE) are solved with an initial guess of  $\varphi$ . From the solution of the governing equations one can solve the corresponding adjoint equations (AE). Once the state and adjoint state are solved, we can construct the gradient of the objective function with respect to the control. We

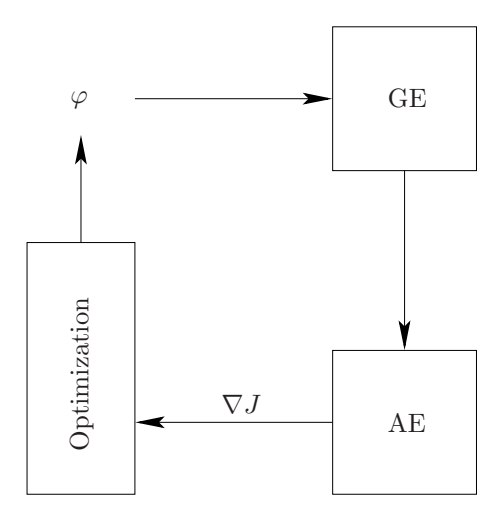


FIGURE 3.1. The optimization procedure. The control is denoted  $\varphi$ . The gradient of the objective function with respect to the control  $\varphi$  is denoted  $\nabla J$  where J is the objective function. The governing equations and associated adjoint equations are denoted GE and AE respectively.

can then update the control with, for example, a conjugate gradient method or a quasi-Newton method. The whole loop is repeated until a satisfactory control is found.

The drawback with this kind of control is that it will only work under exactly the very conditions the control is constructed for. On the other hand, no a priori knowledge of the control is needed, and the performance obtained with the nonlinear optimization procedure often far exceeds the result from other simplified control finding approaches. One obvious application is to determine an upper limit of what is possible to achieve with a certain control scheme, something that might aid in the search for more efficient direct methods of control. Note however that this approach can be extended to a robust formulation that accounts for the worst case disturbances which makes the resulting control more general. This is described in Bewley et al. (2000). Another important issue for adjoint based control schemes is the choice of inner products. This choice could have impact a large impact on the convergence rate of the iterative process and also on how well the "optimal control" will work, see e.g. Protas & Bewley (2002).

## 3.3. Computational issues

The computational effort to solve the adjoint state is comparable to the solution of the state equation. Thus, the gradient can be determined by roughly the computational cost of solving two state equations, this cost being independent of the number of degrees of freedom of the control parameterization. Note that the adjoint equations are always linear equations.

For unsteady simulations where the temporal history of the state equation is needed in the adjoint state computation the storage requirement can be very large. However, this requirement can be lowered using a *checkpointing technique*, see e.g. Berggren (1998). The price for the decreased storage demand is increased execution time. A memory reduction from N to  $\sqrt{N}$ , increases the computational cost with about a factor two.

Another important issue when deriving the discrete adjoint equations to be solved numerically is in what order the discretization takes place. One way is to discretize the expressions for the adjoint equations and the gradient that have been derived on the "continuous" level. An alternative is to discretize the Navier-Stokes equations and the objective function and derive the adjoint equations and the gradient expression on the discrete level. The latter approach leads to more accurate gradient directions, but is difficult to apply for the present discretizations. Issues related to the errors introduced by the approximative (continuous) formulation are discussed in e.g. Glowinski & He (1998) and Gunzburger (1998). The use of the continuous formulation is motivated by the findings in Högberg & Berggren (2000) where one conclusion is that it is sufficient to use the approximative (continuous) formulation in order to control strong instabilities. It was noted that in such cases, most of the reduction of the objective function is achieved in the first few iterations, and additional iterations only result in a fine tuning of the control. The drawback is that it will require more iterations to reach the true optimal solution, if it is even possible, than with the discrete formulation.

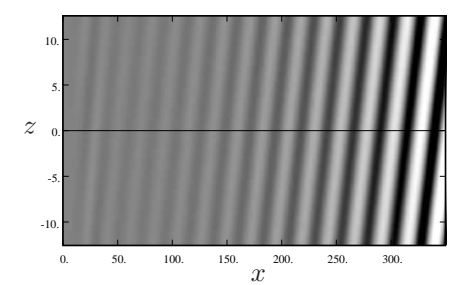
# 3.4. Results

#### 3.4.1. Blowing and suction control

An example of nonlinear optimal control in action is shown in Figure 3.2 where cross-flow vortices in a Falkner–Skan–Cooke boundary layer are developing downstream. In the left plot the flow is uncontrolled whereas the nonlinear optimal control is active in the right plot. The results are taken from simulations in paper 5.

Two other examples are where two different Tollmien–Schlichting waves are introduced in Blasius boundary layer, one weak, and one stronger wave where nonlinear coupling effects start to appear. The weak TS-wave is generated by an oscillating two dimensional volume force with the dimensionless frequency F=200, where  $F=2\pi f\nu/U_{\infty}^2\times 10^6$ . The volume force is centered at x=20 and decays exponentially in both the x- and y-direction.

Domain and resolution data for the TS-wave simulations are given in paper 5. The Reynolds number at x=0 in the computational box is 468.34 for both weak and strong disturbance. In the construction of the linear feedback kernels, the base flow profile is taken at x=150. For the nonlinear optimization



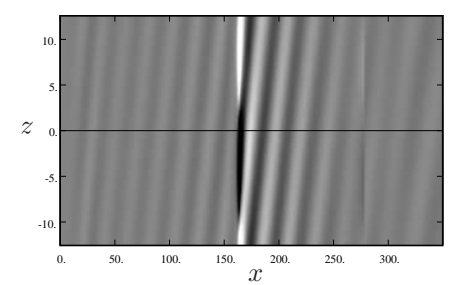


FIGURE 3.2. Snapshot of the wall normal velocity component in an x-z plane at y=0.5 without control (left) and with non-linear control (right). The control is applied in  $x \in (145, 295)$ . The black to white scale lies in the interval  $v \in (-0.001, 0.001)$ .

problem, we specify the observation interval in space and time to  $x \in [75, 375]$  and  $t \in [0, 750]$ , respectively.

In Figure 3.3 the streamwise disturbance energy development of weak TSwaves are plotted. A small transient can be seen in the beginning of the energy curve, an effect that is due to the fact that we do not force a clean TS-wave. However, as the disturbance evolves downstream, a pure TS-wave emerges. The flow is perturbed just upstream of branch I of the neutral stability curve, which is at around  $x \approx 27$ , and the disturbance grows exponentially shown, as the solid line in Figure 3.3. The growth ends when branch II is reached at about  $x \approx 219$ . See for example Schmid & Henningson (2001) for details. The dashed line is the disturbance energy development with linear control active. Note that the exponential growth is switched to an exponential decay. With the nonlinear optimal control applied, the energy development follows the dash-dotted line. Since the energy levels are low and thus nonlinear effects negligible, we can conclude that the deviations originate from differences in the optimization problem and the limitations of the linear control. Analyzing the control signals shows no major differences between the two control approaches. The nonlinear control acts stronger in the beginning of the simulation and also stronger at the upstream part of the spatial control interval. These effects are a direct consequence of the limitations of the linear control problem formulation.

## 3.4.2. Initial value control

In this case the initial condition is constructed out of random modes to see whether the gradient procedure can find the optimal condition "far" from the optimum. For this particular case the gradient is reduced a factor 2000 and we reach a growth factor of in energy of 440.8 which is in good agreement with what linear stability theory predicts.

In figure 3.4 the starting initial condition and final optimal condition are shown. The optimal condition might still be improved somewhat though by,

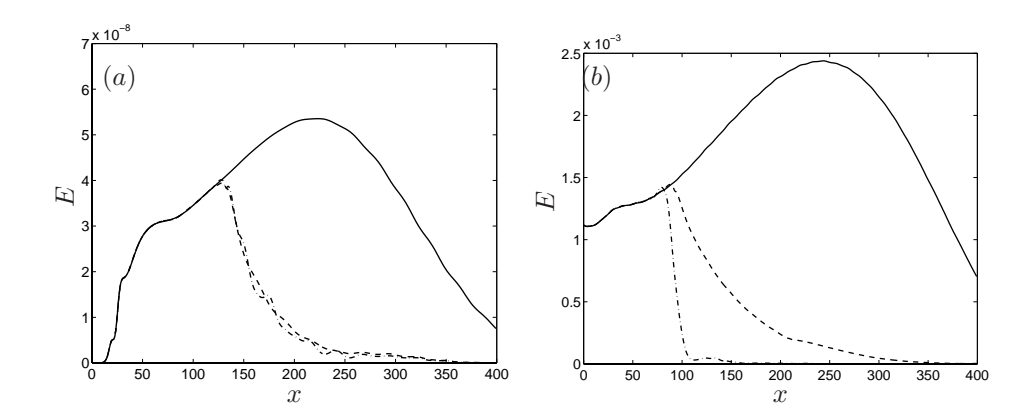


FIGURE 3.3. The spatial energy growth of a linear (a) and weakly nonlinear (b) TS-wave perturbation in a Blasius boundary layer without control from case 4 (solid), with linear control from case 5 (dashed), and nonlinear control from case 6 (dash-dotted). Control is applied in  $x \in [75, 225]$ . The TS-wave is generated at R = 950 for  $\alpha = 0.30$ . The linear controller is centered at x = 150.

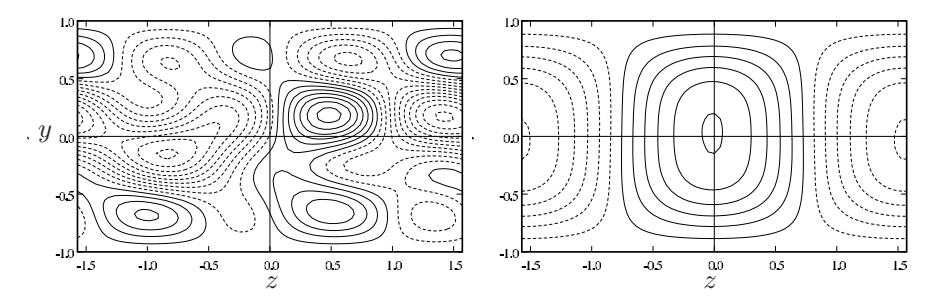


FIGURE 3.4. Contour plots of the wall-normal velocity component. The initial condition before (left) and after optimization (right).

for example, storing more forward velocity field. Note that these results are only a justification of the implementation.

#### CHAPTER 4

# Direct numerical simulations

# 4.1. Pseudo-spectral collocation algorithm

All direct numerical simulations (DNS) of the three-dimensional, time-dependent, incompressible Navier–Stokes equations presented in paper 1, paper 3, paper 4, and paper 5 are performed with different versions of a pseudo-spectral algorithm which was first developed as a channel flow solver, described in Lundbladh et al. (1992). Based on the channel code a separate solver for boundary layer flows was developed which is reported in Lundbladh et al. (1999).

The time marching is performed with a four-step low-storage third-order Runge–Kutta method for advective terms and a Crank–Nicolson scheme for the viscous terms. A spectral method described in Canuto et al. (1988) is used with a Fourier discretization in streamwise and spanwise directions, and a Chebyshev collocation method in the wall-normal direction. The aliasing errors that are introduced when transforming the nonlinear terms back to Fourier space can be removed by increasing the physical space resolution by a factor 3/2 in the streamwise and spanwise directions. This can also be used for the Chebyshev polynomials. The discretization of, and the solution procedure for, the Navier–Stokes equations are described in Lundbladh et al. (1992). A similar algorithm was used by Kim et al. (1987).

Due to the fact that a spectral discretization has been used in the horizontal directions, which by definition means that we need a periodic flow in these directions, and the fact that we want to be able to simulate spatially evolving flows an additional non-physical forcing was added to the momentum equations in a downstream strip of the flow. The forcing blends the downstream base flow to the prescribed inflow condition and removes any disturbances in that the domain with a minimum of upstream influence. This is known as a *fringe region* technique and is described further in Lundbladh *et al.* (1999) and analyzed by Nordström *et al.* (1999). A similar technique was used by Bertolotti *et al.* (1992). The incompressible Navier–Stokes equations with the fringe forcing can be written as

$$\frac{\partial u}{\partial t} = NS(u) + \lambda(x)(u - u_{\lambda}) + F,$$

$$\nabla \cdot u = 0,$$
(4.1)

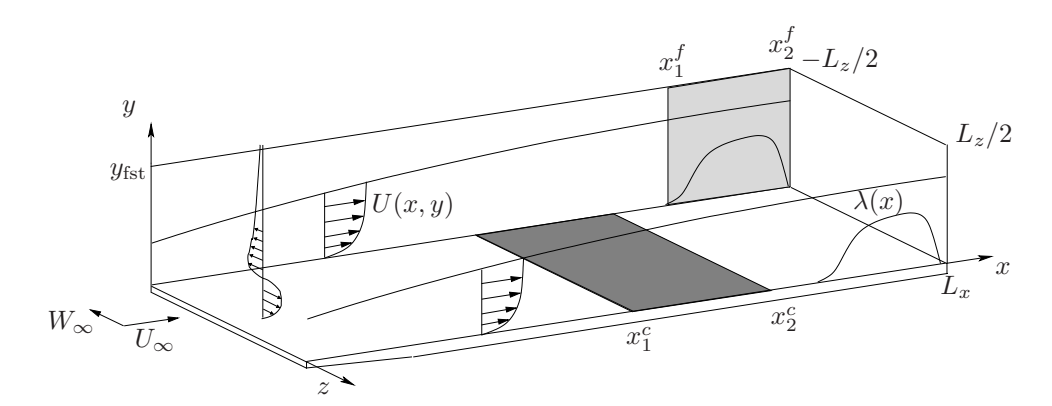


FIGURE 4.1. The computational box  $[0,L_x] \times [0,y_{\rm fst}] \times [-L_z/2,L_z/2]$  for the boundary layer flow case. The fringe forcing is applied in the region  $[x_1^f,x_2^f]$ . For all optimization problems the control region is  $[x_1^c,x_2^c] \times [-L_z/2,L_z/2]$  which can also be limited only to a certain time interval  $\times [T_1^c,T_2^c]$ . The non-physical fringe forcing is applied in the domain  $[x_1^f,x_2^f] \times [0,y_{\rm fst}] \times [-L_z/2,L_z/2]$  where the amplitude is a smooth function  $\lambda(x)$  with support in  $[x_1^f,x_2^f]$ .

where  $\lambda(x)$  is a non-negative function and which is nonzero only at the end of the computational domain. The outflow and inflow conditions are determined by the desired velocity distribution  $u_{\lambda}$ . The additional forcing term  $F = [F_1, F_2, F_3]$  is used for different things in spatial and temporal simulations. In temporal simulations it enforces a parallel mean flow whereas in the spatial simulations perturbations can be introduced with it.

The computational box is depicted in figure 4.1. For the solid walls noslip boundary conditions are used. The freestream boundary condition in the boundary layer code, applied at  $y=y_{\rm fst}$  has to be sufficiently high in order not to influence the computational results. One choice used here is the Neumann boundary condition as an artificial freestream boundary. In order to decrease the box size in the wall-normal direction a generalization of the boundary condition used by Malik *et al.* (1985) can also be applied. It is an asymptotic condition that for each wavenumber pair exactly matches a potential flow solution decaying with the wall distance.

In the spatially evolving flows disturbances can be introduced into the flow by applying a volume forcing, either in the fringe region, or somewhere in the "physical" part of the flow domain, or by adjusting the boundary conditions in order to specify blowing and suction at the wall. In temporal flows disturbances are introduced through the initial condition. Different means of forcing are described in paper 4.

To solve the nonlinear optimization problem outlined in chapter 3, we need to compute the adjoint Navier-Stokes equations. The adjoint equations are solved in the same way as the Navier-Stokes equations, but with small modifications. However, the implementation of the optimization problem also requires the addition of a gradient based optimization routine as an outermost loop in the computations, which iteratively marches the Navier-Stokes equations forward in time and the adjoint Navier-Stokes equations backward in time, in order to compute gradient information which in turn is used to improve the control. For this purpose a limited memory quasi-Newton method is used. The algorithm, L-BFGS-B (Byrd et al. (1994)), is available on the Internet (the web-link is given in the reference list next to Byrd et al. (1994)) and was used without modifications. It is an algorithm well suited for large nonlinear optimization problems, with or without bounds on the control variables. The BFGS method successively computes secant approximations of the Hessian matrix as the iterations proceed. The algorithm has been shown to work well for many different types of optimization problems. Paper 5 deals with the adjoint related simulations.

To solve the state estimation problem, additions were made to the code so that two "independent" simulations could be run side-by-side. Wall measurements are extracted from both simulations and this information is then used together with the estimation feedback law, that has been outlined in chapter 2 and further described in paper 3 and paper 4, to compute the additional volume forcing term applied to the estimator to make that flow converge to the actual flow.

# 4.2. Pseudo-spectral finite difference algorithm

The DNS of turbulent channel flow reported in paper 2 were performed with the code of Bewley  $et\ al.\ (2001)$  which is also a pseudo-spectral code with 3/2 dealiasing in the streamwise and spanwise directions. In the wall-normal direction a second-order finite difference technique is applied which is energy-conserving. The time integration is performed with a hybrid second-order Crank–Nicolson and third order Runge–Kutta method developed by Aksevoll & Moin (1995). In this scheme, the wall-normal derivatives are treated implicitly to improve the stability properties of the code when using blowing and suction boundary conditions at the walls. The pressure is updated through a fractional step method which also ensures the incompressibility condition.

Additions to this code were made in order to investigate estimator performance as well as computing two-point correlation of the forcing vector f described in section 2.2.5.

All the turbulent channel flow simulations are performed for constant massflux flow at  $Re_{\tau} = 100$  in a computational box of size  $4\pi \times 2 \times 4\pi/3$  in  $x \times y \times z$ respectively. The resolution is  $42 \times 64 \times 42$  Fourier, finite difference, Fourier modes. The Reynolds number in the turbulent simulations is kept quite low at this stage for reasons of computational expediency.

#### CHAPTER 5

# Conclusion and summary

The main work in this thesis has been devoted to studies of two different optimal control approaches where the objective has been to estimate and control transitional channel and boundary layer flows. Both approaches aim at finding the optimal blowing and suction control continuously distributed over the walls bounding the flow.

In the first approach we construct a linear optimization problem where the Orr–Sommerfeld/Squire equations are used to model the small perturbation dynamics and an objective function that measures the perturbation energy is chosen. By using tools from linear control theory it is possible to solve the optimization problem off line and construct a feedback control law based on solution of the optimization problem.

In the first study we use linear control theory to solve the optimization problem. Since the linear state-feedback control requires complete flow field information we combine it with a state estimator where noisy measurements of skin-friction and pressure are measured and used to reconstruct the state. The formulation of the state estimator is based on expected statistics of the initial conditions, the sensor noise, and the external disturbances acting on the system. The performance of the estimator is directly related to how well these statistical models describe flow. In the present work physically relevant models are suggested which give good performance of the estimator in transitional channel flows.

The importance of proper stochastic modeling of the sensor noise and the external disturbances is further stressed when a turbulent channel flow is estimated based on similar noisy wall measurements.

Based on the same idea with physically relevant parameterization of the stochastic models for the sensor noise and the external disturbances as for the estimator in channel flow it is demonstrated that the estimator also works in spatially developing boundary layer flows. Furthermore the estimator is combined with linear feedback control into a compensator where the controller is based on the reconstructed state in the estimator. The compensator control is shown to work well for different transition scenarios such as Tollmien–Schlichting waves, optimal perturbations, inflectional instabilities in the form of cross-flow vortices in Falkner–Skan–Cooke boundary layers.

# 40 5. CONCLUSION AND SUMMARY

In the second part of the study we formulate and solve a nonlinear optimization problem which means that we can use the full incompressible Navier—Stokes equations to model the flow. The objective function, which is the quantity we want to minimize, is defined to measure the perturbation energy. A standard method to solve this type of optimization problem is to iteratively solve the Navier—Stokes and adjoint Navier—Stokes equations to compute gradient information of the objective function with respect to the control parameterization which can then be used to update the control signal.

The strength of the nonlinear method is that we can take the complete flow physics into account and that we can optimize basically any property of the flow by constructing the proper objective function. The main drawback when applied to flow control is that it cannot be used online and that it is a computationally expensive method.

The nonlinear optimal control is compared with a linear optimal control computed for the same flow configuration and it is shown that the performance is similar for linear perturbations whereas when the disturbances get stronger the nonlinear optimal control is able to do better. However the main conclusion from this study is that the linear controller performs surprisingly well even when nonlinear interactions start to take place.

#### CHAPTER 6

# Papers and authors contributions

# Paper 1

State estimation of wall bounded flow systems. Part 1. Laminar flows J. Hæpffner (JH), M. Chevalier (MC), T. R. Bewley (TB) & D. S. Henningson (DH). Submitted to J. Fluid Mech.

This paper considers the estimation problem, using a Kalman filter based on the linearized Navier–Stokes equations and appropriate stochastic models for the relevant statistics of the initial conditions, sensor noise, and external disturbances acting on the system. We show that a physically relevant parameterization of these statistics is key to obtaining well resolved feedback kernels with appropriate spatial extent for all three types of flow measurements available on the wall. The control theory aspects have been investigated by JH as well as implementation and testing of the plain Kalman filter. The estimator has been implemented and tested by MC in direct numerical simulations. The paper has mainly been written by JH in collaboration with MC, TB, and DH.

# Paper 2

State estimation of wall bounded flow systems. Part 2. Turbulent flows M. Chevalier (MC), J. Hæpffner (JH), T. R. Bewley (TB) & D. S. Henningson (DH). Submitted to J. Fluid Mech.

This work aims at estimating a turbulent channel flow at based on a time history of noisy wall measurements of the flow. We do this by applying a plain Kalman and an extended Kalman filter based on the linearized Navier–Stokes equations together with a stochastic model based on statistics gathered from a direct numerical simulations (DNS) of the same turbulent flow we aim to estimate. The implementation of the estimator and gathering of the statistics have been performed by MC. The implementation to solve the optimal estimation gains is done by JH. All direct numerical simulations are is done by MC. The writing has been done mainly by MC in collaboration with JH, TB, and DH.

# Paper 3

Linear compensator control of a pointsource induced perturbation in a Falkner–Skan–Cooke boundary layer

M. HÖGBERG (MH), M. CHEVALIER (MC) & D. S. HENNINGSON (DH). *Phys. Fluids* 2003 **15**, 2449–2452

A pointsource induced perturbations on an infinite swept wing is controlled using linear control theory. Based on wall measurements in a spatial simulation of localized disturbances in a Falkner–Skan–Cooke boundary layer, an extended Kalman filter is used to estimate the full three-dimensional wave packet. The estimated field is in turn used to calculate a feedback control which changes the growth of the disturbance into decay. The implementation of the controller and estimator was done by MH. Simulations were performed by MH and MC. Writing was done mainly by MC in collaboration with MH and DH.

#### Paper 4

Linear feedback control and estimation applied to instabilities in spatially developing boundary layers

M. Chevalier (MC), J. Hæpffner (JH), E. Åkervik (EÅ) & D. S. Henningson (DH). To be submitted

This paper considers the estimation problem, using a Kalman filter based on the linearized Navier–Stokes equations and appropriate stochastic models for the relevant statistics of the sensor noise and external disturbances acting on the system. The compensator is applied and tested on a range of different types of transition scenarios. The estimator was implemented and verified by MC in a direct numerical solver. JH implemented the algorithm to compute the optimal estimation gain. The direct numerical simulations were performed by MC and EÅ. The writing of the paper was mainly done by MC in collaboration with JH, EÅ and DH.

#### Paper 5

Adjoint based control of channel and boundary layer flows M. Chevalier (MC), M. Högberg (MH), M. Berggren (MB) & D. S. Henningson (DH). TRITA-MEK 2004:12

The implementation and verification of different adjoint based control strategies are reported. The performance of a linear and nonlinear optimal controller is compared for a few different flow cases. The adjoint channel flow solver to optimize blowing and suction control in the boundaries was implemented by MH. The corresponding adjoint solver for boundary flows was implemented by MC. The adjoint channel code that optimizes the initial condition to maximize the energy growth was implemented and tested by MC. The writing was mainly done by MC and MH in collaboration with DH and MB. The comparison between the linear and nonlinear optimal control has been published as an AIAA paper at the 3rd Theoretical Fluid Mechanics Meeting, St. Louis, MO (AIAA 2002-2755). The development and testing of the adjoint solvers is published as a technical report at the Swedish Defence Research Agency (FOI-R--0182--SE), 2001.

The papers are re-set to the present thesis format.

# Acknowledgment

First of all I would like to thank my advisor Professor Dan Henningson for his guidance in the realm fluid dynamics and for generously sharing his knowledge but also for his complete and dedicated support when needed.

Many thanks also to Professor Thomas Bewley who arranged for an enjoyable four-month stay at UCSD and to his students Haoxiang, Laura, Patricia, and Bartosz.

I also want to thank Doctor Martin Berggren for his invaluable help in everything from mathematics to type setting of reports and Doctor Ardeshir Hanifi for always sharing his time and knowledge.

Thanks also to my colleagues at the Department of Computational Physics at FOI and the Department of Mechanics for providing nice environments to work in. In particular I would like to thank Jerome Hæpffner and Markus Högberg for all their help and assistance and dedicated work. I truly learned a lot from you both. Thanks also to Janne, Ori, Luca, Astrid, Espen, Martin, Arnim, and Erik for always giving me a warm welcome and for sharing your office space.

Finally I want to thank my family and my friends for supporting me throughout my studies.

The financial support from the Swedish Defence Research Agency (FFA/FOI) is greatfully acknowledged.

Tack Anna för allt ditt tålamod och stöd under alla omständigheter  $\heartsuit$ 

Tack Ida för dina mjuka kramar och glada tillrop efter långa dagar ♡

# **Bibliography**

- ABERGEL, F. & TEMAM, R. 1990 On some control problems in fluid mechanics. Theoret. Comput. Fluid Dyn. 1, 303–325.
- AKSEVOLL, K. & MOIN, P. 1995 Large eddy simulations of turbulent confined coannular jets and turbulent flow over a backward facing step. Technical Report Report TF-63. Thermosciences Division, Dept. of Mech. Eng., Stanford University.
- Anderson, B. & Moore, J. 1979 Optimal filtering. Prentice-Hall.
- Andersson, P., Berggren, M. & Henningson, D. S. 1999 Optimal disturbances and bypass transition in boundary layers. *Phys. Fluids* **11**, 134–150.
- BERGGREN, M. 1998 Numerical solution of a flow-control problem: vorticity reduction by dynamic boundary action. SIAM J. Sci. Comp. 19 (3), 829–860.
- Bertolotti, F. P., Herbert, T. & Spalart, P. R. 1992 Linear and nonlinear stability of the Blasius boundary layer. *J. Fluid Mech.* 242, 441–474.
- Bewley, T. R. 2001 Flow control: New Challenges for a New Renaissance. *Prog. Aero. Sci.* 37, 21–58.
- Bewley, T. R. & Liu, S. 1998 Optimal and robust control and estimation of linear paths to transition. *J. Fluid Mech.* **365**, 305–349.
- Bewley, T. R., Moin, P. & Temam, R. 2001 DNS-based predictive control of turbulence: an optimal benchmark for feedback algorithms. *J. Fluid Mech.* 447, 179–225.
- Bewley, T. R. & Protas, B. 2004 Skin friction and pressure: the "footprints" of turbulence. *Physica D* **196**, 28–44.
- Bewley, T. R., Temam, R. & Ziane, M. 2000 A general framework for robust control in fluid mechanics. *Physica D* **138**, 360–392.
- Byrd, R. H., Peihuang, L., Nocedal, J. & Zhu, C. 1994 A limited memory algorithm for bound constrained optimization. Technical Report NAM-08. EECS Department, Northwestern University, http://www.netlib.org/toms/778.
- Canuto, C., Hussaini, M. Y., Quarteroni, A. & Zang, T. A. 1988 Spectral Methods in Fluids Dynamics. Springer.
- Cathalifaud, P. & Bewley, T. R. 2004a A noncausal framework for model-based feedback control of spatially-developing perturbations in boundary-layer flow systems. part 1: Formulation. Systems and Control Letters 51 (1), 1–13.
- Cathalifaud, P. & Bewley, T. R. 2004b A noncausal framework for model-based feedback control of spatially-developing perturbations in boundary-layer flow

- systems. part 2: Numerical simulations using state feedback. Systems and Control Letters 51 (1), 15–22.
- Collis, S., Chang, Y., Kellogg, S. & Prabhu, R. D. 2000 Large eddy simulation and turbulence control. AIAA Paper 2000–2564.
- Gelb, A. 1974 Applied Optimal Estimation. MIT Press.
- GLOWINSKI, R. 1991 Finite element methods for the numerical solution of incompressible viscous flow. Introduction to the control of the Navier–Stokes equations, pp. 219–301. Lectures in Appl. Math. 28. American Mathematical Society, Providence, RI.
- GLOWINSKI, R. & HE, J. 1998 On shape optimization and related issues. In *Computational Methods for Optimal Design and Control* (eds. J. Borggaard, J. Burns, E. Cliff & S. Schreck), pp. 151–179. Birkhäuser, Boston.
- Gunzburger, M., Hou, L.-S. & Svobodny, T. P. 1989 Numerical approximation of optimal control problem associated with the Navier–Stokes equations. *Appl. Math. Lett.* **2**, 29–31.
- Gunzburger, M., Hou, L.-S. & Svobodny, T. P. 1992 Boundary velocity control in incompressible flow with an application to viscous drag reduction. *SIAM J. Control Optim.* **30**, 167–181.
- Gunzburger, M. D. 1998 Sensitivities in computational methods for optimal flow control. In *Computational Methods for Optimal Design and Control* (eds. J. Borggaard, J. Burns, E. Cliff & S. Schreck), pp. 197–236. Birkhäuser, Boston.
- HANIFI, A., SCHMID, P. J. & HENNINGSON, D. S. 1996 Transient growth in compressible boundary layer flow. Phys. Fluids 8, 826–836.
- HE, J.-W., CHEVALIER, M., GLOWINSKI, R., METCALFE, R., NORDLANDER, A. & PERIAUX, J. 2000 Drag reduction by active control for flow past cylinders. In *Computational mathematics driven by industrial problems (Martina Franca, 1999)*, pp. 287–363. Berlin: Springer.
- Henningson, D. S., Lundbladh, A. & Johansson, A. V. 1993 A mechanism for bypass transition from localized disturbances in wall-bounded shear flow. *J. Fluid Mech.* **250**, 169–207.
- HINZE, M. & KUNISH, K. 2000 Three Control Methods for Time Dependent Fluid Flow. Flow, Turbulence and Combustion 65 (3/4), 273–298.
- Ho, C.-M. & Tai, Y.-C. 1998 Micro-electro-mechanical-systems (mems) and fluid flows. Annu. Rev. Fluid Mech. 30, 579–612.
- Hu, H. & Bau, H. 1994 Feedback control to delay or advance linear loss of stability in planar poiseuille flow. In Proc. R. Soc. Lond. A, vol. 447, pp. 299–312.
- $\label{eq:huang} \mbox{Huang, W. \& Sloan, D. M. 1993 The pseudo-spectral method for solving differential eigenvalue problems. } \emph{J. Comp. Phys. 111}, 399–409.$
- HÖGBERG, M. 2001 Optimal Control of Boundary Layer Transition. PhD thesis, Royal Institute of Technology, Department of Mechanics, Stockholm, Sweden.
- HÖGBERG, M. & BERGGREN, M. 2000 Numerical Investigation of Different Discretization Approaches for Optimal Control. Flow, Turbulence and Combustion 65 (3/4), 299–320.
- HÖGBERG, M., BEWLEY, T. R. & HENNINGSON, D. S. 2003a Linear feedback control and estimation of transition in plane channel flow. J. Fluid Mech. 481, 149–175.
- HÖGBERG, M., BEWLEY, T. R. & HENNINGSON, D. S. 2003b Relaminarization of

- $Re_{\tau}$ =100 turbulence using gain scheduling and linear state-feedback control. *Phys. Fluids* **15**, 3572–3575.
- HÖGBERG, M. & HENNINGSON, D. S. 2002 Linear optimal control applied to instabilities in spatially developing boundary layers. *J. Fluid Mech.* **470**, 151–179.
- Joshi, S. S., Speyer, J. L. & Kim, J. 1995 Modeling and control of two dimensional poiseuille flow. 34th IEEE Conf on Decision and Control pp. 921–927.
- Joslin, R. D., Gunzburger, M. D., Nicolaides, R. A., Erlebacher, G. & Hussaini, M. Y. 1997 A Self-contained, Automated Methodology for Optimal Flow Control Validated for Transition Delay. *AIAA Journal* **35** (5), 816–824.
- JOVANOVIĆ, M. R. & BAMIEH, B. 2001 Modelling flow statistics using the linearized Navier–Stokes equations. In *Proceedings of the 40th IEEE Conference on Decision and Control*, pp. 4944–4949. Orlando, FL.
- KAILATH, T. 1973 Some new algorithms for recursive estimation in constant linear systems. *IEEE transaction on information theory* **IT-19** (6), 750–760.
- Kim, J. 2003 Control of turbulent boundary layers. Phys. Fluids 15 (5), 1093–1105.
- KIM, J., MOIN, P. & MOSER, R. D. 1987 Turbulence statistics in fully developed channel flow. J. Fluid Mech. 177, 133–166.
- LEWIS, F. L. 1986 Optimal estimation. New York: Wiley.
- Lewis, F. L. & Syrmos, V. L. 1995 Optimal control. Wiley-Interscience.
- LUCHINI, P. 2000 Reynolds-number-independent instability of the boundary layer over a flat surface: optimal perturbations. J. Fluid Mech. 404, 289–309.
- Lundbladh, A., Berlin, S., Skote, M., Hildings, C., Choi, J., Kim, J. & Henningson, D. S. 1999 An Efficient Spectral Method for Simulations of Incompressible Flow over a Flat Plate. Technical Report TRITA-MEK 1999:11. Department of Mechanics, Royal Institute of Technology, KTH.
- Lundbladh, A., Henningson, D. S. & Johansson, A. 1992 An Efficient Spectral Integration Method for the Solution of the Navier–Stokes Equations. Technical Report FFA TN 1992-28. The Aeronautical Research Institute of Sweden, FFA.
- Malik, M. R., Zang, T. A. & Hussaini, M. Y. 1985 A spectral collocation method for the Navier–Stokes equations. *J. Comp. Phys.* **61**, 64–88.
- NORDSTRÖM, J., NORDIN, N. & HENNINGSON, D. S. 1999 The fringe region technique and the Fourier method used in the direct numerical simulation of spatially evolving viscous flows. SIAM J. Sci. Comp. 20 (4), 1365–1393.
- PROTAS, B. & BEWLEY, T. R. 2002 Regularization opportunities in the adjoint analysis of multiscale systems. In *Advances in Turbulence IX* (eds. I. P. Castro, P. E. Hancock & T. G. Thomas). Proceedings of the Ninth European Turbulence Conference.
- Schmid, P. J. & Henningson, D. S. 2001 Stability and transition in shear flows, Applied Mathematical Sciences, vol. 142. Springer-Verlag.
- Sritharan, S. 1991a Dynamic programming of Navier–Stokes equations. System Control Lett. 16, 299–307.
- SRITHARAN, S. 1991b An optimal control problem for exterior hydrodynamics. In *Distributed Parameter Control Systems: New Trends and Applications* (eds. G. Chen, E. Lee, W. Littman & L. Markus), pp. 385–417. Marcel Dekker, New York.
- Weideman, J. A. C. & Reddy, S. C. 2000 A matlab Differentiation Matrix Suite. ACM Transaction of Mathematical Software 26 (4), 465–519.

# 48 BIBLIOGRAPHY

Yoshino, T., Suzuki, Y. & Kasagi, N. 2003 Evaluation of GA-based feedback control system for drag reduction in wall turbulence. In *Proc. 3rd Int. Symp. on Turbulence and Shear Flow Phenomena*, pp. 179–184.

Part 2

Papers

# Paper 1

# State estimation in wall-bounded flow systems. Part 1. Laminar flows

By Jérôme Hœpffner\*, Mattias Chevalier\*†, Thomas R. Bewley‡ and Dan S. Henningson\*†

Submitted to Journal of Fluid Mechanics

In applications involving the model-based control of transitional wall-bounded flow systems, one often desires to estimate the interior flow state based on a history of noisy measurements from an array of flush-mounted skin-friction and pressure sensors on the wall. This paper considers the estimation problem, using a Kalman filter based on the linearized Navier-Stokes equations and appropriate stochastic models for the relevant statistics of the initial conditions, sensor noise, and external disturbances acting on the system. We show that a physically relevant parameterization of these statistics is key to obtaining well resolved feedback kernels with appropriate spatial extent for all three types of flow measurements available on the wall. The effectiveness of the resulting Kalman and extended Kalman filters that implement this feedback is verified for both infinitesimal and finite-amplitude disturbances in direct numerical simulations of a perturbed laminar channel flow. The consideration of timevarying feedback kernels is shown to be particularly advantageous to accelerate the convergence of the estimator from unknown initial conditions. A companion paper (Part 2) considers the extension of such estimators to the case of fullydeveloped turbulence.

# 1. Introduction

The feedback control of fluid flow systems is a problem that has received growing attention in recent years and has been approached in a number of different manners. One approach is to design controls based on physical insight of dominant flow mechanisms, as by the wave superposition principle (see, e.g., Thomas (1990)). Another approach is to use adaptive or genetic techniques to attempt to learn an effective control strategy by trial and error (see, e.g., Lee et al. (1997)). It is also possible to leverage linear control theory, basing the control algorithm on the linearized Navier–Stokes equations governing small perturbations to the flow system, a mathematical statement of the control objective,

<sup>\*</sup>Department of Mechanics, Royal Institute of Technology (KTH), SE-100 44 Stockholm,

<sup>&</sup>lt;sup>†</sup>The Swedish Defence Research Agency (FOI), SE-172 90 Stockholm, Sweden

 $<sup>^{\</sup>ddagger} Flow$  Control Lab, Dept of MAE, UC San Diego, La Jolla, CA 92093-0411, USA

and a mathematical model of the relevant statistical properties of the unknown initial conditions, sensor noise, and external disturbances acting on the system. The present paper follows this latter approach. Recent reviews of related flow control efforts can be found in, for instance, Bewley (2001), Gunzburger (1996), and Kim (2003).

The problem of linear model-based feedback control based on noisy measurements can be decomposed into two independent subproblems: first, the state-feedback (a.k.a. full-information) control problem, in which full state information is used to determine effective control feedback, and, second, the state estimation problem, in which measurements are continuously used to "nudge" a real-time calculation of the flow system in an appropriate manner such that the calculated flow state eventually approximates the actual flow state.

Once both subproblems are solved, one can synthesize them to control a flow based on limited noisy measurements of the flow system. The overall performance of the resulting linear feedback control scheme is limited by the individual performance of the two subproblems upon which it is based. For the application of linear control theory to wall-bounded flows, though encouraging results have been obtained previously on the state-feedback control problem (see, for example, Bewley & Liu (1998) and Högberg et al. (2003)), the development of effective state estimation strategies remained, until now, largely an open problem. In the present paper, we therefore focus on the state estimation problem exclusively.

One of the primary challenges of the state estimation problem is that its framing is based centrally on quantities which are challenging to model, namely, the expected statistics of the initial conditions, the sensor noise, and the external disturbances acting on the system. The state estimation problem may actually be thought of as a *filtering* problem; that is, the estimator uses the governing equation itself as a filter to extract, from the available noisy measurements of a small portion of the dynamic system, that component of the measurements which is most consistent with the dynamic equation itself. In other words, the estimator uses the governing equation to extract the signal from the noise, and in the process builds up an estimate of the entire state of the system. The purpose of the estimator at time t is to filter the measurements gathered prior to time t to estimate the instantaneous state of the flow field. The purpose of the state-feedback controller at time t, on the other hand, is to apply forcing to the flow such that the subsequent evolution of the flow, after time t, exhibits favorable characteristics. Thus, the controller is based on a metric defining these favorable characteristics (the objective function), whereas the estimator is based on a model describing, to the extent that they are known, the statistical properties of the unknown quantities affecting the system.

Some attention has been paid in the literature to the creative choice of objective functions for the control problem. Kim & Lim (2000), for example, performed a numerical experiment which applied body forcing via linear

feedback everywhere on the interior of a turbulent channel flow. This linear feedback was constructed to exactly cancel the linear coupling term  $[\mathcal{C} \text{ in } (2)]$  in the nonlinear simulation, with the result that the turbulent flow relaminarized. This result lends credibility to the idea of using a more sophisticated objective function which targets this linear coupling (more precisely, one which targets the non-normality of the system eigenvectors) rather than using an objective function which simply targets the energy of the flow perturbations directly. The appropriate selection of the objective function is thus seen to be not a trivial problem, and is closely linked to our understanding of the relevant flow physics. The problem of disturbance modeling for the state estimation problem, which is also inherently linked to our understanding of the relevant flow physics, is perhaps even more subtle.

The importance of appropriate disturbance modeling was previously investigated by Jovanović & Bamieh (2001a). In this work, a stochastic disturbance model was proposed which, when used to force the linearized Navier–Stokes equation, led to a simulated flow state with certain second-order statistics (specifically,  $u_{rms}$ ,  $v_{rms}$ ,  $w_{rms}$ , and the Reynolds stress  $-\overline{uv}$ ) that mimicked, with varying degrees of precision, the statistics from a full DNS of a turbulent flow at  $Re_{\tau}=180$ .

The present work represents the next natural step in this vein, that is, the development of appropriate disturbance parameterizations that facilitate the calculation of well-resolved feedback kernels for the flow estimation problem that both converge upon grid refinement and eventually decay exponentially with distance from the origin (that is, from the corresponding sensor location). These feedback kernels, in turn, facilitate accurate estimation of the state itself when a simulation of the state estimate is coordinated with wall measurements from an actual flow (or a separate direct numerical simulation thereof). Further, the tuning of this disturbance parameterization allows for the tuning of the spatial extent of the resulting feedback convolution kernels in order to modify the communication architecture required in an "overlapping decentralized" implementation of the resulting estimator in hardware (that is, large-scale implementation via an interconnected array of identical tiles, each with actuators, sensors, and control logic incorporated, that communicate only with their neighbors, as described in detail in Bewley (2001)).

It appears as if little has been accomplished to date in terms of the investigation of appropriate disturbance models for specifically the flow estimation problem in the published literature. Bewley & Liu (1998), Joshi, Speyer & Kim (1999), and Högberg et al. (2003) all modeled the covariance of the external disturbances at a single wavenumber pair  $\{k_x, k_z\}$  in a channel flow with a simple identity matrix after the problem was discretized in the wall-normal direction. This assumption effectively implies a constant variance of disturbances at each gridpoint in the wall-normal direction and zero correlation of the disturbances at different gridpoints above the wall. Unfortunately, this covariance model does not converge to a resolved covariance distribution as the

wall-normal grid is refined. We now understand that, as a consequence, this model was responsible for restricting the effectiveness of the resulting estimators in our previous work, and also led to realization problems that required us to limit the number of wall measurements that we could account for while still obtaining convergence of the feedback kernels upon refinement of the numerical grid.

In the present paper, we propose an improved parameterization of the external disturbances (that is, random volume forcing on the interior of the flow domain) that may be used to model the effects of wall roughness, acoustic waves, and neglected dynamics, as well as appropriate parameterizations of the unknown initial conditions and sensor noise. This improved disturbance parameterization converges to a continuous function upon grid refinement, and allows us to account for all three flow measurements available at the wall (that is, streamwise and spanwise wall skin friction and wall pressure).

In previous studies, only time-constant feedback kernels have been considered in the estimator. By introducing time-varying feedback kernels into the estimator, the present paper incorporates plausible models of the statistics of the unknown initial conditions on the flow in order to maximize the speed of convergence of the estimator from unknown initial conditions. As a consequence, the initial transients in the estimation error are shown to be greatly diminished.

In the present paper, we design and test an estimator for the early stages of transition in a laminar 3D plane channel flow (again, see Part 2 of this study for the case of fully-developed turbulence). After describing the system of interest, we propose a stochastic model for the flow's initial conditions, external disturbances, and sensor noise in §2.4. An appropriate Kalman filter is designed in §2.5 in order to determine suitable estimator feedback. After a discussion of the numerical methods employed, we test the estimator in numerical simulations of the linearized system at isolated wavenumber pairs in §3. We then inverse Fourier transform the estimator feedback rules determined on a large array of wavenumber pairs to obtain well resolved, spatially localized feedback convolution kernels in physical space for all three of the measurable quantities on the wall (streamwise and spanwise wall skin friction and wall pressure), as discussed in §4.1. The resulting Kalman filter for the entire 3D channel, and an extended Kalman filter that additionally incorporates the nonlinearity of the full system, are tested in direct numerical simulations of the full nonlinear Navier-Stokes system for both infinitesimal and finite-amplitude perturbations of a laminar channel flow in  $\S4.2$  and  $\S4.3$ .

## 2. Formulation

## 2.1. Flow configuration and governing equations

This paper considers the 3D flow between two infinite flat plates (at  $y = \pm 1$ ) driven by a pressure gradient in the streamwise (x) direction. Scaling the time variable appropriately, the mean velocity profile is given by  $U(y) = 1 - y^2$ . For

computational efficiency, we model the flow as being periodic in the horizontal directions x and z, using a computational domain of sufficient extent in these directions that this non-physical assumption does not significantly affect the statistics of the flow. This approach allows all variables with spatial variation to be expanded in Fourier series. Thus, the state vector describing the wall-normal velocity  $v_{mn}(y,t)$  and wall-normal vorticity  $\eta_{mn}(y,t)$  on the interior of the domain at each wavenumber pair  $\{k_x,k_z\}_{mn}$  may be denoted by

$$q_{mn}(y,t) = \begin{pmatrix} v_{mn}(y,t) \\ \eta_{mn}(y,t) \end{pmatrix}.$$

The evolution of the flow can then be written with the linear terms, M and L, on the left-hand side and the nonlinear terms, N, on the right-hand side, in addition to an external forcing term  $e_{mn}$  to account for unmodeled effects, yielding

$$\underline{\frac{\mathrm{d}}{\mathrm{d}t}Mq_{mn} + Lq_{mn}}_{Linear\ dynamics} = \sum_{\substack{k+i=m\\l+j=n}} N(q_{kl}, q_{ij}) + \underbrace{e_{mn}(y, t)}_{External\ forcing}, \tag{1}$$

where

$$M = \begin{pmatrix} -\Delta & 0 \\ 0 & I \end{pmatrix} \text{ and } L = \begin{pmatrix} \mathcal{L} & 0 \\ \mathcal{C} & \mathcal{S} \end{pmatrix}.$$
 (2)

The operators  $\mathcal{L}$ ,  $\mathcal{S}$ , and  $\mathcal{C}$  relate to the Orr–Sommerfeld/Squire equations and are defined as

$$\begin{cases} \mathcal{L} = -ik_x U \Delta + ik_x U'' + \Delta^2 / Re, \\ \mathcal{S} = ik_x U - \Delta / Re, \\ \mathcal{C} = ik_z U'. \end{cases}$$

The Laplacian operator is denoted  $\Delta = D^2 - k^2$ , where D and  $D^2$  represent first- and second-order differentiation operators in the wall-normal direction, and  $k^2 = k_x^2 + k_z^2$ . The Reynolds number Re is based on the centerline velocity and channel half-width. The double convolution sum in (1) represents the nonlinear "triad" interactions. The boundary conditions on v and  $\eta$  correspond to no-slip solid walls

$$v = Dv = \eta = 0$$
 at  $y = \pm 1$ .

In the following, the right hand side of (1) will be lumped into a forcing function  $f_{mn}(y,t)$ , thereby restricting the flow model to the linear terms, accounting for both the nonlinear terms and the external disturbances with a stochastic model. Suppressing the  $\{\}_{mn}$  subscript for clarity, the resulting flow model can be written as

$$\frac{\mathrm{d}}{\mathrm{d}t}Mq + Lq = Tf(y,t),\tag{3}$$

where the operator

$$T = \left( \begin{array}{ccc} ik_xD & k^2 & ik_zD \\ ik_z & 0 & -ik_x \end{array} \right)$$

transforms the forcing  $f = (f_1, f_2, f_3)^T$  on the evolution equation for the velocity vector  $(u, v, w)^T$  into an equivalent forcing on the  $(v, \eta)^T$  system (see, e.g., Jovanović & Bamieh (2001b) for derivation of this transformation).

#### 2.2. Measurements

The choice of the measurements to be taken in order to obtain the state estimate (without knowledge of the initial conditions of the flow) is ultimately a matter of practicality. In the present work, we will consider an idealized problem in which the continuous distributions of streamwise and spanwise skin friction and pressure on the wall are available as measurements in order to estimate the state of the flow away from the wall. This information is mathematically complete in the following sense: if this information is uncorrupted by noise and the external forcing on the system is known exactly, the entire state of the flow (even in the fully turbulent regime, and at any Reynolds number) is uniquely determined by these measurements at the wall in an arbitrarily small neighborhood of time t (without knowledge of the initial conditions), as shown by Bewley & Protas (2004). However, in any practical problem, the measurements are corrupted by noise, the modeling of the system is not precise, and there are external disturbances on the system which are not accounted for. Thus, in the practical setting, it is essential to filter the measurements appropriately to reconcile the noisy measurements of the system with an approximate dynamic model of the system. The Kalman filter used in the present paper is a mathematicallyrigorous tool to achieve this reconciliation.

In our previous formulations of the estimator problem, as discussed in Högberg et al. (2003), only the feedback gains using the measurement  $\eta_y$ , the first wall-normal derivative of  $\eta$ , were used. In §2.4, we develop an improved formulation based on a more realistic model of the statistics of the external disturbances such that we may now compute well-behaved feedback kernels that converge upon grid refinement for any measurement constructed as a linear combination of the state variables and their derivatives. In particular, the three available measurements at the wall, the streamwise and spanwise wall skin friction and the wall pressure, are related to the quantities v and  $\eta$  in the state model as follows

$$\begin{cases} \tau_x = \tau_{xy}|_{wall} = \frac{1}{Re} \frac{\partial u}{\partial y}\Big|_{wall} = \frac{1}{Re} \frac{i}{k^2} (k_x D^2 v - k_z D \eta)|_{wall}, \\ \tau_z = \tau_{zy}|_{wall} = \frac{1}{Re} \frac{\partial w}{\partial y}\Big|_{wall} = \frac{1}{Re} \frac{i}{k^2} (k_z D^2 v + k_x D \eta)|_{wall}, \\ p = p|_{wall} = \frac{1}{Re} \frac{1}{k^2} D^3 v|_{wall}. \end{cases}$$

Note that these equations are easily verified using the Taylor series expansions for v(y) and  $\eta(y)$  near a solid wall, as written out in, e.g., §2.2 of Bewley & Protas (2004). In the formulation shown in the remainder of §2, for clarity, we focus on the feedback rules related to measurements made at the lower wall

only. The extension of this formulation to the case in which measurements are taken at both walls of the channel, as considered in the simulations reported in §3 and §4, is straightforward.

#### 2.3. Stochastic setting

As described earlier, the modeling of the relevant statistical properties of the stochastic forcing function f in (3), which accounts for the effects of external disturbances on the system, is one of the key steps in the framing of the present estimation problem.

In the present stochastic framework, the mean of any quantity of interest may be obtained using the expectation operator  $E[\cdot]$ , defined as the average over all possible realizations of the stochastic inputs. In particular, the mean of f is modeled as zero, that is, E[f] = 0.

In the present formulation, it is the covariance of f that needs to be modeled carefully. Since f is a continuous function of the spatial coordinate y, the appropriate definition of the covariance in this problem is somewhat abstract, as discussed in detail in Balakrishnan (1976). As shown in Balakrishnan (1976), once this abstraction is made, the resulting Kalman filter in this spatially-continuous formulation is found to be analogous to its well-known counterpart in the finite-dimensional setting. In order to proceed with the modeling of the statistics of f, it is necessary to have a clear understanding of what the covariance means in the spatially-continuous setting.

In the spatially-discrete setting, if u and v are two zero-mean, random vectors of length  $n_1$  and  $n_2$  respectively, their covariance  $R_{uv}$  is defined as a matrix of size  $n_1 \times n_2$  such that  $R_{uv} = E[uv^*]$ , where the symbol \* applied to a vector or scalar denotes conjugate transpose. The covariance of a zero-mean random vector u is defined as  $R_{uu} = E[uu^*]$ .

To extrapolate these definitions to the spatially-continuous setting (see, e.g., Balakrishnan 1976, p. 267), we make use of inner products with arbitrary test functions chosen from the same Hilbert spaces as the random functions we are considering. That is, if  $\xi$  and  $\eta$  are two zero-mean random functions in Hilbert spaces  $H_1$  and  $H_2$  respectively, then their covariance  $R_{\xi\eta}$  is defined such that

$$\langle x, R_{\xi\eta} y \rangle_1 = E[\langle x, \xi \rangle_1 \langle y, \eta \rangle_2^*] \quad \forall (x, y) \in H_1 \times H_2,$$
 (4)

where  $\langle \cdot, \cdot \rangle_1$  and  $\langle \cdot, \cdot \rangle_2$  denote appropriate inner products in the Hilbert spaces  $H_1$  and  $H_2$  respectively. Thus, the covariance  $R_{\xi\eta}$  is seen to be a linear operator from  $H_2$  to  $H_1$ ; this is analogous to the spatially-discrete setting, in which the covariance is a matrix which when multiplied by a rank  $n_2$  vector results in a rank  $n_1$  vector. Further, if  $\xi$  and  $\eta$  are taken to be simple vectors u and v in the above expression, the inner products may be defined using the simple form  $\langle x, y \rangle = x^*y$ , and the spatially-continuous definition of the covariance reduces

immediately to the usual definition given in the spatially-discrete setting:

We will subsequently need to express the covariance of a linear transformation of a random process f of known covariance  $R_{ff}$ . Letting  $g = \mathcal{H}f$  where  $\mathcal{H}$  is a linear differential operator, it follows from (4) that

$$\langle x, R_{gg}y \rangle = E[\langle x, g \rangle \langle y, g \rangle^*] = E[\langle x, \mathcal{H}f \rangle \langle y, \mathcal{H}f \rangle^*]$$

$$= E[\langle \mathcal{H}^*x, f \rangle \langle \mathcal{H}^*y, f \rangle^*] = \langle \mathcal{H}^*x, R_{ff}\mathcal{H}^*y \rangle$$

$$= \langle x, \mathcal{H}R_{ff}\mathcal{H}^*y \rangle$$

$$\Rightarrow R_{gg} = \mathcal{H}R_{ff}\mathcal{H}^*,$$

$$= \langle x, \mathcal{H}R_{ff}\mathcal{H}^*y \rangle$$
(5)

where  $\mathcal{H}^*$  denotes the adjoint of  $\mathcal{H}$ ; note that the adjoint of a linear operator  $\mathcal{H}: H_1 \to H_2$  with inner products  $\langle \cdot, \cdot \rangle_1$  and  $\langle \cdot, \cdot \rangle_2$  on  $H_1$  and  $H_2$  respectively is defined by the equality

$$\langle y, \mathcal{H}x \rangle_2 = \langle \mathcal{H}^*y, x \rangle_1 \quad \forall (x, y) \in H_1 \times H_2.$$

A significant feature of the definition of the covariance is its relation to the expected value of the energy. In the spatially-discrete setting, defining the energy using an unweighted inner product, we may define the trace such that

$$\operatorname{tr}(R_{uu}) \triangleq \sum_{i} \langle \delta_{ji}, (R_{uu})_{jk} \, \delta_{ki} \rangle = \sum_{i} (R_{uu})_{ii}$$
$$= E[u_1 u_1^* + u_2 u_2^* + \ldots + u_n u_n^*] = E[\mathcal{E}(u)],$$

where  $\mathcal{E}(u)$  denotes the energy of the vector u. In the spatially-continuous setting, the corresponding definition is

$$\operatorname{tr}(R_{\xi\xi}) \triangleq \int_{\Omega} \langle \delta(x - x'), R_{\xi\xi}\delta(x - x') \rangle dx'$$

$$= \int_{\Omega} E[\langle \delta(x - x'), \xi(x) \rangle \langle \delta(x - x'), \xi(x) \rangle^*] dx'$$

$$= E[\int_{\Omega} \xi(x') \xi^*(x') dx'] = E[\mathcal{E}(\xi)].$$

Accounting for a weighting function in the definition of the energy in these relations is straightforward.

# 2.4. Models for the stochastic inputs

The flow system that we desire to estimate is affected by its unknown initial conditions, the unknown external disturbances that disrupt the evolution of the state, and the unknown sensor noise that corrupts the measurements. Since the estimator is intended to converge effectively over a large number of different realizations, a statistical description (mean and covariance) of these unknown quantities may be used to tune the feedback in the estimator design. The

estimator which we will design, also known as a Kalman filter, will be optimal in the sense of obtaining the most accurate estimate possible over a large set of realizations of the system in which the initial conditions, external disturbances, and sensor noise have the assumed statistical properties.

# 2.4.1. Modeling of the initial conditions

For the purpose of the present work, we will model the mean of the unknown initial condition as zero (that is, we assume there is no preferred phase in the initial flow structures) and its covariance as  $S_0$ . Since the initial condition in the estimator is always zero,  $S_0$  also represents the covariance of the state estimation error at t = 0.

We want to design an estimator that performs well over a large range of possible initial conditions. It is natural to assume that the initial conditions are completely "random", however, we know from our understanding of the flow physics that there is a tendency for some specific types of flow disturbances to be present in any given flow. For example, Tollmien–Schlichting (TS) waves are likely to be present if the environment is characterized by acoustic waves, streaks are likely to be present if the environment is characterized by high levels of free-stream turbulence, and streamwise vortices are likely to be present if the environment is characterized by wall roughness. The specific initial conditions which we expect to see at each wavenumber pair in a particular problem (though at an unknown phase and amplitude), and for which we would like to tune the estimator to be particularly efficient at capturing, will be denoted here by  $s = s_{mn}(y)$ .

We will model the initial conditions  $q_0$  at each wavenumber pair as a linear combination of a component  $q_s$  of a specified profile s (but with random magnitude and phase) and a component  $q_r$  constructed by a random linear combination of the first p eigenmodes  $\xi^j = \xi^j_{mn}(y)$ , normalized to unit energy, of the system matrix  $M^{-1}L$  in (3) such that

$$q_s = \theta_0 s$$
,  $q_r = \frac{1}{p} \sum_{j=1}^p \theta_j \xi^j$ ,

where the coefficients  $\theta_j, j \in \{0, ..., p\}$  are uncorrelated complex scalar random variables with zero mean and unit variance. The initial condition  $q_0$  is then modeled as a linear combination of these two components such that

$$q_0 = c_1 (c_2 q_s + (1 - c_2) q_r).$$

The design parameter  $c_1 > 0$  is used to specify the expected amplitude of the initial conditions at this wavenumber pair, and the design parameter  $c_2 \in [0,1]$  is used to specify the relative importance of the components  $q_s$  and  $q_r$  in the initial conditions. The corresponding covariance of the unknown initial

conditions is given by

$$S_0 = R_{q_0 q_0} = c_1 \left( c_2 R_{ss} + (1 - c_2) \sum_{j=1}^p R_{\xi^j \xi^j} \right).$$
 (6)

Note that we expect the energy of the initial conditions at both large wavenumber pairs and small wavenumber pairs to be small. We may account for this in the present model of the initial conditions by allowing  $c_1$  to vary in a wavenumber-dependent fashion. In the present work, we will model this dependence with the function

$$c_1(k_x, k_z) = c_a k_c^2 e^{-k_c^2 + 1}$$
 with  $k_c^2 = (k_x/c_x)^2 + (k_z/c_z)^2$ ,

where the design parameters  $c_x$  and  $c_z$  may be tuned to select the peak of the expected energy of the initial condition in wavenumber space and the design parameter  $c_a$  scales the overall amplitude of the initial conditions. Many other assumed forms for  $c_1(k_x,k_z)$  are of course also possible, and may be experimented with in future work.

#### 2.4.2. Modeling of the external disturbances

We will assume the external disturbance forcing  $f = (f_1, f_2, f_3)^T$  in (3) to be a zero-mean  $(E[f_j(x, y, z, t)] = 0)$  stationary white Gaussian process with auto-correlation

$$E[f_j(x, y, z, t)f_k(x + r_x, y', z + r_z, t')] = \underbrace{\delta(t - t')}_{Temporal} \underbrace{Q_{f_j f_k}(y, y', r_x, r_z)}_{Spatial},$$

where  $\delta(\cdot)$  denotes the Dirac  $\delta$ -function. The assumption of a "white" time correlation eases the derivation of the equations for the covariance of the state, and is appropriate when the characteristic time scales of the external disturbances are short as compared with the characteristic time scales of the flow system. When this is not the case, the approach developed herein may be extended to incorporate an additional filter in order to "color" the external disturbances with appropriate self-correlation time scales (see, e.g., Lewis & Syrmos (1995)).

The remaining property to be described is the spatial extent of the two-point, one-time, auto-correlation of f over the whole domain

$$Q_{f_j f_k}(y, y', r_x, r_z) = E[f_j(x, y, z, t) f_k(x + r_x, y', z + r_z, t)].$$

The corresponding quantity in Fourier space is a covariance operator of the form discussed in  $\S 2.3$ , obtained for any wavenumber pair  $\{k_x, k_z\}$  via the following integration over the homogeneous directions

$$R_{f_j f_k}(y, y', k_x, k_z) = \int \int Q_{f_j f_k}(y, y', r_x, r_z) e^{-i(k_x r_x + k_z r_z)} dr_x dr_z.$$

Our model for the covariance of f assumes that the disturbance has a localized structure in space (i.e., the two-point correlation of the disturbance decays exponentially with distance) and that the correlations between forcing terms on different velocity components are zero. In the present work, we assume a

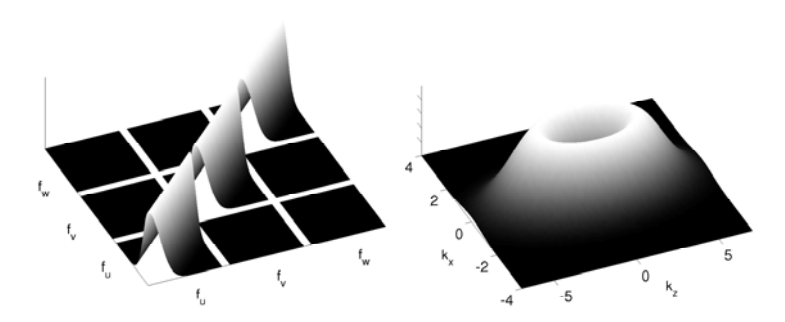


FIGURE 1. Sketch of the assumed covariance of the unknown external disturbance f in Fourier space at a single wavenumber pair  $\{k_x, k_z\}$ , taking  $d_y = 0.1$  (left), and the variation of the amplitude of this forcing with wavenumbers  $k_x$  and  $k_z$ , taking  $d_x = 0.5$  and  $d_z = 3$  (right).

model for the covariance of the external forcing f which is of a similar form to that assumed for the covariance of the initial conditions by taking

$$R_{f_j f_k}(y, y', k_x, k_z) = d_1 \, \delta_{jk} \mathcal{M}^y(y, y'),$$

where

$$d_1(k_x, k_z) = d_a k_d^2 e^{-k_d^2 + 1}$$
 with  $k_d^2 = (k_x/d_x)^2 + (k_z/d_z)^2$ 

and the y variation of  $R_{f_if_k}$  is given by the function

$$\mathcal{M}^{y}(y, y') = e^{-(y-y')^{2}/2d_{y}}. (7)$$

Note that we will denote  $R=R_{ff}=\mathrm{diag}(R_{f_1f_1},R_{f_2f_2},R_{f_3f_3})$  in the sections that follow. The design parameters  $d_x$  and  $d_z$  may be tuned to select the peak of the expected energy of the disturbance forcing in wavenumber space, the design parameter  $d_y$  governs the width of the two-point correlation of the disturbance in the wall-normal direction, and the design parameter  $d_a$  scales the overall amplitude of the disturbance forcing. The variation of  $\delta_{jk}\mathcal{M}^y(y,y')$  as a function of y and y', for the three different values of j and the three different values of k, is depicted graphically in Figure 1a, and the variation of  $k_d^2 e^{-k_d^2}$  as a function of  $k_x$  and  $k_z$  is depicted graphically in Figure 1b. As with the modeling of the covariance of the initial conditions, many other assumed forms for  $d_1(k_x,k_z)$  are also possible, and may be experimented with in future work.

# 2.4.3. Modeling of the sensor noise

Each of the three measurements is assumed to be corrupted by sensor noise, modeled as independent, white (in both space and time), random processes, the amplitude of which is determined by the assumed quality of the sensors. The covariance of the sensor noise vector g can thus be described in Fourier space

by a diagonal  $3 \times 3$  matrix G whose diagonal elements  $\alpha_{\iota}^2$  are the variances of the sensor noise assumed to be associated with each individual sensor

$$R_{g_{\iota}(t),g_{\kappa}(t')} = \delta_{\iota\kappa}\delta(t-t')\alpha_{\iota}^{2},$$

where  $\delta_{\iota\kappa}$  denotes the Kronecker delta. Thus, in the present work, we assume that the sensor noise is uncorrelated in both space and time.

When the signal-to-noise ratio is low, the measured signal must be fed back only gently into the estimator, lest the sensor noise disrupt the estimator. When the signal-to-noise ratio is high, the measured signal may be fed back more aggressively into the estimator, as the fidelity of the measurements can be better trusted. For a given covariance of the initial conditions and external disturbances, the tuning of the assumed overall magnitude of the sensor noise in the Kalman filter design thus provides a natural "knob" to regulate the magnitude of the feedback into the estimator. Note that an intermediate amount of feedback is desired in the estimator design: if the feedback is too weak, the estimator will not converge very quickly or very accurately, and if the feedback is too strong, it may knock the estimated flow out of the small perturbation neighborhood assumed in the linear model used in its design.

## 2.5. The Kalman filter

Noting that the Laplacian  $\Delta$  in the operator M in the forced linear equation (3) may be inverted by enforcement of the homogeneous boundary conditions on Dv, we may write

$$\dot{q} = \underbrace{-M^{-1}L}_{A} q + \underbrace{M^{-1}T}_{B} f,$$

and thus the general state-space formulation for the evolution of the flow state

$$q = q_{mn}(y, t)$$
 at each wavenumber pair  $\{k_x, k_z\}_{mn}$  may be written 
$$\begin{cases} \dot{q} = Aq + Bf, & q(0) = q_0, \\ r = Cq + g; \end{cases}$$
 (8)

note that q is a continuous function of both the wall-normal coordinate y and time t in this formulation. The measurement vector r is constructed using the matrix C, defined here as

$$C = \frac{1}{Re} \frac{1}{k^2} \begin{pmatrix} ik_x D^2|_{wall} & -ik_z D|_{wall} \\ ik_z D^2|_{wall} & ik_x D|_{wall} \\ D^3|_{wall} & 0 \end{pmatrix}.$$

This matrix extracts the two components of wall skin friction and the wall pressure from q.

We now build an estimator of the analogous form

$$\begin{cases} \dot{\hat{q}} = A\hat{q} - v, & \hat{q}(0) = 0, \\ \hat{r} = C\hat{q}, \end{cases}$$
(9)

with feedback

$$v = L\tilde{r} = L(r - \hat{r}). \tag{10}$$

Kalman filter theory, combined with the models outlined in §2.4 for the relevant statistics of the unknown initial conditions  $q_0$ , the unknown external forcing f, and the unknown sensor noise g, provides a convenient and mathematically-rigorous tool for computing the feedback operator L in the estimator described above such that  $\hat{q}$  converges to an accurate approximation of q. Note that the volume forcing v used to apply corrections to the estimator is proportional to the "innovation process"  $\tilde{r} = r - \hat{r}$ , that is, the difference between the measurements of the actual system and the corresponding quantity in the estimator model.

The solution of the Kalman filter problem in the classical, finite-dimensional setting is well known (for a succinct presentation, see, e.g., Lewis & Syrmos (1995) p. 463-470). The corresponding operator equations applicable here, though more involved to derive, are completely analogous (see Balakrishnan 1976). Thus, we will not rederive these equations here. The main results, in both the finite-dimensional and infinite-dimensional settings, are:

1. the covariance  $S(t) = R_{qq}(t)$  of the flow state q(t) is governed by the Lyapunov equation

$$\dot{S}(t) = AS(t) + S(t)A^* + BRB^*, \quad S(0) = S_0, \tag{11}$$

2. for a given L(t), the covariance  $P(t) = R_{\tilde{q}\tilde{q}}(t)$  of the state estimation error  $\tilde{q}(t) = q(t) - \hat{q}(t)$  is governed by the Lyapunov equation

$$\dot{P}(t) = A_0(t)P(t) + P(t)A_0^*(t) + BRB^* + L(t)GL^*(t), \quad P(0) = S_0, \quad (12)$$

where  $A_0(t) = A + L(t)C$ , and

3. the value of L(t) which minimizes the expected energy of the state estimation error (that is, which minimizes the trace of P(t)) is given by the solution of the differential Riccati equation (DRE)

$$\dot{P}(t) = AP(t) + P(t)A^* + BRB^* - P(t)C^*G^{-1}CP(t), \quad P(0) = S_0, \quad (13a)$$

$$L(t) = -P(t)C^*G^{-1}. (13b)$$

Note that, for a linear, time-invariant (LTI) system (that is, for A, B, C, R, G independent of time), the covariance of the estimation error, P(t), and the corresponding feedback which minimizes its trace, L(t), follow a transient near t=0 due to the effect of the initial condition  $S_0$ , eventually reaching a steady state for large t in which  $\dot{P}(t)=0$  and  $\dot{L}(t)=0$ . In order to minimize the magnitude of the transient of the trace of P(t), it is necessary to solve the differential Riccati equation given above. If one is only interested in minimizing the trace of P(t) at statistical steady state, it is sufficient to compute time-independent feedback L by solving the algebraic Riccati equation (ARE) formed by setting  $\dot{P}(t)=0$  in (13a).

#### 2.6. Numerical issues

# 2.6.1. Spatial discretization

In order to actually compute the feedback in this problem, it is necessary to discretize the DRE given in operator form in (13) and solve this equation in the finite-dimensional setting. However, in order to be relevant for the PDE problem of interest, the resulting feedback gains must converge to continuous functions as the numerical grid is refined.

Thus, to proceed, we first need to build the discrete counterparts of the system operators A, B, C, and their respective adjoints as well as the disturbance covariances R, G, and  $S_0$ . In the present work, the discrete operators are obtained through enforcement of the Orr–Sommerfeld/Squire equations at each point of a Gauss–Lobatto grid using a Chebyshev collocation scheme, taking

$$f_i = f(y_i), \quad y_i = \cos\frac{i\pi}{N}, \quad i = 0, \dots, N,$$

where N+1 is the number of gridpoints in the wall-normal direction. The discrete operators and differentiation matrices are determined using the spectral Matlab Differentiation Matrix Suite of Weideman & Reddy (2000). In particular, this suite provides fourth-order differentiation matrices invoking clamped boundary conditions  $(f(\pm 1) = f'(\pm 1) = 0)$ , using the procedure suggested by Huang & Sloan (1993), to give an Orr-Sommerfeld matrix with satisfactory numerical properties, avoiding unstable or lightly-damped spurious eigenmodes. The first-order, second-order, and third-order differentiation matrices so obtained, denoted  $D^1$ ,  $D^2$ , and  $D^3$  respectively, are combined according to the equations given previously to compute the discrete matrices A, B, and C in a straightforward fashion. The calculations reported in this paper use, where needed, the discrete definition for the adjoint of a matrix, that is, its conjugate transpose. The integration weights  $W(y_i)$  for the Chebyshev grid with the Gauss-Lobatto collocation points are computed using the algorithm from Hanifi, Schmid & Henningson (1996). These weights provide spectral accuracy in the numerical integration used to assemble the energy measure matrix Q.

# 2.6.2. Solution of the DRE

The calculation of the differential Riccati equation (DRE) is accomplished in this work using the Chandrasekhar algorithm developed by Kailath (1973). This elegant algorithm solves a factored form of the DRE at the heart of the Kalman filter as given by the spatial discretization of the operator equations in (13a)-(13b). It is particularly efficient when these factors are of low rank, which happens to be the case in the present study.

The main idea in the Chandrasekhar algorithm is to solve an evolution equation for a factored form of the time derivative of the estimation error covariance matrix,  $\dot{P}(t)$ . Since it is symmetric,  $\dot{P}(t)$  can be factored as

$$\dot{P} = L_1 L_1^* - L_2 L_2^* = YHY^*, \quad Y = \begin{pmatrix} L_1 & L_2 \end{pmatrix}, \quad H = \begin{pmatrix} I & 0 \\ 0 & -I \end{pmatrix},$$
 (14)

where the rank of  $L_1L_1^*$  is the number of positive eigenvalues of  $\dot{P}$  and the rank of  $L_2L_2^*$  is the number of negative eigenvalues of  $\dot{P}$ .

By spatial discretization of (13a), differentiation of both sides, and substitution of the factorization given above, assuming the system is LTI (that is, that A, B, C, R, and G are independent of time), it is straightforward to verify that (13a)-(13b) is equivalent to the solution of the following system:

$$\begin{cases}
\dot{L}(t) = -Y(t)HY^*(t)C^*G^{-1}, & L(0) = -P(0)C^*G^{-1}, \\
\dot{Y}(t) = (A + L(t)C)Y(t), & Y(0)HY^*(0) = \dot{P}(0),
\end{cases} (15)$$

where  $\dot{P}(0)$  is easily determined from the spatial discretization of (12) evaluated at t=0.

The key to the efficiency of this scheme is to exploit the possibility for an accurate low-rank approximation of Y. After an eigenvalue decomposition of  $\dot{P}(0)$  to determine  $L_1$  and  $L_2$ , we can perform a singular value decomposition of the matrices  $L_1L_1^*$  and  $L_2L_2^*$  and discard the singular vectors associated with small singular values, constructing an approximation of Y with the remaining singular vectors. In §4, singular values less than 0.01% of the initial  $\dot{P}$  matrix norm were discarded, resulting in a reduction of the rank of Y by approximately 75%. The computations of §3 requires great accuracy and where conducted by directly marching in time the Riccati equation.

In the present work, time integration of the DRE is performed using a standard explicit fourth-order Runge–Kutta scheme. When only constant feedback gains are to be used, we can either march the DRE to steady state using the Chandrasekhar algorithm or solve directly the ARE via standard techniques based on Schur factorization (see Laub (1991)).

# 2.6.3. Computation of the expected energy

In the discretized setting, the expected energy of the state q can be extracted from the discrete covariance matrix S by use of the energy measure matrix Q such that  $E[\mathcal{E}(q(t))] = \operatorname{tr}(QS(t))$ , where  $\mathcal{E}(q(t))$  denotes the instantaneous energy of the state q at time t. The expected energy of the state estimation error  $\tilde{q}$  can be found in a similar manner,  $E[\mathcal{E}(\tilde{q}(t))] = \operatorname{tr}(QP(t))$ .

The time evolution of the expected energy may be computed using the Chandrasekhar method. For example, the expected energy of the state q can be marched forward in time from  $E[\mathcal{E}(q(0))] = \operatorname{tr}(QS_0)$ , its value at t=0, via time integration of  $\frac{d}{dt}E[\mathcal{E}(q)] = \operatorname{tr}(Q\dot{S}(t))$ , where  $\dot{S} = YHY^*$ , and where the evolution equation for Y(t) is simply  $\frac{d}{dt}Y(t) = AY(t)$ , with Y(0) determined by the factorization  $Y(0)HY^*(0) = \dot{S}(0)$  and  $\dot{S}(0)$  determined by evaluation of (11) at t=0. The expected energy of the state estimation error  $\tilde{q}$  can be found in a similar manner, marching forward in time from  $E[\mathcal{E}(\tilde{q}(0))] = \operatorname{tr}(QS_0)$  at t=0 via time integration of  $\frac{d}{dt}E[\mathcal{E}(\tilde{q})] = \operatorname{tr}(Q\dot{P}(t))$ , where  $\dot{P}=YHY^*$  with, for L(t) specified, Y(t) evolving according to  $\frac{d}{dt}Y(t) = (A + L(t)C)Y(t)$  with

Y(0) determined by the factorization of  $\dot{P}(0)$ , which itself is determined by evaluation of (12) at t = 0.

# 3. Fourier-space characterization

By Fourier transforming in the x- and z-directions all variables with spatial variation (that is, the state, the disturbances, the measurements, and the control), the linearized 3D estimation and control problems completely decouple at each wavenumber pair  $\{k_x, k_z\}$ , as observed in Bewley & Liu (1998). Thus, the present section characterizes the performance of the estimator derived in the previous section on the linearized system in Fourier space at three individual wavenumber pairs  $(k_x, k_z) = (0, 2), (1, 0)$ , and (1, 1), where this performance is characterized most clearly. In §4, we inverse transform a large array of such feedback gains to physical space, obtaining more readily implementable spatially-localized 3D convolution kernels, and consider their effect on direct numerical simulations of the full nonlinear system.

Unless stated otherwise, the results reported are computed for R=3000, a subcritical Reynolds number characterized by transient growth phenomena. The design parameters for the stochastic model for the initial conditions (see §2.4.1) are chosen to be  $c_2=0.5$ ,  $c_a=4$ , and  $c_x=c_z=1.7$ . The design parameters for the stochastic model for the external disturbances (see §2.4.2) are chosen to be  $d_a=0.033$ ,  $d_x=0.5$ ,  $d_z=3$ , and  $d_y=0.1$ . The design parameters for the stochastic model for the sensor noise (see §2.4.3) are chosen to be  $\alpha_1^2=\alpha_2^2=0.002$  (for the shear-stress measurements) and  $\alpha_3^2=20$  (for the pressure measurements).

These choices for the design parameters of the stochastic models of the initial conditions, external disturbances, and sensor noise are the result of a combination of parametric tuning and physical arguments. For example, the choice  $c_2 = 0.5$  reflects a 50% confidence in the "specific form" of the assumed statistics of the of the initial conditions. Figure 2 compares the variation with wavenumber of the expected covariance of the initial conditions and disturbance forcing in the model used in this work; these variations excite the wavenumber ranges of interest for the estimation of localized disturbances and the accounting for the early effects of nonlinearity in the transition problem, as studied in §4.2 and §4.3. The amplitude parameters for the initial condition,  $c_a$ , and the external forcing,  $d_a$ , are chosen such that the flow energy initially grows and then slightly decays to statistical steady state, for the wavenumber pair showing the greatest potential for transient growth,  $(k_x, k_z) = (0, 2)$ .

The initial conditions used for the tests at isolated wavenumber pairs are the "worst-case" initial conditions at these wavenumber pairs, i.e., the initial conditions that, leveraging the non-normality of the dynamic operator A to the maximum extent possible, lead to the largest possible transient energy growth. Such initial conditions are of particular concern in a flow transition scenario, as described in, e.g., Schmid & Henningson (2001).

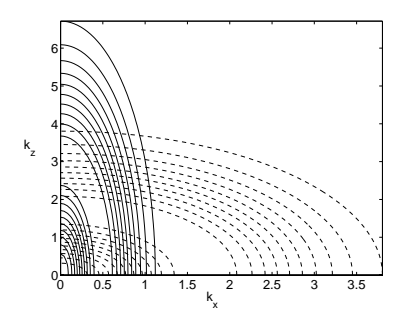


FIGURE 2. Contour plot of the variation of amplitude of the initial conditions, taking  $c_x = c_z = 1.7$  (dashed) and external disturbance forcing, taking  $d_x = 0.5$ , and  $d_z = 3$  (solid), as a function of the wavenumbers  $k_x$  and  $k_z$ . Note that the peak amplitudes are near the design values of  $k_c$  and  $k_d$ , as defined in §2.4.1 and 2.4.2, with reduced amplitudes for smaller and larger values of  $k_c$  and  $k_d$ . The expected covariance of the initial condition is modeled with equal extent in the streamwise and spanwise directions, while the expected covariance of the disturbance forcing is tuned for structures that are elongated in the streamwise direction.

The plots in this section show the evolution of the expected value of the energy of both the flow state and the state estimation error for initial conditions, sensor noise, and external disturbances distributed as described in the stochastic models presented in §2.4. Thus, these plots can be interpreted as an average over a large number of realizations of these stochastic inputs. They illustrate the effectiveness of the estimator feedback in the presence of the types of disturbances for which the estimator feedback was designed, namely, uncorrelated, zero-mean, random Gaussian distributions of the same covariance as specified in the estimator design.

# 3.1. Evolution of the expected energy of the flow state and the state estimation

Figure 3 shows the evolution of both the expected energy of the flow state and the expected energy of the state estimation error using time-varying feedback gains for three cases, each of which including the effect of sensor noise:

1) Nonzero initial conditions with zero external disturbances (dot-dashed curves): the expected energy of the state estimation error follows an initial transient, eventually tending exponentially to zero at the decay rate of the least-stable eigenmode of A+LC since there is no additional excitation. In all flows considered, the expected energy of the state estimation error is rapidly reduced to over two orders of magnitude below the expected energy of the flow state.

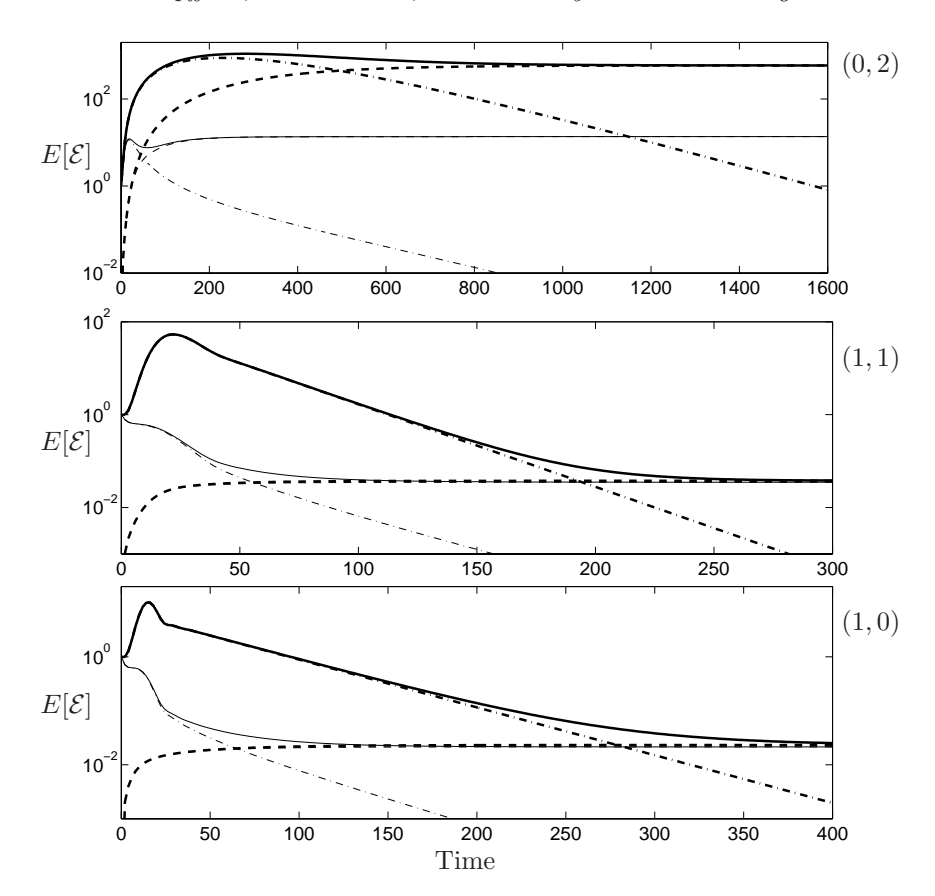


FIGURE 3. Evolution of the expected energy versus time for three flows of interest at three representative wavenumber pairs: (top) (0,2), (center) (1,1), and (bottom) (1,0). The stochastic inputs driving each simulation are: (solid) initial conditions plus external disturbances, (dashed) external disturbances only, (dot-dashed) initial conditions only; note that each simulation accounts for the effect of sensor noise corrupting the measurements. Thick lines represent the expected energy of the flow disturbance and thin lines represent the expected energy of the estimation error.

2) Nonzero external disturbances with zero initial conditions (dashed curves): the expected energy of the estimation error monotonically increases towards a statistical steady state. In the flow considered at wavenumber pair (0,2), the expected energy of the state estimation error rapidly approaches a value close to two orders of magnitude below the expected energy of the flow state, indicating effective estimator convergence. In the flows considered at wavenumber pairs (1,1) and (1,0), however, the expected energy of the state estimation error is

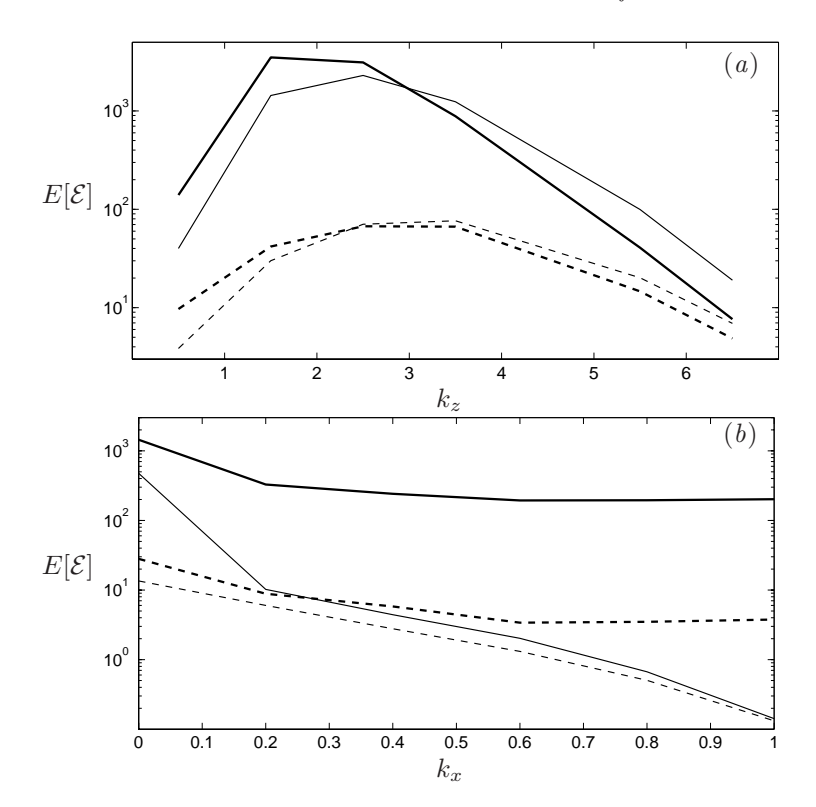


FIGURE 4. Maximum (thick lines) and statistical steady state (thin lines) of the total expected energy of the flow (solid) and the estimation error (dashed) over a range of wavenumber pairs for (a)  $k_x = 0$  with varying  $k_z$ , and (b)  $k_z = 1$  with varying  $k_x$ .

nearly as large as the expected energy of the flow state itself, indicating poor convergence of the estimator in these particular flows. This issue is discussed in  $\S 3.2$ .

3) Both nonzero initial conditions and nonzero external disturbances (solid curves): as expected, due to the linearity of the system and the additive effects of the stochastic inputs on the expected energy of the system, this case is given precisely by the sum of cases (1) and (2).

It is also worth noting that the transient in the expected energy of the state estimation error is not only of lower amplitude, but is typically much faster than the transient in the expected energy of the flow state.

Figure 4 shows how the peak and statistical steady state of the expected energy of the flow state and state estimation error depend on the wavenumber pair, quantifying the effects seen in Figure 1 for a range of different wavenumbers.

# 3.2. The difficulty of detecting structures in the center of the channel with wall sensors

The reason the estimator discussed in the previous section fails to converge effectively in the flows at wavenumber pairs (1,1) and (1,0) when external disturbances are present is interesting. Bewley & Liu (1998), hereafter referred to as BL98, studied extensively the Kalman filter problem in the present flow system for the following two cases:

case (i): 
$$Re = 10000$$
,  $(k_x, k_z) = (1, 0)$ , case (ii):  $Re = 5000$ ,  $(k_x, k_z) = (0, 2)$ .

As shown in Figure 1b of BL98, the leading eigenvectors of A in the (1,0) case include several "center" modes with nearly zero support near the wall\*. These modes, which are absent in the (0,2) case, would be continuously excited by the external disturbances, and are nearly impossible to detect with wall measurements even if the sensor noise is very low. To quantify this notion, the corresponding "modal observation residuals"  $g_{\kappa}$  are tabulated for both cases in Tables 1 and 2 of BL98.

Because of the presence of these nearly-unobservable center modes, the estimation problem is inherently difficult at certain wavenumber pairs when both external disturbances and sensor noise are present. Thus, the failure of the Kalman filter developed here to converge accurately for the externally-disturbed flows in the (1,0) case and the (1,1) case, which is characterized by similar unobservable center modes, is a reflection of the fundamental difficulty of this estimation problem when only wall measurements are employed, and is not a shortcoming of the estimation strategy applied in the present work.

To investigate the excitation of the flow by external disturbances which do not significantly excite such center modes, we may augment the definition of  $\mathcal{M}^y$  in (7), which models the wall-normal distribution of the covariance of the external disturbances f, as

$$\mathcal{M}^{y}_{augmented} = C(p) \left(\frac{y+y'}{2}\right)^{2p} \, \mathcal{M}^{y}.$$

The parameter p may be chosen to tune the profile of the external disturbances, with uniform intensity in y if p=0 or with intensity increasing near the walls if p>0, as shown in Figure 5. In the simulations reported here, the coefficient C(p) is selected such that the total expected energy of the flow is identical in each case.

The effect of this biasing of the external disturbances towards the walls is plotted in Figure 6. For the three wavenumber pairs tested, Figure 6 illustrates the wall-normal distribution of the expected energy of both the flow and the estimation error at statistical steady state. The flow is forced both with the external disturbance with p=0 (solid lines) and p=5 (dashed lines).

<sup>\*</sup>Note that the shapes of these modes are only weak functions of Reynolds number, so the same general comments hold true for the Re=3000 case studied here.

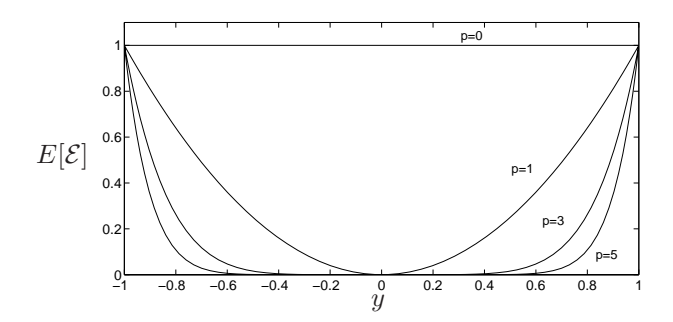


FIGURE 5. The wall-normal distribution of the variance in the augmented form of the external disturbance parameterization. Four cases are shown, corresponding to p = 0, 1, 3, 5.

For the wavenumber pair (0,2), the biasing of the external disturbance towards the walls has relatively little effect. In both cases tested, most of the energy of the resulting flow perturbation is located in the region of high shear, as explained by the lift-up effect. This perturbation is easily detected by the sensors on the walls, so the corresponding expected energy of the estimation error is relatively small.

For the wavenumber pair (1,0), on the other hand, the biasing of the external disturbance towards the walls has a relatively strong influence on where the expected energy of the flow is located. When excitation is present in the center of the channel (for p=0), it is seen that the expected energy of the flow is relatively large near the center of the channel. In this case, the estimator performance is poor, and the value of the expected energy of the estimation error is relatively large, especially near the center of the channel. On the other hand, when the excitation is focused near the walls of the channel (for p=5), the so-called "center modes" are not excited, and the estimator performance is very substantially improved.

The characteristics of the case at wavenumber pair (1,1) are essentially intermediate between the two other cases, at (1,0) and (0,2).

These results are further reinforced in Table 1, where the total expected energy of the estimation error is tabulated for  $p=0,\,1,\,3,\,$  and 5. When the external disturbances are uniformly distributed across the channel (for p=0), the estimator performance is substantially degraded for the (1,0) and, to a lesser extent, the (1,1) cases as compared to the (0,2) case, as already seen in Figure 6. As the excitation is focused closer to the walls (that is, as p is increased), the estimator performance is substantially improved, as the nearly unobservable center modes are no longer excited.

The flow structures that typically play the dominant role in the transition process (and, thus, the flow structures which we are most interested in estimating accurately in the present work) are elongated in the streamwise direction. That is, the modes of maximum concern in the transition process are

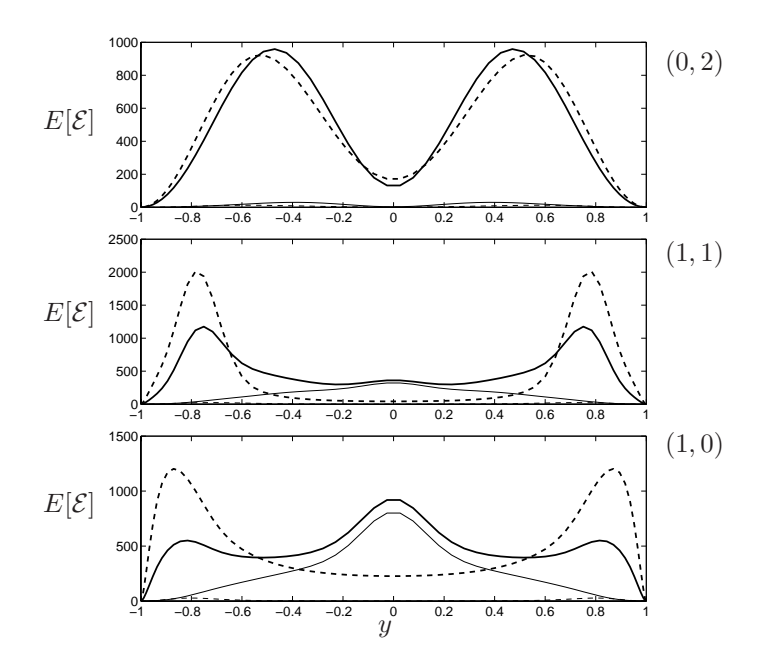


FIGURE 6. The distribution in y of the expected energy at statistical steady state of the flow (thick lines) and the estimation error (thin lines) for three wavenumber pairs: (top) (0,2), (center) (1,1), and (bottom) (1,0), and for two different wall-normal distributions of the external perturbations: p=0 (solid) and p=5 (dashed).

the highly non-normal modes at relatively small  $k_x$  and large  $k_z$ . Fortunately, this is the wavenumber regime that is not characterized by the problematical center modes that are nearly impossible to estimate based on wall measurements alone. Thus, the estimator developed and tested here appears to be promising for estimating the components of the state that are most relevant to the transition problem. It is also significant to point out that, to model the effects of wall roughness in linearized Navier–Stokes models, it is common practice to tune the parameterization of the external disturbances to focus them near the wall, as done here for large values of p. In this setting, the resulting flow disturbances are well estimated at all wavenumber pairs, as reflected in Table 1.

# 3.3. The utility of time-varying gains in the estimator

The feedback gains L determined by the Kalman filter, computed according to (13a)–(13b), are inherently a function of time. Thus, as stated previously, in order to minimize the trace of P(t) during the transient which ensues after the estimator is turned on, it is necessary to use time-varying feedback gains. However, for large times, P(t) and L(t) eventually approach constants as the

$(k_x, k_z)$	(0,2)	(1,1)	(1,0)
p = 0	28.8	289.5	548.4
p = 1	26.4	112.0	178.4
p = 3	16.3	38.3	43.8
p = 5	12.4	17.9	16.7

TABLE 1. The total expected energy of the estimation error at statistical steady state for three wavenumber pairs and four wall-normal distributions of the variance of the external disturbances. For each case, the magnitude of the external disturbances was scaled so that the total expected energy of the flow was 1000.

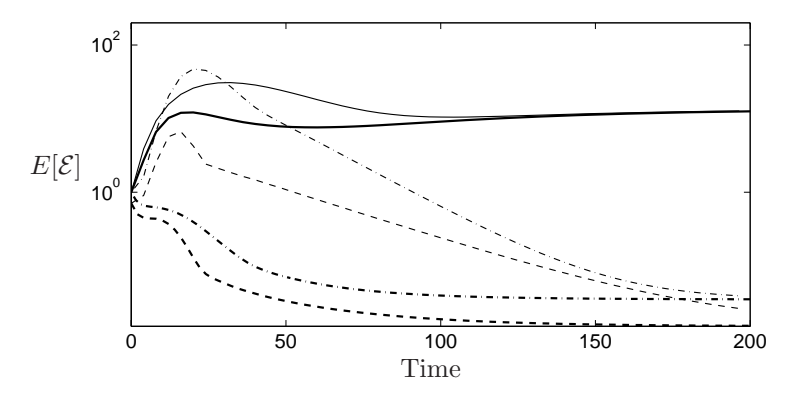


FIGURE 7. Comparison of the expected energy of the estimation error using the time-varying gains (thick lines) and constant gains (thin lines) for three wavenumber pairs: (0,2) solid, (1,1) dash-dot and (1,0) dash.

estimation error approaches statistical steady state. Thus, if one is not interested in minimizing this transient, one can simply apply constant feedback gains designed to minimize the expected energy of the state estimation error at statistical steady state.

It is interesting to compare the possible utility of time-varying gains for the control and estimation problems. Consider first the problems of optimal control and optimal estimation over the finite time horizon [0,T]. As already seen, the optimal estimation (Kalman filter) problem is solved by a DRE that marches forward in time from t=0 to t=T. On the other hand, the optimal control problem is solved by a (closely-related) DRE that marches backward in time, from t=T to t=0. For time invariant systems over a long time horizon (that is, for large T), the resulting feedback gains for the estimation problem

exhibit a transient near t=0 and approach a constant for the remainder of the march towards t=T, whereas the resulting feedback gains for the control problem exhibit a transient near t=T and approach a constant for the remainder of the march towards t=0. In the limit that  $T\to\infty$ , the transient in the gains in the control problem becomes unimportant; however, the transient in the gains in the estimation problem is still significant, especially if one is concerned with how rapidly the estimator converges after the estimator is turned on. Failure to appreciate this point can lead to the implementation of constant-gain estimators which do not converge as rapidly as one might desire.

In our previous research on dynamic compensation (Högberg et al. (2003)), constant feedback gains for both the control and estimation problems were used, taking no account of the transient due to the initial condition in the estimator. The full-state feedback control problem was found to be solved successfully with this approach for a large number of relevant flow cases. However, the state estimation problem was not found to be solved effectively by this approach, and was left as an important open problem.

It is now clear that we cannot expect optimal estimator performance during the initial transient when using constant estimation gains if the initial condition has a significant effect on the flow. This can be seen in Figure 7, where the evolution of the expected energy of the estimation error is plotted for the case of constant gains (thin lines) and the time-varying gains (thick lines). Both the constant and the time-varying gains give identical expected energy of the estimation error at large times, but the peak in the expected energy of the estimation error at short times is substantially diminished when the time-varying gains are employed. By taking the covariance of the initial condition into account, the utilization of the time-varying gains gives us a direct means to leverage any knowledge we might have about the expected structure of the initial conditions in the flow case of interest.

# 3.4. Relative importance of the different measured quantities

As described in the introduction, the new disturbance parameterization proposed in the present work allows us now to feed back into the estimator all three types of measurements available at the wall, that is, the streamwise skin-friction  $\tau_x$ , the spanwise skin-friction  $\tau_z$ , and the wall pressure p. Figure 8 explores the relative importance of each of these individual measurements in the convergence of the estimator for the three wavenumber pairs studied previously. It is seen that the measurement of  $\tau_x$  is the most significant for the estimator convergence for wavenumber pairs with relatively small  $k_x$ ; as mentioned in the last paragraph of §3.2, one might consider these modes as the ones of maximum concern in the early stages of transition. Physically, one might say that, in this case, the estimator can leverage the strong streamwise skin friction footprint associated with the streamwise streaks created be the lift-up of low momentum fluid by low amplitude streamwise vortices. With the present parameterization (high expected noise variance for the pressure measurement),

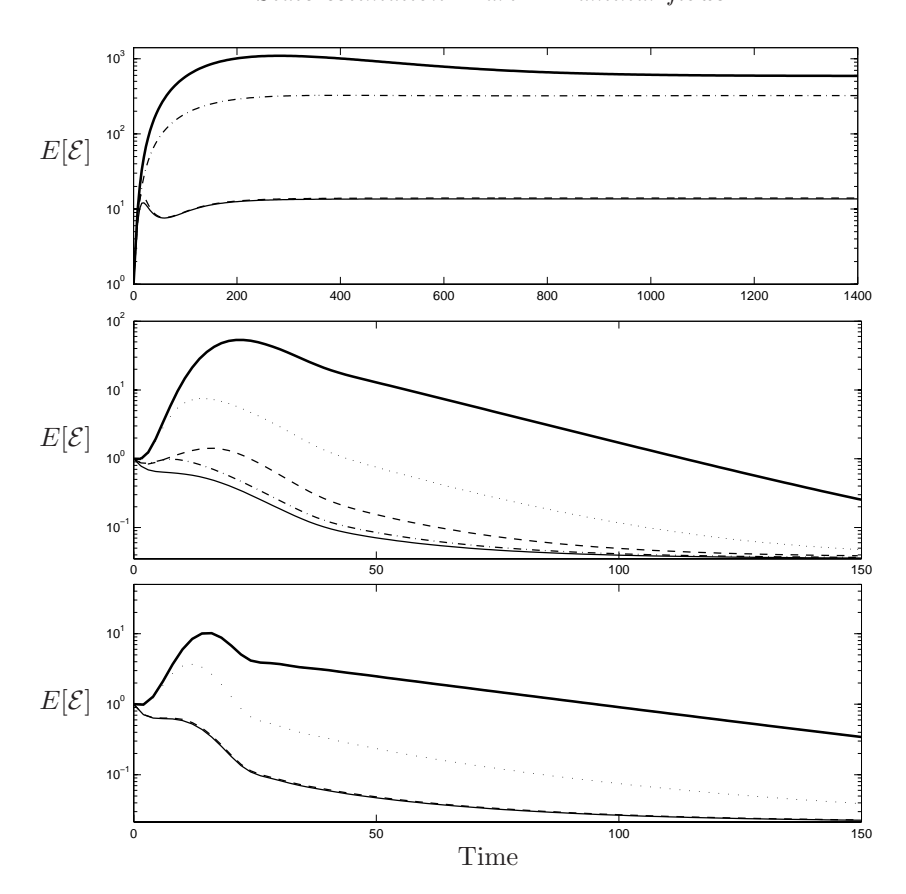


FIGURE 8. Expected energy of the flow (solid thick line) and estimation error when (solid thin line) all measurements are used, (dashed line) only measurements of  $\tau_x$  are used, (dot-dashed line) only measurements of  $\tau_z$  are used, and (dotted line) only measurements of wall pressure are used, at the wavenumber pairs (top) (0,2), (middle) (1,1), and (bottom) (1,0).

the pressure do not contribute significantly to the estimation performance, but in a sense, pressure might be thought of as an "integral" quantity that is more significantly affected by flow events focused farther from the wall.

The evolution in time of the peak amplitudes of the feedback gains for the three different types of measurements, as well as the variance of the measured signals (that is, the expected value of the measurement signal squared), is depicted in Figure 9 for the wavenumber pair (0,2). It is seen that the transient in the feedback gains due to the effects of the initial conditions is clearly significant.

78

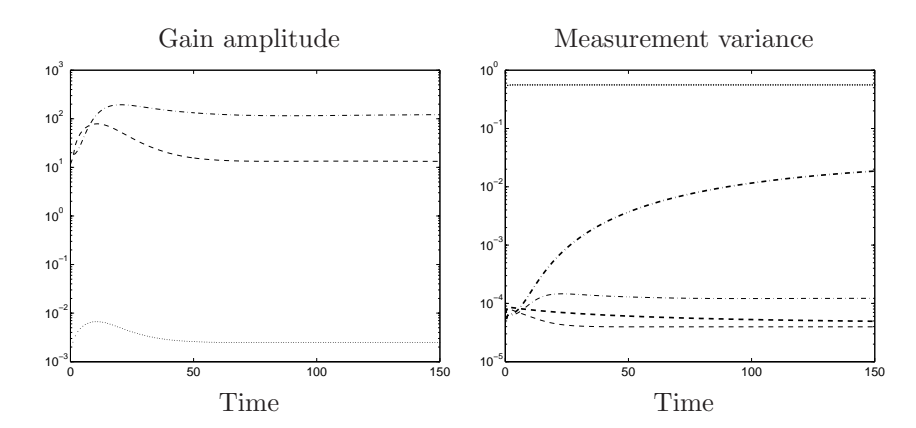


FIGURE 9. Time evolution of the peak absolute value of the gains and the variance of the measurements for the wavenumber pair (0,2). (a) Peak absolute value of the gains for the measurements of (dot-dashed)  $\tau_x$ , (dashed)  $\tau_z$ , and (dotted) wall pressure. (b) Variance of the measured signal (thick lines) and the measurement error (thin lines), with same line types as in part (a).

# 3.5. The effectiveness of freezing selected gains based on the unsteady solution of the DRE

The present section attempts to give some practical insight into the behavior of selected feedback gains chosen from snapshots of the full solution of the DRE. To this end, the expected energy of the estimation error when using constant gains that were determined from snapshots of the unsteady solution to the DRE is illustrated in Figure 10. It is seen that, when gains from early in this time evolution are used, the early stages of the transient are estimated effectively, but there is increased error in the estimate as statistical steady state is approached. When gains from later in this time evolution are used, the estimate of the transient is degraded, but the estimate of the statistical steady state is significantly improved.

# 4. Physical-space characterization

In the previous section, the estimator was tested in the linear setting in Fourier space at individual wavenumber pairs. In this section, we inverse transform the gains computed on a large array of wavenumber pairs to obtain spatially-localized convolution kernels in physical space ( $\S4.1$ ). We then investigate the estimation (in physical space) of two flows of interest, one at very small amplitude, in which nonlinear effects may be neglected ( $\S4.2$ ), and one at a finite amplitude, in which nonlinear effects are significant ( $\S4.3$ ).

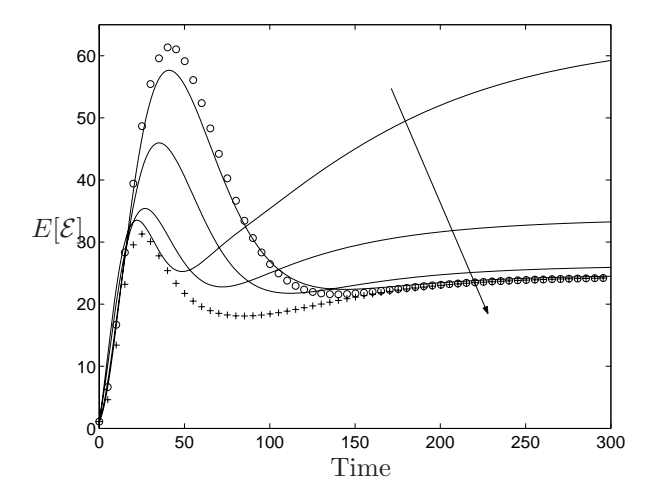


FIGURE 10. Energy of the expected estimation error for gains selected from the time-varying solution to the DRE and applied as constant-gain feedback, tested at the wavenumber pair (0,2). Gains are selected from times 20, 40, 60, and 80 (solid lines, with later times in the direction of the arrow), as compared with the (constant) solution of the ARE ( $\circ$ ) and the full (time-varying) solution of the DRE (+).

# 4.1. Physical-space feedback convolution kernels

The feedback gains for the estimator, as formulated in §2 and tested at individual wavenumber pairs  $\{k_x,k_z\}_{mn}$  in §3, are functions of the wall-normal coordinate y. By computing such feedback gains on a large array of wavenumber pairs and then performing an inverse Fourier transform in x and z, 3D (physical-space) feedback convolution kernels are obtained. Such convolution kernels relate the measurement at a given sensor location on the wall to the forcing of the estimator model in the vicinity of that point, and eventually decay exponentially with distance far from the corresponding sensor. For further discussion of the interpretation of such convolution kernels, the reader is referred to Bewley (2001) and Högberg  $et\ al.\ (2003)$ .

The results presented in this section were computed with p=0, i.e. assuming a constant amplitude of the external disturbance forcing in the wall-normal direction.

# 4.1.1. Time variation of the kernels

To illustrate the time variation of the kernels computed via solution of the DRE, the evolution in time of the kernels corresponding to the measurement of the streamwise skin friction is shown in Figure 11. Note that the shape of this kernel varies rapidly near t=0, then gradually approaches a steady-state. Also note that, near t=0, the kernel is similar in its streamwise and spanwise

extent, but, as time evolves, the kernel becomes elongated in its streamwise extent. This is consistent with the fact that structures with relatively small  $k_x$  are persistent in time and typically dominate such flows.

### 4.1.2. Steady-state shapes of the kernels

The time-varying kernels computed via the solution of the DRE eventually converge to steady-state. Figure 12 shows these steady-state shapes for each of the three measurement and the two evolution equations. Note the close correspondence between the steady-state kernels for the  $\tau_x$  measurement in Figure 12 and the corresponding kernels at t=60 in Figure 11.

It is important to note that the spatial extent of the convolution kernels is related, to some degree, to the correlation length scales chosen during the disturbance parameterization defining the estimation problem. Specifically, the parameters  $d_x$ ,  $d_y$ , and  $d_z$  parameterizing the correlation length scales of the disturbances in §2.4.2 have a direct effect on the spatial extent of the present kernels. For example, Figure 13(a) shows, for three different values of  $d_z$ , the spanwise extent of the pressure kernel forcing the streamwise velocity component of the state estimate, integrated in the streamwise and wall-normal directions. It is clear that, when designing feedback for disturbances which are more "spread out" in the spanwise direction (that is, disturbances with greater two-point correlation length scales in the spanwise direction), the corresponding convolution kernel has a broader spanwise extent. It is also seen that this broader kernel has a lower peak amplitude, since the corresponding forcing is more distributed.

The streamwise extent of the kernel is less sensitive to the streamwise correlation length scale of the disturbances, but is a strong function of the Reynolds number. In a flow with a higher Reynolds number, the effect of flow advection is more pronounced, and information from wall sensors can be related to the interior flow structures responsible for this wall footprint that have since advected further downstream. This effect can be clearly seen in Figure 13(b), which shows the same kernel as in Figure 13(a) but integrated in the spanwise and cross-flow directions for three different Reynolds numbers.

# 4.2. Estimation of an infinitesimal localized flow perturbation

The localized flow perturbation studied by Henningson, Lundbladh & Johansson (1993) is now used to test the convergence of the estimator in physical space. In this section, we will consider the direct numerical simulation of an infinitesimal flow perturbation, so that nonlinear effects in this section can effectively be neglected.

Recall that the estimator initializes the state estimate as zero; that is, it assumes no a priori knowledge of the location of the initial flow perturbation. In the following, we explore different models for the assumed covariance of the initial estimation error by varying the design parameter  $c_2$  in (6). This parameter effectively reflects our level of confidence in our knowledge of the relevant

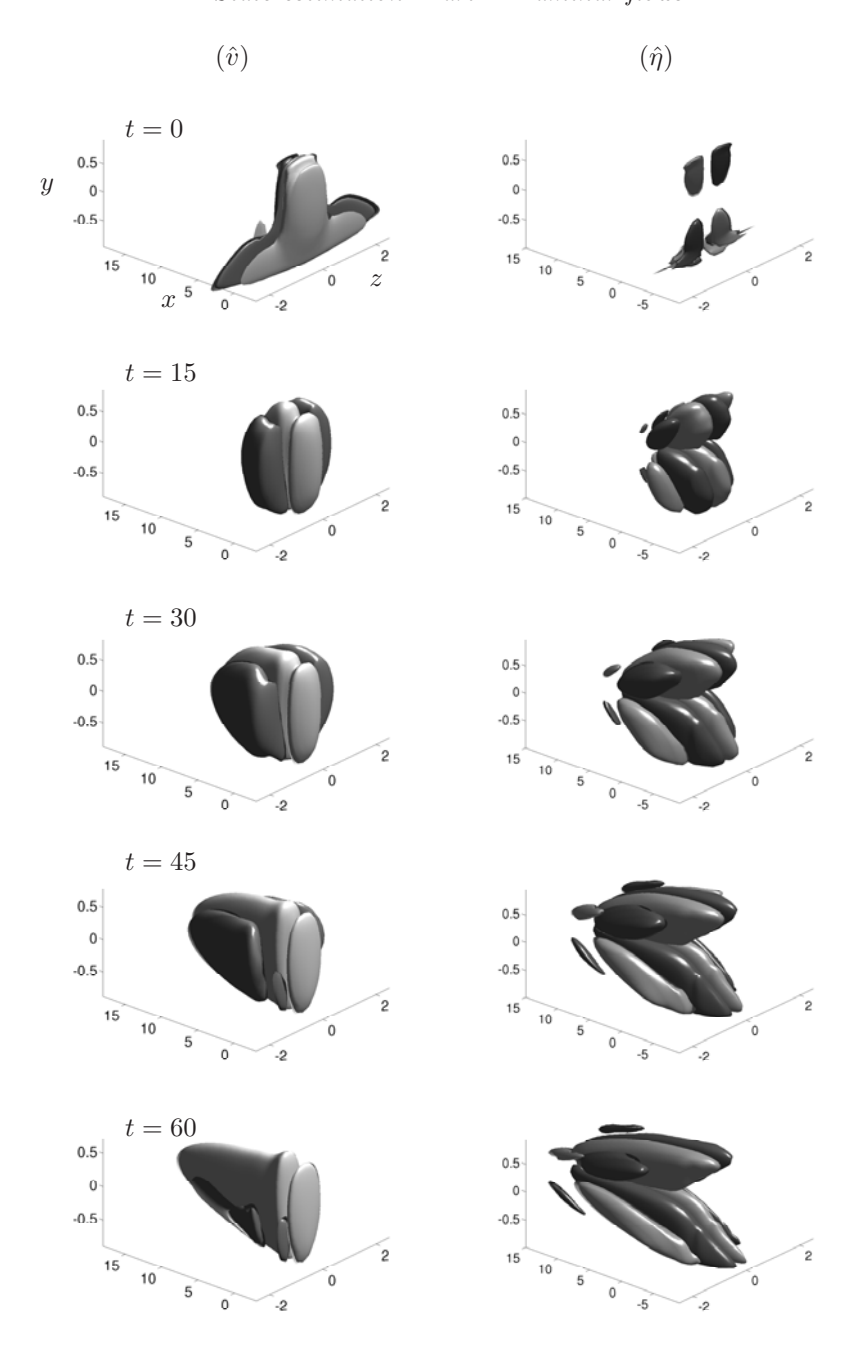


FIGURE 11. The time-varying kernel for times (top to bottom)  $t=0,\ 15,\ 30,\ 45,\ {\rm and}\ 60,\ {\rm relating}\ {\rm the}\ {\rm streamwise}\ {\rm component}$  of the shear stress measurement at the point  $\{x=0,\ y=-1,\ z=0\}$  on the wall to the estimator forcing on the interior of the domain for the evolution equation for the estimate of  $(left)\ (\hat v)\ {\rm and}\ (right)\ (\hat\eta).$  Visualized are positive (dark) and negative (light) isosurfaces with isovalues of  $\pm 5\%$  of the maximum amplitude for each kernel illustrated.

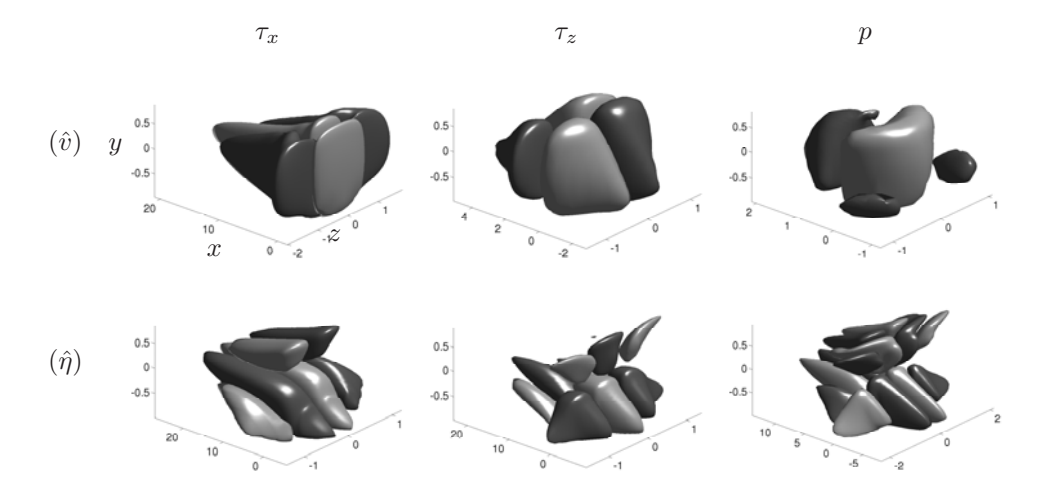


FIGURE 12. The steady-state convolution kernels relating the (left)  $\tau_x$ , (center)  $\tau_z$ , and (right) p measurements at the point  $\{x=0,\ y=-1,\ z=0\}$  on the wall to the estimator forcing on the interior of the domain for the evolution equation for the estimate of (top)  $\hat{v}$  and (bottom)  $\hat{\eta}$ . Visualized are positive (dark) and negative (light) isosurfaces with isovalues of  $\pm 5\%$  of the maximum amplitude for each kernel illustrated.

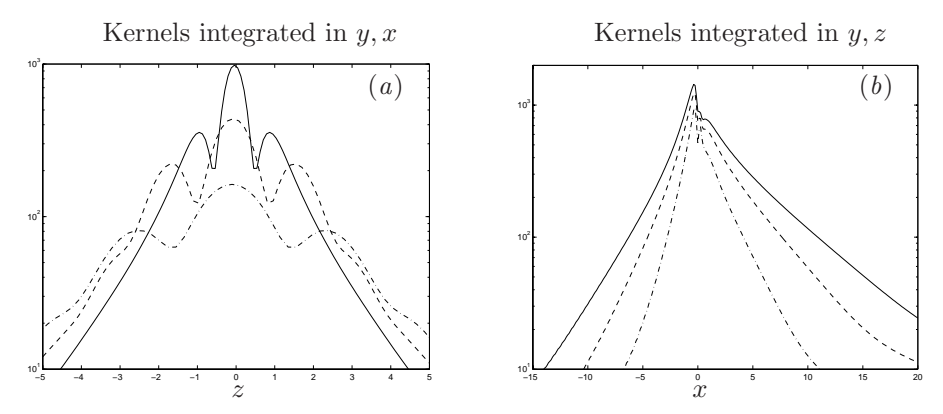


FIGURE 13. Decay of the pressure kernel forcing the streamwise velocity component of the state estimate, (a) integrated in the streamwise and wall normal direction for (solid)  $d_x = d_z = 0.2$ , (dashed) 0.7, and (dot-dashed) 1.3, and (b) integrated in the spanwise and wall-normal directions for (solid) Re = 3000, (dashed) 2000, (dot-dashed) 1000.

statistical properties of the initial conditions, ranging from 0.05 (little specific knowledge of the statistical properties of the initial conditions) to 1 (accurate knowledge of these statistics, but no knowledge of the actual location of the

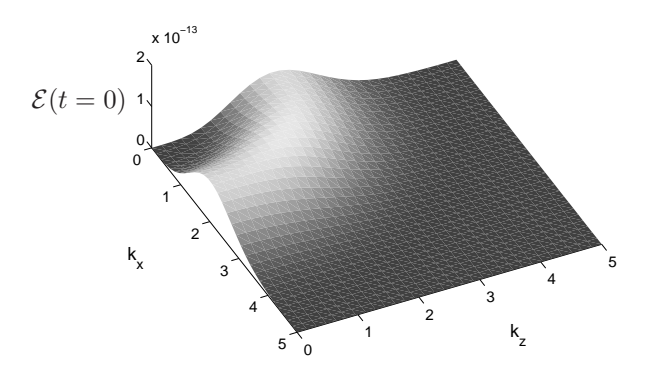


FIGURE 14. Energy content (in Fourier space) of the initial condition for the case studied in §4.2 & §4.3.

initial flow perturbation). For the simulations reported here, the exact initial condition of the flow perturbation, described below, is used as the "specific" component s in the parameterization of the initial covariance of the estimation error, P(0), for the purpose of the computation of the feedback kernels.

The external disturbance forcing of the flow considered in this section is taken as zero, so the resulting simulation might be characterized as a "deterministic" case with no stochastic forcing. The initial condition of the flow considered in this section consists of an axisymmetric disturbance of the form

$$\begin{cases}
\psi = \frac{1}{2}\varepsilon f(y)r^{2}e^{-(r/l)^{2}}, \\
f(y) = (1+y)^{2}(1-y)^{5}, \\
(u,v,w) = (-\frac{x}{r^{2}}\psi_{y}, \frac{1}{r}\psi_{r}, -\frac{z}{r^{2}}\psi_{y}).
\end{cases} (16)$$

Here (x,y,z) are the streamwise, wall-normal, and spanwise coordinates respectively,  $r^2=x^2+z^2$ , and (u,v,w) are the corresponding velocity components. The horizontal extent of this perturbation may be adjusted with the parameter l, which is set equal to 1 for the presented simulations so that the maximum energy of the initial flow perturbation in Fourier space is at the wavenumber pairs showing the greatest transient energy growth, as illustrated in Figure 14. The parameter  $\varepsilon$  scaling the amplitude of the initial flow perturbation is taken as 0.001.

Five different estimators, as formulated in the previous sections with feedback gains computed by selecting  $c_2 = 0.05$ , 0.1, 0.25, 0.5, and 1 respectively, were tested on the problem of estimating this flow. It is seen in Figure 15 that the variation of  $c_2$  between 1 and 0.25 had a relatively small effect on the resulting estimator performance, and that all four of the estimators tested in this range significantly outperformed the estimator that used only the steady

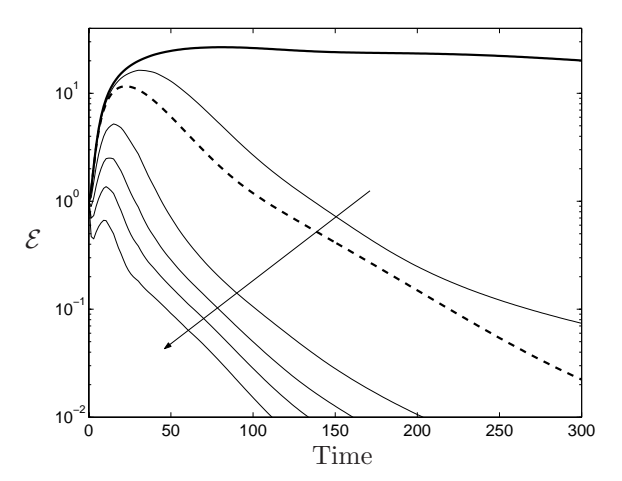


FIGURE 15. The time evolution of the energy of an infinitesimal localized flow perturbation (thick solid line) and the energy of the estimation error of the same flow using (dashed line) the steady state kernels determined from the solution of the ARE as well as (thin solid lines) a gain scheduled set of kernels computed using values of  $c_2 = 0.05, 0.1, 0.25, 0.5,$  and 1, increasing in the direction of the arrow. Note that the energy  $\mathcal{E}$  has been normalized by energy of the initial flow perturbation.

state kernels (dashed line), which does not depend on the parameterization of the statistics of the initial conditions. On the other hand, the estimator in the case with  $c_2 = 0.05$  significantly under-performed the others, indicating that, when no useful information is available concerning the statistics of the initial conditions, one might be better off simply using the steady-state kernels computed via solution of the ARE.

Figure 16 visualizes the evolution of this flow perturbation (left) as it evolves from the initial conditions provided, as well as the evolution of the state estimate (right) as it evolves from the initial condition of zero and is forced by the feedback of the measurement error term as formulated in (9)-(10). It is seen that, by time t=60, all of the major features of the flow are apparently well reproduced by the state estimate. Additionally, as seen in Figure 15, the time t=60 is rather early in the evolution of the flow perturbation—the energy of the flow perturbation is still growing substantially at this point, while the energy of the state estimation error is by now decaying exponentially, indicating successful convergence of the estimator.

# $4.3.\ Estimation\ of\ a\ finite-amplitude\ flow\ perturbation$

We now test the same estimator as used previously on the problem of estimating a flow with the same initial conditions as considered in  $\S4.2$ , but with an initial

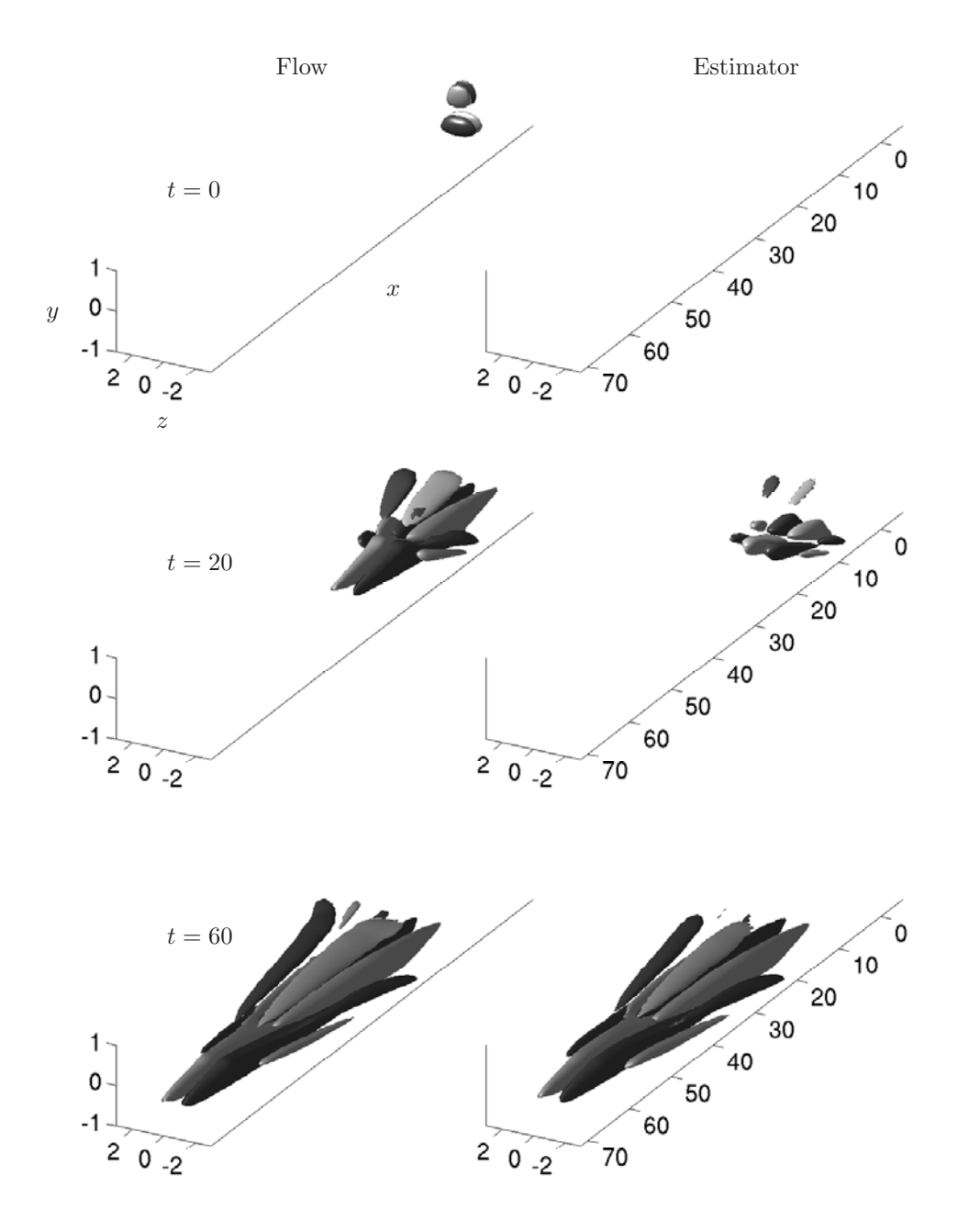


FIGURE 16. Evolution of a localized disturbance to the state (left) and the corresponding state estimate (right) at time t=0 (top), t=20 (middle), and t=60 (bottom), computed with  $c_2=0.08$ . Visualized are positive (light) and negative (dark) isosurfaces of the streamwise component of the velocity. The isovalues are  $\pm 10\%$  of the maximum streamwise velocity of the flow during the time interval shown.

amplitude now almost an order of magnitude larger, such that nonlinear effects play a significant role. We take  $\varepsilon=0.00828$ , which corresponds to a maximum wall normal velocity of 0.0117 at t=0 (this is approximately  $\approx 1.2\%$  of the maximum velocity of the mean flow).

As in §4.2, the direct numerical simulation reported here used the code described in Lundbladh et al. (1992), which uses a pseudo-spectral scheme with Fourier, Chebyshev, and Fourier techniques in the streamwise, wall-normal, and spanwise directions respectively. The time advancement was a third order Runge–Kutta method for the nonlinear terms and a second order Crank–Nicolson method for the linear terms. The box size is  $48 \times 2 \times 24$  and the grid resolution is  $96 \times 65 \times 192$ .

As mentioned in the third paragraph of §3, the estimator used in this work has already been designed to handle well the leading-order effects of nonlinearity. Since we know from Henningson  $et\ al.$  (1993) that nonlinear effects will be most pronounced at wavenumber pairs with lower  $k_x$  and higher  $k_z$  than the initial conditions, we have tuned the covariance of the external disturbance model upon which the estimator is based to account specifically for unmodeled dynamics at these wavenumbers, as depicted in Figure 2. The model for the external disturbances accounts here for a forcing of higher amplitude than for the tests on single wavenumber pairs of §3, with  $d_a=0.25$ , and located closer to the walls, with p=1. With this choice of parameters, the expected flow energy grows due to the initial condition, and continues to grow due to the forcing f, in a way similar to the nonlinear evolution of the flow.

The evolution of the energy of the state and the estimation error for both the moderate-amplitude case ( $\S4.3$ ) and the small-amplitude case ( $\S4.2$ ) are plotted in Figure 17. To facilitate comparison, all curves have been normalized to unity at t=0. Note the significant difference in the normalized energy evolution of the state in the two cases considered (compare the thick solid line and the thick dashed line); this reflects the significant effects of nonlinearities in the moderate amplitude case. For both cases, the initial stage of the evolution (during which nonlinear effects are fairly small in both cases) is well estimated (thin lines). As the moderate-amplitude perturbation evolves and its amplitude grows, nonlinear effects become significant, and the performance of the linear estimator (thin solid line) is degraded as compared with the performance of the linear estimator in the small-amplitude case (thin dashed line).

The Kalman filter is an "optimal" estimator (in several rigorous respects—see Anderson & Moore (1979) for a detailed discussion) in the linear setting. As seen in Figure 17 and discussed in the previous paragraph, when a Kalman filter is applied to a nonlinear system, its performance is typically degraded, due to the fact that the linear model upon which the Kalman filter is based does not include all the terms of the (nonlinear) equation governing the actual system. A common (though somewhat ad hoc) patch which partially accounts for this deficiency is to reintroduce the system nonlinearity to the estimator model after the Kalman filter is designed. This approach is called an extended

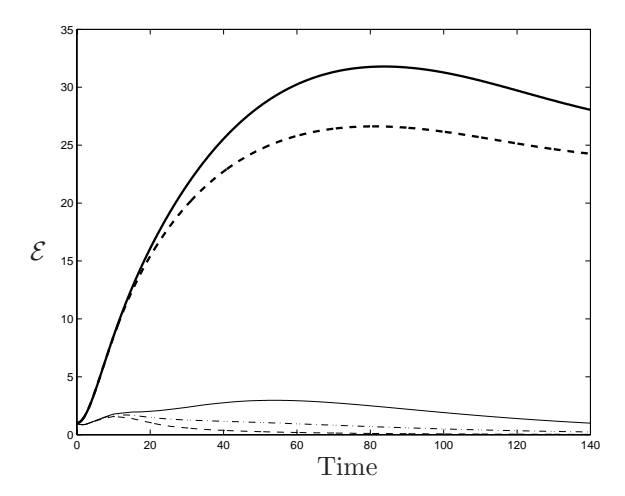


FIGURE 17. Evolution of the normalized flow energy (thick lines) and normalized estimation error energy (thin lines) for the case with moderate-amplitude initial conditions (solid) and low-amplitude initial conditions (dashed). The evolution of the normalized estimation error energy for the extended Kalman filter in the case with moderate-amplitude initial conditions is also plotted (thin dot-dashed line), illustrating a significant improvement as compared with the performance of the corresponding Kalman filter (thin solid line) when nonlinearities are significant.

Kalman filter. This type of estimator is identical to the Kalman filter except for the presence of the system's nonlinearity in the estimator model. This addition makes some sense: if the estimate of the state happens to match the actual state, no feedback from measurements is required for the extended Kalman filter to track the actual flow state. This is not the case for the standard (linear) Kalman filter. As seen clearly in Figure 17, the extended Kalman filter (thin dot-dashed line) enjoys a substantial performance improvement compared with its standard Kalman filter counterpart (the thin solid line) for estimating finite-amplitude flow perturbations when nonlinearities in the system model are significant.

# 5. Conclusions

A canonical feedback control problem in fluid mechanics, which undoubtedly sets the stage for several follow-on flow control problems that incorporate greater geometric complexity, is the feedback control of a near-wall flow system based on limited noisy measurements from flush wall-mounted sensors in order to stabilize the flow and inhibit transition to turbulence. In such problems, it is natural to apply model-based linear control theory, as the equations of motion

of the system are well known and the linearization of these equations are valid, at least during the early stages of the transition process when all flow perturbations are small. The mathematical framework for the linear control theory we have chosen to apply in the present study, commonly called "optimal" or " $\mathcal{H}_2$ " control theory, is well known in both the finite- and infinite-dimensional setting. However, the fact that the flow system is infinite dimensional and that regularity issues play a very subtle roll in the well posedness of this control problem in the infinite-dimensional setting, compounded by the fact that the theory of well posedness of the equations of motion of the system of interest (that is, the 3D Navier–Stokes equation) is not yet even complete, leads to some peculiar challenges in the well-posed framing and subsequent numerical solution of this challenging flow control problem.

Via the so-called Separation Principle, such linearized flow control problems in the optimal setting break up into two independent subproblems: control of the flow with whatever actuators are available based on full state information, and estimation of the full flow state with whatever sensors are available. Once both subproblems are solved effectively, they may be combined to develop a dynamic compensator to control the flow system using limited actuation authority (with, for example, actuators mounted on the walls) based only on limited noisy measurements of the flow (with, for example, sensors mounted on the walls). In previous work, excellent results had been obtained on the full-state feedback control problem, but certain unresolved difficulties remained on the estimation problem. The present work thus focused exclusively on the estimation problem.

The first important development in this work was the introduction of a physically relevant parameterization of the external disturbances acting on the system that converges upon refinement of the numerical grid. This disturbance parameterization is fairly generic, and can easily be used to leverage one's physical insight concerning the initial conditions likely to be encountered in a given flow (for example, Tollmien–Schlichting (TS) waves, streaks, or streamwise vortices). Also, the disturbance parameterization can be tuned in order to modify (at least, to some degree) the spatial extent of the resulting convolution kernels.

Using this disturbance parameterization, together with appropriate parameterizations of the initial conditions and the measurement noise, feedback gains for the estimation problem were computed (using a efficient Chandrasekhar method) for the near-wall flow system in Fourier space on a large array of (decoupled) wavenumber pairs  $\{k_x, k_z\}$ , then inversed transformed to obtain physical-space convolution kernels. The improved disturbance parameterization proposed in this study facilitated, for the first time, the computation of measurement feedback gains in the discretized problem that converged upon grid refinement (and thus are relevant for the infinite-dimensional problem upon which the numerical problem solved in the computer was derived) for all three

types of measurements that are available on the wall (that is, streamwise and spanwise wall skin friction and wall pressure).

The second significant development in this work was the recognition that for the problem of transition control, though time-invariant feedback gains (computed from a corresponding algebraic Riccati equation) are sufficient for the full-state feedback control problem, time-varying feedback gains (computed from a differential Riccati equation) are necessary for the estimation problem in order to minimize the initial transient in the estimation error when the estimator is turned on.

The estimator feedback rules that resulted from these two developments were tested extensively in both in Fourier space (in the linearized setting) and in physical space (in direct numerical simulations of both infinitesimal and finite-amplitude disturbances for which the effects of nonlinearity are significant). The estimator was shown to perform well for all cases studied except when the external disturbances excited center modes, which can happen sometimes for wavenumber pairs with relatively large streamwise component (that is, for modes which are relatively large in their spanwise extent). Fortunately, it was recognized that such cases are not the primary cases of interest in most transition scenarios. It was also found that, when the flow perturbations were large enough that the nonlinearities of the system were significant, an extended Kalman filter which incorporated the system nonlinearity in the estimator model outperformed the standard (linear) Kalman filter.

The reader is referred to Part 2 of this study for a summary of recent work considering the extension of such estimation strategies to the problem of fully-developed near-wall turbulence.

# Acknowledgement

The authors sincerely acknowledge the funding provided by the Swedish research council (VR), the Swedish Defence Research Agency (FOI), and the Dynamics and Control directorate of the Air Force Office of Scientific Research (AFOSR) in support of this work. The authors also thank Espen Åkervik for performing some supporting computations.

# References

Anderson, B. & Moore, J. 1979 Optimal filtering. Prentice-Hall.

Balakrishnan, A. V. 1976 Applied functional analysis. Springer.

Bewley, T. R. 2001 Flow control: new challenges for a new Renaissance. *Progress in Aerospace Sciences* 37, 21–58.

Bewley, T. R. & Liu, S. 1998 Optimal and robust control and estimation of linear paths to transition. *J. Fluid Mech.* **365**, 305–349.

Bewley, T. R. & Protas, B. 2004 Skin friction and pressure: the "footprints" of turbulence. *Physica D* **196**, 28–44.

- Gunzburger, M. D. 1996 Perspectives in flow control and optimization. SIAM.
- Hanifi, A., Schmid, P. J. & Henningson, D. S. 1996 Transient growth in compressible boundary layer flow. *Phys. Fluids* 8, 826–836.
- Henningson, D. S., Lundbladh, A. & Johansson, A. V. 1993 A mechanism for bypass transition from localized disturbances in wall-bounded shear flow. *J. Fluid Mech.* **250**, 169–207.
- HUANG, W. & SLOAN, D. M. 1993 The pseudo-spectral method for solving differential eigenvalue problems. J. Comp. Phys. 111, 399–409.
- HÖGBERG, M., BEWLEY, T. R. & HENNINGSON, D. S. 2003 Linear feedback control and estimation of transition in plane channel flow. J. Fluid Mech. 481, 149–175.
- JOSHI, S. S., SPEYER, J. L. & KIM, J. 1999 Finite dimensional optimal control of Poiseuille flow. J. Guid. Control Dyn. 22, 340.
- Jovanović, M. R. & Bamieh, B. 2001a Modelling flow statistics using the linearized Navier–Stokes equations. In *Proceedings of the 40th IEEE Conference on Decision and Control*, pp. 4944–4949. Orlando, FL.
- Jovanović, M. R. & Bamieh, B. 2001b The spatio-temporal impulse response of the linearized Navier–Stokes equations. In *Proceedings of the 2001 American Control Conference*, pp. 1948–1953. Arlington, VA.
- KAILATH, T. 1973 Some new algorithms for recursive estimation in constant linear systems. *IEEE transaction on information theory* **IT-19** (6), 750–760.
- Kim, J. 2003 Control of turbulent boundary layers. Phys. Fluids 15 (5).
- KIM, J. & LIM, J. 2000 A linear process in wall-bounded turbulent shear flows. Phys. Fluids 12 (8), 1885–1888.
- LAUB, A. J. 1991 Invariant subspace methods for the numerical solution of Riccati equations. Springer.
- Lee, C., Kim, J., Babcock, C. & Goodman, R. 1997 Application of neural network to turbulence control for drag reduction. *Phys. Fluids* 9, 1740–1747.
- Lewis, F. L. & Syrmos, V. L. 1995 Optimal control. Wiley-Interscience.
- Lundbladh, A., Henningson, D. & Johansson, A. 1992 An efficient spectral integration method for the solution of the Navier–Stokes equations. *Tech. Rep.*. Aeronautical Research institute of Sweden, Bromma.
- Schmid, P. J. & Henningson, D. S. 2001 Stability and transition in shear flows. Springer.
- Thomas, A. S. W. 1990 Active wave control of boundary-layer transition. In *Viscous Drag Reduction in Boundary Layers* (eds. D. M. Bushnell & J. N. Hefner), *Progress in Astronautics and Aeronautics*, vol. 123. Washington, D.C: American Institute of Aeronautics and Astronautics.
- Weideman, J. A. C. & Reddy, S. C. 2000 A matlab Differentiation Matrix Suite. ACM Transaction of Mathematical Software **26** (4), 465–519.

Paper 2

2

# State estimation in wall-bounded flow systems. Part 2. Turbulent flows

By Mattias Chevalier\*†, Jérôme Hœpffner\*, Thomas R. Bewley‡ and Dan S. Henningson\*†

Submitted to Journal of Fluid Mechanics

This work extends the estimator developed in Part 1 of this study (Hoepffner et al., J. Fluid Mech., submitted) to the problem of estimating a turbulent channel flow at  $Re_{\tau} = 100$  based on a history of noisy measurements on the wall. The key advancement enabling this work is the development and implementation of an efficient technique to extract, from direct numerical simulations, the relevant statistics (mean and covariance) of an appropriately-defined "external forcing" term on the Navier-Stokes equation linearized about the mean turbulent flow profile. This forcing term is designed to account for the unmodelled (nonlinear) terms during the computation of the (linear) Kalman filter feedback gains at each wavenumber pair  $\{k_x, k_z\}$ . The statistics of this forcing term are found to have some similarities to the parameterization of the external disturbances considered in Part 1 of this study, which dealt with the estimation of the early stages of transition in the same domain. Three key steps were identified in obtaining adequate estimator performance in the near-wall region: 1) linearization the flow system about the mean turbulent flow profile, accounting for the statistics of the additional forcing term during the computation of the feedback gains, 2) extraction of these statistics from a direct numerical simulation, and 3) incorporation of the nonlinearity of the actual system into the estimator model at the final step in the development of the estimator (using an extended Kalman filter). Upon inverse transform of the resulting feedback gains computed on an array of wavenumber pairs, we obtain, as in Part 1, effective and well-resolved feedback convolution kernels for the estimation problem.

It is demonstrated that by applying the optimal feedback gains, for all three measurements, satisfactory correlation between the actual and estimated flow is obtained in the near-wall regions. The correlation eventually decays as the wall distance increases but the decay sets in later compared to using estimation gains based on a statistically uncorrelated stochastic models. Both Kalman and extended Kalman filters are evaluated and naturally the extended filter is giving better correlations between the actual and estimated flow, however the Kalman filter gives good performance in the near-wall regions.

<sup>\*</sup>Department of Mechanics, Royal Institute of Technology (KTH), SE-100 44 Stockholm, Sweden

<sup>&</sup>lt;sup>†</sup>The Swedish Defence Research Agency (FOI), SE-172 90 Stockholm, Sweden

 $<sup>^{\</sup>ddagger}$ Flow Control Lab, Department of MAE, UC San Diego, La Jolla, CA 92093-0411, USA

#### 1. Introduction

This paper builds directly on Part 1 of this study (Hœpffner et al., J. Fluid Mech., submitted, hereafter referred to as Part 1). It extends the estimator developed there, for the case of perturbed laminar channel flow, to the problem of fully-developed channel-flow turbulence. The reader is referred to Part 1 for related general references, background information on optimal state estimation (Kalman filter) theory, and a description of what it takes to apply this theory to a well-resolved discretization of a fluid system in a manner that is consistent with the continuous PDE system upon which this discretization is based (that is, in a manner such that the resulting feedback convolution kernels converge upon refinement of the numerical grid). The present paper effectively picks up where Part 1 left off, and treats specifically the issues involved in extending the estimator developed in Part 1 to the problem of estimating a fully-developed turbulent channel flow based on wall measurements.

# 1.1. Model predictive estimation

There are two natural approaches for model-based estimation of near-wall turbulent flows: model predictive estimation and extended Kalman filtering. Bewley & Protas (2004) discusses the model predictive estimation approach, which is based on iterative state and adjoint calculations, optimizing the estimate of the state of the system such that the nonlinear evolution of the system model, over a finite horizon in time, matches the available measurements to the maximum extent possible. This is typically accomplished by optimizing the initial conditions in the estimator model in order to minimize a cost function measuring a mean-square "misfit" of the measurements from the corresponding quantities in the estimator model over the time horizon of interest. This optimization is performed iteratively, using gradient information provided by calculation of an appropriately-defined adjoint field driven by the measurement misfits at the wall. The technique provides an optimized estimate of the state of the system which accounts for the full nonlinear evolution of the system, albeit over a finite time horizon and providing only a local optimal which might be far from the actual flow state sought. The technique is typically expensive computationally, as it requires iterative marches of the state and adjoint fields over the time horizon of interest in order to obtain the state estimate; for this reason, this approach is often quickly disqualified from consideration as being computationally intractable for practical implementation. The model predictive estimation approach is closely related to the adjoint-based approach to weather forecasting, commonly known as 4D-var. For further discussion of model predictive estimation as it applies to near-wall turbulence, the reader is referred to Bewley & Protas (2004).

# 1.2. Extended Kalman filtering

The extended Kalman filter approach, which is the focus of the present paper, is described in detail in Part 1 of this study. To summarize it briefly, the estimation problem is first considered in the linearized setting. Define  $\hat{r}_m$  as the Fourier transform of the vector of all three measurements available on the walls in the actual flow system at wavenumber pair  $\{k_x, k_z\}$ , and define  $\hat{r}$  as the corresponding quantity in the estimator model. At each wavenumber pair  $\{k_x, k_z\}$ , a set of feedback gains L is first computed such that a forcing term  $\hat{v} = L(\hat{r}_m - \hat{r})$  on the (linearized) estimator model results in a minimization of the energy of the estimation error (that is, this feedback minimizes the trace of the covariance of the estimation error, usually denoted P), assuming the flow state itself is also governed by the same linearized model. This is called a Kalman filter, and the theory for the calculation of the optimal feedback gain L in the estimator is elegant, mathematically rigorous, and well known\*.

Upon inverse transform of the resulting feedback gains computed on an array of wavenumber pairs, we seek (and, indeed, find) well resolved feedback convolution kernels for the estimation problem that, far enough from the origin (that is, from , decay exponentially with distance from the origin. The reader is referred to Bamieh (1997), Bewley (2001) and Högberg  $et\ al.\ (2003a)$  for further discussion of

- 1. the technique used to transform feedback gains in Fourier space to feedback convolution kernels in physical space,
- 2. interpretation of what these convolution kernels mean in both the control and estimation problems, and
- 3. description of the overlapping decentralized control implementation facilitated by this approach, which is built from an interconnected array of identical tiles, each with actuators, sensors, and control logic incorporated, that communicate only with their neighbors.

Ultimately, the estimator feedback  $\hat{v} = L(\hat{r}_m - \hat{r})$  is applied to a full (nonlinear) model of the flow system. This final step of reintroducing the nonlinearity of the system into the estimator model results in what is called an extended Kalman filter. In practice, the extended Kalman filter has proved to be one of the most reliable techniques available for estimating the evolution of nonlinear systems.

# 1.3. On the suitability of linear models of turbulence for state estimation and

As described in the previous section, the feedback kernels used in the extended Kalman filter are calculated based on a linearized model of the fluid system.

<sup>\*</sup>For a succinct introduction in the spatially-discrete (ODE) setting, see, e.g., p. 463–470 of Lewis & Syrmos (1995). For a more comprehensive presentation in the ODE setting, see Anderson & Moore (1979). For the corresponding derivation in the spatially-continuous (PDE) setting, see Balakrishnan (1976).

Thus, the applicability of the extended Kalman filtering strategy to turbulence is predicated upon the hypothesis that linearized models faithfully represent at least some of the important dynamic processes in turbulent flow systems.

The fluid dynamics literature of the last decade is replete with articles aimed at supporting this hypothesis. For example, Farrell & Ioannou (1996) used these linearized equations in an attempt to explain the mechanism for the turbulence attenuation that is caused by the closed-loop control strategy now commonly known as opposition control. Jovanović & Bamieh (2001) proposed a stochastic disturbance model which, when used to force the linearized open-loop Navier–Stokes equation, led to a simulated flow state with certain second-order statistics (specifically,  $u_{rms}$ ,  $v_{rms}$ ,  $w_{rms}$ , and the Reynolds stress  $-\overline{uv}$ ) that mimicked, with varying degrees of precision, the statistics from a full DNS of a turbulent flow at  $Re_{\tau}=180$ .

Clearly, however, the hypothesis concerning the relevance of linearized models to the turbulence problem can only be taken so far, as linear models of fluid systems do not capture the nonlinear "scattering" or "cascade" of energy over a range of length scales and time scales, and thus linear models fail to capture an essential dynamical effect that endows turbulence with its inherent "multiscale" characteristics. The key philosophy of the present work (and, indeed, the key philosophy motivating our application of linear control theory to turbulence in general), is that the fidelity required of a model for it to be adequate for control (or estimator) design is in fact much lower than the fidelity required of a model for it to be adequate for accurate simulation of the system. Thus, for the purpose of computing feedback for the control and estimation problems, linear models might well be good enough, even though the fidelity of linear models as simulation tools to capture the open-loop statistics of turbulent flows is still the matter of some debate in the fluids literature. All that the feedback in an extended Kalman filter has to do is to give the estimator model a "nudge" in approximately the right direction when the state and the state estimate are diverging. The extended Kalman filter contains the full nonlinear equations of the actual system in the estimator model, so if the state and the state estimate are sufficiently close, the estimator will accurately track the state, for at least a short period of time, with little or no additional forcing necessary.

Stating this philosophy another way, in the control problem, the model upon which the control feedback is computed need only include the key terms responsible for the production of energy. Since the nonlinear terms in the Navier–Stokes equations are conservative, and thereby do not contribute directly to energy production, we can expect that a linear model may suffice. For Navier–Stokes systems near solid walls, there is evidence that this is in fact true, at least for sufficiently low Reynolds number. Kim & Lim (2000) showed that interior body forcing (applied everywhere inside the flow domain) that was constructed to exactly cancel the linear coupling term in the linear part of the nonlinear Navier–Stokes equation (that is, canceling the  $\mathcal{L}_C$  term in (4)) was

sufficient to completely relaminarize the turbulent flow. Högberg  $et\ al.\ (2003b)$  showed that blowing and suction distributed on the channel walls that was determined using full-information linear control theory (scheduling the feedback gains based on the instantaneous shape of the mean velocity profile) was also sufficient to completely relaminarize the turbulent flow.

The present work on the estimation problem is based on the related philosophy that, in a similar manner, the model upon which the estimator feedback is computed need only capture the key terms responsible for the production of energy in the system describing the estimation error.

# 1.4. The problem of nearly unobservable modes

The problem of estimating the state of a chaotic nonlinear system based on limited noisy measurements of the system is inherently difficult. When posed as an optimization problem (for example, in the model predictive estimation approach described previously), one can expect that, in general, multiple local minima of such a nonconvex optimization problem will exist, many of which will be associated with state estimates that are in fact poor. These difficulties are exacerbated in the case of the estimation of near-wall turbulence by the fact that turbulence is a multiscale phenomenon (that is, it is characterized by energetic motions over a broad range of length scales and time scales that interact in a nonlinear fashion), with significant nonlinear chaotic dynamics evolving far from where sensors are located (that is, on the walls).

As illustrated, e.g., in Figure 1b of BL98 (that is, Bewley & Liu 1998), quantified by the "observation residual" in Table 1 of BL98, and discussed further in Part 1, even in the laminar case, at  $k_x = 1$ ,  $k_z = 0$  a significant number of the leading eigenmodes of the system are "center modes" with very little support near the walls, and are thus are nearly unobservable with wall-mounted sensors. As easily shown via similar plots in the turbulent case at the same and higher bulk Reynolds numbers, an even higher percentage of the leading eigenmodes of the linearized system are nearly unobservable (that is, have very little support near the walls) in the turbulent case, with the problem getting worse as the Reynolds number is increased. We thus see that the problem of estimating turbulence is fundamentally harder than the problem of estimating perturbations to a laminar flow even if the linear model of turbulence is considered as valid, simply due to the heightened presence of nearly unobservable modes.

In the present work we focus our attention primarily on getting an accurate state estimate fairly close to the walls, where the sensors are located. This is done with the idea in mind that, in the problem of turbulence control (which is our ultimate long-term objective in this effort, and the reason we are pursuing this line of investigation in the first place), it is the near-wall region only that, on average, turbulence "production" substantially exceeds "dissipation", as pointed out in Jimenez (1999). Thus, we proceed with the objective that, if we can

- 1. estimate the fluctuations in the near-wall region with a sufficient degree of accuracy, then
- 2. subdue these near-wall fluctuations with appropriate control feedback,

then we will have a net stabilizing effect on the turbulent motions in the entire flow system, even if we don't completely relaminarize the turbulent flow. It is thus, we hypothesize, unnecessary for us to estimate the precise motions of the flow far from the wall in order to realize our ultimate objective in this work. Flow-field fluctuations far from the wall, which will not be estimated accurately in this work, will (through nonlinear interactions) act as disturbances to excite continuously the state estimation error, while feedback from the sensors will be used to subdue continuously this error in the near-wall region.

# 1.5. Comparison of the estimation and control problems applied to near-wall turbulence

Another significant difference between the turbulence control and turbulence estimation problems is that, in the control problem, once (if) the control becomes effective, the system approaches a stationary state in which the linearization of the system is valid. In the estimation problem, on the other hand, even if the estimate at some time is quite accurate, the system is still moving on its chaotic attractor, so the linearization of the system about some mean state is not strictly valid. Thus, in this respect, it is seen that the turbulence estimation problem might be considered as being fundamentally harder than the turbulence control problem.

# 1.6. Outline

A brief review of the governing equations and some of the particular properties of the extended Kalman filter used in this work is given in §2. Section 3 collects and analyzes the relevant statistics from a direct numerical simulation of a turbulent channel flow at  $Re_{\tau}=100$  in order to build the estimator. The statistical data from §3 is then used in §4 to compute feedback gains (in Fourier space) and kernels (in physical space) for the estimator. The performance of the resulting estimator is evaluated via DNS in §5, and §6 presents some concluding remarks and suggestions for future improvements.

# 2. Governing equations

# 2.1. State equation and identification of terms lumped into the "external forcing" f

The system model considered in this work is the Navier–Stokes equation for the three velocity components  $\{U,V,W\}$  and pressure P of an incompressible channel flow, written as a (nonlinear) perturbation about a base flow profile

 $\bar{u}(y)$  and bulk pressure variation  $\bar{p}(x)$  such that, defining

$$\begin{pmatrix} U \\ V \\ W \\ P \end{pmatrix} = \begin{pmatrix} u \\ v \\ w \\ p \end{pmatrix} + \begin{pmatrix} \bar{u}(y) \\ 0 \\ 0 \\ \bar{p}(x) \end{pmatrix},$$

where  $\{u, v, w, p\}$  denote the temporally-fluctuating components of the flow, we have

$$\frac{\partial u}{\partial t} + \bar{u}\frac{\partial u}{\partial x} + v\frac{\partial \bar{u}}{\partial y} = -\frac{\partial p}{\partial x} + \mu \Delta u + n_1, \tag{1a}$$

$$\frac{\partial v}{\partial t} + \bar{u}\frac{\partial v}{\partial x} = -\frac{\partial p}{\partial u} + \mu \Delta v + n_2, \tag{1b}$$

$$\frac{\partial v}{\partial t} + \bar{u} \frac{\partial v}{\partial x} = -\frac{\partial p}{\partial y} + \mu \Delta v + n_2,$$

$$\frac{\partial w}{\partial t} + \bar{u} \frac{\partial w}{\partial x} = -\frac{\partial p}{\partial z} + \mu \Delta w + n_3,$$
(1b)

$$\frac{\partial u}{\partial x} + \frac{\partial v}{\partial y} + \frac{\partial w}{\partial z} = 0, \tag{2}$$

where

$$n_{1} = -u\frac{\partial u}{\partial x} - v\frac{\partial u}{\partial y} - w\frac{\partial u}{\partial z} - \frac{\partial \bar{p}}{\partial x} + \mu\frac{\partial^{2}\bar{u}}{\partial y^{2}},$$

$$n_{2} = -u\frac{\partial v}{\partial x} - v\frac{\partial v}{\partial y} - w\frac{\partial v}{\partial z},$$

$$n_{3} = -u\frac{\partial w}{\partial x} - v\frac{\partial w}{\partial y} - w\frac{\partial w}{\partial z}.$$
(3)

By selecting the base flow profile  $\bar{u}(y)$  as the mean flow,

$$\bar{u}(y) = \lim_{T \to \infty} \frac{1}{T L_x L_z} \int_0^T \int_0^{L_x} \int_0^{L_z} U dz dx dt,$$

and selecting  $\bar{p}(x)$  to account for the mean pressure gradient sustaining the flow, it follows that the mean value of the terms  $\{n_1, n_2, n_3\}$ , in addition to the mean value of the fluctuating velocity components,  $\{u, v, w\}$ , are zero everywhere. Note that we assume no-slip solid walls (U = V = W = u = v = w = 0 on y = w = w = 0) $\pm 1$ ) and that periodic boundary conditions are applied in the x and z directions to the perturbations variables  $\{u, v, w, p\}$ . This facilitates decomposition of the perturbation problem (1) in the x and z directions using a Fourier series.

We now apply such a Fourier decomposition to (1), using hat subscripts (^) to denote the Fourier representation. The system may then be transformed to  $\{\hat{v},\hat{\eta}\}$  form in a straightforward fashion. Applying the Laplacian  $\Delta = \partial^2/\partial y^2 - k^2$ , where  $k^2 = k_x^2 + k_z^2$ , to the Fourier transform of (1b), substituting for  $\Delta \hat{p}$  from the divergence of the Fourier transform of (1), and applying the Fourier transform of (2) gives the equation for  $\hat{v}$ . Subtracting  $ik_x$  times the Fourier transform of (1c) from  $ik_z$  times the Fourier transform (1a) gives the equation for  $\hat{\eta} = ik_z\hat{u} - ik_x\hat{w}$ . The result is the linear Orr-Sommerfeld/Squire equations at each wavenumber pair  $\{k_x, k_z\}$  with an extra term accounting for the nonlinearity of the system

$$\begin{pmatrix} \Delta & 0 \\ 0 & I \end{pmatrix} \begin{pmatrix} \dot{\hat{v}} \\ \dot{\hat{\eta}} \end{pmatrix} = \begin{pmatrix} \mathcal{L}_{OS} & 0 \\ \mathcal{L}_{C} & \mathcal{L}_{SQ} \end{pmatrix} \begin{pmatrix} \hat{v} \\ \hat{\eta} \end{pmatrix} + \begin{pmatrix} ik_{x}D & k^{2} & ik_{z}D \\ ik_{z} & 0 & -ik_{x} \end{pmatrix} \begin{pmatrix} \hat{n}_{1} \\ \hat{n}_{2} \\ \hat{n}_{3} \end{pmatrix}, \quad (4)$$

where

$$\mathcal{L}_{OS} = -ik_x U \Delta + ik_x U'' + \Delta^2 / Re,$$

$$\mathcal{L}_{SQ} = -ik_x U + \Delta / Re,$$

$$\mathcal{L}_C = -ik_z U',$$
(5)

where  $\{\hat{n}_1, \hat{n}_2, \hat{n}_3\}$  are given by the Fourier transform of (3), taking (from the Fourier transform of (2) and the definition of  $\hat{\eta}$ )

$$\hat{u} = \frac{i}{k^2} \left( k_x \frac{\partial \hat{v}}{\partial y} - k_z \hat{\eta} \right), \quad \hat{w} = \frac{i}{k^2} \left( k_z \frac{\partial \hat{v}}{\partial y} + k_x \hat{\eta} \right),$$

and where, with the walls located at  $y=\pm 1$  and the velocities normalized such that the peak value of  $\bar{u}(y)$  is 1, Re is the Reynolds number based on the centerline velocity and channel half-width. Note that, for  $k_x=k_z=0$ , it follows immediately from the definition of this system that  $\hat{v}=\hat{\omega}=0$  for all y. For all other wavenumber pairs, multiplying (4) by the inverse of the matrix on its LHS, it is straightforward to write the governing equation as

$$\dot{\hat{q}} = A\hat{q} + B\hat{n},\tag{6}$$

where

$$\hat{q} = \begin{pmatrix} \hat{v} \\ \hat{\eta} \end{pmatrix}, \quad \hat{n} = \begin{pmatrix} \hat{n}_1 \\ \hat{n}_2 \\ \hat{n}_3 \end{pmatrix}, \quad A = \begin{pmatrix} \Delta^{-1} \mathcal{L}_{OS} & 0 \\ \mathcal{L}_C & \mathcal{L}_{SQ} \end{pmatrix},$$

$$B = \begin{pmatrix} \Delta^{-1} i k_x D & \Delta^{-1} k^2 & \Delta^{-1} i k_z D \\ i k_z & 0 & -i k_x \end{pmatrix}.$$

Note that the terms in this expression depend on the wavenumber pair being considered,  $\{k_x, k_z\}$ , and that the state  $\hat{q}$  is a continuous function of both the wall-normal coordinate y and the time coordinate t. Implementation of this equation in the computer requires discretization of this system in the wall-normal direction y and a discrete march in time t.

The present system may be linearized by replacing the exact expression for n by an appropriate stochastic model, which we will denote f, thereby obtaining the linear state-space model

$$\dot{\hat{q}} = A\hat{q} + B\hat{f},\tag{7}$$

As the mean of n is everywhere zero, it is logical to select this stochastic model such that E[f] = 0, where the expectation operator  $E[\cdot]$  is defined as the average over many many realizations of the stochastic quantity in brackets. The covariance of f will be modeled carefully based on the covariance of n observed in DNS, as discussed further in §2.3.

#### 2.2. Measurements

The present work attempts to develop the best possible estimate of the state based on measurements of the flow on the walls. As discussed in Part 1, and in greater detail in Bewley & Protas (2004), the three measurements available on the walls are the distributions of the streamwise and spanwise wall skin friction and the wall pressure. This information is mathematically complete in the following sense: if this information is uncorrupted by noise and the external forcing on the system is known exactly, the entire state of the flow (even in the fully turbulent regime, and at any Reynolds number) is uniquely determined by these measurements at the wall in an arbitrarily small neighborhood of time t(without knowledge of the initial conditions). However, the actual identification of this state is quite another matter, as it reflects an ill-posed problem that is hyper-sensitive to all sorts of errors (e.g., modeling errors, measurement errors, numerical errors, series truncation errors, etc.). These errors are unavoidable, even in relatively "clean" numerical experiments. Thus, the problem of estimation may be viewed as a "smoothing problem", or an attempt to reconcile noisy measurements with an approximate dynamic model of the system.

In the present paper, we have chosen to transform the three measurements available on the walls (of streamwise and spanwise wall skin friction and wall pressure) to a slightly different form such that their effects on the estimation of the system (7), which is in  $\{v,\eta\}$  form, is a bit more transparent. There is a bit of flexibility here; in the present work, we have chosen to define this transformed measurement vector r to contain scaled versions of the wall values of the wall-normal derivative of the wall-normal vorticity,  $\frac{1}{Re}\eta_y$ , the second wall-normal derivative of the wall-normal velocity,  $\frac{1}{Re}v_{yy}$ , and the pressure, p. Note that we can easily relate this transformed measurement vector to the raw measurements of  $\tau_x = \frac{1}{Re}u_y$ ,  $\tau_z = \frac{1}{Re}w_y$ , and p on the walls, which might be available from a lab experiment, via the relation (in Fourier space)

$$\hat{r} \triangleq \begin{pmatrix} \frac{1}{Re} \hat{\eta}_y |_{wall} \\ \frac{1}{Re} \hat{v}_{yy} |_{wall} \\ \hat{p}|_{wall} \end{pmatrix} = \begin{pmatrix} ik_z & -ik_x & 0 \\ -ik_x & -ik_z & 0 \\ 0 & 0 & I \end{pmatrix} \begin{pmatrix} \hat{\tau}_x |_{wall} \\ \hat{\tau}_z |_{wall} \\ \hat{p}|_{wall} \end{pmatrix} \triangleq T \begin{pmatrix} \hat{\tau}_x |_{wall} \\ \hat{\tau}_z |_{wall} \\ \hat{p}|_{wall} \end{pmatrix}, \quad (8)$$

and we may relate the transformed measurement vector  $\boldsymbol{r}$  to the state  $\boldsymbol{q}$  via the simple relation

$$r = Cq + g \quad \text{with} \quad C = \frac{1}{Re} \begin{pmatrix} 0 & \frac{\partial}{\partial y} \Big|_{wall} \\ \frac{\partial^2}{\partial y^2} \Big|_{wall} & 0 \\ \frac{1}{k^2} \frac{\partial^3}{\partial y^3} \Big|_{wall} & 0 \end{pmatrix}, \tag{9}$$

where g accounts for the measurement noise. The last row of the above relation is easily verified by taking  $\partial/\partial x$  of the x-momentum equation plus  $\partial/\partial z$  of the z-momentum equation, then applying continuity and the boundary conditions.

For the purpose of posing the present state estimation problem, the measurements are assumed to be corrupted by uncorrelated, zero-mean, white

Gaussian noise processes, which are assembled into the vector  $\hat{g}$  with an assumed covariance (in Fourier space) of

$$G = \begin{pmatrix} \alpha_{\eta}^2 & 0 & 0\\ 0 & \alpha_v^2 & 0\\ 0 & 0 & \alpha_p^2 \end{pmatrix}. \tag{10}$$

Note that such an assumption of uncorrelated, white (in space and time) noise is in fact a fairly realistic model for electrical noise in the sensors. Note also that, for a given covariance of f, which we shall define in the following section, the diagonal components of G effectively parameterize the balance between the two types of stochastic forcing in this problem, the measurement noise g and the stochastic forcing f, and thus reflect how much we "trust" our three types of measurements. If our trust in the measurements is increased (that is, if the diagonal components of G are reduced), then generally more feedback is applied by the resulting Kalman filter gains in order to correct the estimator more aggressively based on the information contained in the measurements.

A different parameterization for the noise covariance that might be of interest in a practical implementation, in which the physical sensors measure  $\tau_x$ ,  $\tau_y$ , and p, is

$$G = T \begin{pmatrix} \alpha_{\tau_x}^2 & 0 & 0 \\ 0 & \alpha_{\tau_y}^2 & 0 \\ 0 & 0 & \alpha_p^2 \end{pmatrix} T^*, \tag{11}$$

where T is defined in (8) and the convenient relation given in (2.5) of Part 1 has been used to relate the covariance of the noise on the raw measurements to the present formulation. This parameterization should also be explored numerically in future work.

## 2.3. Extracting the relevant statistics for state estimation from resolved simulations

The performance of the estimator may be tuned by accurate parameterization of the relevant statistical properties of the forcing term f in the linearized state model, in addition to adjusting the parameterization of the statistical properties of the measurement noise g. These statistics play an essential role in the computation of the Kalman filter feedback gains.

In the present work, we will assume that f is effectively uncorrelated from one time step to the next (that is, we assume that f is "white" in time) in order to simplify the design of the estimator. Subject to this central assumption, we proceed by developing an accurate model for the assumed spatial correlations of f. As the system under consideration is statistically homogeneous in the x and z directions, the covariance of the stochastic forcing f may be parameterized in physical space as

$$E[f_i(x, y, z, t)f_i(x + r_x, y', z + r_z, t')] = \delta(t - t')Q_{f_i f_i}(y, y', r_x, r_z),$$

where  $\delta(t)$  denotes the Dirac delta and where the covariance  $Q_{f_if_j}$  is determined by calculating the statistics of the actual nonlinear forcing term n in a DNS,

$$Q_{f_i f_j}(y, y', r_x, r_z) = \lim_{T \to \infty} \frac{1}{T L_x L_z} \int_0^T \int_0^{L_x} \int_0^{L_z} n_i(x, y, z) n_j(x + r_x, y', z + r_z) dz dx dt.$$
(12)

As the system under consideration is statistically homogeneous, or "spatially invariant", in the x and z directions, it is more convenient to work with the Fourier transform of the two-point correlation  $Q_{f_if_j}$  rather than working with  $Q_{f_if_j}$  itself, as the calculation of  $Q_{f_if_j}$  in physical space involves a convolution sum, which reduces to a simple multiplication in Fourier space. The Fourier transform of  $Q_{f_if_j}$ , which we identify as the spectral density function  $R_{\hat{f}_i\hat{f}_j}$ , is defined as

$$R_{\hat{f}_i\hat{f}_j}(y, y', k_x, k_z) = \frac{1}{4\pi} \int_{-L_x/2}^{L_x/2} \int_{-L_z/2}^{L_z/2} Q_{f_i f_j}(y, y', r_x, r_z) e^{-ik_x r_x - ik_z r_z} dr_x dr_z.$$
(13)

Note that, due to the statistical homogeneity of the system in x and z, the spectral density function  $R_{\hat{f}_i\hat{f}_j}$  is a decoupled at each wavenumber pair  $\{k_x,k_z\}$ , and thus may be determined from the DNS according to

$$R_{\hat{f}_i\hat{f}_j}(y, y', k_x, k_z) = \lim_{T \to \infty} \frac{1}{T} \int_0^T \hat{n}_i(y, k_x, k_z) \hat{n}_j^*(y', k_x, k_z) dt.$$
 (14)

Certain symmetries may be applied to accelerate the convergence of the statistics determined from the DNS and to reduce the amount of covariance data that needs to be stored, which is in fact quite large. Since  $Q_{f_if_j}$  is a real-valued function,  $R_{\hat{f}_i\hat{f}_j}$  is Hermitian, so

$$R_{\hat{f}_i\hat{f}_j}(y, y', k_x, k_z) = R^*_{\hat{f}_i\hat{f}_j}(y, y', -k_x, -k_z).$$
(15)

By (14), it follows immediately that

$$R_{\hat{f}_i\hat{f}_j}(y, y', k_x, k_z) = R_{\hat{f}_j\hat{f}_i}^*(y', y, k_x, k_z).$$
 (16)

Due to the up/down and left/right statistical symmetry in the flow, it also follows that

$$R_{\hat{f}_i,\hat{f}_j}(y,y',k_x,k_z) = \pm R_{\hat{f}_i,\hat{f}_j}^*(-y,-y',k_x,k_z), \tag{17a}$$

$$R_{\hat{f}_i\hat{f}_j}(y, y', k_x, k_z) = \pm R_{\hat{f}_i\hat{f}_j}^*(y, y', k_x, -k_z), \tag{17b}$$

$$R_{\hat{f}_1\hat{f}_3}(y, y', k_x, k_z) = R_{\hat{f}_2\hat{f}_3}(y, y', k_x, k_z) = 0, \tag{17c}$$

where, in (17a), the minus sign is used for the cases  $\{i=2, j\neq 2\}$  and  $\{i\neq 2, j=2\}$ , and the positive sign is used for all other cases and, in (17b), the minus sign is used for the cases  $\{i=3, j\neq 3\}$  and  $\{i\neq 3, j=3\}$ , and the positive sign is used for all other cases. The reader is referred to, e.g., Moin

& Moser (1989) for similar computations. Finally, for later use, the individual components of the spectral density function  $R_{\hat{f}\hat{f}}$  at each wavenumber pair  $\{k_x, k_z\}$  are denoted by

$$R_{\hat{f}\hat{f}}(y,y',k_x,k_z) = \begin{pmatrix} R_{\hat{f}_1\hat{f}_1} & R_{\hat{f}_1\hat{f}_2} & R_{\hat{f}_1\hat{f}_3} \\ R_{\hat{f}_2\hat{f}_1} & R_{\hat{f}_2\hat{f}_2} & R_{\hat{f}_2\hat{f}_3} \\ R_{\hat{f}_3\hat{f}_1} & R_{\hat{f}_3\hat{f}_2} & R_{\hat{f}_3\hat{f}_3} \end{pmatrix}.$$

#### 3. Statistics of the nonlinear term n

We now perform a direct numerical simulation of the nonlinear Navier–Stokes equation in a turbulent channel flow at  $Re_{\tau} = 100$ , gathering the statistics of the nonlinear term n identified in (3), which combines all those terms which will be supplanted by the stochastic forcing f in the linearized model (7) upon which the Kalman filter will be based.

Note that all DNS calculations performed in this work used the code of Bewley, Moin & Temam (2001). For the spatial discretization, this code uses dealiased pseudospectral techniques in the streamwise and spanwise directions and an energy-conserving second-order finite difference technique in the wall-normal direction. For the time march, the code uses a fractional step implementation of a hybrid second-order Crank–Nicolson / third-order Runge–Kutta–Wray method, as described in Aksevoll & Moin (1995). In all simulations, the overall pressure gradient is adjusted at each time step in order to maintain a constant mass flux in the flow, and a computational domain of size  $4\pi \times 2 \times 4\pi/3$  in the  $x \times y \times z$  directions is used. The resolution is  $42 \times 64 \times 42$  Fourier, finite difference, Fourier modes (that is,  $64 \times 64 \times 64$  dealiased collocation points). The numerical scheme used to discretize the Orr–Sommerfeld/Squire equations in this work is the spectral Differentiation Matrix Suite of Weideman & Reddy (2000); for details on how that scheme has been applied to our estimation problem, see Högberg et al. (2003a).

The covariance of the forcing term  $n=(n_1,n_2,n_3)^T$  identified in (3) was sampled during a DNS calculation long enough to obtain statistical convergence. During the simulation, the full covariance matrices were computed at each wavenumber pair, creating a very large four-dimensional data set. The size of the covariance data is  $N_x \times N_z \times N_y^2$  for each correlation component of the forcing vector (before exploiting any symmetries), where  $N_x$ ,  $N_y$ , and  $N_z$  denote the resolution in the corresponding directions. As resolution requirements of turbulence simulations increase quickly with increasing Reynolds number, at higher Reynolds numbers it soon becomes necessary to represent only the most significant components of these correlations via some sort of reduced-order modeling technique, such as Proper Orthogonal Decomposition via the "snapshot" method. The symmetries mentioned in §2.3 were then applied in post processing to improve the statistical convergence. These statistics are subsequently used in §4, where the optimal estimation feedback gains are computed. In §5, the feedback gains so determined are used in order to estimate a fully

turbulent flow based on wall measurements alone. Both Kalman filters and extended Kalman filters are investigated.

In Figure 1 the magnitude of the spectral density function at four representative wavenumber pairs  $\{k_x, k_z\}$  are plotted. As seen in the figure (plotted along the main diagonal), the variance of the forcing terms is stronger in the high shear regions near the walls, as expected. Note also that there is a pronounced cross-correlation between  $f_1$  and  $f_2$ , accounting for the Reynolds stresses in the flow, with the other cross-correlations converging towards zero as the statistical basis is increased. Figure 3a shows the corresponding variation of the maximum magnitude of the spectral density function as a function of the wavenumbers  $k_x$  and  $k_z$ . As expected, the stochastic forcing is stronger for lower wavenumber pairs.

Figure 2, a corresponding plot of the magnitude of the spectral density function of the stochastic forcing model defined in Part 1 is given. Note that the shape of this covariance model is invariant with  $\{k_x, k_z\}$ , it is only the overall magnitude of this covariance model that varies with  $\{k_x, k_z\}$ , in contrast with the covariance data determined from the DNS data, as reported in Figure 1. Figure 3b shows the corresponding variation of the maximum magnitude of the spectral density function as a function of the wavenumbers  $k_x$  and  $k_z$ .



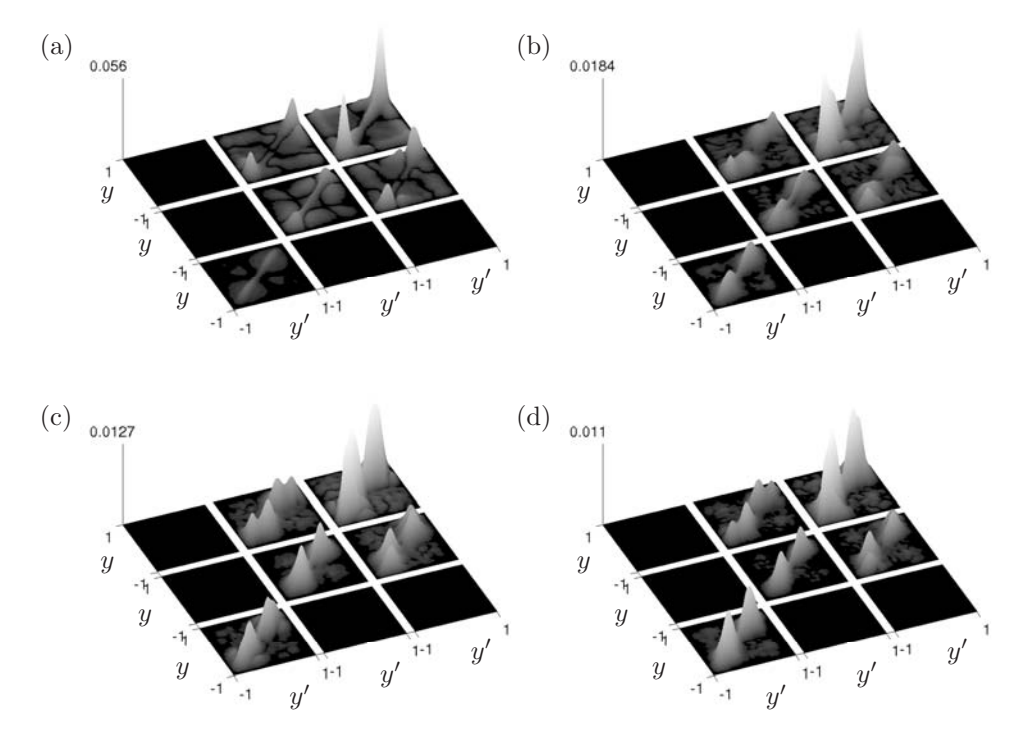


FIGURE 1. The magnitude of the spectral density function  $R_{\hat{f}\hat{f}}(y,y',k_x,k_z)$  of  $\hat{f}$ , computed from the DNS of a turbulent channel flow at  $Re_{\tau}=100$ , at wavenumber pairs  $\{k_x,k_z\}$  of (a)  $\{1.0,3.0\}$ , (b)  $\{3.0,1.5\}$ , (c)  $\{0.0,1.5\}$ , and (d)  $\{4.0,4.5\}$ . The nine "squares" correspond to the correlation between the various components of the forcing vector; from furthest to the viewer to closest to the viewer, the squares correspond to the  $\hat{f}_1$ ,  $\hat{f}_2$ , and  $\hat{f}_3$  components on each axis. The width of each side of each square represents the width of the channel, [-1,1]. The variance is plotted along the diagonal of each square.

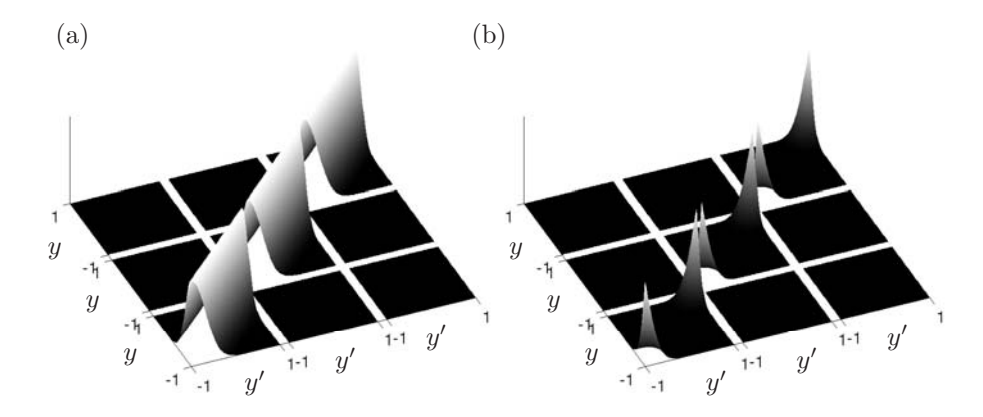


FIGURE 2. The magnitude of the spectral density function  $R_{\hat{f}\hat{f}}(y,y',k_x,k_z)$  of  $\hat{f}$ , as parameterized in the laminar model proposed in Part 1 of this study, taking p=0 (left) and p=3 (right); see Figure 1 for further explanation of the plot.

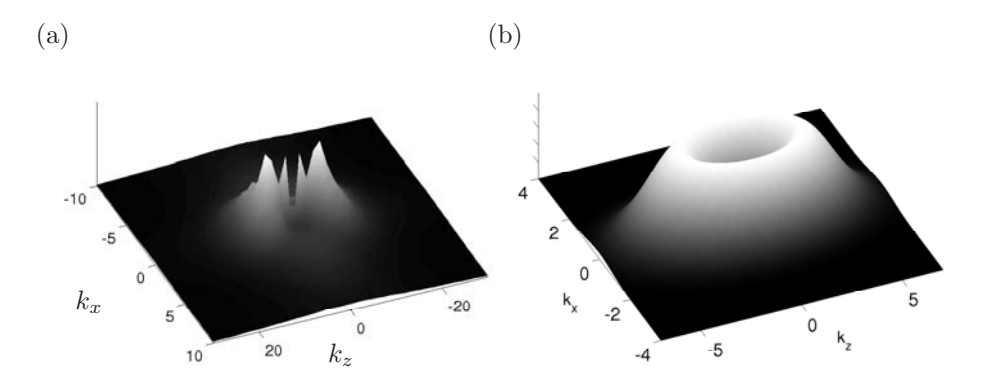


FIGURE 3. The variation of the maximum amplitude of the spectral density function as a function of the wavenumbers  $k_x$  and  $k_z$  for the DNS data (left) and the statistical model of Part 1 (right).

## 4. Estimator gains and the corresponding physical-space kernels

In previous studies the covariance Q has been modeled with a spatially uncorrelated stochastic forcing, as for example in Högberg  $et\ al.\ (2003a)$ . With that model it proved to be impossible to compute well resolved estimation gains for more than one measurement (of  $\eta_y$ ). In contrast, the present study models the stochastic forcing Q based on R, as defined in (13) and determined from a DNS database. Basing the stochastic model on the turbulent statistics makes it possible to render well resolved gains for all three measurements,  $\eta_y$ ,  $v_{yy}$ , and p. In Part 1 it is shown that well resolved estimation gains for the three measurements  $\tau_x$ ,  $\tau_z$ , and p, can be achieved by designing the covariance model to be more physically realistic. The definition and solution procedure for the state estimation problem in order to solve for the Kalman filter gains in the estimator in the present work is identical to that described in Part 1 of this study, to which the reader is referred for details.

Figure 4 illustrates isosurfaces of the physical-space convolution kernels based on the statistics of the neglected terms in the linearized model, as determined from DNS. (Note, however, that these gains are transformed to gains based on  $\eta_y$ ,  $v_{yy}$ , and p in the estimator simulations presented in §5). Note that these kernels depicted in Figure 4 are substantially different in shape from those used in the laminar case, as reported in Figure 12 of Part 1; in particular, note that they are generally more focused in the region adjacent to the lower wall, likely as consequence of the fuller mean velocity profile about which the system is linearized in the turbulent case.

The sensor noise, described in §2.2, is a natural "knob" to tune the strength of the individual measurements as well as their relative strength. Note that the sensor noise level will also affect the shape of the estimation gains. In an attempt to make a reasonably fair comparison between the different stochastic models we consider the following measure

$$J = \int_{-1}^{1} \int_{0}^{L_x} \int_{0}^{L_z} L_{\eta_y}^2 \,\mathrm{d}x\,\mathrm{d}y\,\mathrm{d}z,$$

i.e., the integral in all three spatial directions of the gain corresponding to the  $\eta_y$  measurement,  $L_{\eta_y}$ . Three cases were studied, as shown in Table 1. In all three cases, the relevant  $\alpha$  parameters were tuned so that the integrated strength J is approximately equal. Each measurement captures different features of the flow field and by this study we want to characterize what additional information we get when the two new measurements are added and the covariance of the system accurately modeled, rather than investigating how the strength is distributed over estimator gains and how that affects the estimation process. Note that the resulting strength of the gains require no adjustment of the time step in the extended Kalman filter DNS to run properly.

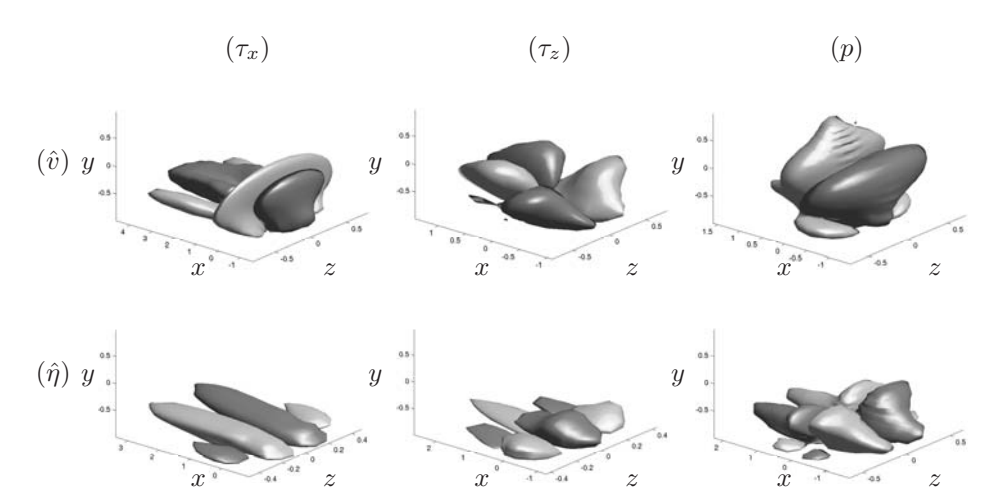


FIGURE 4. Isosurfaces of the physical space convolution kernels determined for  $Re_{\tau} = 100$  turbulent channel flow based on the statistics of the neglected terms in the linearized model, as determined by DNS and plotted in Figures 1 and 3a. Shown are the steady-state convolution kernels relating the (left)  $\tau_x$ , (center)  $\tau_z$ , and (right) p measurements at the point  $\{x=0, y=-1, z=0\}$  on the wall to the estimator forcing on the interior of the domain for the evolution equation for the estimate of (top) v and (bottom)  $\eta$ . Visualized are positive (dark) and negative (light) isosurfaces with isovalues of  $\pm 5\%$  of the maximum amplitude for each kernel illustrated. Note that these kernels are substantially different in shape with those used in the laminar case, as reported in Figure 12 of Part 1; in particular, note that they are generally more focused in the region adjacent to the lower wall, likely as consequence of the fuller mean velocity profile about which the system is linearized in the turbulent case.

Case	$\alpha_{\eta}$	$\alpha_v$	$\alpha_p$	Q	$J^{1/2}$
1	0.1200	_	_	I	52
2	0.0037	_	_	$R_{\hat{f}_1\hat{f}_1}$	52
3	0.0030	0.0030	0.0075		53

TABLE 1. The estimation simulations. For the cases when using one measurement, only the corresponding  $\alpha$  is relevant since the other measurements are excluded from the C-matrix.

#### 5. Estimator performance

#### 5.1. Estimator algorithm

In order to quantify the performance of the Kalman filter developed in this work, we run two direct numerical simulations in parallel. One simulation represents the "real" flow, where the initial condition is a fully developed turbulent flow field. The other simulation is the estimated flow field. The real flow is modeled by the the Navier-Stokes equations. In the estimator simulations we have tested both the Kalman filters (with the state model being the linearized Navier-Stokes equation) and extended Kalman filter (with the state model being the full nonlinear Navier-Stokes equation). The initial condition for the estimator simulations is a turbulent mean flow profile with all fluctuating velocity components set to zero. In both estimator simulations the volume forcing v, defined in §1.2, is added. The additional forcing is based on wall measurements and the precomputed estimation gains. For the Kalman filter simulations we enforce the turbulent mean flow profile that we linearized about and allow no nonlinear interactions to take place in the estimator, by scaling down the fluctuations to a sufficiently small amplitude to suppress nonlinear interactions (This method was necessary with the present version of our DNS code to enforce a linear simulation).

To evaluate the performance of the Kalman and extended Kalman filters the correlation between the actual and estimated flow is computed throughout the wall-normal extent of the domain at each instant of time,

$$\operatorname{corr}_{y}(s, \hat{s}) = \frac{\int_{0}^{L_{x}} \int_{0}^{L_{z}} s \hat{s} \, dx \, dz}{\left(\int_{0}^{L_{x}} \int_{0}^{L_{z}} s^{2} \, dx \, dz\right)^{1/2} \left(\int_{0}^{L_{x}} \int_{0}^{L_{z}} \hat{s}^{2} \, dx \, dz\right)^{1/2}},$$
(18)

where s and  $\hat{s}$  represent either u, v, w, or p from the actual and estimated flow, respectively. A correlation of one means perfect correlation whereas zero correlation zero means no correlation at all.

Another useful quantity to study is the error between the actual and estimated flow state, defined as

$$\operatorname{errn}_{y}(s,\hat{s}) = \frac{\left(\int_{0}^{L_{x}} \int_{0}^{L_{z}} (\hat{s} - s)^{2} \, \mathrm{d}x \, \mathrm{d}z\right)^{1/2}}{\left(\int_{0}^{L_{x}} \int_{0}^{L_{z}} s^{2} \, \mathrm{d}x \, \mathrm{d}z\right)^{1/2}}.$$
(19)

The error (19) ranges from zero, which means no error between the real and estimated flow fields, and infinity. However the most pertinent quantity to measure is the total energy of the error between the real and estimated flow fields defined as

$$\operatorname{errn}_{y}^{\text{tot}}(q,\hat{q}) = \frac{\left(\int_{0}^{L_{x}} \int_{0}^{L_{z}} (\hat{q} - q)^{*} \mathcal{Q}(\hat{q} - q) \, \mathrm{d}x \mathrm{d}z\right)^{1/2}}{\left(\int_{0}^{L_{x}} \int_{0}^{L_{z}} q^{*} \mathcal{Q}q \, \mathrm{d}x \mathrm{d}z\right)^{1/2}}.$$
 (20)

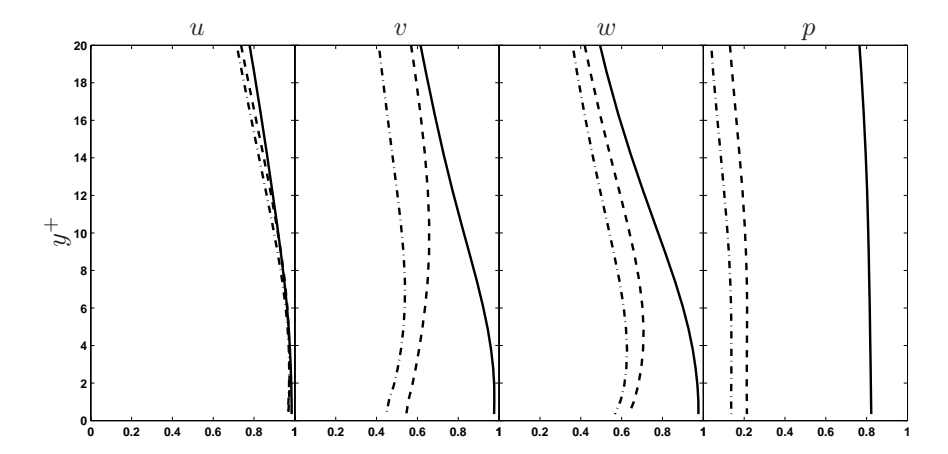


FIGURE 5. The figure shows  $\operatorname{corr}_y(s,\hat{s})$  for  $s=u,\ s=v,\ s=w,$  and p obtained using Kalman filter. The solid line denotes estimation using all three measurements and noise statistics as discussed in §3. The dashed line denotes the estimator performance using only the  $\eta_y$  measurement. The dash-dotted line is obtained using the spatially uncorrelated stochastic model for noise statistics.

since this is the quantity that we, in an average sense, are minimizing for in the construction of the optimal estimation gains. Operator Q represent the energy inner-product in  $(v, \eta)$  coordinates (see e.g. Schmid & Henningson 2001).

#### 5.2. One measurement — two stochastic models

To compare the gains based on a spatially uncorrelated stochastic model with the estimation gains based on the stochastic model suggested in this study, we first compare the performance of the estimator using only the  $\eta_y$  measurement. This is because we only obtained a well-resolved estimation gain for the  $\eta_y$  measurement when using the spatially uncorrelated stochastic model.

The correlation between the real and estimated flow, for one measurement, is depicted in Figure 5 and Figure 6 for the Kalman and extended Kalman filters respectively. The dashed lines represent the stochastic model developed in this work whereas the dash-dotted lines represent the spatially uncorrelated stochastic model. The correlation for the u-component is almost the same close to the wall for the two filters but there is an increasing difference both for the Kalman and extended Kalman filter as the wall distance increases. For v, w, and p the difference is larger. In Figure 7 and Figure 8 we can see similar trends for all the primitive variables and for both the Kalman and extended Kalman filter. We anticipated a more pronounced difference between the two stochastic models but apparently the importance of the stochastic model is not crucial for the performance of the  $\eta_y$  measurement, alone.

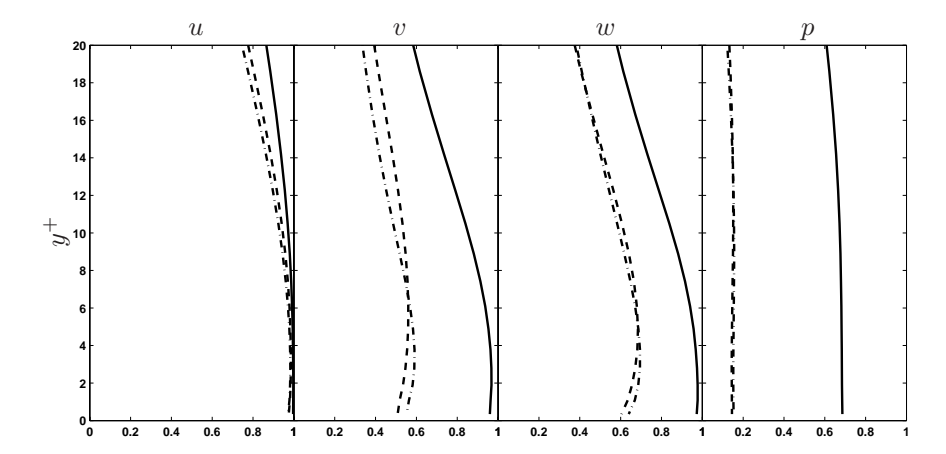


FIGURE 6. The figure shows  $\operatorname{corr}_y(s,\hat{s})$  for  $s=u,\ s=v,\ s=w,$  and p obtained using extended Kalman filter. For a definition of the curves see, Figure 5.

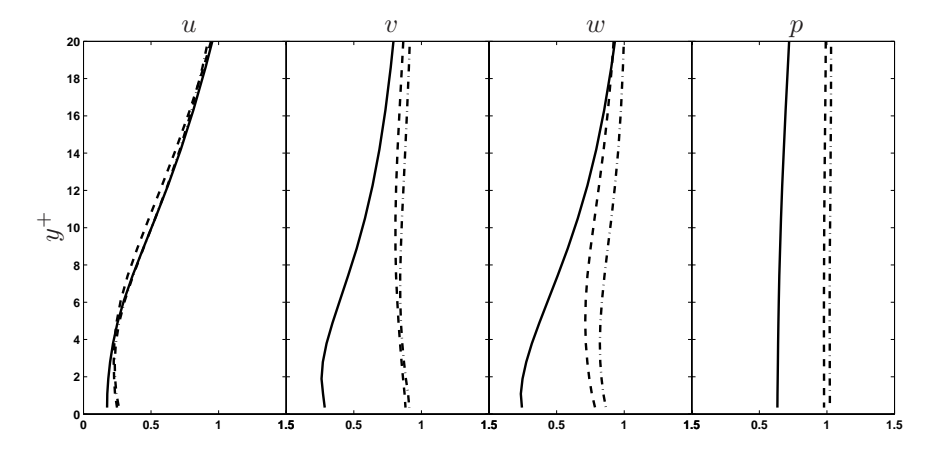


FIGURE 7. The relative estimation error  $\text{errn}_y(s,\hat{s})$ , defined as in equation (19) plotted for the Kalman filter. The solid line denotes estimation performed with all three measurements and gains based on turbulence statistics. The dashed line denotes the estimator performance using only the  $\eta_y$  measurement. The dash-dotted line is the correlation when using the spatially uncorrelated stochastic model.

The correlation for the u-velocity component is close to one (perfect correlation) while the other components show only weak correlation. This is due to the fact that the streamwise disturbance velocity contains more energy than the other components and that with only the  $\eta_y$  measurement we are missing important information about the flow behavior.

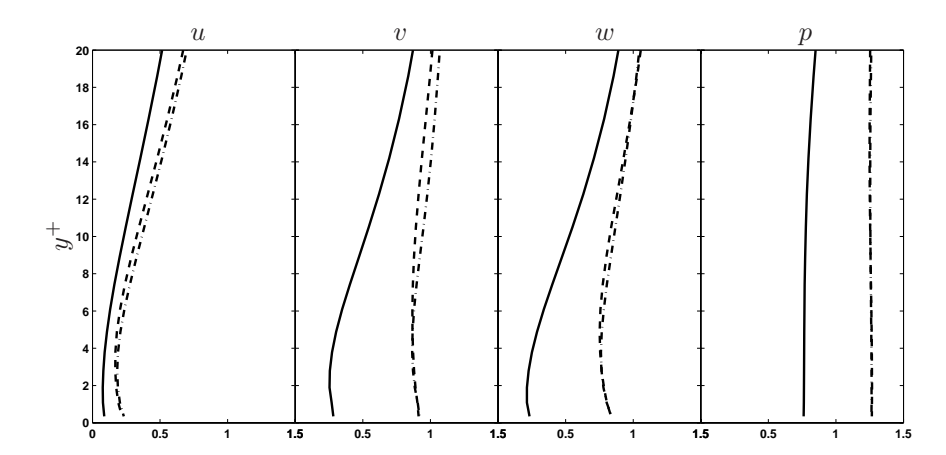


FIGURE 8. The relative estimation error, defined as in equation (19), plotted for the extended Kalman filter. For a definition of the curves see, Figure 7.

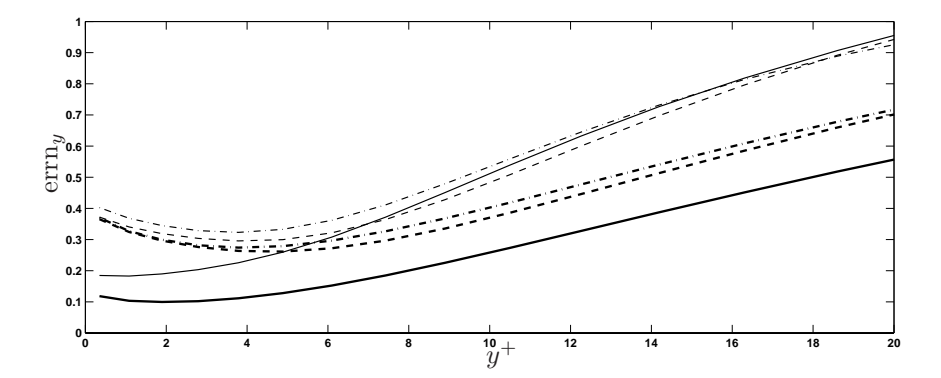


FIGURE 9. The total energy of the estimation error is shown as a function of the wall-normal distance. The solid line denotes the error when all three measurements are applied in the estimator. The dashed and dash-dotted lines represent the estimator performance when using only the  $\eta_y$  measurement with the stochastic model based on turbulence statistics and the spatially uncorrelated stochastic model respectively. The thick lines show the extended Kalman filter and the thin lines the Kalman filter data.

For both the estimators with the present  $\eta_y$  gains and the estimator with gains based on the previous stochastic model, the correlation and error for the u-component, decay quickly once we get beyond  $y^+ \approx 8$  and in the center region of the channel both the error and correlation measures are performing poorly. v, w, and p are clearly not estimated very well with only the  $\eta_y$  measurement.

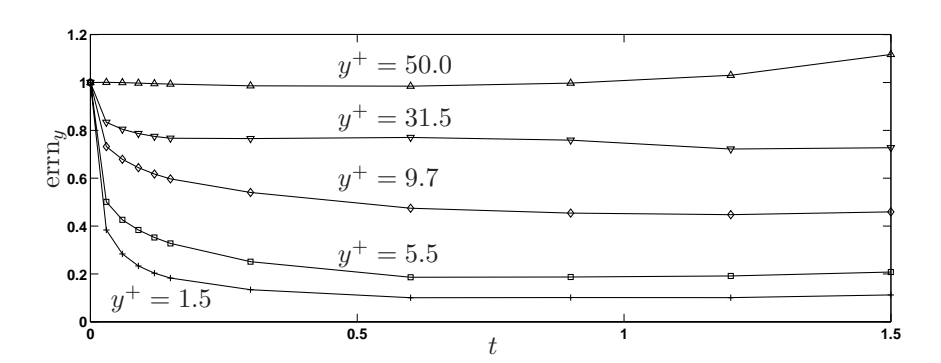


FIGURE 10. The transient behavior of the total error energy at  $y^+ = 1.5$ ,  $y^+ = 5.5$ ,  $y^+ = 9.7$ ,  $y^+ = 31.5$ , and along the channel centerline for case 3 in table 1. All three measurements are used together with the Kalman filter.

p is constantly on a low level whereas v and w experiences a similar decay as u once the wall distance increases.

#### 5.3. Three measurements — one stochastic model

The performance of all three measurements combined, with the relative weighting presented in table 1, are shown as solid lines in Figure 5-8. In these figures it is clearly seen that the correlation and error between the real and estimated flow for all quantities v, w, and p is greatly improved when the additional measurements are included. The strongest improvement appears for the pressure, due to the addition of a pressure measurement.

In Figure 9 the total estimation error, averaged in time, is plotted as a function of wall-normal distance. The thin lines show the Kalman filter results and the thick lines the corresponding extended Kalman filter results. The improved estimation possibilities with the stochastic model presented in this study over a spatially uncorrelated one is clearly seen in Figure 9. The improvement is more pronounced closer to the wall.

For both the estimator with the present  $\eta_y$  gains and the estimator with gains based on the previous stochastic model, the correlation and error for the u, v, and w quantities drop off quickly once we get beyond  $y^+ \approx 10$  and in the center region of channel both the error and correlation measures are performing poorly.

The total energy of the estimation error displays a transient phase when the two simulations are started. This transient is depicted in Figure 10 for the Kalman filter simulation. Closer to the wall the transient is stronger and the error reaches a lower level than further into the flow domain. The transient is due to the fact that the estimated flow is initiated with only a turbulent mean flow profile.

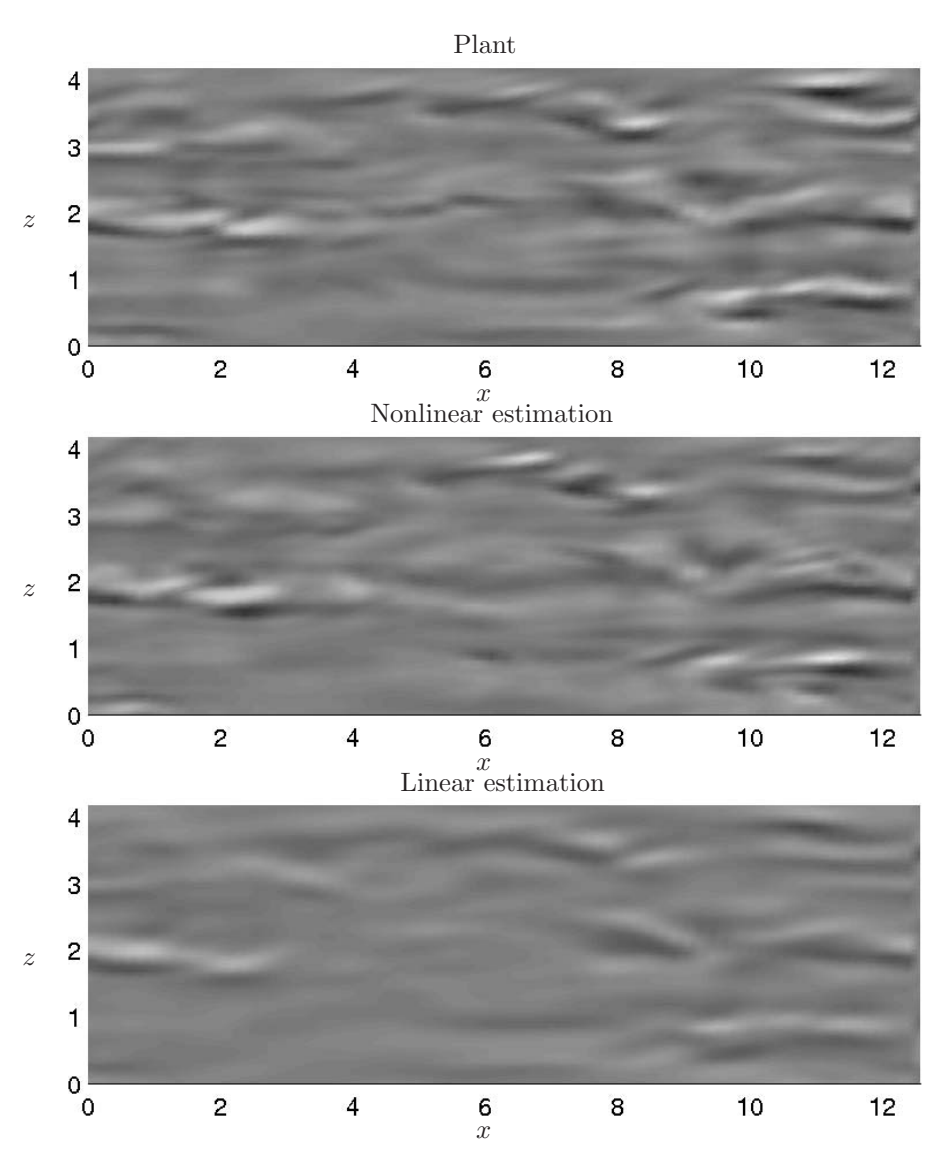


FIGURE 11. Wall-normal velocity component v plotted at  $y^+=9.7$  at an instant in time. In the top figure the flow velocity itself is plotted. The middle plot shows the velocity field reproduced by the extended Kalman filter, and the bottom plot shows the velocity field reproduced by the Kalman filter. The contour levels range from -1 to 1, where black and white represent the lower and upper bound respectively.

The performance of our estimator can be compared with the result reported in Bewley & Protas (2004), where a turbulent channel flow at  $Re_{\tau} = 180$  is estimated from limited measurements as discussed in §1.1. The adjoint method is computationally demanding but gives the optimal estimate of the flow at a certain time with respect to the chosen objective function. Since the present results are computed for a lower Reynolds number we can compare only qualitatively the performances. The adjoint simulation results show the same overall trends both correlation as well as in terms of estimation error.

In Figure 11, an instantaneous plot of the v velocity component is shown at  $y^+ = 9.7$  for the flow field and the two different filters (based on three measurements). Similar structures are present in all three cases. At some instants of time the Kalman filter even has a better match compared to the extended Kalman filter with the real flow but Figure 11 gives an idea of the general trend. The Kalman filter performance also deteriorates more quickly as the wall normal distance is increased and the structures are slightly weaker than in the extended Kalman filter.

#### 6. Summary and conclusions

A key step in the framing the Kalman filter problem is the accurate statistical description of the system dynamics not fully described by the estimator model. The present paper has shown that, by determining the appropriate second-order statistical information in a full nonlinear DNS of the channel flow system, then incorporating this statistical information in the computation of the estimator feedback gains, an effective estimator may be built based on all three measurements available at the wall. For a given feedback amplitude, this estimator provides a better correlation between the real turbulent flow and the estimate thereof than the corresponding estimators considered for this problem in previous work. Significant improvements are obtained, as compared with estimators based on spatially uncorrelated stochastic models, in terms of both the maximum correlation as well as how far into the channel an accurate correlation extends. Also, the estimation gains may be transformed to physical space to obtain well-resolved convolution kernels that eventually decay exponentially with distance from the origin, thereby, ultimately, facilitating decentralized implementation.

In Part 1 of this study, Hoepffner et al. (2004), the estimation of a perturbed laminar flow was investigated, and it was shown that an artificial, but physically reasonable, Gaussian distribution model for the spectral density function was adequate to obtained effective, well-behaved estimation feedback kernels for the problem of estimating the perturbed laminar flow. That result, together with the result from the present study for the problem of estimating turbulence, indicate that the choice of the disturbance model is quite significant in the estimation problem, but a highly accurate statistical model is actually not essential.

As expected, the (nonlinear) extended Kalman filter was found to outperform a (linear) Kalman filter on this nonlinear estimation problem. The estimated state in the Kalman filter deteriorates more rapidly with the distance from the wall. The extended Kalman filter captures better the structures further into the domain, both in magnitude and phase. In terms of both correlation and estimation error, we also observed an approximate correspondence with the performance of the present extended Kalman filter with the adjoint-based estimation procedure reported in Bewley & Protas (2004). The adjoint-based approach is vastly more expensive computationally, and, at least in theory, can account for the nonlinear dynamics of the system more accurately, so this correspondence reflects favorably on the performance of the present extended Kalman filter.

The admittedly artificial assumption of the external disturbance forcing  $\tilde{f}$  being "white" in time may be relaxed in future work, "coloring" the noise with the time dynamics of f, by performing a spectral factorization of f in both space and time and augmenting the estimator model to account for the dominant time dynamics in  $\tilde{f}$ . This approach, while in theory tractable for this problem, involves estimators of substantially higher dimension than the present (which is already large), and might facilitate substantial performance improvements. Development of this approach is thus deferred for the time being as a promising area for future work on this problem.

#### Acknowledgement

The authors sincerely acknowledge the funding provided by the Swedish research council (VR), the Swedish defence research agency (FOI), and the Dynamics and Control directorate of the Air Force Office of Scientific Research (AFOSR) in support of this work.

#### References

AKSEVOLL, K. & MOIN, P. 1995 Large eddy simulations of turbulent confined coannular jets and turbulent flow over a backward facing step. Technical Report Report TF-63. Thermosciences Division, Dept. of Mech. Eng., Stanford University.

Anderson, B. & Moore, J. 1979 Optimal filtering. Prentice-Hall.

Balakrishnan, A. V. 1976 Applied functional analysis. Springer.

Bamieh, B. 1997 The structure of the optimal controller of spatially invariant ditributed parameter systems. In *Proc. 36th IEEE Conf. on Decision and Control*.

Bewley, T. R. 2001 Flow control: new challenges for a new Renaissance. *Progress in Aerospace Sciences* 37, 21–58.

Bewley, T. R., Moin, P. & Temam, R. 2001 DNS-based predictive control of turbulence: an optimal benchmark for feedback algorithms. *J. Fluid Mech.* 447, 179–225.

- Bewley, T. R. & Protas, B. 2004 Skin friction and pressure: the "footprints" of turbulence. *Physica D* **196**, 28–44.
- FARRELL, B. F. & IOANNOU, P. J. 1996 Turbulence suppression by active control. *Phys. Fluids*  $\bf 8$ , 1257–1268.
- Hœpffner, J., Chevalier, M., Bewley, T. R. & Henningson, D. S. 2004 State estimation in wall-bounded flow systems, Part 1. Laminar flows. *J. Fluid Mech.* Submitted.
- HÖGBERG, M., BEWLEY, T. R. & HENNINGSON, D. S. 2003a Linear feedback control and estimation of transition in plane channel flow. J. Fluid Mech. 481, 149–175.
- HÖGBERG, M., BEWLEY, T. R. & HENNINGSON, D. S. 2003b Relaminarization of  $Re_{\tau}=100$  turbulence using gain scheduling and linear state-feedback control. Phys. Fluids 15, 3572–3575.
- JIMENEZ, J. 1999 The physics of wall turbulence. Physica A 263, 252–262.
- JOVANOVIĆ, M. R. & BAMIEH, B. 2001 Modelling flow statistics using the linearized Navier–Stokes equations. In *Proceedings of the 40th IEEE Conference on Decision and Control*, pp. 4944–4949. Orlando, FL.
- KIM, J. & LIM, J. 2000 A linear process in wall-bounded turbulent shear flows. Phys. Fluids 12 (8), 1885–1888.
- Lewis, F. L. & Syrmos, V. L. 1995 Optimal control. Wiley-Interscience.
- Moin, P. & Moser, R. D. 1989 Characteristic-eddy decomposition of turbulence in a channel. *J. Fluid Mech.* **200**, 471–509.
- Schmid, P. J. & Henningson, D. S. 2001 Stability and transition in shear flows. Springer.
- Weideman, J. A. & Reddy, S. 2000 A matlab Differentiation Matrix Suite. *ACM Transaction of Mathematical Software* **26** (4), 465–519.

3

# Linear compensator control of a pointsource induced perturbation in a Falkner–Skan–Cooke boundary layer

By Markus Högberg\*†, Mattias Chevalier\*†, and Dan S. Henningson\*†

Published in Physics of Fluids 2003 15, 2449–2452

We focus on the problem of controlling pointsource induced perturbations on an infinite swept wing using linear control theory. Based on wall measurements in a spatial simulation of localized disturbances in Falkner–Skan–Cooke boundary layers, an extended Kalman filter is used to estimate the full three-dimensional wave packet. The estimated field is in turn used to calculate a feedback control which changes the growth of the disturbance into decay. This is the first time that optimal control and estimation concepts are successfully applied to construct a dynamic output feedback compensator which is used to control disturbances in spatially-developing boundary layers.

By applying control to flows with strong inherent instabilities, through sensors and devices acting only on small parts of the flow, one may achieve dramatic effects by only minute amounts of control energy expenditure. Such control devices can be used in a wide variety of applications, for example, maintaining laminar flow on aircraft wings, relaminarizing/decreasing drag in turbulent flows and enhancing mixing in turbulent flows.

The linear optimal control approach introduced in Bewley & Liu (1998) was in a recent study by Högberg & Henningson (2002) applied to a spatial boundary layer to control a few different disturbance types. The control is shown to work well. However, one drawback with this approach is that full state information is needed when computing the optimal control. In the present study an estimation technique and a full-state feedback controller are combined to obtain a wall-information-based compensator. The same compensator approach has been applied to temporal simulations of transitional channel flows in a recent article Högberg et al. (2003). For the channel flow case, alternative but similar approaches to developing a practical compensator have been pursued by e.g. Cortelezzi et al. (1998) and Joshi et al. (1999). One difference is that

<sup>\*</sup>Department of Mechanics, Royal Institute of Technology (KTH), SE-100 44 Stockholm, Sweden

 $<sup>^{\</sup>dagger} \text{The Swedish Defence Research Agency (FOI), SE-172 90 Stockholm, Sweden$ 

in the present work no effort is put into model reduction other than that obtained from discretizing the continuous system. The aim is to first design a compensator, still incorporating non-parallel and non-linear effects, and then find a reduced order model for the compensator based on this system.

In order to investigate a compensator control scheme, direct numerical simulations (DNS) are performed for a Falkner–Skan–Cooke boundary layer flow with an adverse pressure gradient where a pointsource perturbation is introduced upstream in the computational domain. This flow case has an inviscid instability due to the inflection point in the base flow profile and a disturbance can grow exponentially downstream. However, the disturbance energy levels are chosen so that nonlinear interactions are negligible within the limits of the computational box.

For design of the compensator system we use a model of the linearized three dimensional, time dependent, incompressible Navier–Stokes equations in the form of the Orr–Sommerfeld/Squire equations. The details of the problem formulation and numerical issues regarding computations of feedback control kernels can be found in Högberg & Henningson (2002). For the estimator problem we refer to Bewley & Liu (1998) and Högberg et al. (2003). Here only the main results from the derivation will be stated.

Control is introduced through a blowing and suction boundary condition  $(\varphi)$  on the wall. The boundary condition is lifted through linear super-position into the domain and the governing equations can be expressed in the standard form for control theory for each horizontal wavenumber pair as,

$$\dot{\hat{\mathbf{x}}} = \hat{A}\hat{\mathbf{x}} + \hat{B}\hat{\phi}, \quad \hat{\mathbf{x}} = [\hat{v}, \, \hat{\eta}, \, \hat{\varphi}]^T, \quad \hat{\phi} = \frac{\partial \hat{\varphi}}{\partial t},$$

where  $\hat{v}=\hat{v}(y,t)$  and  $\hat{\eta}=\hat{\eta}(y,t)$  are the wall-normal velocity and vorticity components respectively. The operator  $\hat{A}$  represents the Orr–Sommerfeld/Squire operator and  $\hat{B}$  represents the blowing and suction boundary control. If  $\mathcal{Z}$  is a stationary solution to the inhomogeneous Orr–Sommerfeld/Squire equation with  $\hat{\varphi}=1$  the operators can be written,

$$\hat{A} = \begin{bmatrix} \hat{N} & 0 \\ 0 & 0 \end{bmatrix}, \quad \hat{B} = \begin{bmatrix} -\mathcal{Z} \\ 1 \end{bmatrix}, \quad \text{where} \quad \hat{N} = \begin{bmatrix} \mathcal{L}_{\mathcal{OS}} & 0 \\ \mathcal{L}_{\mathcal{C}} & \mathcal{L}_{\mathcal{SQ}} \end{bmatrix},$$

and  $\mathcal{L}_{OS}$ ,  $\mathcal{L}_{SQ}$  and  $\mathcal{L}_{C}$  denote the different parts of the Orr–Sommerfeld/Squire operator. Throughout the text hats (^) will denote the Fourier coefficients of the corresponding quantity.

Our goal is to minimize the objective function:

$$J(\varphi) = \frac{1}{2} \int_{0}^{T} \int_{\Omega} |\mathbf{u}|^{2} d\Omega dt + \frac{\ell^{2}}{2} \int_{0}^{T} \int_{\Gamma} \left| \frac{\partial \varphi}{\partial t} \right|^{2} d\Gamma dt$$
$$= \sum_{\alpha,\beta} \frac{1}{2} \int_{0}^{T} (\hat{\mathbf{x}}^{*} \hat{Q} \hat{\mathbf{x}} + \ell^{2} \hat{\phi}^{*} \hat{\phi}) dt,$$

where **u** is the disturbance velocity vector,  $\hat{Q}$  is a measure of the energy of the perturbation, and l is a parameter penalizing the magnitude of the control  $\hat{\phi}$ . From linear control theory we know that if  $T \to \infty$  in the objective function the optimal controller is given through

$$\hat{\phi} = \hat{K}\hat{\mathbf{x}}, \text{ where } \hat{K} = -\frac{1}{\ell^2}\hat{B}\hat{X}$$

and  $\hat{X}$  is the positive self-adjoint solution to the Riccati equation,

$$\left(\hat{X}\,\hat{A} + \hat{A}^*\,\hat{X} - \hat{X}\,\frac{1}{\ell^2}\,\hat{B}\,\hat{B}^*\,\hat{X} + \hat{Q}\right)\hat{\mathbf{x}} = 0, \quad \forall \hat{\mathbf{x}}.$$

To find the optimal forcing of our estimator we solve a similar problem for the estimated flow  $\hat{\mathbf{x}}_e$ . We now model the state equation and the wall measurements  $\hat{\mathbf{y}}$  of our system as disturbed by a random (zero-mean white Gaussian) process  $\hat{\mathbf{w}}$  such that

$$\dot{\hat{\mathbf{x}}} = \hat{A}\,\hat{\mathbf{x}} + \hat{B}_1\,\hat{\mathbf{w}} + \hat{B}\hat{\phi},$$

$$\hat{\mathbf{y}} = \hat{C}\hat{\mathbf{x}} + \hat{D}\hat{\mathbf{w}},$$

where the operators  $\hat{B}_1$  and  $\hat{D}$  are used to describe the variance of the noise in the model. The noise is modeled to vary inversely proportional to the wavenumber by introducing such a weighting in  $\hat{B}_1$ . The operator  $\hat{C}$  takes wall measurements of the wall-normal derivative of the wall normal vorticity. Furthermore, the model of the estimated flow has the form

$$\dot{\hat{\mathbf{x}}}_{e} = \hat{A}\hat{\mathbf{x}}_{e} + \hat{B}\hat{\phi} - \hat{\psi}, 
\dot{\hat{\mathbf{y}}}_{e} = \hat{C}\hat{\mathbf{x}}_{e}, 
\dot{\hat{\psi}} = \hat{L}\Delta\hat{\mathbf{y}} = \hat{L}(\hat{\mathbf{y}} - \hat{\mathbf{y}}_{e}),$$

where  $\hat{\mathbf{y}}_e$  is the measurement in the estimator. An estimator forcing can be computed for each wavenumber pair as

$$\hat{L} = -\frac{1}{\alpha^2} \hat{Y} \, \hat{C}^*,$$

where  $\hat{Y}$  is the positive self-adjoint solution to the Riccati equation,

$$\left(\hat{N}^*\hat{Y} + \hat{Y}\hat{N} - \hat{Y}\frac{1}{\alpha^2}\hat{C}^*\hat{C}\hat{Y} + \hat{B}_1\hat{B}_1^*\right)\hat{\mathbf{x}}_h = 0, \quad \forall \hat{\mathbf{x}}_h,$$

and  $\hat{\mathbf{x}}_h$  to denote the homogeneous part of the flow field. The parameter  $\alpha$  models the assumed quality of the measurements.

The compensator problem is stated for a parallel flow. In order the extend the use of the model to a spatially evolving flow two locations need to be specified, one for the control and one for the estimator, where the local velocity profiles are taken to be used in the Orr–Sommerfeld/Squire operator. The flow is then assumed to be locally parallel around these locations in order to solve the control or estimation problem. Based on this this assumption the controller

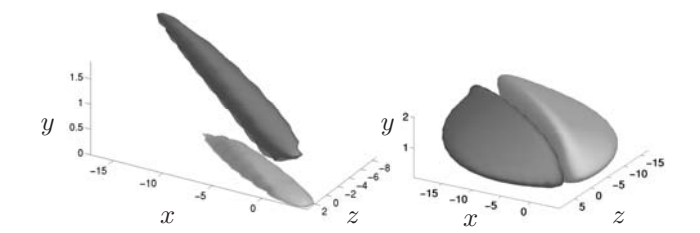


FIGURE 1. Isosurfaces of control kernels of v (left) and  $\eta$  (right) computed with  $\ell=100$  for base flow at position x=150. Contour levels at  $\pm 80 (\approx 25\%$  of the maximum absolute value) and  $\pm 1.3 (\approx 25\%)$  for v and  $\eta$  respectively.

and estimator will have good performance close to the location where they were computed whereas the performance will be degraded further away. This is not expected to cause any problems since the actuation region is limited to a strip on the wall centered at the location where the control was computed, and the estimator only uses measurements from a corresponding measurement region. Since we are using an extended Kalman filter (Gelb (1974)) the spatial evolution and non-linear effects of perturbations generated by the estimator forcing is correctly accounted for in the estimator.

By discretizing the problem we can compute the optimal controller and estimator for a large array of wavenumber pairs we can combine them through an inverse Fourier transform and get an approximation of their physical space representation. Iso-surfaces of control convolution kernels for normal velocity and normal vorticity are shown in Fig. 1. The control signal for each point on the wall is computed through a three dimensional convolution integral of these kernels and the corresponding velocity/vorticity components at each time step. The corresponding estimator forcing is computed through a two dimensional convolution of the forcing kernels, illustrated with the iso-surfaces in Fig. 2, and the measurement error. The estimation kernel for v has a particularly elongated shape and all kernels are aligned with the local direction of the freestream at approximately 27 degrees.

Combining the controller and estimator results in an output feedback dynamic compensator. In this case we apply the estimator forcing given from the linear problem in nonlinear, non-parallel DNS, and this is known as an extended Kalman filter. Figure 3 illustrates the process of the compensator where the upper boundary layer represents the flow we wish to control, the "real" flow, and the lower one represents the estimated flow. The compensator process can be written in the following three steps, also marked in the figure,

- 1. Compute the difference between the measurements from the estimator flow and the "real" flow.
- 2. Compute and apply the estimator forcing to the estimated flow and then compute the control signal based on the state in the estimator.

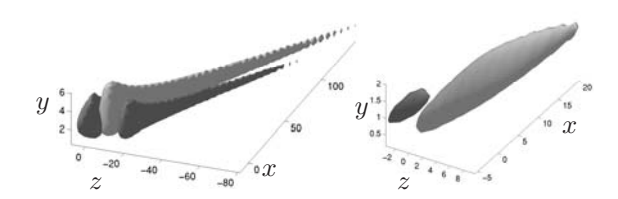


FIGURE 2. Isosurfaces of estimator kernels of v (left) and  $\eta$  (right) computed with  $\alpha=10$  for base flow at position x=50. Contour levels at  $\pm 2187 (\approx 25\%)$  and  $\pm 13134 (\approx 25\%)$  for v and  $\eta$  respectively. Notice that elongated shape of the kernel for v.

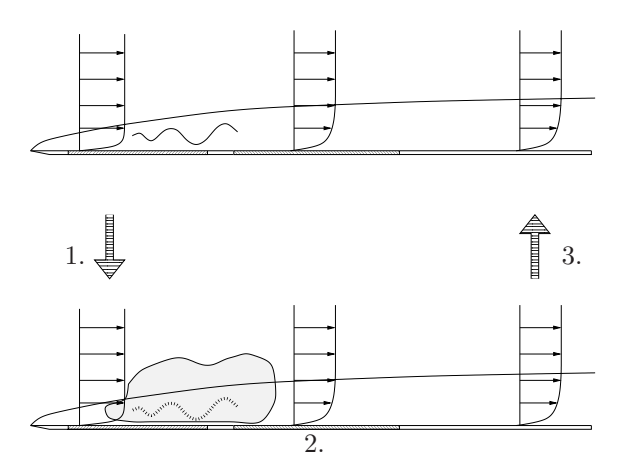


FIGURE 3. The compensator procedure. Measurements (left marked wall region) are made in the "real" disturbed flow (upper) and the estimated flow (lower). A volume forcing (light-gray) is computed and an updated control (right marked wall region) is applied to both flows.

3. Apply the computed control signal to both the "real" flow and the estimator simulations.

In our numerical experiment we march two velocity fields simultaneously forward in time by solving the incompressible Navier–Stokes equations. (Remember that we are using an extended Kalman filter.) One for the actual flow where measurements are taken and one for the estimator in which we try to reconstruct the flow based on the measurements. A well established spectral DNS code has been used in the simulations. The code uses a *fringe region* technique (Nordström *et al.* (1999)) to make the flow field periodic in the streamwise direction so that Fourier modes can be used. Information about the DNS code can be found in e.g. Högberg & Henningson (2002).

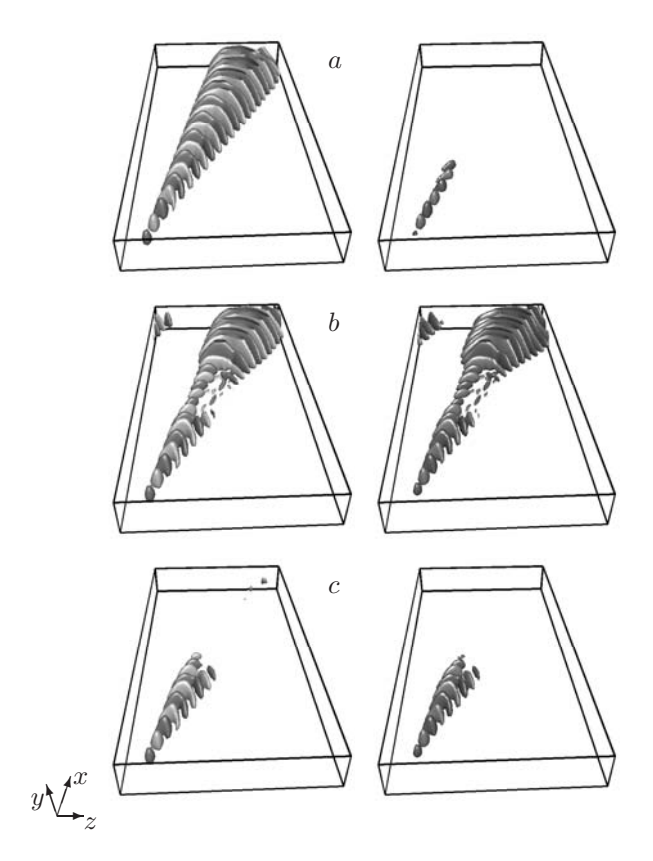


FIGURE 4. Isosurfaces of the normal velocity at  $\pm 8 \times 10^{-4}$  for the real (left) and estimated flow (right) at three different points in time. a) Estimated flow is started, the control is off (t=612). b) The control has been turned on (t=1248). c) The control lowers the disturbance amplitude over the control area (t=1800).

We have chosen to study a flow case with Reynolds number  $Re_{\delta_0^*}=499$  at x=0 based on the displacement thickness  $\delta_0^*$  at the same location. The box size, also scaled with  $\delta_0^*$ , is  $x\in[0,400]$  in the streamwise direction,  $y\in[0,10]$  in the normal direction, and  $z\in[-100,100]$  in the spanwise direction with a resolution of  $384\times65\times64$  Fourier, Chebyshev, Fourier modes. An adverse pressure gradient is applied in the streamwise direction with the parameter m=-0.0312, where m is defined as,

$$U_{\infty} = \left(x/x_0 + 1\right)^m,$$

where  $x_0 = 134$ . The spanwise freestream base flow component is constant  $W_{\infty} = 0.5$ . These parameters have been chosen in order to partly match an experimental setup used in a study by Chernoray *et al.* (2001).

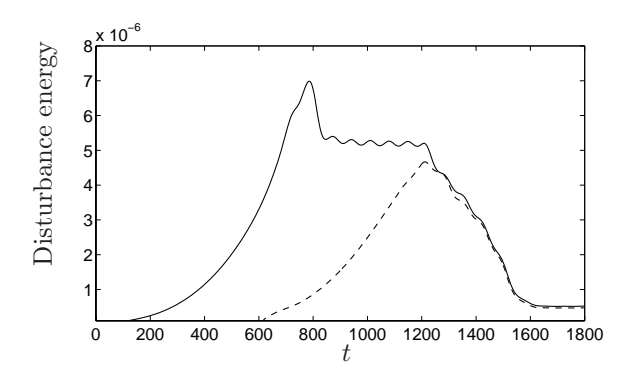


FIGURE 5. Disturbance energy growth as a function of time. The "real" flow (blue/solid) starts from a pure base flow. The disturbance is then introduced and develops downstream. At t=600 the estimated flow is started (red/dashed). At t=1200 the control is turned on and the disturbance energy starts to decrease. For comparison the full information control case is also plotted (dash-dot).

A localized volume force generates a wave like disturbance at x=20 and z=-80. The wall measurements are taken over the interval  $x\in[0,100]$  in both simulations. From these measurements an error can be computed which is used to compute the volume forcing in the estimator simulation. The control is applied over the interval  $x\in[100,200]$  in both simulations.

The disturbance energy growth is depicted in Fig. 5 as a function of time. In the first third of the interval only the "real flow" is simulated without control. At t=600 also the estimator simulation is started and in Fig. 4a a snapshot at t=612 of the flow shows what the disturbance looks like in the two simulations. Figure 4b shows a snapshot at t=1248 where the control, which was turned on at t=1200, is beginning to make the disturbance decay directly over the control area. In Fig. 4c (t=1800) the remains of the downstream disturbance have propagated out of the computational domain and the control dampens the incoming disturbance effectively. In Fig. 5 the dash-dotted line corresponds to the full information control case, when no estimator is used. It is barely distinguishable, but the energy level is slightly lower than for the compensator case. When comparing iso-surfaces at t=1800 the full information case looks identical to the flow in the estimator in Fig. 4c.

Successfully control of a wave-like disturbance in a spatial Falkner–Skan–Cooke boundary layer flow through a combination of a full-state information linear optimal control scheme and an estimator using only wall measurements is for the first time presented in this paper. The performance of the general approach of linear control and estimation demonstrated shows a great potential for practical flow control, particularly for transition delay, in the future. The next step in our approach is to do model reduction of the compensator trying

to capture spatial and non-linear effects in a simulation of computationally tractable size.

#### References

- Bewley, T. R. & Liu, S. 1998 Optimal and robust control and estimation of linear paths to transition. *J. Fluid Mech.* **365**, 305–349.
- Chernoray, V. G., Bakchinov, A. A., Kozlov, V. V. & Löfdahl, L. 2001 Experimental study of the K-regime of breakdown in straight and swept wing boundary layers. *Phys. Fluids* **13** (7), 2129–2132.
- CORTELEZZI, L., LEE, K. H., KIM, J. & SPEYER, J. L. 1998 Skin-friction drag reduction via robust reduced-order linear feedback control. *Int. J. Comp. Fluid Dyn.* 11, 79.
- Gelb, A. 1974 Applied Optimal Estimation. MIT Press.
- HÖGBERG, M., BEWLEY, T. R. & HENNINGSON, D. S. 2003 Linear feedback control and estimation of transition in plane channel flow. J. Fluid Mech. 481, 149–175.
- HÖGBERG, M. & HENNINGSON, D. S. 2002 Linear optimal control applied to instabilities in spatially developing boundary layers. *J. Fluid Mech.* 470, 151–179.
- JOSHI, S. S., SPEYER, J. L. & KIM, J. 1999 Finite dimensional optimal control of Poiseuille flow. J. Guid. Control Dyn. 22, 340.
- NORDSTRÖM, J., NORDIN, N. & HENNINGSON, D. S. 1999 The fringe region technique and the Fourier method used in the direct numerical simulation of spatially evolving viscous flows. SIAM J. Sci. Comp. 20 (4), 1365–1393.

Paper 4

4

### Linear feedback control and estimation applied to instabilities in spatially developing boundary layers

By Mattias Chevalier\*†, Jérôme Hæpffner\*, Espen Åkervik\* and Dan S. Henningson\*†

To be submitted

This paper presents the application of feedback control to spatially developing boundary layers. Development of a proper stochastic model for the external sources of disturbances allows the efficient use of several wall measurement for estimation of the flow evolution in transitional flow cases: the two components of the skin-friction and the pressure fluctuation at the wall. Perturbations to mean flow profiles of the family of Falkner-Skan-Cooke boundary layers are estimated by use of wall measurements. The estimated state is in turn fed back for control in order to reduce the kinetic energy of the perturbations. The control actuation is achieved by means of unsteady blowing and suction at the wall. Flow perturbations are generated at the upstream region in the computational box and propagate in the boundary layer. Measurement are extracted downstream over a thin strip, followed by a second thin strip where the actuation is performed. It is shown that flow disturbances can be efficiently estimated and controlled in spatially evolving boundary layers for a wide range of mean flows and disturbances.

#### 1. Introduction

There is much to be gained in the application of control to fluid mechanical systems, the most widely recognized and targeted aim being the reduction of skin friction drag on airplane wings. Flow control is a growing field and much research effort is spent in both fundamental understanding and direct application of control methods. For a review see e.g. Bewley (2001) and Högberg & Henningson (2002).

Linear control theory gives powerful model-based tools for application of control to fluid systems provided the system at hand can be well described by a linear dynamic model. The theory of Linear-Quadratic-Gaussian control (LQG) is one of the major achievement in the field of control theory. It gives

<sup>\*</sup>Department of Mechanics, Royal Institute of Technology (KTH), SE-100 44 Stockholm, Sweden

 $<sup>^{\</sup>dagger} \text{The Swedish Defence Research Agency (FOI), SE-172 90 Stockholm, Sweden$ 

a methodology to compute the optimal measurement based control when the dynamic model is linear, the objective is quadratic, and the external sources of excitations are stochastic. This theory is applied to boundary layer control in the present work.

Feedback control design can be conceptually and computationally split into two subproblems. The first one is to estimate the flow state from noisy wall measurements. In our case, the state is the flow perturbation about the known mean flow profile. The estimator is a simulation of the dynamic system that is run in parallel to the flow. Its state is forced as a feedback of the measurements in order to converge to the real flow state. The estimated state is in turn used for feedback control of the flow which is the second one. The closed loop system with estimation and control is commonly referred to as measurement feedback control or compensator.

One of the major limitations to the application of control to spatially distributed systems (system in space and time, usually described by partial differential equations) is the realization of the sensing and actuation that would handle relatively fast events as well as small scales of fluid motion. In addition, control over physical surfaces typically requires dense arrays of sensors and actuators. Recent development in MEMS technology and related research may lead to solutions of this problem. For application of MEMS technology to flow control see e.g. Yoshino et al. (2003).

Several recent investigations have pursued the application of LQG-type feedback control to wall-bounded flow systems. A recent overview of this progress is given in Kim (2003). Högberg & Bewley (2001) demonstrated the localization of the feedback kernels. This property allows a local application of the control, i.e. only the local properties of the system (dynamics, disturbance sources and measurement information) are necessary for control locally. The efficiency of the control scheme we use here was illustrated in Högberg et al. (2003a), where relaminarization of a fully developed turbulent flow was achieved. In Hoepffner et al. (2004) and Chevalier et al. (2004), the focus was on the estimation performance. By introducing a relevant model for the external source of disturbance, it was possible to improve the estimation performance on both transitional and turbulent flows. Application of the full information controller, also known as a linear quadratic regulator (LQR), to spatially developing flows was first done in Högberg & Henningson (2002), and extended to a simple flow case with both control and estimation in Högberg et al. (2003b). The present paper builds on those two latter papers, applying the recent improvement of the estimation.

The procedures of control design are based on the manipulations of a linear dynamic model for the flow system, which is typically of large order. In the case of spatially invariant systems, i.e. system for which the dynamics is independent of some spatial coordinates, the problem can be decoupled in a parameterized family of smaller systems. In our case, we assume spatial homogeneity over the two horizontal directions. After Fourier transforming, this

allows to design and tune the controller and estimator for individual wavenumber pairs.

In a spatially developing flow like the boundary layer, this procedure can still be used, even though the spatial invariance in the streamwise direction is lost. Indeed, the localization of the control and estimation kernels ensures that the feedback is local, so that the flow can be assumed to be locally parallel. In Högberg & Henningson (2002), the actuation was successfully applied over a strip parallel to the leading edge in Falkner–Skan–Cooke (FSC) boundary layers, and the control feedback law was computed based upon the local Reynolds number. In Högberg  $et\ al.\ (2003b)$ , a measurement strip was added, and the subsequent state estimate was used for control. The present paper aims at the application of the recent development and improvement on the estimation of the complex flow cases where the full information control was shown to be successful in Högberg & Henningson (2002).

The structure of this paper is as follow. In  $\S 2$ , the flow system is described: dynamics, input and output. In  $\S 3$ , we outline the main issues for the feedback control and estimation. The numerical method is described in  $\S 4$ . The performance of the control in several flow cases is shown in  $\S 5$ , and concluding remarks are given in  $\S 6$ .

#### 2. System description

#### 2.1. Flow dynamics

The Navier–Stokes equations are linearized about solutions of the FSC boundary layer. Favorable and adverse pressure gradients can be accounted for as well as the effect of a sweep. To obtain the family of FSC similarity solutions we assume that the chordwise outer-streamline velocity obeys the power law  $U_{\infty}^* = U_0^* (x^*/x_0^*)^m$  and that the spanwise velocity  $W_{\infty}^*$  is constant. In the expression above,  $U_0^*$  is the freestream velocity at the beginning of the computational box and the asterisks (\*) denote dimensional quantities. Note that the Blasius profile is a special case of FSC with zero cross flow component and pressure gradient. If we choose the similarity variable  $\eta$  as

$$\eta(y^*) = y^* \sqrt{\frac{m+1}{2} \frac{U_{\infty}^*}{2\nu x^*}}$$

one can derive the following self-similar boundary layer profiles,

$$f''' + ff'' + \beta_h (1 - f'^2) = 0,$$
  
$$g'' + fg' = 0,$$

where the Hartree parameter  $\beta_h$  relates to the power law exponent m as  $\beta_h = 2m/(m+1)$ . The accompanying boundary conditions are

$$f = f' = g = 0$$
, for  $\eta = 0$ ,  
 $f' \to 1$ ,  $g \to 1$ , as  $\eta \to \infty$ .

134

The complete derivation can be found in e.g. Schlichting (1979) and Cooke (1950). From the FSC similarity solutions, we construct the nondimensional velocity profiles

$$U(y) = f'(\eta(y)), \tag{1a}$$

$$W(y) = \frac{W_{\infty}}{U_{\infty}} g(\eta(y)), \tag{1b}$$

for a fixed x and where  $y = y^*/\delta_0^*$ . The velocity profiles (1a) and (1b) are then used as base flow when constructing the linear dynamic model for the flow disturbance and the initial conditions for the direct numerical simulations.

Once linearized, the system can be transformed to Fourier space by assuming local spatial invariance. This implies that the non-parallel effects are small, i.e. the mean flow is slowly developing in the streamwise direction. After transformation to the velocity–vorticity  $(v-\eta)$  formulation, we obtain the Orr–Sommerfeld/Squire equations (see e.g. Schmid & Henningson 2001)

$$\begin{pmatrix} \dot{v} \\ \dot{\eta} \end{pmatrix} = \begin{pmatrix} \mathcal{L}_{OS} & 0 \\ \mathcal{L}_{C} & \mathcal{L}_{SQ} \end{pmatrix} \begin{pmatrix} v \\ \eta \end{pmatrix}, \tag{2}$$

where

$$\mathcal{L}_{OS} = \Delta^{-1}[-i(k_xU + k_zW)\Delta + ik_xU'' + ik_zW'' + \Delta^2/Re],$$

$$\mathcal{L}_{SQ} = -i(k_xU + k_zW) + \Delta/Re,$$

$$\mathcal{L}_{C} = i(k_xW' - k_zU'),$$
(3)

with the boundary conditions

$$v(0,t) = \varphi, \quad Dv(0,t) = 0, \quad \eta(0,t) = 0,$$
  
 $v(y,t) = 0, \quad Dv(y,t) = 0, \quad \eta(y,t) = 0, \quad \text{as} \quad y \to \infty.$  (4)

The control actuation affects the system through a non-homogeneous boundary condition on wall-normal velocity  $\varphi$  (wall blowing and suction). The Reynolds number Re is based on freestream velocity and displacement thickness at x = 0 (denoted  $\delta_0^*$ ).

In order to fit the controlled Orr–Sommerfeld/Squire system into the formalism of (12) we perform a lifting procedure ((see e.g. Högberg & Bewley 2001)) where the control at the wall  $v_{\rm wall}$  now enters the flow through a volume forcing term instead of as an inhomogeneous boundary condition at the wall. This is done by decomposing the flow state into homogeneous (subscript h) and particular (subscript p) component

$$\begin{pmatrix} v \\ \eta \end{pmatrix} = \begin{pmatrix} v_h \\ \eta_h \end{pmatrix} + \begin{pmatrix} v_p \\ \eta_p \end{pmatrix} \varphi. \tag{5}$$

The augmented state q, incorporating the actuation variable thus reads

$$q = \begin{pmatrix} v(y,t) \\ \eta(y,t) \\ \varphi(t) \end{pmatrix}, \tag{6}$$

and augmented operator A and operator B can be written

$$A = \begin{pmatrix} \mathcal{L}_{OSS} & 0\\ 0 & 0 \end{pmatrix}, \quad B = \begin{pmatrix} -q_p\\ 1 \end{pmatrix}, \tag{7}$$

with

$$\mathcal{L}_{OSS} = \begin{pmatrix} \mathcal{L}_{OS} & 0\\ \mathcal{L}_{C} & \mathcal{L}_{SQ} \end{pmatrix}, \tag{8}$$

and where the particular solution  $q_p$  is chosen to satisfy the numerically convenient equation  $\mathcal{L}_{OSS}\,q_p=0$  with a unity boundary condition on the wall-normal velocity at the wall. The Laplacian operator is denoted  $\Delta=D^2-k^2$ , where D is the wall-normal derivative and  $k^2=k_x^2+k_z^2$ .

#### 2.2. Stochastic disturbances

#### 2.2.1. Modeling of the external disturbances

The complete description of a dynamical system also includes a description of its input (external sources of excitations) and its output (measurements, possibly corrupted by noise). The performance of the state estimation relies on the construction of a proper model for the flow disturbances. Indeed, if the external sources of perturbations in the flow are well identified, it becomes an easy task to estimate the flow evolution using a dynamic model of the system.

The external sources of perturbations in typical aeronautical applications can be wall roughness, acoustic waves, and freestream turbulence. When using a linear model of the flow, the nonlinear effects can be seen as additional disturbances to the dynamic evolution.

We will assume the external disturbance forcing  $f = (f_1, f_2, f_3)^T$  in (18) to be a zero-mean stationary white Gaussian process with auto-correlation

$$E[f_j(x, y, z, t)f_k(x + r_x, y', z + r_z, t')] = \underbrace{\delta(t - t')}_{\text{Temporal}} \underbrace{Q_{f_j f_k}(y, y', r_x, r_z)}_{\text{Spatial}},$$

where  $\delta(\cdot)$  denotes the Dirac  $\delta$ -function.

The remaining property to be described is the spatial extent of the two-point, one-time, auto-correlation of f over the whole domain

$$Q_{f_i f_k}(y, y', r_x, r_z) = E[f_j(x, y, z, t) f_k(x + r_x, y', z + r_z, t)].$$

The corresponding quantity in Fourier space is a covariance operator, obtained for any wavenumber pair  $\{k_x, k_z\}$  via the following integration over the homogeneous directions

$$R_{f_j f_k}(y, y', k_x, k_z) = \int \int Q_{f_j f_k}(y, y', r_x, r_z) e^{-i(k_x r_x + k_z r_z)} dr_x dr_z.$$

Our model for the covariance of f assumes that the disturbance has a localized structure in space (i.e., the two-point correlation of the disturbance decays exponentially with distance) and that the correlations between forcing terms on

different velocity components are zero. We assume a model for the covariance of the external forcing f of the form

$$R_{f_j f_k}(y, y', k_x, k_z) = d(k_x, k_z) \, \delta_{jk} \mathcal{M}^y(y, y'),$$

where

$$d(k_x, k_z) = \exp\left[-\left(\frac{k_x - k_x^0}{d_x}\right)^2 - \left(\frac{k_z - k_z^0}{d_z}\right)^2\right].$$

The model parameters  $k_x^0$  and  $k_z^0$  can be used to locate the peak energy of the disturbances in Fourier space, and  $d_x$  and  $d_z$  to tune the width of this peak. These parameters are specific for each flow case, e.g. for a typical TS-wave the peak energy will be at  $k_x^0 = 0.3$  and  $k_z^0 = 0$ , or for a typical streamwise streak, the choice will be  $k_x^0 = 0$  and  $k_z^0 = 0.5$ . The parameters for our flow cases are given in table 2. The y variation of  $R_{f_j f_k}$  is given by the function

$$\mathcal{M}^{y}(y, y') = w((y + y')/2) \exp\left[-\frac{(y - y')^{2}}{2d_{y}}\right].$$
 (9)

where the design parameter  $d_y$  governs the width of the two-point correlation of the disturbance in the wall-normal direction. The function  $w(\xi)$  describes the variances at different distances from the wall. In the present paper, the estimator will be applied to disturbances inside the boundary layer, we thus use the wall-normal derivative of the mean flow,

$$w(\xi) = \frac{U'(\xi)}{U'(0)},\tag{10}$$

so that the variance of the disturbance varies as the mean shear: greatest close to the wall and vanishing in the freestream.

Other forms for  $d(k_x, k_z)$  are also possible, and may be experimented with in future work. Note that we will denote  $R = R_{ff} = \text{diag}(R_{f_1f_1}, R_{f_2f_2}, R_{f_3f_3})$  in the sections that follow.

#### 2.2.2. Modeling of the sensor noise

The measurements used in this study are the streamwise and spanwise shear stresses and wall pressure fluctuations.

$$\begin{cases} \tau_x = \tau_{xy}|_{\text{wall}} = \frac{1}{Re} \left. \frac{\partial u}{\partial y} \right|_{\text{wall}} = \frac{1}{Re} \frac{i}{k^2} (k_x D^2 v - k_z D \eta)|_{\text{wall}}, \\ \tau_z = \tau_{zy}|_{\text{wall}} = \frac{1}{Re} \left. \frac{\partial w}{\partial y} \right|_{\text{wall}} = \frac{1}{Re} \frac{i}{k^2} (k_z D^2 v + k_x D \eta)|_{\text{wall}}, \\ p = p|_{\text{wall}} = \frac{1}{Re} \frac{1}{k^2} D^3 v|_{\text{wall}}. \end{cases}$$

which yields the following measurement matrix C

$$C = \frac{1}{Re} \frac{1}{k^2} \begin{pmatrix} ik_x D^2|_{\text{wall}} & -ik_z D|_{\text{wall}} \\ ik_z D^2|_{\text{wall}} & ik_x D|_{\text{wall}} \\ D^3|_{\text{wall}} & 0 \end{pmatrix}.$$

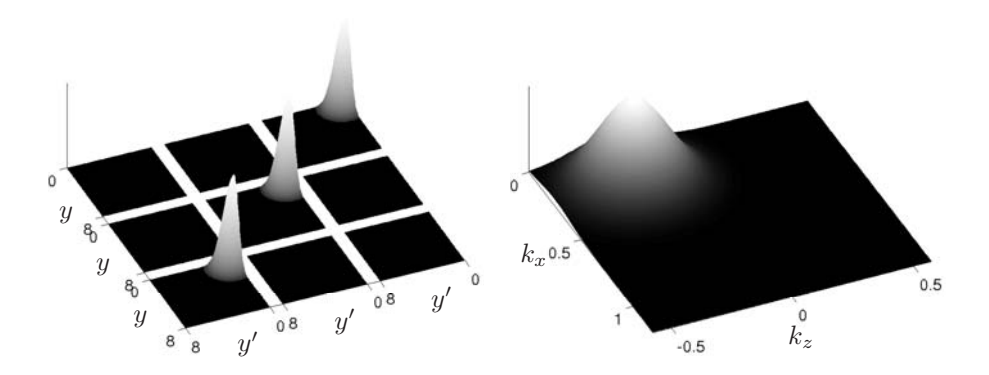


FIGURE 1. The covariance of f, for the FSC problem (cases 12–13 in table 1) is depicted in (a). The covariance is stronger in the interior of the boundary layer. From top to bottom and right to left each square represent to covariance for  $f_1$ ,  $f_2$ , and  $f_3$ . The wavenumber space amplitude function is shown in (b). The peak is moved to  $\{0.25, -0.25\}$  which is the mode that is triggered in the FSC simulations.

Each of the three measurements is assumed to be corrupted by random sensor noise processes, the amplitude of which is determined by the assumed quality of the sensors. The covariance of the sensor noise vector g can thus be described in Fourier space by a  $3\times 3$  matrix G whose diagonal elements  $\alpha_t^2$  are the variances of the sensor noise assumed to be associated with each individual sensor

$$R_{g_{\iota}(t),g_{\kappa}(t')} = \delta_{\iota\kappa}\delta(t - t')\alpha_{\iota}^{2}, \tag{11}$$

where  $\delta_{\iota\kappa}$  denotes the Kronecker delta. Thus, in the present work, we assume that the sensor noise is uncorrelated in both space and time.

When the signal-to-noise ratio is low, the measured signal must be fed back only gently into the estimator, lest the sensor noise disrupt the estimator. When the signal-to-noise ratio is high, the measured signal may be fed back more aggressively into the estimator, as the fidelity of the measurements can be better trusted. For a given covariance of the external disturbances, the tuning of the assumed overall magnitude of the sensor noise in the Kalman filter design thus provides a natural "knob" to regulate the magnitude of the feedback into the estimator.

## 3. Compensation

The system is now described: its dynamics is governed by (2), it is excited by external sources of disturbance as in (9) and the sensor information is corrupted by noise as in (11). We can now apply the procedure of LQG control and estimation.

Our system can be written on the general state-space form

$$\dot{q} = Aq + Bu + B_1 f, \quad q(0) = q_0,$$
  
 $y = Cq + q,$  (12)

where q is the state, A is the linear operator representing the dynamics of the system. The external disturbances, denoted by f, force the state through the input operator  $B_1$ , and  $q_0$  is the initial condition. The operator  $B_1$  transforms a forcing on (u, v, w) to a forcing on  $(v, \eta)$ . The control signal u affects the system through the input operator B. Operator C extracts the measurements from the state variable, and g adds a stochastic measurement noise with given statistical properties. The noisy measurement is then g. Once we have the physical model on this form, we can apply the tools from control theory, see for example Lewis & Syrmos (1995).

#### 3.1. Controller

To construct an optimization problem we need to define an objective function. The performance measure for optimality is chosen as a weighted sum of the flow kinetic energy and the control effort. We thus aim at preventing small disturbances from growing, and achieve this goal with the minimum possible actuation energy. The objective functional thus reads

$$J = \int_{0}^{\infty} (q^* \mathcal{Q}q + l^2 u^* u) dt$$
 (13)

where  $l^2$  is included to penalize the time derivative of the control  $\dot{\varphi}$ , and

$$Q = \begin{pmatrix} Q & Qq_p \\ q_p^* & (1+r^2)q_p^*Qq_p \end{pmatrix}$$
 (14)

where the term  $r^2$  is an extra penalty on the control signal itself. The operator Q represents the energy inner-product in the  $(v, \eta)$  space

$$\begin{pmatrix} v^* & \eta^* \end{pmatrix} Q \begin{pmatrix} v \\ \eta \end{pmatrix} = \frac{1}{8k^2} \int_{-1}^{1} \left( k^2 |v|^2 + \left| \frac{\partial v}{\partial y} \right|^2 + |\eta|^2 \right) dy, \tag{15}$$

with  $k^2 = k_x^2 + k_z^2$ .

We now want to find the optimal K that feeds back the state to update the control u=Kq. It can be found as the solution of a algebraic Riccati equation (ARE)

$$A^*X + XA - \frac{1}{l^2}XBB^*X + Q = 0 (16)$$

where X is the unique non-negative self-adjoint solution. Note that the linear feedback law does not depend on the disturbances present in the flow and is thus computed once and for all for a given objective function and base flow. The optimal control gain K is

$$K = -\frac{1}{12}B^*X. (17)$$

A sufficient range of wavenumber pairs are computed and after Fourier transform in both horizontal directions, we obtain physical space control convolution kernels. Examples of such control kernels are depicted in figure 2.

#### 3.2. Estimator

We build an estimator analogous to the stochastic dynamical system (12) as

$$\dot{\hat{q}} = A\hat{q} + Bu - L(y - \hat{y}), \quad \hat{q}(0) = \hat{q}_0, 
\hat{y} = C\hat{q},$$
(18)

where  $\hat{q}$  is the estimated state and  $\hat{y}$  represents the measurements in the estimated flow.

Kalman filter theory, combined with the models outlined in §2.2.1 and §2.2.2 for the statistics of the unknown external forcing f and the unknown sensor noise g respectively, provides a convenient and mathematically-rigorous tool for computing the feedback operator L in the estimator described above such that  $\hat{q}(t)$  converges to an accurate approximation of q(t) (see e.g. Lewis & Syrmos 1995, p. 463–470). Note that the volume forcing  $v = L(y - \hat{y})$  used to apply corrections to the estimator trajectory is proportional to the measurement error  $\tilde{y} = y - \hat{y}$ .

The problem reduces to solving an algebraic Riccati equation similar to equation (16)

$$0 = AP + PA^* + BRB^* - PC^*G^{-1}CP, (19)$$

where P is the unique non-negative self-adjoint solution. The optimal gain L that minimizes the expected energy of the state estimation error at steady state is

$$L = -PC^*G^{-1}. (20)$$

## 3.3. Extension to spatially developing flows

When solving the linear control problem and computing optimal control and estimation gains we have linearized about a specific mean flow profile. When the gains are applied in the control and measurement strip, the mean flow varies along those regions i.e. errors will be introduced due to the changes of the mean flow. Based on findings in Högberg & Henningson (2002), Högberg et al. (2003a), Högberg et al. (2003b), and Chevalier et al. (2004) it was expected that the controller and the estimator had some robustness properties with respect to changes in the mean flow profile. Due to the fact that the convolution kernels themselves, for proper choices of parameters, are localized indicates that only local information is needed which relaxes the requirement of constant mean flow profile. For all control and estimation gains used in this study the mean flow profile in the center of the control and measurement regions have been used except for the control gains for the longer control interval in the optimal perturbation flow case where the same gains were used as for the shorter interval.

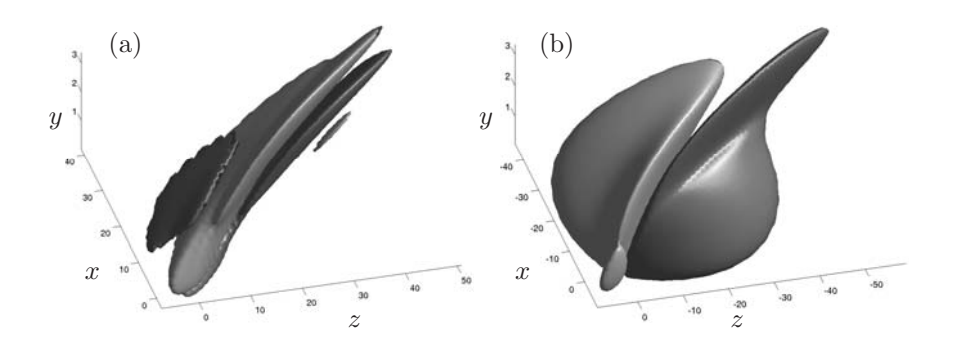


FIGURE 2. Steady-state control convolution kernels relating the flow state  $\hat{v}$  (a) and  $\hat{\eta}$  (b) to the control at  $\{x=0,\ y=0,\ z=0\}$  on the wall. Positive (dark) and negative (light) isosurfaces with isovalues of  $\pm 20\%$  of the maximum amplitude for each kernel are illustrated.

The control and estimation convolution kernels for the Falkner–Skan–Cooke boundary layer flow, described in §2, are depicted in figures 2 and 3.

## 4. Numerical issues

## 4.1. Direct numerical simulations

All direct numerical simulations have been performed with the code reported in Lundbladh *et al.* (1992) and Lundbladh *et al.* (1999), which solves the incompressible Navier–Stokes equations

$$\frac{\partial u}{\partial t} = NS(u) + \lambda(x)(u - u_{\lambda}) + F,$$

$$\nabla \cdot u = 0,$$
(21)

by a pseudo-spectral approach. In order to allow spatially developing flows, a fringe region technique as described in e.g. Nordström et al. (1999) has been applied. This forcing is implemented in the term  $\lambda(x)(u-u_{\lambda})$ , where  $\lambda(x)$  is a non-negative function which is nonzero only in the fringe region located in the downstream end of the computational box. The outflow and inflow conditions are determined by the desired velocity distribution  $u_{\lambda}$ . The other additional forcing term  $F = [F_1, F_2, F_3]^T$  is used e.g. to enforce a parallel mean flow in temporal simulations, or to introduce perturbations in the spatial simulations.

At the lower wall a no-slip boundary condition is applied where it is also possible to apply zero mass-flux blowing and suction. An asymptotic freestream boundary condition is used to limit the computational box in the wall-normal direction, at a constant height from the lower wall (see e.g. Malik *et al.* 1985).

The computational domain is discretized in space by Fourier series in both horizontal directions and with Chebyshev polynomials in the wall-normal direction. The time integration is done using a four-step low-storage third-order

Case	Flow	Perturbation	n Estimation		Control	
			$x_m \in$	$r^2$	l	$x_c \in$
0	A	Eigenmode				_
1	A	Eigenmode	_	0	$10^{2}$	[0, 25.14]
2	A	Eigenmode	[0, 25.14]	0	$10^{2}$	[0, 25.14]
3	В	TS-wave	_	_	_	_
4	В	TS-wave	_	0	$10^{2}$	[175, 325]
5	В	TS-wave	[40, 150]	0	$10^{2}$	[175, 325]
6	$^{\rm C}$	Optimal	_	_	_	_
7	$^{\rm C}$	Optimal	_	0	$10^{2}$	[300, 450]
8	$^{\mathrm{C}}$	Optimal	[0, 300]	0	$10^{2}$	[300, 450]
9	$^{\rm C}$	Optimal	_	0	$10^{2}$	[300, 750]
10	$^{\mathrm{C}}$	Optimal	[0, 300]	0	$10^{2}$	[300, 750]
11	D	Random	_	_	_	_
12	D	Random	_	0	$10^{2}$	[175, 325]
13	D	Random	[40, 150]	0	$10^{2}$	[175, 325]
Letter	r Flo	W	Resolution		В	OX
A	Ten	nporal FSC	$4 \times 129 \times 4$	25.1	$14 \times 2$	$0 \times 25.14$
В		tial Blasius	$576 \times 65 \times 4$	500	$500 \times 20 \times 12.83$	
$^{\mathrm{C}}$	_	tial Blasius	$576 \times 65 \times 4$	112	$1128 \times 20 \times 12.83$	
D	-	tial FSC	$192 \times 49 \times 48$	50	$00 \times 8$	$\times$ 251.4
	Le	tter	Fringe			
		$x_{ m start}$	$x_{\rm mix}$ $\Delta_{\rm mix}$	$\Delta_{\rm rise}$	$\Delta_{\mathrm{fal}}$	1
		$B = \frac{350}{350}$	425 25	75	25	<u> </u>
		C 1028	1028 40	100	20	
		D 350	400 40	100	20	

TABLE 1. The tables contain detailed information about all the simulations performed in this study. Both the control and estimation kernels are computed based on a velocity profile from the centre of each domain except for cases 9–10 where the same control kernels were used as for cases 7–8. The rise and fall distance of the control region and the measurement regions are always  $\Delta x=5$ . The domain  $x_m$  denotes the measurement region used in the estimator and the domain  $x_c$  denotes the region where blowing and suction is applied in the control part of the simulations. The parameters  $\alpha_{\tau_x}$ ,  $\alpha_{\tau_z}$ , and  $\alpha_p$  are the sensor noises for each measurement which is used when computing the estimation gains and determines their relative and total strength. This is described in §2.2.2.

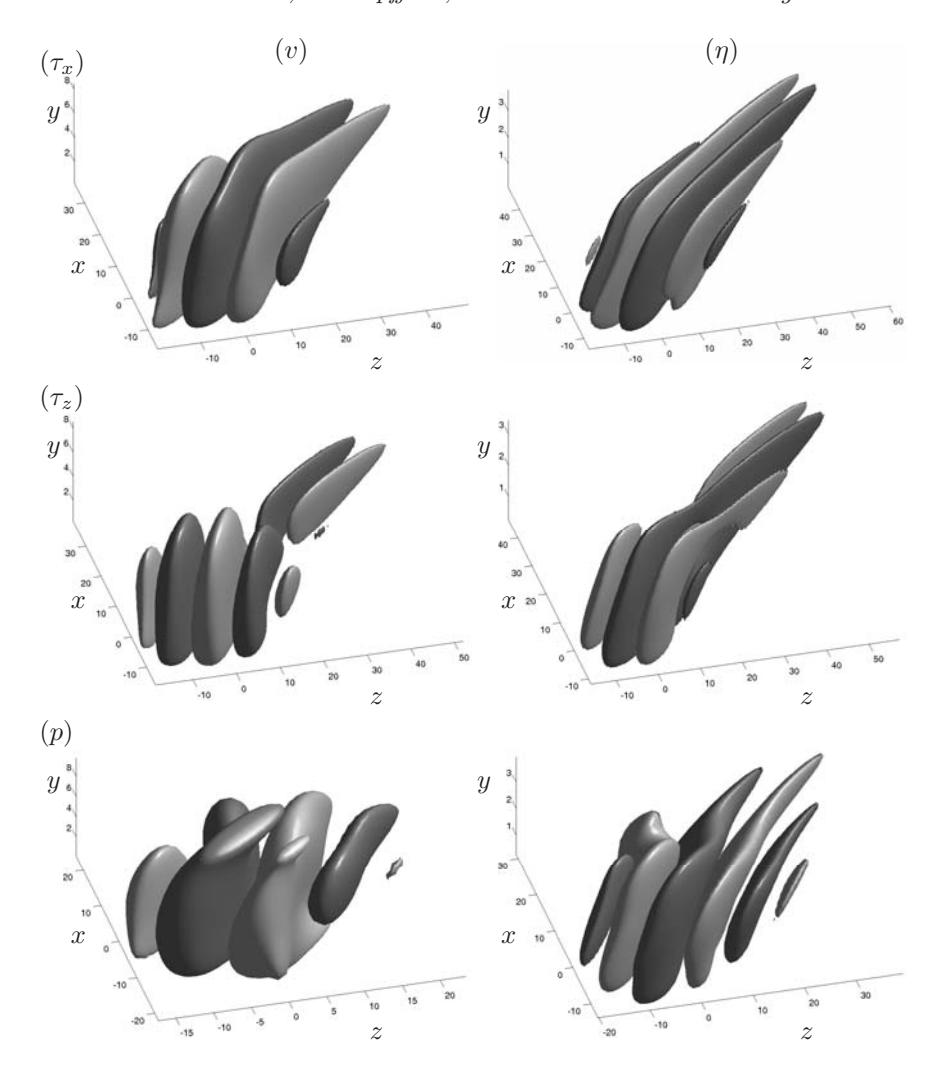


FIGURE 3. Steady-state estimation convolution kernels relating the measurements  $\tau_x$ ,  $\tau_z$ , and p at the point  $\{x=0,\ y=0,\ z=0\}$  on the wall to the estimator forcing on the interior of the domain for the evolution equation for the estimate of (left)  $\hat{v}$  and (right)  $\hat{\eta}$ . Positive (dark) and negative (light) isosurfaces with isovalues of  $\pm 10\%$  of the maximum amplitude for all kernels illustrated except for the  $\tau_z$  kernel for  $\eta$  which is plotted at  $\pm 20\%$ .

Runge–Kutta method for the advective and forcing terms whereas the viscous

terms are treated with a Crank-Nicolson method. The incompressibility condition is enforced implicitly by expressing the flow state in the wall-normal velocity and wall-normal vorticity state space.

## 4.2. Temporal simulations

To enforce parallel flow we add a volume forcing vector  $F = [F_1, F_2, F_3]^T$ , defined as

$$F_{1} = -\frac{\partial U(y,t)}{\partial t} - \frac{1}{Re} \frac{\partial^{2} U(y,t)}{\partial y^{2}},$$

$$F_{2} = 0,$$

$$F_{3} = -\frac{1}{Re} \frac{\partial^{2} W(y,t)}{\partial y^{2}}.$$
(22)

The velocity profiles U(y,t) and W(y,t) are given for a spatial position  $x_r$ . To further allow for a moving frame we make the following variable transformation  $x_r = x_0 + ct$  where c is the reference frame speed and let  $U(x_r, y) = U(x_0 + ct, y) = U(t, y)$ 

Different flow cases are obtained by supplying different initial conditions. We use here an eigenvector of the linearized Orr–Sommerfeld/Squire system defined in (2) and (3).

#### 4.3. Spatial simulations

#### 4.3.1. Fringe region

By adding the fringe forcing mentioned in §4.1 we can enforce flow periodicity and thus apply spectral methods to also solve spatially developing flows. The fringe function is defined as

$$\lambda(x) = \lambda_{\text{max}} \left[ S\left(\frac{x - x_{\text{start}}}{\Delta_{\text{rise}}}\right) - S\left(\frac{x - x_{\text{end}}}{\Delta_{\text{fall}}}\right) \right]$$
(23)

where the step function S is defined as

$$S(x) = \begin{cases} 0, & x \le 0, \\ 1/\left[1 + \exp\left(\frac{1}{x-1} + \frac{1}{x}\right)\right], & 0 < x < 1, \\ 1, & x \ge 0. \end{cases}$$
 (24)

The parameters  $x_{\rm start}$  and  $x_{\rm end}$  define the start and end location of the fringe domain. The parameters  $\Delta_{\rm rise}$  and  $\Delta_{\rm fall}$  define the rise and fall distance of the fringe function respectively.

In order to enforce the inflow boundary condition at the downstream end of the domain we construct the following blending function which gives a smooth

Parameter	Cases			
	3–5	11–13		
$x_0$	20	20.95		
$a_t$		0.001		
$a_s$	0.0001			
$x_{\rm scale}$	5	10		
$y_{\rm scale}$	1	1		
$z_{ m scale}$	0			
$z_{ m center}$	0	0		
$l_{ m skew}$				
$n_{\mathrm{modes}}$		21		
$t_{dt}$		1		
$\omega_h$	0.093668			

Table 2. Volume forcing parameters for the spatial simulations.

interpolation between two velocity profiles,

$$u_{\lambda} = U(x,y) + [U(x - l_{x}, y) - U(x,y)] S\left(\frac{x - x_{\text{mix}}}{\Delta_{\text{mix}}}\right) + u_{f}(x - l_{x}, y, z, t),$$

$$w_{\lambda} = W(x,y) + [W(x - l_{x}, y) - W(x,y)] S\left(\frac{x - x_{\text{mix}}}{\Delta_{\text{mix}}}\right) + w_{f}(x - l_{x}, y, z, t),$$
(25)

where  $l_x$  is the box length in the streamwise direction. The parameters  $x_{\rm mix}$  and  $\Delta_{\rm mix}$  are both blending parameters. The former is the start of the blending region and the latter is the rise distance of the blending. Additional forcing to add streaks or different wave forms can be added through the velocity components  $u_f$  and  $w_f$ , and  $v_\lambda$  directly in the fringe.

#### 4.3.2. Perturbations

To introduce perturbations into the spatially evolving flow an external volume force can be applied locally in the computational domain. This forcing can be applied either in the fringe region, as for the optimal disturbance case, or in the physical flow domain.

For unsteady perturbations we use a random forcing, acting only on the wall-normal component of the momentum equations

$$F_2^{\text{rand}} = a_t \exp[-((x - x_0)/x_{\text{scale}})^2 - (y/y_{\text{scale}})^2]f(z, t),$$
 (26)

where

$$f(z,t) = [(1 - b(t))h^{i}(z) + b(t)h^{i+1}(z)]$$
(27)

and

$$i = \text{int}(t/t_{dt}),$$
  
 $b(t) = 3p^2 - 2p^3,$  (28)  
 $p = t/t_{dt} - i,$ 

where  $h^j(z)$  is a Fourier series of unit amplitude functions with random phase generated at every time interval j. Within each time interval  $t_{\rm d}t$ , the function b(t) ramps the forcing smoothly in time. The maximum amplitude is determined by  $a_t$  and the forcing is exponentially decaying in both streamwise and wall-normal direction centered at  $x_0$ . The number of modes with non-zero amplitude is determined by the parameter  $n_{\rm modes}$ . This forcing has been used to generate the traveling cross-flow vortices described as cases 11–13 in table 1 with the corresponding parameters given in table 2.

Another option to generate perturbations is to use the harmonic forcing function defined as

$$F_2^{\text{harm}} = a_s \exp[-(y/y_{\text{scale}})^2]g(x, z)r(t),$$
 (29)

where

$$g(x,z) = \begin{cases} \cos[2\pi(z - x \, l_{\text{skew}})/z_{\text{scale}}] \exp[-((x - x_0)/x_{\text{scale}})^2], & \text{if } z_{\text{scale}} \neq 0, \\ \exp[-((x - x_0)/x_{\text{scale}})^2], & \text{if } z_{\text{scale}} = 0, \end{cases}$$
(30)

and

$$r(t) = \cos(\omega_h t),\tag{31}$$

where  $\omega_h$  is the frequency of the forcing. For stationary forcing  $\omega_h$  is set to zero. Also the harmonic forcing is exponentially decaying in both streamwise and wall-normal direction whereas in the spanwise direction we can choose whether to align the forcing with streamlines or have no spanwise dependence at all.

## 4.3.3. Zero mass-flux actuation

The numerical model in the DNS does not allow for net inflow, we thus have to enforce a zero-mass flux through the actuation strip by the transformation

$$\hat{\varphi}(x,z) = (\varphi(x,z) + c)H(x), \tag{32}$$

where

$$c = -\frac{\int \int \int \varphi(x, z) H(x) dx dz}{z_l \int \int H(x) dx}$$
(33)

and

$$H(x) = S\left(\frac{x - (x_{\text{center}} - l_x^c)}{\Delta x}\right) - S\left(\frac{x - (x_{\text{center}} - l_x^c)}{\Delta x}\right). \tag{34}$$

The parameter S(x) is defined as in equation (24) and  $x_{\text{center}}$  denotes the center of the control interval. Parameters  $l_x^c$  and  $l_z^c$  are respectively the length and width of the control domain and  $\Delta x$  is the rise and fall distance of the actuation.

# 4.4. Compensator algorithm

The compensator algorithm is depicted in figure 4. The "real" flow could be an experimental setup where only wall information is extracted. In our studies the "real" flow is represented by a DNS. The estimator is another DNS, which is used to recover the state from sensor information. The compensation algorithm can be sketched in the following steps

- 1. Take wall measurements in both flow and estimated flow
- 2. Compute the estimator volume forcing based on precomputed estimation gains and the difference of the wall measurements from the flow and estimated flow
- 3. Apply the volume forcing to the estimator flow to make it converge to the flow
- 4. Compute the control signal as a feedback of the reconstructed state in the estimator
- 5. Apply the control signal in both the flow and estimated flow

#### 5. Flow cases

In order to evaluate the compensator performance in transitional flows we test a range of different flow cases. To ease the comparison with the full information controller results reported in Högberg & Henningson (2002) we study the same flow cases and the same control parameters, r=0 and  $l^2=100$  has been used. However, the control region have been set further downstream to fit also a measurement region in the computational domain. Note that in principle we could have overlapping control and measurement regions. The computational parameters for each flow type are listed in table 1.

#### 5.1. Single eigenmode

To validate the numerical implementation of the control and the estimator forcing we studied a temporal FSC boundary layer flow where the Reynolds number at the beginning of the simulation box was Re=337.9 with a freestream cross-flow velocity component  $W_{\infty}=1.44232\,U_{\infty}(x=0)$  and a favorable pressure gradient m=0.34207 as defined in §2.1. The same flow setup is also studied in a spatial setting in §5.4. In this case of temporal flow the measurement and control regions overlap since they both extend over the whole wall.

The initial disturbance is the unstable eigenvector associated with the eigenvalue c = -0.15246 + i0.0382 that appears at  $k_x = 0.25$  and  $k_z = -0.25$ . The exponential energy growth of the uncontrolled eigenmode is depicted in figure 5 as a thick solid line. In the same figure the full information controller

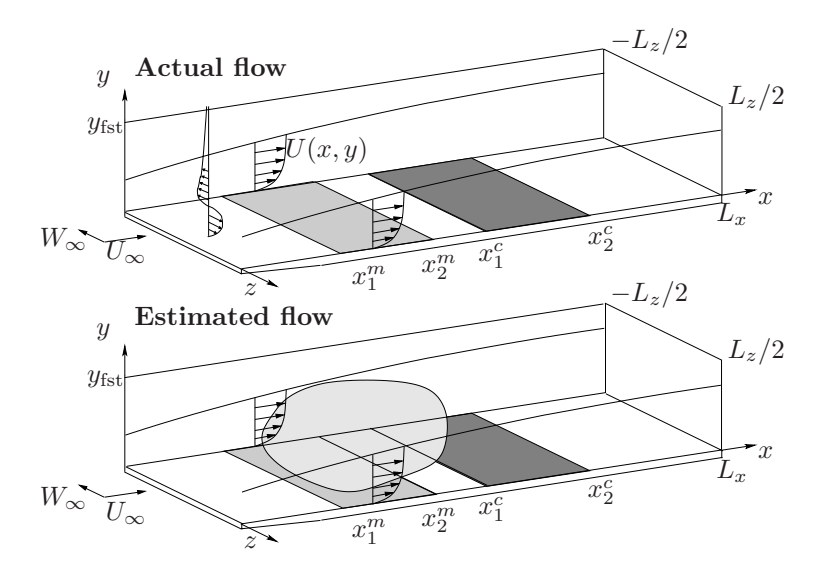


FIGURE 4. Compensator configuration. The upper box represents the "real" flow where the light grey rectangle along the wall is the measurement region  $(x \in [x_1^m, x_2^m])$  and the corresponding dark grey rectangle is the control area  $(x \in [x_1^c, x_2^c])$ . In the beginning of the box a perturbation is indicated as a function of the wall-normal direction. This perturbation will evolve as we integrate the system in time. The estimated flow system is depicted in the lower box. Here the volume force that is based on the wall measurements and the estimation gains is shown as a grey cloud in the computational domain.

is plotted as thick dashed line. The disturbance energy decays rapidly in time and levels out. The thin lines are all related to the compensator simulation. The thin solid line represents the disturbance energy in the estimator and it increases initially to quickly align with the energy growth of the actual state. This can also be viewed through the estimation error plotted as a thin dash-dotted line which decays exponentially in time. The compensator control is shown as the thin dashed line. Initially when the estimated state is poor the controller is not very efficient. However as the estimated state improves the compensator control is also improving.

# 5.2. TS-wave

The TS-wave perturbation is applied in a spatially developing Blasius boundary layer which corresponds to setting m=0 i.e. without pressure gradient in the streamwise direction. We have no mean-flow component in the z-direction. The wave is introduced by applying an oscillating volume force localized in x z far upstream in the computational box. The dimensionless oscillating frequency is

Parameter	Cases			
	3	5	8 & 10	13
$k_x^0$	0.25	0.28	0	0.25
$k_x^0 \ k_z^0$	-0.25	0	0.49	-0.25
$d_x$	0.1	0.25	0.15	0.2
$d_y$	0.1	0.1	0.1	0.1
$d_z$	0.1	0.25	0.15	0.2
$\alpha_{ au_x}$	29.56	4	0.2	0.2
$lpha_{ au_z}$	2.21	0.3	0.2	0.2
$\alpha_n$	14781.97	2000	300	30000

Table 3. Estimator model parameters. The parameters  $k_x^0$ ,  $k_z^0$ ,  $d_x$ ,  $d_y$ , and  $d_z$  all relate to the covariance model of the external disturbances and the parameters  $\alpha_{\tau_x}$ ,  $\alpha_{\tau_z}$ , and  $\alpha_p$  relate to the modeling of the sensor noise.

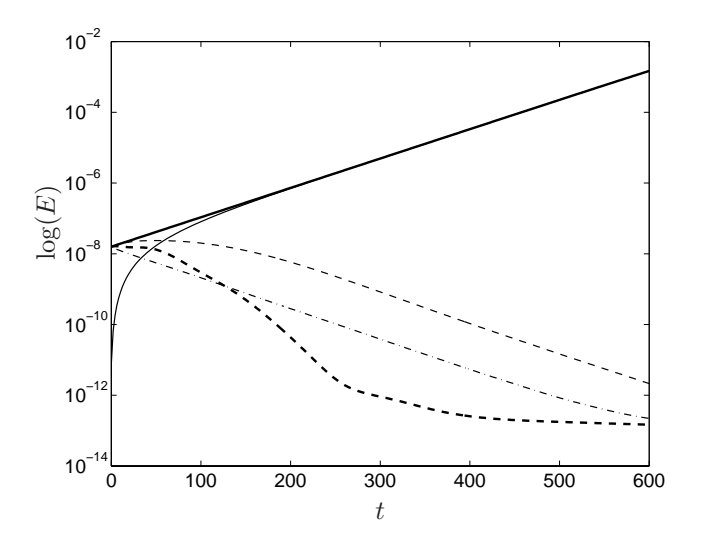


FIGURE 5. Time evolution of the perturbation energy of the uncontrolled unstable eigenmode at  $k_x=0.25, k_z=-0.25$  in a FSC boundary layer and the corresponding controlled system. Solid: uncontrolled energy growth (case 1). Dashed: full information control applied (case 2). Solid-thin: energy growth in the estimator when no control is applied. Dash-dotted-thin: the estimation error when no control is applied. Dashed-thin: compensator control is applied (case 3). The simulations correspond to cases 1–3 in table 1.

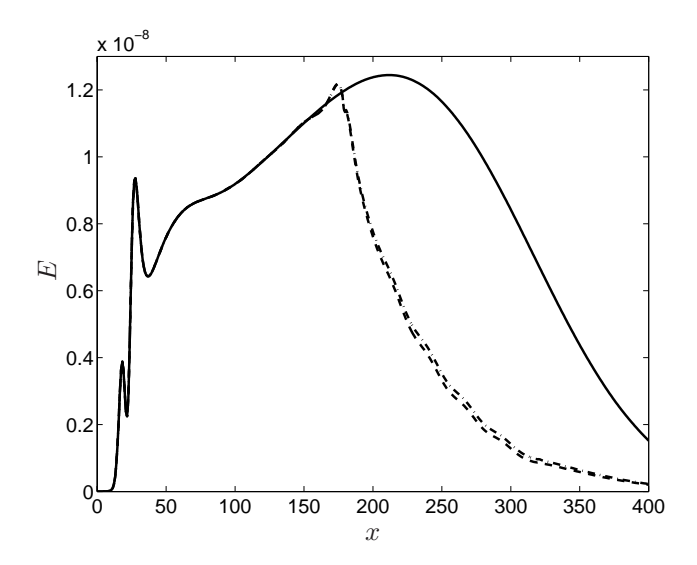


FIGURE 6. Spatial evolution of the perturbation energy of a TS-wave in a spatially growing boundary layer. Solid: no control. Dashed: energy growth and decay with full information control. Dash-dotted: energy growth and decay with compensator control.

F=200 where  $F=10^62\pi f\nu/U_\infty^2$ . The unstable area for this waves extends from Branch I at x=27 ( $Re\approx507$ ) to branch II at x=219 ( $Re\approx723$ ). The measurement region is  $x\in[40,150]$  and the control region is  $x\in[175,325]$  so that they both overlap with the exponential growth region. The simulation parameters correspond to cases 4–6 in table 1 and the parameters defining the volume forcing are stated in table 2.

Figure 6 shows the uncontrolled energy growth and decay as a solid line. After a short spatial transient, the volume forcing induces a TS-wave with the expected exponential growth. Dashed and dash-dotted lines show respectively the energy evolution in the beginning of the control region when the full information and compensator control are applied. Despite the approximative estimated flow state information, the compensator is able to turn the exponential growth into exponential decay.

Figure 7(a) shows a snapshot of an x-y plane of the wall-normal velocity field. The forcing has been turned on long enough to let the waves propagate through the whole computational box. In figure 7(b) the compensator control have been turned on for 1341 time units which corresponds to twenty periods of the forcing. Full information and compensator control have similar performance.

The control signals for the full information control and the compensator control are shown in figure 8. The control signals mimic waves with sharp peaks

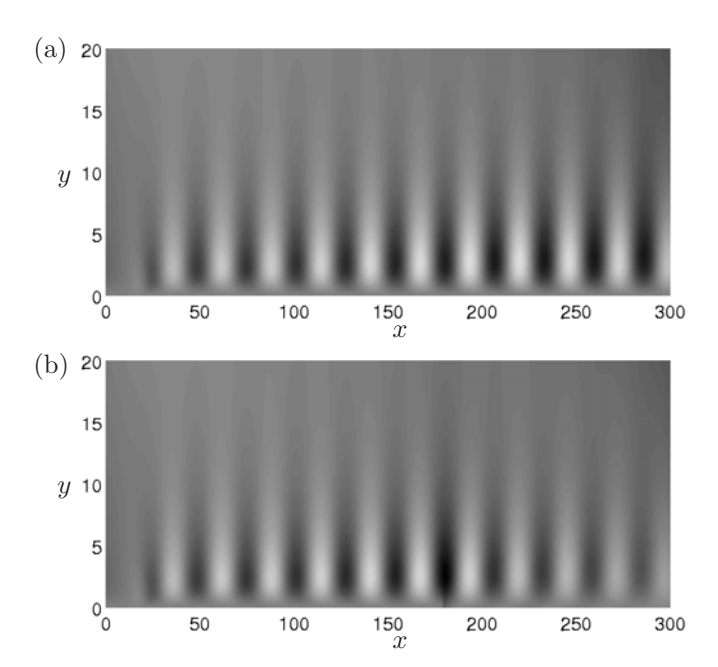


FIGURE 7. A snapshot of the wall-normal perturbation velocity for controlled and uncontrolled TS-waves. (a) The TS-wave at t=1341 with no control. (b) Compensator control applied during twenty TS-wave periods which corresponds to 1341 time units.

in the beginning and end of the control interval, probably due to the artificial spatial cut-off out of the actuation strip.

## 5.3. Optimal perturbation

The compensator performance is also studied for transiently growing perturbations, see i.e. Butler & Farrell (1992). The spatial optimal perturbations in a Blasius boundary layer have been computed by Andersson et al. (1999) and Luchini (2000). The optimal perturbation is introduced at x=-158.16 and then marched forward to x=0 with the technique developed in Andersson et al. (1999). The perturbation is introduced in the fringe region to give the proper inflow condition, see §4.3 and table 2 for numerical details and choice of parameters. The perturbation is optimized to peak at x=237.24.

The same base flow parameters have been used as was used for the TS-wave simulations described in  $\S5.2$ , but with a larger box size in the streamwise direction. The local Reynolds number at inflow is Re = 468.34. The simulation parameters are given in table 1 as cases 6-10.

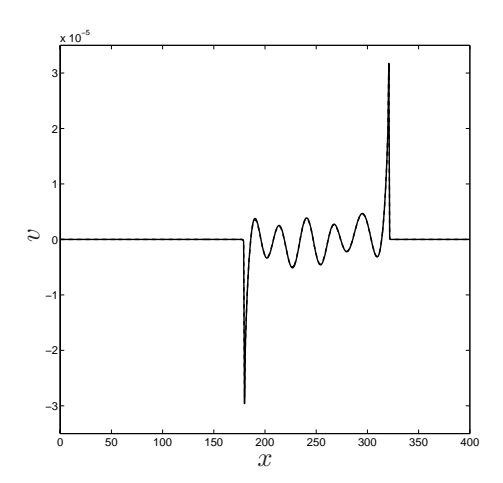


FIGURE 8. Control signal when the control has been turned on for 1341 time units. Solid: full information control. Dashed: compensator control.

In figure 9 the perturbation energy is defined as

$$E = \int_{0}^{2\pi/\beta_0} \int_{0}^{\infty} (u^2 + v^2 + w^2) \, \mathrm{d}y \, \mathrm{d}z, \tag{35}$$

where the spanwise wave number is  $k_z^0=0.4897$ . The figure shows the energy of the uncontrolled flow, full information control and compensator control once steady state has been reached. Two different lengths of the control regions have been implemented. Both types of controller for both control intervals work well at reducing the perturbation energy. In the case with a narrow control strip the perturbation energy starts to grow again since a stronger component of the growing disturbance remains.

Note that the estimated flow energy does not reach the exact perturbation energy level, but this does not seem to affect strongly the compensator performance.

The control signal for the full information and compensator control cases, for the control interval  $x \in [300,750]$ , are depicted in figure 10. The actuation presents a peak at the beginning of the control region and then a fast decay which levels out progressively. A similar feature is reported in Cathalifaud & Luchini (2000) where control is applied over the whole domain.

## 5.4. Traveling cross-flow vortices

The FSC boundary layer flow studied in this paper is subject to several other studies, for example Högberg & Henningson (1998) and Högberg & Henningson (2002). Originally it was an attempt to reproduce experimental results where traveling cross-flow modes have been observed (see e.g. Müller & Bippes 1988).

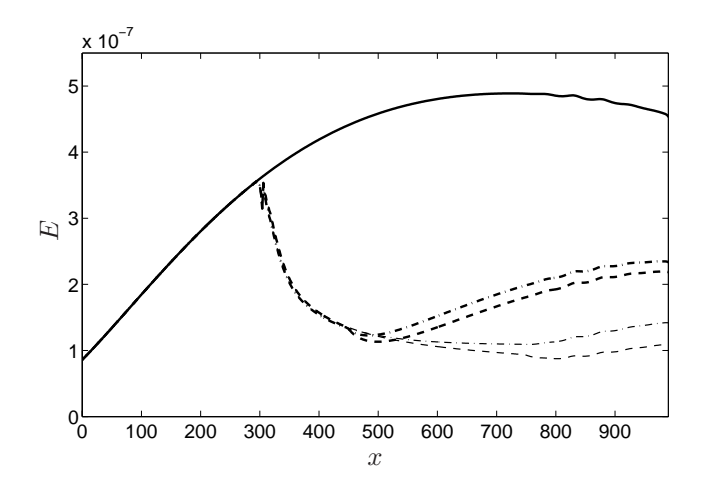


FIGURE 9. Spatial energy evolution of the optimal perturbation. Solid: no control. Dashed: full information control applied in region  $x \in [300, 450]$ . Dash-dotted: compensator control with measurement region  $x_m \in [0, 300]$  and the control region  $x_c \in [300, 450]$ . Thin-solid: estimated flow energy. Thin-dashed: full information control applied in region  $x \in [300, 725]$ . Thin dash-dotted: compensator control with the measurement region  $x_m \in [0, 300]$  and the control region  $x_c \in [300, 725]$ . The flow cases correspond to cases 6–10 in table 1.

A random perturbation in space and time that generates cross-flow vortices downstream is applied, see equation 26 with parameters in table 2. The simulation box and other numerical details can be found as cases 11–13 in table 1.

In case 11 we compute the time evolution of the forcing as it develops downstream and forms the cross-flow vortices depicted with a solid line in figure 11. In case 12 we apply full information control. Exponential decay replaces then the uncontrolled exponential growth, as shown by the dashed line in figure 11. However almost adjacent to the downstream end of the control region the disturbances start to grow exponentially. Indeed, this wave is unstable over the whole box, and resumes growth behind the control strip. In the same figure also the perturbation energy for the compensator is plotted as a dash-dotted line.

The simulations are run until we reach a stationary state where we sample and time average the disturbance energy in the streamwise direction as shown in figure 13. The control gains are computed for the base flow at position x = 250 which is the center of the control domain  $x \in [175, 325]$ . The estimator gains are centered at x = 95 and the measurements are taken in  $x \in [40, 150]$ . In figure 13(a) the uncontrolled flow for the wall-normal perturbation velocity is

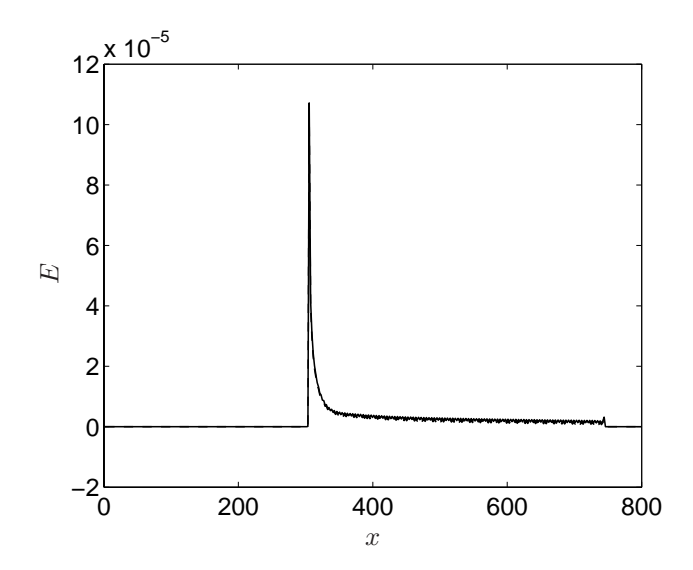


FIGURE 10. The control signals for the optimal disturbance case after initial transient. Dashed: full information control applied in region  $x \in [300, 750]$ . Dash-dotted: compensator control in domain  $x \in [300, 750]$ .

plotted at y = 0.5. The corresponding plot for the compensated flow is depicted in figure 13(b).

### 6. Conclusion

Based on findings on how to improve the performance of the state estimator, reported in Hoepffner  $et\ al.\ (2004)$ , combined with the state-feedback control used in, for example, Bewley & Liu (1998) and Högberg & Henningson (2002) viscous instabilities, non-modal transient energy growth and inflectional instabilities in spatially developing boundary layer flows are controlled based on wall measurement.

The key to the improved performance of the estimator is the design of a physically relevant stochastic model for the external sources of disturbances. The external disturbances should account for as much as possible of the flow system that cannot be taken into account in the linear dynamic model that is used to formulate the control and estimator problem. For this purpose we choose a correlation length which is weighted to be stronger in the interior of the boundary layer than outside. We also choose an amplitude distribution in wavenumber space such that it represents the main wavenumbers to be active in the specific flow that we study. This procedure leads to well resolved estimation gains for the three measurements streamwise and spanwise shear stresses and pressure. Both the sensor noise and the external disturbances are assumed to

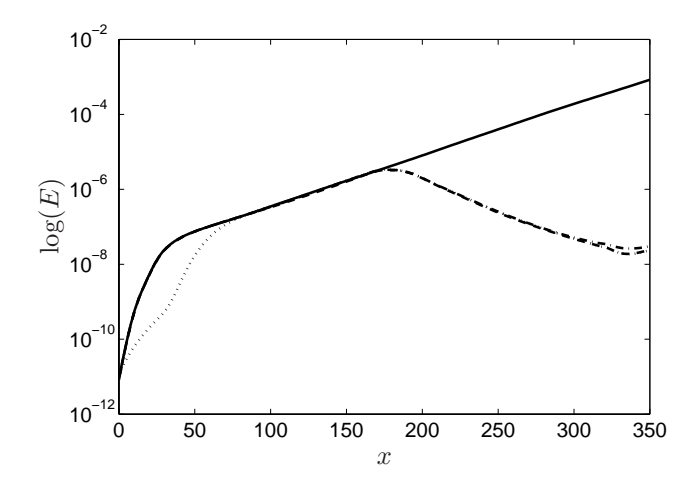


FIGURE 11. Time averaged perturbation energy for cross-flow vortices in a Falkner–Skan–Cooke boundary layer. Solid: uncontrolled. Dashed: full information control. Dash-dotted: compensator control. The simulations correspond to cases 11–13 in table 1.

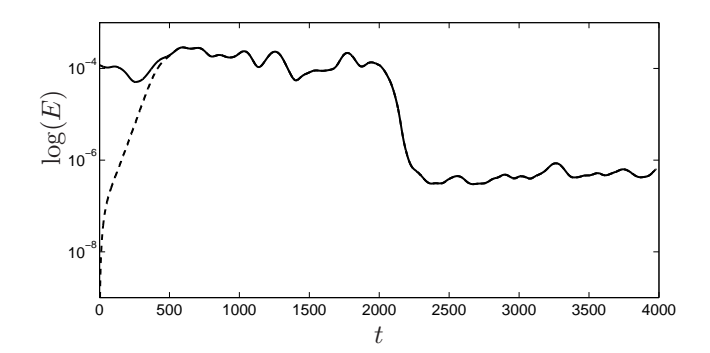


FIGURE 12. Time evolution of the disturbance energy integrated throughout the computational box. During the first 2000 time units the flow is uncontrolled. At time t=2000 the compensator is turned on. Solid: energy in the flow. Dashed: energy in the estimator.

be white noise processes. The sensor noise becomes a natural parameter to tune the strength of the feedback to the estimator.

Note that so far we have given the estimator ample time to converge before turning on the compensator control except for in the temporal flow case. In future work one could reduce the time frame for the estimator to converge as well as experiment with smaller measurement regions.

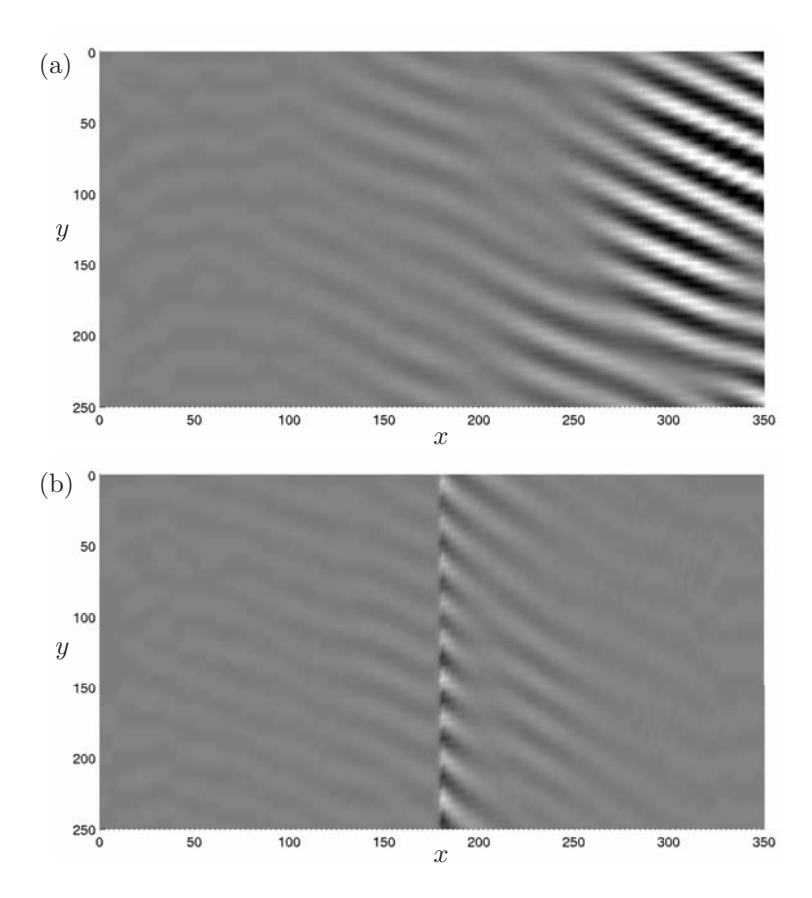


FIGURE 13. Snapshots of the wall-normal velocity component at y=0.5. The flow state is depicted in part (a). In (b) the effect of the compensator control is shown. In both controlled flows the actuation was applied for 2000 time units, and reached its steady state. The black to white scales lies within  $v \in [-0.00045, 0.00045]$ .

# Acknowledgment

This work has been partially financed by the Innovation fund at the Swedish Defence Reseach Agency (FOI) which is greatfully acknowledged.

# References

Andersson, P., Berggren, M. & Henningson, D. S. 1999 Optimal disturbances and bypass transition in boundary layers. *Phys. Fluids* 11, 134–150.

- Bewley, T. R. 2001 Flow control: new challenges for a new Renaissance. *Progress in Aerospace Sciences* 37, 21–58.
- Bewley, T. R. & Liu, S. 1998 Optimal and robust control and estimation of linear paths to transition. *J. Fluid Mech.* **365**, 305–349.
- Butler, K. M. & Farrell, B. F. 1992 Three-dimensional optimal perturbations in viscous shear flow. *Phys. Fluids A* 4, 1637–1650.
- CATHALIFAUD, P. & LUCHINI, P. 2000 Algebraic Growth in Boundary Layers: Optimal Control by Blowing and Suction at the Wall. Eur. J. Mech. B Fluids 19, 469–490.
- Chevalier, M., Hæpffner, J., Bewley, T. R. & Henningson, D. S. 2004 State estimation of wall bounded flow systems. Part 2. Turbulent flows. *J. Fluid Mech.* Submitted.
- COOKE, J. C. 1950 The boundary layer of a class of infinite yawed cylinders. *Proc. Camb. Phil. Soc.* 46, 645–648.
- Hœpffner, J., Chevalier, M., Bewley, T. R. & Henningson, D. S. 2004 State estimation in wall-bounded flow systems, Part 1. Laminar flows. *J. Fluid Mech.* Submitted.
- HÖGBERG, M. & BEWLEY, T. R. 2001 Spatially-localized convolution kernels for decentralized control and estimation of transition of plane channel flow. *Automatica* Submitted.
- HÖGBERG, M., BEWLEY, T. R. & HENNINGSON, D. S. 2003a Relaminarization of  $\text{Re}_{\tau}$ =100 turbulence using gain scheduling and linear state-feedback control. *Phys. Fluids* **15**, 3572–3575.
- HÖGBERG, M., CHEVALIER, M. & HENNINGSON, D. S. 2003b Linear compensator control of a pointsource induced perturbation in a Falkner–Skan–Cooke boundary layer. *Phys. Fluids* **15** (8), 2449–2452.
- HÖGBERG, M. & HENNINGSON, D. S. 1998 Secondary instability of cross-flow vortices in Falkner–Skan–Cooke boundary layers. *J. Fluid Mech.* **368**, 339–357.
- HÖGBERG, M. & HENNINGSON, D. S. 2002 Linear optimal control applied to instabilities in spatially developing boundary layers. *J. Fluid Mech.* 470, 151–179.
- Kim, J. 2003 Control of turbulent boundary layers. Phys. Fluids 15 (5), 1093-1105.
- Lewis, F. L. & Syrmos, V. L. 1995 Optimal control. Wiley-Interscience.
- Luchini, P. 2000 Reynolds-number-independent instability of the boundary layer over a flat surface: optimal perturbations. *J. Fluid Mech.* 404, 289–309.
- Lundbladh, A., Berlin, S., Skote, M., Hildings, C., Choi, J., Kim, J. & Henningson, D. S. 1999 An Efficient Spectral Method for Simulations of Incompressible Flow over a Flat Plate. Technical Report TRITA-MEK 1999:11. Department of Mechanics, Royal Institute of Technology, KTH.
- Lundbladh, A., Henningson, D. S. & Johansson, A. 1992 An Efficient Spectral Integration Method for the Solution of the Navier–Stokes Equations. Technical Report FFA TN 1992-28. The Aeronautical Research Institute of Sweden, FFA.
- Malik, M. R., Zang, T. A. & Hussaini, M. Y. 1985 A spectral collocation method for the Navier–Stokes equations. *J. Comp. Phys.* **61**, 64–88.
- MÜLLER, B. & BIPPES, H. 1988 Experimental study of instability modes in a three-dimensional boundary layer. AGARD-CP 438 18.
- NORDSTRÖM, J., NORDIN, N. & HENNINGSON, D. S. 1999 The fringe region technique

- and the Fourier method used in the direct numerical simulation of spatially evolving viscous flows. SIAM J. Sci. Comp. 20 (4), 1365–1393.
- Schlichting, H. 1979  $Boundary\text{-}Layer\ Theory,$  seventh edn. Springer.
- Yoshino, T., Suzuki, Y. & Kasagi, N. 2003 Evaluation of GA-based feedback control system for drag reduction in wall turbulence. In *Proc. 3rd Int. Symp. on Turbulence and Shear Flow Phenomena*, pp. 179–184.

Paper 5

# Adjoint based control in channel and boundary layer flows

By Mattias Chevalier\*†, Markus Högberg†, Martin Berggren†‡ and Dan S. Henningson\*†

Published as a technical report, TRITA-MEK 2004:12

Optimal control by means of blowing and suction control of transition in channel flow and boundary layer flow is attempted. First the optimization problem is stated and the corresponding adjoint equations used to compute the gradient of the objective function are derived for both the channel flow and boundary layer flow problems. A solver for the adjoint equations has been implemented in a spectral direct numerical simulation code used when solving the Navier–Stokes equations. This method adapts naturally, without modification, to nonlinearities such as a strongly varying mean flow. However, it is computationally expensive and storage demanding, needing numerous solves of the Navier–Stokes and associated adjoint equations.

To test the performance of the solver of the optimization problem for the channel flow, the derived formulation is applied to different stages of the oblique transition scenario. The boundary layer optimization problem is applied on different instabilities in parallel and spatially-developing three-dimensional boundary layers. Both the channel and boundary layer flows are controlled through blowing and suction at the wall.

Furthermore, for boundary layer flows the nonlinear optimization results are compared with feedback controllers based on linear optimal control theory. The feed-back operator is constructed from the Orr–Sommerfeld/Squire equations. Assuming the flow to be locally parallel makes it feasible to solve the associated Riccati equations for each wave number pair in the stream- and spanwise directions. The feed-back is applied to a DNS of the flows mentioned above. This method is much less computationally costly than the first nonlinear method.

Finally, adjoint equations are also derived and implemented for an optimization problem where the objective is to find the optimal initial condition

<sup>\*</sup>Department of Mechanics, Royal Institute of Technology (KTH), SE-100 44 Stockholm, Sweden

 $<sup>^{\</sup>dagger} \mathrm{The}$ Swedish Defence Research Agency (FOI), SE-172 90 Stockholm, Sweden

 $<sup>^{\</sup>ddagger}$  Department of Information Technology, Uppsala University (UU), SE-751 05 Uppsala, Sweden

that produces the highest energy growth at a specified time. This implementation is aimed for future studies of secondary instabilities on a streaky base flow.

#### 1. Introduction

In the last decade, one topic in fluid mechanics that has been subject to an increasing interest is *flow control*. The fast development in computer performance has made it possible to approach these problems from a numerical point of view, and also to construct small devices to be used for measurements and actuation in experiments. Mathematical aspects of the flow control problem is the topic of the books edited by Gunzburger (1995) and Sritharan (1998). Computational approaches to flow control are reviewed in the paper by Hinze & Kunish (2000). Optimal control of channel flow using direct numerical simulations was previously considered using by Bewley *et al.* (2001) and using large eddy simulations by Collis *et al.* (2000). In addition to channel flow Joslin *et al.* (1997) also considered the boundary layer case with a two dimensional flow in direct numerical simulations.

In flow systems where strong inherent instabilities are present, like in a transitional flow, small perturbations can alter the flow features dramatically. In such flows, there is therefore a potential to improve the quality of the flow using small devices with a localized action and with a minimum of energy expenditure. This is one of the main ideas behind flow control. Such control strategies could be used, for example, to reduce drag on bodies, increase lift on wings, increase propulsion efficiency, heat- and mass-transfer reduction or enhancement, control of vortex shedding or to control separation and aeroacoustic pressure fluctuations.

Generally, the different control techniques are divided into two groups. The first group, where no auxiliary power is used, includes the passive control methods. These methods are usually implemented through geometrical modifications. This has been the traditional way of controlling fluid mechanical systems. The other large group of control methods is the active control methods where the control is adjusted dynamically to the state of the system. One of the first attempts was, for example, to cancel TS waves by anti-phase modal suppression to prevent transition. Early work is reviewed in Thomas (1990) and a brief, later review is given in Metcalfe (1994). These efforts showed that instabilities may indeed be significantly suppressed, but complete elimination of the primary instability is not achieved.

As opposed to earlier attempts of controlling fluid flows, when thorough understanding of the phenomena involved was necessary, optimal control theory requires no *a priori* knowledge about the functional behavior of an effective control. The theoretical framework is general and applies to a broad spectra of applications where just a small selection is listed here: finding optimal shape of wings under certain conditions (Jameson (1989)), minimizing the vorticity of

an unsteady internal flow by manipulating the inlets (Berggren (1995)), as well as controlling boundary layer transition (Joslin  $et\ al.\ (1997)$ ) and turbulence (Bewley  $et\ al.\ (2001)$ ). Optimal control based on linear theory has also been investigated and has shown to work very well in recent applications such as in channel flow (Joshi  $et\ al.\ (1997)$ , Bewley & Liu (1998) and Högberg & Bewley (2001)). In this approach modern linear control theory is used to construct feedback control laws for online control.

In this report both the linear control approach from Högberg & Bewley (2001) and Högberg & Henningson (2002) and a nonlinear control approach are applied to spatially evolving boundary layer flows in cases representing three fundamentally different paths to transition. Our goal is to measure the effectiveness of the optimal nonlinear controller versus the linear counterpart and how much the restrictions in the linear optimal control limits its performance. Note however that the two optimization formulations differ in terms of objective functions. See text below for details.

This report summarizes the work from two different studies described in Högberg et al. (2001) and Chevalier et al. (2002). It consider the problem of control of transition from laminar to turbulent flow in channel and boundary layers. In many applications there is a large potential benefit from the ability to prevent transition whereas in other applications the turbulent state is the desired one. Our objective is to delay or prevent transition at low Reynolds numbers, particularly focusing on the bypass transition (Morkovin (1969)) scenarios, not originating from an exponential instability. The problem of bypass transition is important in many practical applications, and considerable amounts of research has been done on this subject see e.g. the recent book by Schmid & Henningson (2001). The second optimization problem aims at finding the initial condition that gives maximum energy growth at a specified time. Here only the optimization problem will be stated, the corresponding adjoint will be derived, and the implementation verified. The derivation and implementation is primarily intended for future studies of secondary instabilities on streaks.

In section 2 the different optimization problems are formulated and explained in detail, and a short description of the numerical methods used are described in section 3 and 4.1. Section 5 contains some simple test cases to verify that the implementations are working properly.

In section 6 the linear and nonlinear control approaches are applied to three different flow scenarios and results from these simulations are presented. Finally, a summary and conclusions follow in section 7.

## 2. Optimization problem formulations

The formulation of an optimal control problem is based on three important decisions. The choice of governing equations, determining what means of actuation to use, and what properties of the flow to control. For a particular flow

geometry and with given fluid properties, these choices have to be made with care.

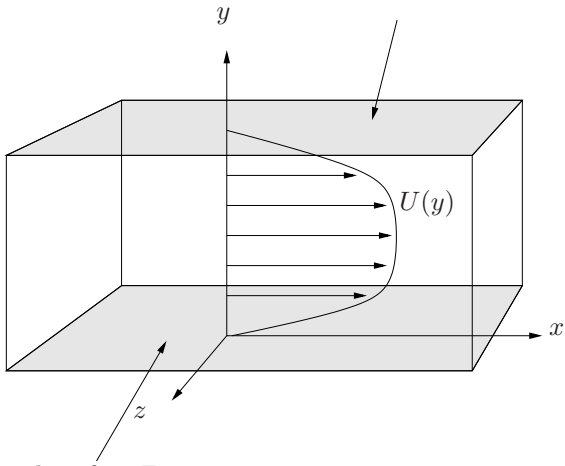
In this work the governing equations are the incompressible Navier–Stokes equations. In a recent study, successful application of feedback controllers computed from the linearized Navier–Stokes equations was performed by Högberg & Bewley (2001) in temporal channel flow. Changes in the mean flow is not easily taken into account using this formulation. Thus, a proper treatment of problems where this is important, such as a flow with local separation, requires the use of the full Navier–Stokes equations.

Since no particular quantity is known that establishes where we are on the path to transition the choice of objective function is difficult. The mean skin friction drag could be used as an indicator, since it has a jump at transition, and can be used to define a transition point, as for example in Reddy et al. (1998). On the other hand, Bewley et al. (2001) showed that the mean drag was not a good choice for the objective function when the purpose was to relaminarize turbulence in a channel flow, and concluded that the turbulent kinetic energy was a more appropriate choice. Since we are interested in control of transition rather than turbulence, the energy of the deviation from the mean flow appears to be an appropriate quantity to minimize. An increased physical understanding of the transition process and the crucial mechanisms of turbulence could provide a guide to the best choice of objective function as pointed out by Kim & Lim (2000).

It is important to choose the properties of the control in such a way that it is able to do its task in an efficient way. For our study, we have chosen to use blowing and suction at the wall during a specified period in time. The state of the flow is observed during another, possibly overlapping, period in time. When a spatially rather than a temporally evolving flow is considered it is physically meaningful to specify also the spatial extent of the control and observation regions. The control is restricted to have zero mass flux, in order to limit the ability to affect the mean flow and focus the control effort on the perturbations.

The gradient of the objective function may be expressed in terms of the solution of an adjoint equation. Here, we discretize the expressions for the adjoint equations and the gradient that have been derived on the "continuous" level. An alternative is to discretize the Navier–Stokes equations and the objective function and derive the adjoint equations and the gradient expression on the discrete level. The latter approach leads to more accurate gradient directions, but it seems difficult to apply for the present discretizations. Issues related to the errors introduced by the approximative (continuous) formulation are discussed in e.g. Glowinski & He (1998), Gunzburger (1995), and Gunzburger (1998). The use of the continuous formulation is motivated by the findings in Högberg & Berggren (2000) where one conclusion was that it is sufficient to use the approximative (continuous) formulation in order to control strong instabilities. It was noted that in such cases most of the reduction of the objective

Upper control surface  $\Gamma_U$ 



Lower control surface  $\Gamma_L$ 

FIGURE 1. Geometry of flow domain  $\Omega$  for channel flow simulations.

function is achieved in the first few iterations, and additional iterations only result in a fine-tuning of the control. The drawback is that it will require more iterations to reach the true optimal solution, if it is even possible, than with the discrete formulation.

# $2.1.\ Nonlinear\ blowing\ and\ suction\ control$

#### 2.1.1. Governing equations

In this section we consider the channel flow problem and the details of the method used to solve the optimization problem. The boundary layer problem is basically an extension of the channel flow case. The differences are outlined in section 2.1.3, and a full description of the boundary layer case is provided in appendix Appendix A.

Our computational domain depicted in Figure 1 is

$$\Omega = (-x_L/2, x_L/2) \times (-1, 1) \times (-z_L/2, z_L/2),$$

in x, y, z, and we define

$$\Gamma_L = \Omega(y = -1), \quad \Gamma_U = \Omega(y = 1) \quad \text{and} \quad Q = \Omega \times (0, T).$$

The non-dimensional, incompressible Navier–Stokes equations with a Reynolds number, Re, based on the centerline velocity and half the channel height are,

$$\begin{cases} \frac{\partial u}{\partial t} + (u \cdot \nabla)u - \frac{1}{Re}\Delta u + \nabla \pi = -\nabla P & \text{in } Q, \\ \nabla \cdot u = 0 & \text{in } Q, \\ u|_{t=0} = u_0, \end{cases}$$
 (1)

where  $u = (u_1, v, w)$  is the velocity vector,  $\pi$  is the pressure and  $\nabla P$  represents the pressure gradient driving the flow and can either be constant or used to ensure constant mass flux. Periodic boundary conditions in x and z, and control through blowing and suction together with a no-slip condition for the directions parallel to the wall gives the complete set of boundary conditions,

$$u|_{x=-x_L/2} = u|_{x=x_L/2},$$

$$u|_{z=-z_L/2} = u|_{z=z_L/2},$$

$$e_i \cdot u|_{y=-1} = \begin{cases} \varphi_L^T \psi_L = \sum_{m=1}^{M_L} \varphi_{L,m}(t) \, \psi_{L,m}(x,z) & \text{in } (T_1^c, T_2^c) \\ 0 & \text{otherwise,} \end{cases}$$

$$e_i \cdot u|_{y=1} = \begin{cases} \varphi_U^T \psi_U = \sum_{m=1}^{M_U} \varphi_{U,m}(t) \, \psi_{U,m}(x,z) & \text{in } (T_1^c, T_2^c) \\ 0 & \text{otherwise,} \end{cases}$$

$$(2)$$

where  $e_i$  are unit basis vectors in the coordinate directions, and  $\psi$  are basis functions for the control designed to have zero net mass flux. We can now introduce the control variable  $\varphi$  defined as:

$$\varphi = (\varphi_L, \varphi_U)^T, \begin{cases} \varphi_L = (\varphi_{L,1}, \dots, \varphi_{L,M_L})^T, \\ \varphi_U = (\varphi_{U,1}, \dots, \varphi_{U,M_U})^T. \end{cases}$$

To completely specify the optimal control problem we also need an objective function. If we choose to minimize the energy of the deviation from a target velocity distribution, the objective function is:

$$J(\varphi) = \frac{\varepsilon}{2} \int_{T_c^c}^{T_c^c} \int_{\Gamma} |v|^2 d\Gamma dt + \frac{1}{2} \int_{T_c^o}^{T_c^o} \int_{\Omega} |u - u_T|^2 dQ,$$
 (3)

where  $(T_1^c, T_2^c)$  is the control time period and  $(T_1^o, T_2^o)$  is the observation time period. The target velocity profile is denoted  $u_T$ . The optimization problem is then: find  $\varphi^*$  which satisfies

$$J(\varphi^*) \leq J(\varphi) \quad \forall \ v(\varphi)|_{\Gamma} \in \mathcal{U}_{ad}$$

where  $\mathcal{U}_{ad}$  has been used to denote the set of admissible controls which is a subset of  $L^2((T_1^c, T_2^c); \mathbb{R}^{M_L + M_U})$ .

## 2.1.2. Derivation of objective function gradient

The gradient of the objective function  $\nabla J$  is defined by

$$\delta J(\varphi) = \lim_{s \to 0} \frac{J(\varphi + s \,\delta\varphi) - J(\varphi)}{s} = \langle \nabla J, \delta\varphi \rangle$$

$$= \left\langle \frac{\partial J}{\partial \varphi_L}, \delta\varphi \right\rangle + \left\langle \frac{\partial J}{\partial \varphi_U}, \delta\varphi \right\rangle, \tag{4}$$

where  $\delta \varphi$  is the first variation of the control. The functional  $\delta J$  is the first variation of J with respect to  $\delta \varphi$ . To find an expression for  $\nabla J$  we start by

differentiating the objective function (3) to get,

$$\delta J(\varphi) = \varepsilon \int_{T_c^c}^{T_2^c} \int_{\Gamma} \delta v \, v \, d\Gamma \, dt + \int_{T_c^o}^{T_2^o} \int_{\Omega} \delta u \cdot (u - u_T) \, dQ, \tag{5}$$

where  $\delta v = e_2 \cdot \delta u$  and  $\delta u$  is the first variation of u with respect to  $\delta \varphi$ . To find an expression for the relation between  $\delta u$  and  $\delta \varphi$  we differentiate state equation (1),

$$\begin{cases} \frac{\partial \delta u}{\partial t} + (\delta u \cdot \nabla)u + (u \cdot \nabla)\delta u - \frac{1}{Re}\Delta \delta u + \nabla \delta \pi = 0 & \text{in } Q, \\ \nabla \cdot \delta u = 0 & \text{in } Q, \\ \delta u|_{t=0} = 0, \end{cases}$$
 (6)

and boundary conditions (2),

$$\delta u|_{x=-x_L/2} = \delta u|_{x=x_L/2},$$

$$\delta u|_{z=-z_L/2} = \delta u|_{z=z_L/2},$$

$$e_i \cdot \delta u|_{y=-1} = \begin{cases} \delta \varphi_L^T \psi_L = \sum_{m=1}^{M_L} \delta \varphi_{L,m}(t) \psi_{L,m}(x,z) & \text{in } (T_1^c, T_2^c) \\ 0 & \text{otherwise,} \end{cases}$$

$$e_i \cdot \delta u|_{y=1} = \begin{cases} \delta \varphi_U^T \psi_U = \sum_{m=1}^{M_U} \delta \varphi_{U,m}(t) \psi_{U,m}(x,z) & \text{in } (T_1^c, T_2^c) \\ 0 & \text{otherwise.} \end{cases}$$

$$(7)$$

Now we introduce a vector function p = p(x, y, z, t) such that  $e_i \cdot p = p_i$  and require p to satisfy the boundary conditions:

$$p|_{x=-x_L/2} = p|_{x=x_L/2},$$

$$p|_{z=-z_L/2} = p|_{z=z_L/2},$$

$$p|_{y=-1} = p|_{y=1} = 0.$$
(8)

The boundary conditions may be chosen during the derivation but in order to simplify the presentation they are introduced already at this point. Taking the dot product between p and equation (6) and integrating over Q yields

$$\int_{Q} p \cdot \left( \underbrace{\frac{\partial \delta u}{\partial t}}_{1} + \underbrace{(\delta u \cdot \nabla)u}_{2} + \underbrace{(u \cdot \nabla)\delta u}_{3} - \underbrace{\frac{1}{Re} \Delta \delta u}_{4} + \underbrace{\nabla \delta \pi}_{5} \right) dQ = 0.$$
 (9)

Then, step by step, we apply integration by parts to move derivatives from  $\delta u$  to p. We start with the first term in the integral (9), containing the time derivative:

$$\int_{Q} p \cdot \frac{\partial \delta u}{\partial t} dQ = \int_{\Omega} (p(T) \cdot \delta u(T) - p(0) \cdot \delta u(0)) d\Omega - \int_{Q} \delta u \cdot \frac{\partial p}{\partial t} dQ$$

$$= \int_{\Omega} p(T) \cdot \delta u(T) d\Omega - \int_{Q} \delta u \cdot \frac{\partial p}{\partial t} dQ,$$
(10)

where we have used that  $\delta u(t=0)=0$ . Then consider the fourth and fifth terms in integral (9), involving  $\Delta \delta u$  and  $\delta \pi$ :

$$-\frac{1}{Re} \int_{Q} p \cdot \Delta \delta u \, dQ + \int_{Q} (p \cdot \nabla) \delta \pi \, dQ$$

$$= -\frac{1}{Re} \int_{0}^{T} \left[ \int_{\Gamma} \frac{\partial \delta u}{\partial n} \cdot p \, d\Gamma - \int_{\Omega} \nabla p : \nabla \delta u \, d\Omega \right] dt$$

$$+ \int_{0}^{T} \left[ \int_{\Gamma} n \cdot p \, \delta \pi \, d\Gamma - \int_{\Omega} \delta \pi (\nabla \cdot p) \, d\Omega \right] dt$$

$$= \int_{0}^{T} p \cdot \left( n \, \delta \pi - \frac{1}{Re} \frac{\partial \delta u}{\partial n} \right) \, d\Gamma dt$$

$$+ \frac{1}{Re} \int_{0}^{T} \left[ \int_{\Gamma} \delta u \cdot \frac{\partial p}{\partial n} d\Gamma - \int_{\Omega} \delta u \cdot \Delta p \, d\Omega \right] dt - \int_{Q} \delta \pi (\nabla \cdot p) \, dQ$$

$$= \frac{1}{Re} \int_{T_{1}^{c}}^{T_{2}^{c}} \left[ \delta \varphi_{L}^{T} \int_{\Gamma_{L}} \psi_{L} \frac{\partial p_{2}}{\partial n} \, d\Gamma + \delta \varphi_{U}^{T} \int_{\Gamma_{U}} \psi_{U} \frac{\partial p_{2}}{\partial n} \, d\Gamma \right] dt$$

$$- \frac{1}{Re} \int_{Q} \delta u \cdot \Delta p \, dQ - \int_{Q} \delta \pi (\nabla \cdot p) \, dQ.$$
(11)

where : denotes a complete contraction; that is,

$$\nabla p : \nabla \delta u = \sum_{i,j=1}^{3} \frac{\partial (e_i \cdot p)}{\partial x_j} \frac{\partial (e_i \cdot \delta u)}{\partial x_j}.$$
 (12)

In the third equality of (11), we use the boundary condition on  $\delta u$  from (7) and on p from (8).

We can simply rewrite the second term in (9):

$$\int_{Q} p \cdot (\delta u \cdot \nabla) u \, dQ = \int_{Q} \delta u \cdot (\nabla u)^{T} p \, dQ.$$
(13)

For the third term in (9), we use Gauss theorem, the boundary condition on p in (8) and the incompressibility condition,

$$\int_{Q} p \cdot (u \cdot \nabla) \delta u \, dQ$$

$$= \iint_{0}^{T} (p \cdot \delta u)(n \cdot u) \, d\Gamma \, dt$$

$$- \int_{Q} (p \cdot \delta u)(\nabla \cdot u) \, dQ - \int_{Q} \delta u \cdot (u \cdot \nabla) p \, dQ$$

$$= - \int_{Q} \delta u \cdot (u \cdot \nabla) p \, dQ,$$
(14)

Then by inserting (10), (11), (13) and (14) into (9) we get:

$$\int_{\Omega} p(T) \, \delta u(T) \, d\Omega$$

$$+ \frac{1}{Re} \int_{T_{1}^{c}}^{T_{2}^{c}} \left[ \delta \varphi_{L}^{T} \int_{\Gamma_{L}} \psi_{L} \frac{\partial p_{2}}{\partial n} \, d\Gamma + \delta \varphi_{U}^{T} \int_{\Gamma_{U}} \psi_{U} \frac{\partial p_{2}}{\partial n} \, d\Gamma \right] dt$$

$$+ \int_{Q} \delta u \cdot \left( -\frac{\partial p}{\partial t} - \frac{1}{Re} \Delta p + (\nabla u)^{T} p - (u \cdot \nabla) p \right) dQ$$

$$- \int_{Q} \delta \pi \left( \nabla \cdot p \right) dQ = 0. \tag{15}$$

If we then require p to satisfy the adjoint equations:

$$\begin{cases}
-\frac{\partial p}{\partial t} - \frac{1}{Re} \Delta p + (\nabla u)^T p - (u \cdot \nabla) p + \nabla \sigma = \begin{cases} u - u_T & \text{in } (T_1^o, T_2^o) \\ 0 & \text{otherwise} \end{cases} & \text{in } Q, \\
\nabla \cdot p = 0 & \text{in } Q, \\
p|_{t=T} = 0,
\end{cases}$$
(16)

with the boundary conditions from (8) and where  $\sigma$  is a scalar field (the "adjoint pressure"). Then (15) becomes

$$\int_{T_1^o}^{T_2^o} \int_{\Omega} \delta u \cdot (u - u_T) \, dQ - \int_{Q} \delta u \cdot \nabla \sigma \, dQ = 0,$$
 (17)

since  $\partial p_2/\partial n$  is zero at the boundaries  $y=\pm 1$ . This follows from the fact that the no-slip condition implies

$$\frac{\partial p_1}{\partial x} = \frac{\partial p_3}{\partial z} = 0$$

on the walls and from the condition requiring p to be divergence-free. Also, note that the initial condition for the adjoint equations (16) is set at t=T and that the equations are integrated backwards in time.

Integrating the second term in the integral (17) by parts yields

$$-\int_{Q} \delta u \cdot \nabla \sigma \, dQ = -\iint_{0}^{T} n \cdot \delta u \, \sigma \, d\Gamma \, dt + \int_{Q} \sigma \, \nabla \cdot \delta u \, dQ$$

$$= -\iint_{0}^{T} n \cdot \delta u \, \sigma \, d\Gamma \, dt,$$
(18)

since  $\nabla \cdot \delta u = 0$ . Inserting the boundary condition on  $\delta u$  from (7) into (18) we get,

$$- \iint_{0}^{T} n \cdot \delta u \, \sigma \, d\Gamma \, dt$$

$$= \int_{T_{1}^{c}}^{T_{2}^{c}} \int_{\Gamma_{L}} \delta \varphi_{L}^{T} \psi_{L} \sigma \, d\Gamma \, dt - \int_{T_{1}^{c}}^{T_{2}^{c}} \int_{\Gamma_{U}} \delta \varphi_{U}^{T} \psi_{U} \sigma \, d\Gamma \, dt.$$

$$(19)$$

If we now insert (18) and (19) into (17) we get,

$$\int_{T_1^c}^{T_2^c} \left[ \delta \varphi_L^T \int_{\Gamma_L} \psi_L \sigma \, d\Gamma - \delta \varphi_U^T \int_{\Gamma_U} \psi_U \sigma \, d\Gamma \right] dt 
+ \int_{T_1^c}^{T_2^c} \int_{\Omega} \delta u \cdot (u - u_T) \, dQ = 0.$$
(20)

Finally we can now insert (20) into (5) using (2) to eliminate  $\delta u$ 

$$\delta J(\varphi) = \left\langle \frac{\partial J}{\partial \varphi_L}, \delta \varphi \right\rangle + \left\langle \frac{\partial J}{\partial \varphi_U}, \delta \varphi \right\rangle$$

$$= \int_{T_1^c}^{T_2^c} \left\{ \delta \varphi_L^T \left[ \int_{\Gamma_L} \psi_L \left( \varepsilon \varphi_L^T \psi_L - \sigma \right) d\Gamma \right] \right\}$$

$$+ \delta \varphi_U^T \left[ \int_{\Gamma_U} \psi_U \left( \varepsilon \varphi_U^T \psi_U + \sigma \right) d\Gamma \right] \right\} dt.$$
(21)

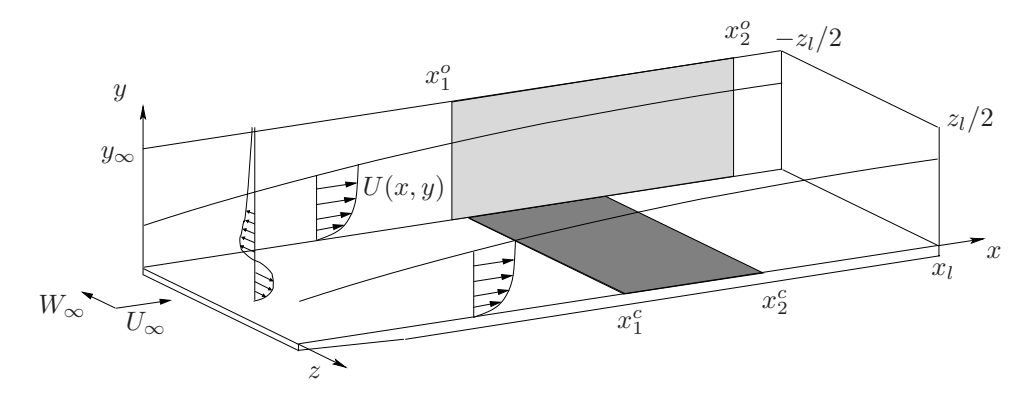


FIGURE 2. The computational domain. In the nonlinear optimization problem the flow is observed in the region  $[x_1^o, x_2^o] \times [0, y_\infty] \times [-z_l/2, z_l/2] \times [T_1^o, T_2^o]$ . For both optimization problems the control region is  $[x_1^c, x_2^c] \times [-z_l/2, z_l/2] \times [T_1^c, T_2^c]$ .

From expression (21) we can identify the gradient of the objective function (3),

$$\frac{\partial J}{\partial \varphi_L} = \int_{\Gamma_L} \psi_L \left( \varepsilon \varphi_L^T \psi_L - \sigma \right) d\Gamma, \tag{22}$$

and

$$\frac{\partial J}{\partial \varphi_U} = \int_{\Gamma_U} \psi_U \left( \varepsilon \varphi_U^T \psi_U + \sigma \right) d\Gamma. \tag{23}$$

The optimization procedure can now be summarized as follows: pick an initial guess of the control, solve the Navier–Stokes equations (1), solve the adjoint equations (16), compute the gradient (22)–23 of the objective function (3), update the control and repeat as long as the optimization problem has not converged.

Note that the adjoint equations are solved backwards in time and that the velocity u appears in the equations. This means that we have to store the temporal history of the velocity data from the solution of the Navier–Stokes equations. Numerical issues related to this are discussed in section 4.1.

# 2.1.3. Extension to boundary layer

Only minor changes are needed to rephrase the channel flow problem to the boundary layer flow depicted in Figure 2. A complete derivation of the boundary layer counterpart of the channel flow optimization problem can be found in Appendix A. In this section only the key differences will be pointed out and commented.

The growing boundary layer is modeled by

$$\begin{cases}
\frac{\partial u}{\partial t} + (u \cdot \nabla)u - \frac{1}{Re}\Delta u + \nabla \pi = \lambda(x)(U - u) & \text{in } Q, \\
\nabla \cdot u = 0 & \text{in } Q, \\
u|_{t=0} = u_0,
\end{cases} (24)$$

with periodic boundary conditions in the horizontal directions, that is, the xand z-directions,

$$u|_{x=-x_{l}/2} = u|_{x=x_{l}/2},$$

$$u|_{z=-z_{l}/2} = u|_{z=z_{l}/2}.$$
(25)

The term  $\lambda(x)(U-u)$  is a forcing term used to make the flow situation sketched in Figure 2 periodic, enabling the use of Fourier discretization in simulations of the physical flow. This is known as a fringe region technique and is described further in Lundbladh et al. (1999) and analyzed by Nordström et al. (1999). Left to be specified are the conditions on the wall and in the free-stream. On the wall the boundary condition for the horizontal velocities is a no-slip condition and the wall normal velocity  $v_c$  is given by the control. The free-stream boundary condition should be applied at  $y=y_{\rm fst}$  where the flow is not influenced by the existence of the boundary layer, but the simulation box has to be of reasonable height. An artificial boundary condition modeling the existence of the free-stream is thus used to allow truncation of this large domain. Here a Neumann condition is used at the artificial free-stream boundary. This choice requires that the simulation box is high enough for the perturbations in the boundary layer not to influence the flow at the upper boundary.

$$u|_{y=y_{\rm fst}} = U_{\infty}$$
 (which is approximated by  $\frac{\partial u}{\partial n}\Big|_{\Gamma_u} = 0$ ),  
 $u|_{\Gamma_c} = nv_c$ , (26)  
 $u|_{\Gamma_l \setminus \Gamma_c} = 0$ ,

where  $\Gamma_u$  and  $\Gamma_l$  represent the upper and lower part of the boundary respectively. The part of the boundary where control is applied is denoted  $\Gamma_c$ .

As for the channel flow case we expand the control  $v_c$  in basis functions  $\psi_{l,m}$  with zero mass flux, where  $\varphi_{l,m}$  are time dependent coefficients for the basis functions,

$$v_c(x, z, t) = \begin{cases} \varphi_l^T \psi_l = \sum_{m=1}^M \varphi_{l,m}(t) \psi_{l,m}(x, z) & \text{in } (T_1^c, T_2^c), \\ 0 & \text{otherwise.} \end{cases}$$
(27)

Where we have introduced the control vector  $\varphi_l$  defined as:

$$\varphi_l = (\varphi_{l,1}, \dots, \varphi_{l,M}).$$

Comparing with the corresponding equation for channel flow, equation (1) and the associated boundary conditions, there are two differences. The boundary

condition at the upper wall is now replaced by a free-stream velocity condition. Also the aforementioned fringe forcing term which is needed only for spatial simulations is added to the right hand side. The scalar function  $\lambda = \lambda(x)$  is nonzero only in the fringe region and is defined as follows:

$$\lambda(x) = \lambda_{\text{max}} \left[ S\left(\frac{x - x_{\text{start}}}{\Delta_{\text{rise}}}\right) - S\left(\frac{x - x_{\text{end}}}{\Delta_{\text{fall}}} + 1\right) \right]$$

where  $\lambda_{\text{max}}$ ,  $x_{\text{start}}$ ,  $x_{\text{end}}$ ,  $\Delta_{\text{rise}}$  and  $\Delta_{\text{fall}}$  are parameters used to specify the strength, extent and shape of the fringe forcing. The S-function is defined as

$$S(r) = \begin{cases} 0 & r \le 0, \\ \frac{1}{1 + \exp(1/(1-r) + 1/r)} & 0 < r < 1, \\ 1 & r \ge 1. \end{cases}$$

Another difference from the channel flow problem formulation appears in the second term of the objective function J, equation (3), where the observation of state can now be limited in space as well as in time which yields,

$$J(\varphi_l) = \frac{\varepsilon}{2} \int_{T_1^c}^{T_2^c} \int_{\Gamma_c} |v_c|^2 d\Gamma dt + \frac{1}{2} \int_{T_1^o}^{T_2^o} \int_{\Omega_o} |u - u_T|^2 dQ,$$
 (28)

where  $(T_1^c, T_2^c)$  is the control time period and  $(T_1^o, T_2^o)$  is the observation time period and  $\Omega_o$  is the part of the spatial domain  $\Omega$  where the state of the flow is observed. This is only used for spatial simulations.

As for the channel flow derivation, we get to the stage where the adjoint equations with the variables p and  $\sigma$  are introduced:

$$\begin{cases}
-\frac{\partial p}{\partial t} + (\nabla u)^T p - (u \cdot \nabla)p \\
-\frac{1}{Re} \Delta p + \lambda(x)p + \nabla \sigma = \begin{cases} u - u_T & \text{in } (T_1^o, T_2^o) \times \Omega_o \\ 0 & \text{otherwise} \end{cases} & \text{in } Q, \quad (29) \\
\nabla \cdot p = 0 & \text{in } Q, \\
p|_{t=T} = 0.
\end{cases}$$

along with the boundary conditions:

$$\begin{aligned} p|_{x=-x_{l}/2} &= p|_{x=x_{l}/2}, \\ p|_{z=-z_{l}/2} &= p|_{z=z_{l}/2}, \\ p|_{\Gamma_{l}} &= 0, \\ p|_{y=y_{\mathrm{fst}}} &= 0, \quad \bigg( \text{which is approximated by} \quad \frac{\partial p}{\partial n}\Big|_{\Gamma_{u}} = 0 \bigg). \end{aligned} \tag{30}$$

As with the free-stream boundary condition in (26) we have introduced an artificial boundary, to truncate the adjoint domain, where the adjoint "free-stream" is modeled.

Due to the fringe forcing, the additional term  $\lambda(x)p$  has to be included in the adjoint equations. The forcing  $u-u_T$  is now confined to the spatial domain  $\Omega_o$  due to the variable spatial extent of the observation. These adjustments lead to following the expression for the gradient:

$$\frac{\partial J}{\partial \varphi_l} = \int_{\Gamma_c} \psi_l \left( \varepsilon \varphi_l^T \psi_l - \sigma \right) d\Gamma. \tag{31}$$

### 2.2. Nonlinear initial condition control

#### 2.2.1. Governing equations

Here we consider the optimization problem where we want to find the initial condition that, at a specific time, maximizes the disturbance energy growth between t=0 and t=T. The optimization problem is stated for channel flow.

Our computational domain is defined as

$$\Omega = (-x_L/2, x_L/2) \times (-1, 1) \times (-z_L/2, z_L/2),$$

in x, y, z, and we define

$$\Gamma_L = \Omega(y = -1), \quad \Gamma_U = \Omega(y = 1), \quad \text{and} \quad Q = \Omega \times (0, T).$$

The non-dimensional, incompressible Navier–Stokes equations with Reynolds number, Re, based on the centerline velocity and half the channel height are,

$$\begin{cases}
\frac{\partial u}{\partial t} + (u \cdot \nabla)u - \frac{1}{Re}\Delta u + \nabla \pi = -\nabla P & \text{in } Q, \\
\nabla \cdot u = 0 & \text{in } Q, \\
u|_{t=0} = \varphi + u_T(0),
\end{cases}$$
(32)

where  $u=(u_1,v,w)$  is the velocity vector,  $\pi$  is the pressure and  $\nabla P$  represents the pressure gradient driving the flow and can either be constant or used to ensure constant mass flux. The control  $\varphi$  is entering the equations through the initial condition as a disturbance on top of a laminar flow. Periodic boundary conditions in the x- and z-directions, together with a no-slip condition for the directions parallel to the wall give the complete set of boundary conditions,

$$u|_{x=-x_L/2} = u|_{x=x_L/2},$$

$$u|_{z=-z_L/2} = u|_{z=z_L/2},$$

$$u|_{y=-1} = 0,$$

$$u|_{y=1} = 0.$$
(33)

To completely specify the optimal control problem we also need an objective function. If we choose to maximize the disturbance energy growth the objective

function is

$$J(\varphi) = -\frac{\int_{\Omega} |u(T) - u_T(T)|^2 d\Omega}{\int_{\Omega} |\varphi|^2 d\Omega}.$$
 (34)

Time T denotes the final simulation time. The target velocity profile is denoted  $u_T$  and represents the laminar flow field. The optimization problem is then: find  $\varphi^*$  which satisfies

$$J(\varphi^*) \le J(\varphi) \quad \forall \ \varphi \in \mathcal{U}_{ad}$$

where  $\mathcal{U}_{ad}$  has been used to denote the set of admissible controls (initial conditions) which is a subset of  $L^2(\mathbb{R}^{3\cdot N_x\cdot N_y\cdot N_z})$ .

#### 2.2.2. Derivation of objective function gradient.

The gradient of the objective function,  $\nabla J$ , is defined by

$$\delta J(\varphi) = \lim_{s \to 0} \frac{J(\varphi + s \,\delta\varphi) - J(\varphi)}{s} = \langle \nabla J, \delta\varphi \rangle = \left\langle \frac{\partial J}{\partial \varphi}, \delta\varphi \right\rangle, \tag{35}$$

where  $\delta \varphi$  is the first variation of the control. The functional  $\delta J$  is the first variation of J with respect to  $\delta \varphi$ . To find an expression for  $\nabla J$  we start by differentiating the objective function (34) to get,

$$\delta J(\varphi) = \int_{\Omega} |u(T) - u_T(T)|^2 d\Omega \int_{\Omega} \delta \varphi \cdot \varphi d\Omega / \left[ \int_{\Omega} |\varphi|^2 d\Omega \right]^2$$

$$- \int_{\Omega} \delta u(T) \cdot (u(T) - u_T(T)) d\Omega \int_{\Omega} |\varphi|^2 d\Omega / \left[ \int_{\Omega} |\varphi|^2 d\Omega \right]^2$$
(36)

where  $\delta u$  is the first variation of u with respect to  $\delta \varphi$ . To find an expression for the relation between  $\delta u$  and  $\delta \varphi$  we differentiate the state equation (32),

$$\begin{cases} \frac{\partial \delta u}{\partial t} + (\delta u \cdot \nabla)u + (u \cdot \nabla)\delta u - \frac{1}{Re}\Delta \delta u + \nabla \delta \pi = 0 & \text{in } Q, \\ \nabla \cdot \delta u = 0 & \text{in } Q, \\ \delta u|_{t=0} = \delta \varphi, \end{cases}$$
(37)

and boundary conditions (33),

$$\delta u|_{x=-x_{L}/2} = \delta u|_{x=x_{L}/2}, 
\delta u|_{z=-z_{L}/2} = \delta u|_{z=z_{L}/2}, 
\delta u|_{y=-1} = 0, 
\delta u|_{y=1} = 0.$$
(38)

Now we introduce a vector function p = p(x, y, z, t) such that  $e_i \cdot p = p_i$  and require p to satisfy the boundary conditions:

$$p|_{x=-x_L/2} = p|_{x=x_L/2},$$

$$p|_{z=-z_L/2} = p|_{z=z_L/2},$$

$$p|_{y=-1} = p|_{y=1} = 0.$$
(39)

The boundary conditions may be chosen during the derivation but in order to simplify the presentation they are introduced already at this point. Taking the dot product between p and equation (37) and integrating over Q yields

$$\int_{Q} p \cdot \left( \underbrace{\frac{\partial \delta u}{\partial t}}_{1} + \underbrace{(\delta u \cdot \nabla)u}_{2} + \underbrace{(u \cdot \nabla)\delta u}_{3} - \underbrace{\frac{1}{Re} \Delta \delta u}_{4} + \underbrace{\nabla \delta \pi}_{5} \right) dQ = 0.$$
 (40)

Then, step by step, we apply integration by parts to move derivatives from  $\delta u$  to p. We start with the first term in the integral (40), containing the time derivative:

$$\int_{Q} p \cdot \frac{\partial \delta u}{\partial t} dQ = \int_{\Omega} (p(T) \cdot \delta u(T) - p(0) \cdot \delta u(0)) d\Omega - \int_{Q} \delta u \cdot \frac{\partial p}{\partial t} dQ$$

$$= \int_{\Omega} (p(T) \cdot \delta u(T) - p(0) \cdot \delta \varphi) d\Omega - \int_{Q} \delta u \cdot \frac{\partial p}{\partial t} dQ$$
(41)

where we have used that  $\delta u(t=0) = \delta \varphi$ . Then consider the fourth and fifth terms in integral (40), involving  $\Delta \delta u$  and  $\delta \pi$ 

$$-\frac{1}{Re} \int_{Q} p \cdot \Delta \delta u \, dQ + \int_{Q} (p \cdot \nabla) \delta \pi \, dQ$$

$$= -\frac{1}{Re} \int_{0}^{T} \left[ \int_{\Gamma} \frac{\partial \delta u}{\partial n} \cdot p \, d\Gamma - \int_{\Omega} \nabla p : \nabla \delta u \, d\Omega \right] dt$$

$$+ \int_{0}^{T} \left[ \int_{\Gamma} n \cdot p \, \delta \pi \, d\Gamma - \int_{\Omega} \delta \pi (\nabla \cdot p) \, d\Omega \right] dt$$

$$= \int_{0}^{T} \int_{\Gamma} p \cdot \left( n \, \delta \pi - \frac{1}{Re} \frac{\partial \delta u}{\partial n} \right) \, d\Gamma dt$$

$$+ \frac{1}{Re} \int_{0}^{T} \left[ \int_{\Gamma} \delta u \cdot \frac{\partial p}{\partial n} d\Gamma - \int_{\Omega} \delta u \cdot \Delta p \, d\Omega \right] dt - \int_{Q} \delta \pi (\nabla \cdot p) \, dQ$$

$$= -\frac{1}{Re} \int_{Q} \delta u \cdot \Delta p \, dQ - \int_{Q} \delta \pi (\nabla \cdot p) \, dQ.$$
(42)

where: denotes a complete contraction; that is,

$$\nabla p: \nabla \delta u = \sum_{i,j=1}^{3} \frac{\partial (e_i \cdot p)}{\partial x_j} \frac{\partial (e_i \cdot \delta u)}{\partial x_j}.$$
 (43)

In the third equality of (42), we use the boundary condition on  $\delta u$  from (38) and on p from (39).

We can simply rewrite the second term in (40)

$$\int_{Q} p \cdot (\delta u \cdot \nabla) u \, dQ = \int_{Q} \delta u \cdot (\nabla u)^{T} p \, dQ.$$
(44)

For the third term in (40), we use Gauss theorem, the boundary condition on p in (39) and the incompressibility condition,

$$\int_{Q} p \cdot (u \cdot \nabla) \delta u \, dQ$$

$$= \int_{0}^{T} \int_{\Gamma} (p \cdot \delta u) (n \cdot u) \, d\Gamma \, dt$$

$$- \int_{Q} (p \cdot \delta u) (\nabla \cdot u) \, dQ - \int_{Q} \delta u \cdot (u \cdot \nabla) p \, dQ$$

$$= -\int_{Q} \delta u \cdot (u \cdot \nabla) p \, dQ.$$
(45)

Then by inserting (41), (42), (44) and (45) into (40) we get

$$\int_{\Omega} p(T) \, \delta u(T) \, d\Omega - \int_{\Omega} p(0) \, \delta \varphi \, d\Omega$$

$$+ \int_{Q} \delta u \cdot \left( -\frac{\partial p}{\partial t} - \frac{1}{Re} \Delta p + (\nabla u)^{T} p - (u \cdot \nabla) p \right) dQ$$

$$- \int_{Q} \delta \pi \, (\nabla \cdot p) \, dQ = 0.$$
(46)

If we then require p to satisfy the adjoint equations

$$\begin{cases}
-\frac{\partial p}{\partial t} - \frac{1}{Re} \Delta p + (\nabla u)^T p - (u \cdot \nabla) p + \nabla \sigma = 0 & \text{in } Q, \\
\nabla \cdot p = 0 & \text{in } Q, \\
p|_{t=T} = u(T) - u_T(T),
\end{cases} (47)$$

with the boundary conditions from (39) and where  $\sigma$  is a scalar field (the "adjoint pressure"). Then (46) becomes

$$\int_{\Omega} (u(T) - u_T(T)) \cdot \delta u(T) \, d\Omega + \int_{\Omega} \delta u \cdot \nabla \sigma \, dQ - \int_{\Omega} p(0) \cdot \delta \varphi \, d\Omega = 0.$$
 (48)

Also, note that the initial condition for the adjoint equations (47) is set at t=T and that the equations are integrated backwards in time.

Integrating the second term in the integral (48) by parts yields

$$-\int_{Q} \delta u \cdot \nabla \sigma \, dQ = -\iint_{0}^{T} n \cdot \delta u \, \sigma \, d\Gamma \, dt + \int_{Q} \sigma \, \nabla \cdot \delta u \, dQ$$

$$= -\iint_{0}^{T} n \cdot \delta u \, \sigma \, d\Gamma \, dt = 0,$$
(49)

since  $\nabla \cdot \delta u = 0$  and due to the boundary condition on  $\delta u$ .

If we now insert (49) into (48) we get,

$$\int_{\Omega} (u(T) - u_T(T)) \cdot \delta u(T) \, d\Omega - \int_{\Omega} p(0) \cdot \delta \varphi \, d\Omega = 0.$$
 (50)

Finally, we can now insert (50) into (36) to eliminate  $\delta u$ 

$$\delta J(\varphi) = \left\langle \frac{\partial J}{\partial \varphi}, \delta \varphi \right\rangle = \frac{1}{c} \int_{\Omega} \left[ a \varphi - b p(0) \right] \cdot \delta \varphi \, d\Omega. \tag{51}$$

From expression (51) we can identify the gradient of the objective function (34),

$$\frac{\partial J}{\partial \varphi} = \frac{1}{c} \left[ a \, \varphi - b \, p(0) \right]. \tag{52}$$

The first term of the gradient is due to the normalization of the objective function. Note that when we have reached optimum and the gradient is zero the initial condition is equal to the adjoint field times a scaling factor. Thus the optimality condition reads

$$\frac{\varphi}{E'(0)} = \frac{p(0)}{E'(T)},\tag{53}$$

where E' denotes the disturbance energy.

#### 2.3. Feedback blowing and suction control

Also a linear optimization problem is solved in order to be able to make comparisons with the nonlinear control problem. By applying control theory using the Navier–Stokes equations linearized around some mean flow, we can directly compute an on-line feedback law. In recent studies, such linear feedback controllers have shown to be effective for both channel and boundary layer flows.

A brief introduction to the linear control theory applied to flow control problems can be found in Chevalier *et al.* (2002). More thorough descriptions can be found in, for example, Högberg & Henningson (2002).

The control problem is solved for an array of wave number pairs, corresponding to a sufficient resolution for the flow of interest, and the resulting controllers are combined into a physical space controller through an inverse Fourier transform. The feedback law is then represented as a convolution of this physical space control law and the velocity field.

The limitations of this approach are mainly that nonlinear as well as non-parallel effects are neglected. The optimization is performed over an infinite time horizon, and thus no guarantees can be made regarding instantaneous behavior and initial transients.

### 3. Adapting to the simulation codes

#### 3.1. Reformulation of the adjoint equations

To be able to use existing spectral channel flow and boundary layer flow codes by Lundbladh et al. (1992) and Lundbladh et al. (1999) respectively, we need to reformulate the adjoint equations into a similar form to the one used there. The simulation code for the boundary layer problem is based on the channel flow code and the solution procedure is identical. The Navier–Stokes equations are implemented in a  $v-\omega$  formulation, where linear and nonlinear terms are treated separately. We can write the adjoint equations (16), (29) or (47) as,

$$\begin{cases}
-\frac{\partial p}{\partial t} - \frac{1}{Re}\Delta p - H + \nabla(u \cdot p) + \nabla\sigma = 0, \\
\nabla \cdot p = 0, \\
p|_{t=T} = 0,
\end{cases} (54)$$

with the boundary conditions (8), (30) or (39), and where H in the following denotes either  $H_{ch}$  or  $H_{bl}$  corresponding to the forcing terms in the channel and boundary layer cases respectively. In order to avoid derivatives of u in the adjoint equations, terms involving such derivatives are reformulated. Using the identity

$$u \times (\nabla \times p) - 2(\nabla p)^T u + \nabla (u \cdot p) = (\nabla u)^T p - (u \cdot \nabla) p$$

the forcing in the channel flow case is given by

$$H_{ch} = -u \times (\nabla \times p) + 2(\nabla p)^T u + \begin{cases} u - u_T & \text{in } (T_1^o, T_2^o), \\ 0 & \text{otherwise,} \end{cases}$$

for blowing and suction control and

$$H_{\rm ch} = -u \times (\nabla \times p) + 2(\nabla p)^T u,$$

for initial condition control. In the boundary layer case, again for blowing and suction control, we use

$$H_{bl} = -u \times (\nabla \times p) + 2(\nabla p)^T u - \lambda(x) p + \begin{cases} u - u_T & \text{in } (T_1^o, T_2^o) \times \Omega_o, \\ 0 & \text{otherwise,} \end{cases}$$

but apart from this, the procedure is the same in all cases. If we take the divergence of equation (54) we get a Poisson equation for the adjoint pressure:

$$\Delta \sigma = \nabla \cdot H - \Delta(u \cdot p). \tag{55}$$

We can then apply the Laplace operator to equation (54), take the second component, and combine with (55) to get:

$$-\frac{\partial \Delta p_2}{\partial t} - \frac{1}{Re} \Delta^2 p_2 - \left(\frac{\partial^2}{\partial x^2} + \frac{\partial^2}{\partial z^2}\right) H_2 + \frac{\partial}{\partial y} \left(\frac{\partial H_1}{\partial x} + \frac{\partial H_3}{\partial z}\right) = 0.$$
 (56)

Then we take the second component of the equation obtained by taking the curl of equation (54) and again making use of (55) to get,

$$-\frac{\partial(\nabla \times p)_2}{\partial t} - \frac{1}{Re}\Delta(\nabla \times p)_2 - \left(\frac{\partial H_1}{\partial z} - \frac{\partial H_3}{\partial x}\right) = 0.$$
 (57)

We can write equation (56) as a system of two second order equations:

$$\begin{cases}
-\frac{\partial \phi}{\partial t} = h_{p_2} + \frac{1}{Re} \Delta \phi, \\
\Delta p_2 = \phi, \\
p_2(y = \pm 1) = \frac{\partial p_2}{\partial y} (y = \pm 1) = 0,
\end{cases} (58)$$

where

$$h_{p_2} = \left(\frac{\partial^2}{\partial x^2} + \frac{\partial^2}{\partial z^2}\right) H_2 - \frac{\partial}{\partial y} \left(\frac{\partial H_1}{\partial x} + \frac{\partial H_3}{\partial z}\right). \tag{59}$$

Written on the same form equation (57) reads:

$$\begin{cases}
-\frac{\partial(\nabla \times p)_2}{\partial t} = h_{(\nabla \times p)_2} + \frac{1}{Re} \Delta(\nabla \times p)_2, \\
(\nabla \times p)_2(y = \pm 1) = 0,
\end{cases} (60)$$

where

$$h_{(\nabla \times p)_2} = \left(\frac{\partial H_1}{\partial z} - \frac{\partial H_3}{\partial x}\right). \tag{61}$$

Equations (58), (59), (60) and (61) are identical to those solved by the spectral channel flow and boundary layer codes with slight changes to H and a negative time derivative. Since the adjoint equations are solved backwards in time, we can in practice use the same solver.

# $3.2. \ \textit{Gradient evaluation} - \textit{blowing and suction control}$

In the gradient of the objective function for blowing and suction control we need the adjoint pressure at the wall. This is not available directly since we have eliminated the adjoint pressure term from the equations, and thus the pressure is not computed explicitly. If we evaluate equation (16) or (29) at the walls, we get

$$\sigma_{x} \Big|_{W} = \frac{1}{Re} \frac{\partial^{2} p_{1}}{\partial y^{2}} \Big|_{W} + v \frac{\partial p_{1}}{\partial y} \Big|_{W},$$

$$\sigma_{z} \Big|_{W} = \frac{1}{Re} \frac{\partial^{2} p_{3}}{\partial y^{2}} \Big|_{W} + v \frac{\partial p_{3}}{\partial y} \Big|_{W},$$
(62)

where W denotes the value at the wall and v is the wall normal velocity at the wall, or rather the control input. Note that in the channel flow case there are

two walls and in the boundary layer flow there is only one. Since the constant part of the adjoint pressure disappears in the integral over the basis functions  $\psi$  in (22) and (23) we can compute the objective function gradient by integration of these adjoint pressure gradients at the wall.

### 4. Implementation issues

#### 4.1. Simulation codes

The implementation of the adjoint solver is based on existing direct numerical simulation codes for channel and boundary layer flows. These codes have been extensively used and are thoroughly verified. The channel flow code is described in Lundbladh  $et\ al.\ (1992)$  and the boundary layer code in Lundbladh  $et\ al.\ (1999)$ . The time marching is performed with a third order Runge–Kutta method for advective terms and a Crank–Nicolson scheme for the viscous terms. A spectral method described in Canuto  $et\ al.\ (1988)$  is used with a Fourier discretization in  $et\ al.\ (1988)$  and a Chebyshev method in  $et\ al.\ (1988)$  is described in Lundbladh  $et\ al.\ (1992)$ . The adjoint equations are solved in exactly the same way, with the formulation of the equations described in section 3.1. For the boundary layer case the code described in Lundbladh  $et\ al.\ (1999)$  is used and since it is based on the channel flow code the implementation is similar.

The solution of the adjoint equations require knowledge about the full state in space and time from the solution of the Navier–Stokes system. This is achieved by saving a large number of velocity fields equidistant in time and interpolating linearly in time when the adjoint equations are solved. This introduces an error, but if the time step between saved field is small enough, we expect a sufficiently accurate approximation. The number of saved velocity fields can become large especially if the time domain is long. An efficient way of reducing the memory requirement is to use a checkpointing technique, see for example Berggren (1998). This decreases the memory requirement at the cost of increased computational time. For the simple test cases presented in this paper check-pointing has not been necessary, but for larger cases, especially simulations requiring high spatial resolution, it will be needed.

#### 4.2. Optimization routine

Optimization is performed with a limited memory quasi-Newton method. The algorithm, L-BFGS-B (Byrd et al. (1994)), is available on the Internet (the web-link is given in the reference list next to Byrd et al. (1994)) and was downloaded and compiled without modifications. It is an algorithm well suited for large non-linear optimization problems, with or without bounds on the control variables. The BFGS method uses an approximation of the Hessian matrix of the objective function, instead of the full matrix. The algorithm has been shown to work well for many different types of optimization problems. The flow of the optimization process is described in Figure 3. The limited memory BFGS algorithm differs from the standard BFGS algorithm in that it

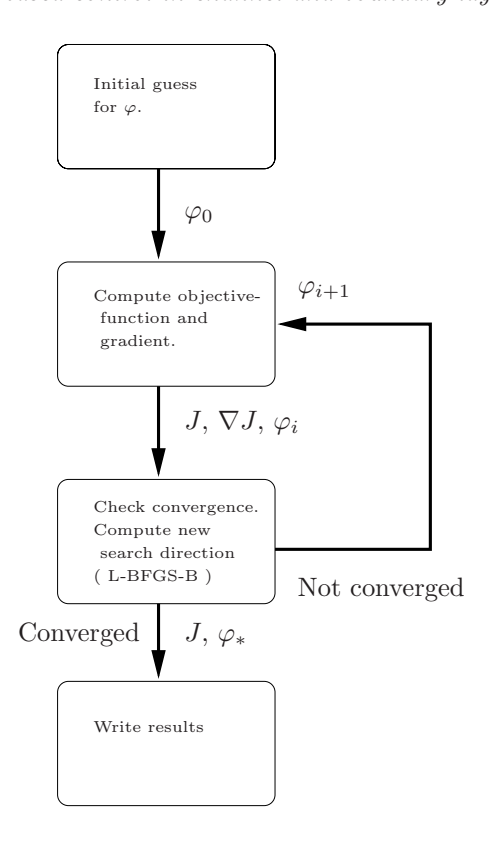


FIGURE 3. The flow in the optimization with L-BFGS-B.

never stores the Hessian matrix. Instead only a certain number of gradient and control updates from earlier optimization iterations are stored. These are then used to build an approximation of the Hessian matrix. Consult Byrd et al. (1994) for details. The inputs to the optimization routine are the control, the gradient of the control and the value of the objective function. A new control is then obtained as output and applied in the next iteration until the convergence criterion has been met. There are a few different convergence criteria that can be used simultaneously or separately such as the norm of the gradient and the relative reduction of the objective function between iterations.

#### 4.3. Implementation of blowing and suction control

The control is implemented as the Fourier coefficients of the v velocity at the wall(s). The control function is discretized in time with a fixed time step that can be used to change the time resolution of the control and there is one set of coefficients for each control time. Linear interpolation is used for the control in times between the discrete control times. The control always starts and ends with zero velocity, and has zero mass flux. The time step in the solution of

both the forward and adjoint equations is adjusted to be small enough to at least resolve the control in time, even if the time step allowed for numerical stability is larger.

When simulating a spatial boundary layer the control is applied only on  $\Gamma_c$  which extends over the interval  $(x_1^c, x_2^c)$  in the chordwise direction. In the code a filtering is added to handle this, and to ensure that the zero mass flux condition on the control is enforced,

$$\int_{\Gamma_l} v_c \, \mathrm{d}\Gamma = 0. \tag{63}$$

The control is then modified to have zero velocity outside  $\Gamma_c$ ,

$$\int_{\Gamma_l} \tilde{\varphi}_l^T \psi_l \, d\Gamma = \int_{\Gamma_l} (\varphi_l^T \psi_l + c) \chi(x_1^c, x_2^c) \, d\Gamma = 0$$
 (64)

which yields,

$$c = -\frac{\int_{\Gamma_l} \varphi_l^T \psi_l \chi(x_1^c, x_2^c) d\Gamma}{\int_{\Gamma_l} \chi(x_1^c, x_2^c) d\Gamma},$$
(65)

and where  $\chi(r_1, r_2) = \chi[r_1, r_2](r)$  is defined as:

$$\chi[r_1, r_2](r) = \begin{cases} 1 & \text{if } r \in (r_1, r_2), \\ 0 & \text{otherwise.} \end{cases}$$
 (66)

The procedure for modifying the control can be summarized as follows:

$$\hat{\varphi}_l \xrightarrow{\text{inverse FFT}} \varphi_l \xrightarrow{\text{Filtering and mass flux correction}} \tilde{\varphi}_l \xrightarrow{\text{FFT}} \hat{\tilde{\varphi}}_l$$

assuming that we denote the original Fourier space control with  $\hat{\varphi}_l$  and the final control in Fourier space with  $\hat{\varphi}_l$ . This final control constitutes the boundary condition in the simulation when the spatial extent of the control is limited.

### 4.4. Objective function gradient of blowing and suction control

The gradient of the objective function is evaluated from the adjoint pressure on the walls as described in section 3.2. When the adjoint equations are solved, the adjoint pressure on the walls must also be computed simultaneously in the control interval. Since the  $p_1$  and  $p_3$  velocities are available at each time step we can compute the pressure gradients  $\sigma_x$  and  $\sigma_z$  using (62). The corresponding pressure is then computed by integrating these gradients with the constant part of the adjoint pressure set to zero, since it does not enter the gradient computation. The adjoint pressure is then projected onto the basis functions of the control using (22), (23) or (31). In the spatial boundary layer case the gradient (31) is computed in Fourier space, but we should only integrate over  $\Gamma_c$ . The gradient is transformed to physical space and there a step function

which cuts out the region  $\Gamma_c$  is applied. This filtering procedure is similar to that for the control. The resulting gradient is then transformed back to Fourier space.

#### 5. Verification

#### 5.1. Gradient accuracy

To verify that the implementation is correct as well as that the problem has been formulated correctly, one can check the accuracy of the gradient of the objective function. By perturbing one degree of freedom of the control and computing the resulting change in the objective function the gradient with respect to that degree of freedom can be approximated. Performing this procedure for all degrees of freedom gives the complete objective function gradient. The gradient so computed can then be used to verify that the gradient obtained from the adjoint equation approach is correct. This has been done at different stages of the optimization process for a number of different cases, varying the flow perturbation as well as the initial guess for the control. The accuracy of the gradient direction for blowing and suction control is quantified by normalizing the two gradients and computing the norm of the difference between them. This difference is less than 1% for all channel and boundary layer flow cases tested when the optimization routine is in the initial iterations. When the gradient accuracy is computed for solutions close to the optimal solution, the accuracy is degraded and the error can be as large as 10% - 20%. This degraded accuracy slows down the convergence of the optimization routine and makes it difficult to reach the true optimal solution.

#### 5.2. Control of oblique transition in channel flow

As a first test case, we study the oblique transition scenario. Oblique waves are introduced in the flow, where they grow and induce streamwise vortices. The vortices then produce streamwise streaks that grow until they finally break down and transition occurs. The threshold energies for this type of bypass transition are studied in Reddy et al. (1998). The initial stage of this scenario is the growth of oblique waves. If the amplitude is low, this is all that happens before the flow returns to the laminar state. With a higher amplitude, the oblique waves induce enough streamwise vorticity to generate streaks. The streaks grow to a much higher amplitude than the oblique waves. If the initial disturbance is large enough, we get transition to turbulence.

Testing the optimal control on this scenario is done at three different stages and with different time resolution. First control is applied at the very beginning where only the oblique waves are present, secondly the control is applied in the beginning of the streak growth, where both streaks and oblique waves are present. The last case application of the control to the growing streaks. The results in this section were previously reported in Högberg et al. (2000).

Five different simulations are performed using the same initial condition. The objective is to minimize the integral of the deviation from the laminar

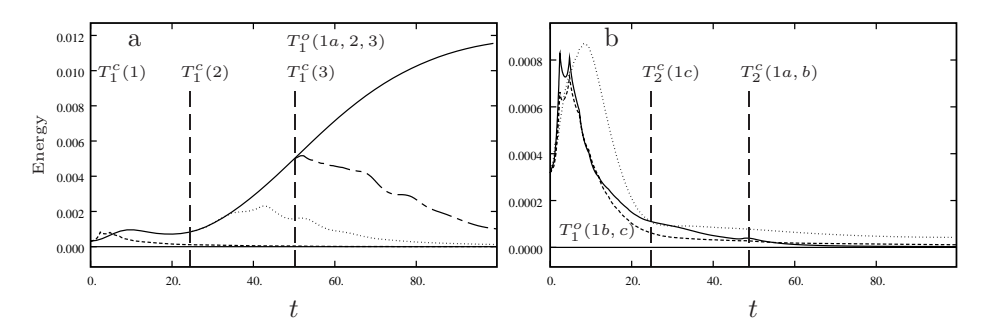


FIGURE 4. [a] Solid: the energy growth without control; dashed: case 1a; dotted: case 2; dash-dot: case 3. [b] solid: case 1a; dashed: case 1b; dotted: case 1c.

flow profile from time  $T_1^o$  to  $T_2^o = 100$ . The Reynolds number is 1500 and the box size is  $2\pi \times 2 \times 2\pi$  in x,y,z. In case 1a,b,c the control is applied from time  $T_1^c = 0$  until  $T_2^c = 50$  in a,b and  $T_2^c = 25$  in c. The objective function is measured from  $T_1^o = 50$  in case 1a and from  $T_1^o = 0$  in cases 1b and 1c. For cases 2 and 3 the control is applied from  $T_1^c = 25$  and  $T_1^c = 50$  respectively, and the objective function from  $T_1^o = 50$ . The resulting control velocity in all cases is of the order 2% of the centerline velocity. The reduction of the gradient norm is about three orders of magnitude after 10-15 optimization iterations.

The energy evolution of the controlled flows is shown in Figure 4a. The growth of the oblique waves is efficiently hindered by the control formulation in 1a,b,c and the growth of streaks is eliminated also in cases 2 and 3. In case 2 the control is applied during the formation of the streaks. Initially the energy is allowed to grow but then the growth is hindered by the control and energy decays as. In case 3 the streaks have formed and are growing when control is applied.

In Figure 4b the differences between the controlled flows in cases 1a,b and c are shown. In case 1a the energy is not penalized by the objective function initially as it is in 1b, and this results in lower energy after t=50 than in case 1b. A higher temporal resolution of the control is applied during a shorter time in case 1c. The result is a smoother energy curve but not as low energy at a later time as in the other two cases.

#### 5.3. Control in a parallel boundary layer flow

In order to evaluate this type of control strategy for a parallel boundary layer flow we consider an inviscid instability. Inviscid instabilities can exist only if the velocity profile has an inflection point. In a boundary layer flow with a three-dimensional velocity profile, there is always a direction in which such an inflection point exists. In this direction an unstable eigenvalue to the linearized problem was found. The corresponding eigenmode is added to an undisturbed

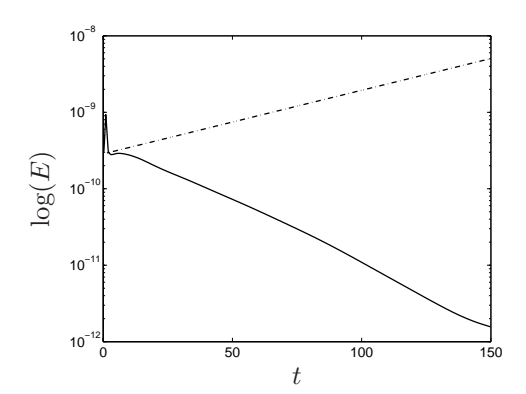


FIGURE 5. Solid: the disturbance energy growth with optimal control; dash-dot: the disturbance energy growth for temporal FSC flow without control.

base flow, and the sum is then used as the initial velocity field for the simulations. The base flow is chosen as a Falkner–Skan–Cooke (FSC) flow with the same parameters as are used in the investigation by Högberg & Henningson (2002) where the Reynolds number is  $Re_{\delta_0^*} = 337.9$ . The spatial variation of the chordwise mean flow is given through,

$$U_{\infty} = \left(\frac{x}{x_0} + 1\right)^m,$$

where  $x_0 = 354.0$ . Furthermore, the cross-flow velocity was  $W_{\infty} = 1.44232$  and m = 0.34207. The box dimensions for our simulations are  $25.14 \times 20 \times 25.14$  measured in  $\delta^*$  with a resolution of  $4 \times 129 \times 4$  in  $x \times y \times z$  respectively. The resolution in the y-direction is chosen fairly large to ensure high accuracy for the y-derivatives needed in the adjoint computation.

For the temporal simulation we use the Falkner–Skan–Cooke flow at x=0. The eigenvalue of the mode used in the simulation is  $\omega=(-0.15246+i0.0382)$ , for the parameter choice  $\alpha=0.25,\ \beta=-0.25$ . The control is applied from  $T_1^c=0$  to  $T_2^c=150$  and over the entire boundary  $(\Gamma_c=\Gamma_l)$ . The objective function is measured from  $T_1^o=0$  to  $T_2^o=150$  and over the whole spatial domain  $(\Omega_o=\Omega)$ .

Figure 5 shows the disturbance energy growth due to the eigenmode and also the result when the optimal control is applied. As we can see from the figure the exponential energy growth is stopped almost immediately by the control. The first energy peak is mostly due to the energy expenditure to exert control. The maximum magnitude of the control is of the order of 0.02% of the free-stream velocity. The gradient norm is reduced about two orders of magnitude after 5-10 optimization iterations.

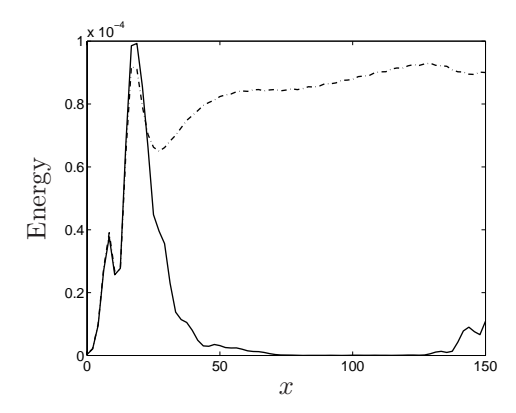


FIGURE 6. Solid: the disturbance energy growth with optimal control; dash-dot: the disturbance energy growth for a spatial Blasius boundary layer flow without control.

#### 5.4. Control in a spatial boundary layer flow

A more general flow case to study is when we let the boundary layer grow in the chordwise direction. For this case we have chosen to study a Tollmien-Schlichting (TS) wave in a Blasius boundary layer. The dimensions of the simulation box are  $200\times20\times10$  measured in  $\delta_0^*$  with a resolution of  $96\times129\times4$  in  $x\times y\times z$  respectively. The TS wave is triggered by an oscillating volume force at x=10 which is slightly upstream of branch I, located at  $x\approx40$  where it becomes unstable. The volume forcing does not introduce a pure TS-eigenmode into the flow and this will result in a varying growth of the total energy of the perturbation.

The control is allowed to be active between  $T_1^c = 0$  and  $T_2^c = 400$  and is located on  $\Gamma_c = (20, 70) \times (-5, 5)$ . The control is localized in space to give us a region to observe its action downstream of the control area.

The observation time interval is also limited to give the control enough freedom to act initially since we are more interested in the final results. Thus, the objective function is measured from  $T_1^o = 380$  to  $T_2^o = 400$  over the domain  $\Omega_o = (20, 150) \times (0, 20) \times (-5, 5)$  that includes only the physical solution meaning that the fringe region is omitted.

Without the control we can see how the disturbance energy grows in Figure 6, whereas with the optimal control applied on  $\Gamma_c$  the energy growth is efficiently interrupted.

### 5.5. Initial condition control

To test the convergence of the iterative procedure to find the optimal initial condition, several simulations have been run with different guesses of the initial condition.

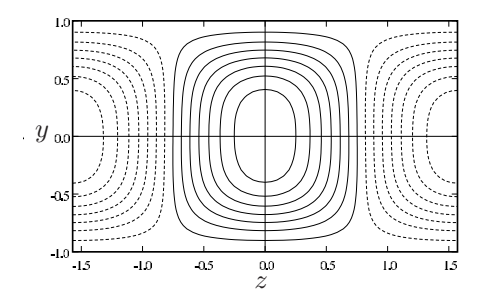


FIGURE 7. Contour plot of the wall-normal velocity component of the optimal initial condition that maximizes the disturbance energy growth at t = 115.

The test cases are run at Re = 1500 in plane Poiseuille flow with a box size  $x_L = 6.2831853$ ,  $z_L = 3.1415927$ . The simulations are run to time T = 115 which should be close to where the maximum transient growth occurs. The optimal initial condition amplifies the perturbation energy a factor 440.8.

### 5.5.1. Optimal initial condition

As a first test case we set the starting guess for the optimization to be the optimal perturbation as computed in for example Schmid & Henningson (2001). The optimal perturbation, in figure 7, was computed by Carlo Cossu, private communication. Contours of the wall-normal velocity component are shown. As expected the optimization routine is not able to improve the initial condition.

#### 5.5.2. Random initial condition

In this case the initial condition is constructed out of random modes to see whether the gradient procedure can find the optimal condition "far" from the optimum. From figure 8 it can be seen that the optimization procedure works well. The maximum transient growth is a factor of 440.8 in energy and the gradient has been reduced a factor 2000 which can be seen in figure 8.

In figure 9 the starting initial condition and final optimal condition are shown. The optimal condition might still be improved somewhat though by, for example, storing more forward velocity fields.

#### 6. Linear versus nonlinear control

Flows with three fundamentally different mechanism for disturbance energy growth are studied: TS waves, optimal disturbances, and stationary cross-flow vortices. The TS wave and optimal disturbance are applied to a Blasius boundary layer, and the cross-flow vortices to a Falkner–Skan–Cooke boundary layer. Direct numerical simulations are performed for each one of these perturbations, first without any control, then with linear control, and finally with nonlinear

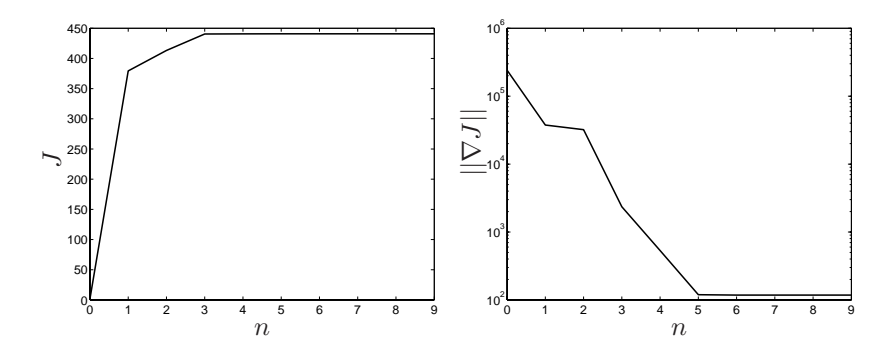


FIGURE 8. The objective function (left) and the  $L^2$  norm of the gradient (right) as functions of number of iterations in the optimization loop.

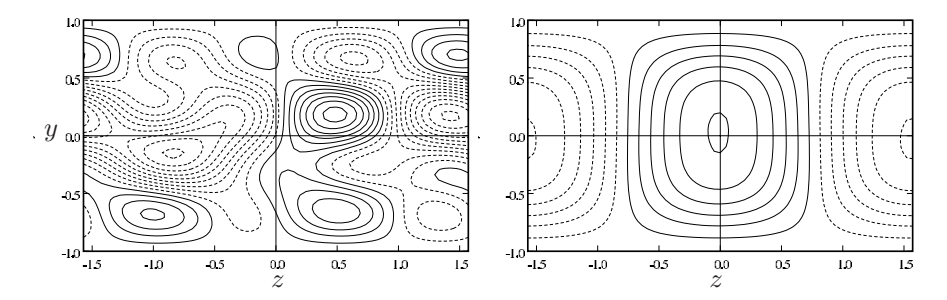


FIGURE 9. The initial condition before (left) and after optimization (right).

control. The nonlinear optimization loop is initiated with the linear optimal control. Note that the fringe region is excluded from the pictures below.

The energy measure that will be used in the following plots is

$$E(u(x)) = \frac{1}{y_{\infty} z_l} \int_{y} \int_{z} (u_1^2 + v^2 + w^2) \, dy \, dz.$$
 (67)

This energy measure naturally includes the control energy itself.

## 6.1. Tollmien-Schlichting waves

A TS wave is introduced in a Blasius boundary layer and develops as it propagates downstream. The Blasius mean flow is a special case of the Falkner–Skan–Cooke profiles without pressure gradient (m=0) and with no mean flow component in the z-direction.

Two different disturbances are applied, one weak TS wave, and one stronger wave where nonlinear coupling effects start to appear. The weak TS wave is generated by an oscillating two dimensional volume force with the dimensionless

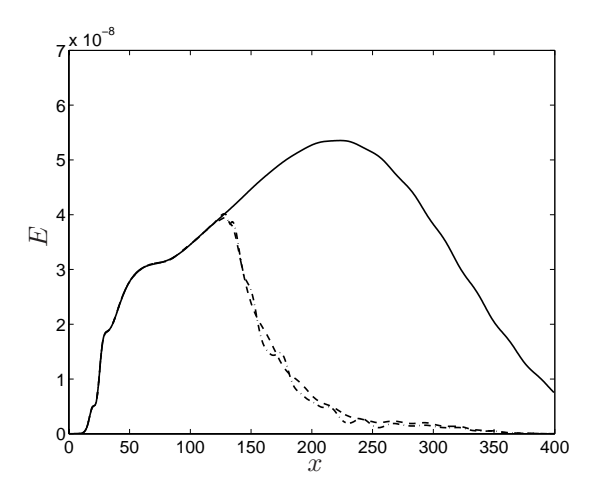


FIGURE 10. The spatial energy growth of a linear TS wave perturbation in a Blasius boundary layer without control from case 1 (solid), with linear control from case 2 (dashed), and nonlinear control from case 3 (dash-dotted). Control is applied in  $x \in [75, 225]$ . The TS wave is generated as a volume force centered at x = 20 for F = 200. The linear controller is centered at x = 150.

frequency F=200, where  $F=2\pi f\nu/U_{\infty}^2\times 10^6$ . The volume force is centered at x=20 and decays exponentially in both the x- and y-direction.

The stronger wave is generated in the fringe region by forcing toward the least stable Orr–Sommerfeld–Squire eigenmode computed for  $\alpha=0.30$  at R=950, a Reynolds number that corresponds to a spatial location close to the end of the computational box. This TS wave will then be exponentially unstable in the computational box.

Domain and resolution data for the TS wave simulations is given in Table 1, cases 1-6. The Reynolds number at x=0 is Re=468.34 for both the weak and strong disturbance. In the construction of the linear feedback kernels, the base flow profile is taken at x=150. For the nonlinear optimization problem, we specify the observation interval in space and time to  $x\in[75,375]$  and  $t\in[0,750]$ , respectively.

In Figure 10 the streamwise disturbance energy development of weak TS waves are plotted for cases 1-3 in Table 1. A small transient can be seen in the beginning of the energy curve, an effect that is due to the fact that we do not force a clean TS wave. However, as the disturbance evolves downstream, a pure TS wave emerges. The flow is perturbed just upstream of branch I of the neutral stability curve, which is at around  $R \approx 507$  ( $x \approx 27$ ), and the disturbance grows exponentially shown, as the solid line in Figure 10. The growth ends when branch II is reached at about  $R \approx 723$  ( $x \approx 219$ ). See for example Schmid

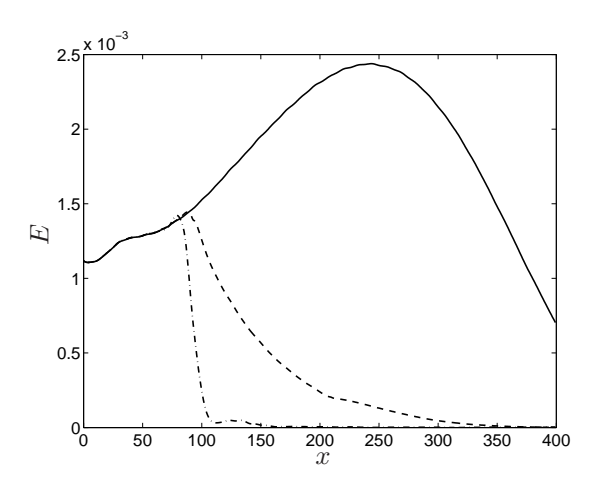


FIGURE 11. The spatial energy growth of a weakly nonlinear TS wave perturbation in a Blasius boundary layer without control from case 4 (solid), with linear control from case 5 (dashed), and nonlinear control from case 6 (dash-dotted). Control is applied in  $x \in [75, 225]$ . The TS wave is generated at R = 950 for  $\alpha = 0.30$ . The linear controller is centered at x = 150.

& Henningson (2001) for details. The dashed line is the disturbance energy development with linear control active. Note that the exponential growth is completely removed and replaced by an exponential decay. With the nonlinear optimal control applied, the energy development follows the dash-dotted line. Since the energy levels are very low and thus nonlinear effects negligible, we can conclude that the deviations originate from differences in the optimization problem and the limitations of the linear control. Analyzing the control signals shows no major differences between the two control approaches. The nonlinear control acts stronger in the beginning of the simulation and also stronger at the upstream part of the spatial control interval. These effects are a direct consequence of the limitations of the linear control problem formulation.

With no control at all, the objective function is  $5.291 \cdot 10^{-4}$ , and when the linear control is turned on the value is reduced to  $5.263 \cdot 10^{-4}$ . The relatively low reduction of the objective function is due to the fact that the simulation time is only as long as is needed for the control signal and the transients it cause to propagate out of the computational box. This means that it is only at the last part of the simulation all transient effects are gone and the disturbance energy is kept on a low level. The nonlinear control reduces the objective function value to  $5.260 \cdot 10^{-4}$ .

In Figure 11, the disturbance energy development in the streamwise direction for cases 4-6 from Table 1 are plotted. Again, the dashed line denotes the disturbance energy development with linear control turned on. Also for

this much stronger TS wave, the exponential growth is completely suppressed. The differences between the nonlinear control and the linear control is more pronounced than for the weak wave. Initially, the nonlinear control signal is higher over the whole control region. The downstream part of the control is quickly dampened to the linear control levels whereas the upstream region stays higher throughout the complete control time. Strong transients with nonlinear interactions are produced by the upstream control. As these transients are convected downstream there is a distinct difference in how the linear and nonlinear control behave. The nonlinear control signal becomes irregular whereas the linear control stays more or less sinusoidal.

The objective function value is reduced from 0.564 to 0.204 by the linear control and further down to 0.077 by the nonlinear control. The nonlinear control was picked after 24 iterations in the optimization loop which still has potential to decrease the value more.

### 6.2. Optimal disturbances

Here the performance of the controller for a transiently growing perturbation is studied. The same base flow as for the TS wave simulations is used but now with a larger box in the streamwise direction, see Table 1, cases 7-9, for details.

The spatial optimal perturbations in a Blasius boundary layer have been computed by Andersson et al. (1999) and Luchini (2000). The particular optimal spatial perturbation used here is introduced at  $R_0=395.4$  and then marched forward using the linear equations to the position where R=468.34. By introducing the optimal disturbance in the fringe region, we get a clean perturbation already in the beginning of the computational box. The perturbation is optimized to be the one with maximum growth at x=237.24 in the simulation box.

The linear control kernels are computed from the base flow at position x=150. Furthermore, the spatial and temporal observation region is  $x\in[75,975]$  and  $t\in[0,1500]$  respectively. The solid line in Figure 12 shows the disturbance energy growth without any control. In the same figure, the dashed line marks the evolution of the disturbance energy when linear control is applied, and the dash-dotted line shows the nonlinear control after ten iterations in the optimization loop. In these controlled cases, we still have transient growth, although substantially weaker. Cathalifaud & Luchini (2000) have computed the optimal control over the whole wall using the linearized boundary layer equations as state equation. Their optimal control is similar in shape as to what we have obtained.

After the disturbance energy reduction in the beginning of the control domain, the nonlinear control causes the energy to start growing earlier than the linear control does. This is an effect of our choice of spatial observation region. To keep the disturbance from growing to fast behind the control region, stronger control has to be applied, especially at the downstream part of the control region.

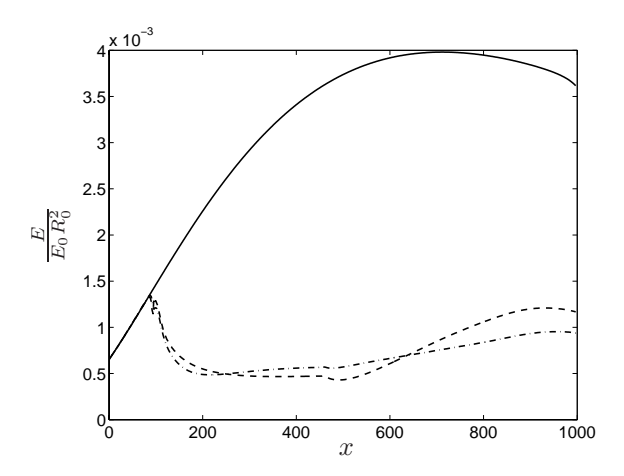


FIGURE 12. Spatial energy growth of a linear optimal disturbance in a Blasius boundary layer without control from case 7 (solid), with linear control from case 8 (dashed), and nonlinear control from case 9 (dash-dotted). Control is applied in  $x \in [75,475]$ . The optimal disturbance has the maximum growth at x=237.24. The linear controller is centered at x=150.  $E_0$  is the disturbance energy at  $R_0=395.4$ .

No control, for the current observation region, gives an objective function value of  $8.955 \cdot 10^{-4}$ . Linear control lowers the objective function to  $8.695 \cdot 10^{-4}$ . After six optimization iterations for the nonlinear control, the objective function reaches  $8.531 \cdot 10^{-4}$ . The small reduction of the objective function value is due to the fact that the observation time interval captures not only the results at the end of the simulation but also the transient process when the disturbance, already present in the flow, is acted on by the control. The energy curves are just snapshots of the streamwise energy distribution in the flow at the end of the simulation (T=1500).

#### 6.3. Cross-flow vortices

In a three dimensional boundary layer flow, where the direction of the base flow is a function of the wall normal coordinate, the velocity profile usually has an inflection point. This in turn means that there usually exists an inviscid inflectional instability, see e.g. Gregory et al. (1955). This primary instability may result in amplification of oblique traveling waves and of stationary vortices. Local linear stability theory predicts non-stationary modes to be more amplified than stationary modes. In the present work, we have chosen to study a stationary disturbance due to the somewhat smaller computational requirements in such a flow.

If large enough amplitude of the disturbance is used, stationary nonlinearly saturated cross-flow vortices will develop downstream. These instabilities have

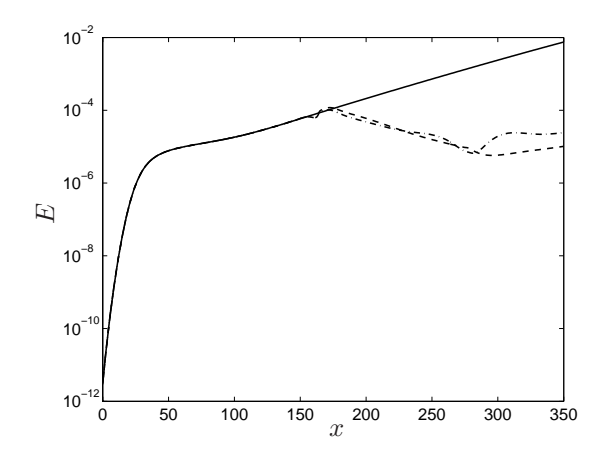


FIGURE 13. Spatial energy growth in the  $\beta=1$  mode of cross-flow vortices in a Falkner–Skan–Cooke boundary layer  $(m=0.34207 \text{ and } W_{\infty}=1.442)$  without control from case 10 (solid), with linear control from case 11 (dashed), and nonlinear control from case 12 (dash-dotted). Control is applied in  $x \in [145, 295]$ . The linear control kernels are computed with base flow from position x=220.

been thoroughly investigated both experimentally, by e.g. Lerche (1997) and Kawakami et al. (1999), and numerically, by Högberg & Henningson (1998) and Malik et al. (1999). In the present paper only results from lower amplitude disturbance simulations are reported. To mimic a base flow prone to the above behavior, a Falkner–Skan–Cooke boundary layer for an infinitely swept wing with a positive pressure gradient is modeled. Stationary perturbations are introduced in the beginning of the simulation box at Re=337.34 with m=0.34207 and  $W_{\infty}=1.442$ . The same flow case is studied numerically in Högberg & Henningson (1998).

The box size, resolution, and other details are given in Table 1 as cases 10-12. The linear control kernels are constructed from the base flow profile at x=220. For the nonlinear optimization problem, we have chosen the observation interval in space as  $x \in [145, 335]$  and in time as  $t \in [0, 800]$ .

In Figure 13, the solid line shows the growth of the disturbance energy in the  $\beta=1$  mode. As expected from linear stability theory, it grows exponentially. When applying linear control, the energy growth is efficiently stopped which is shown with the dashed line. However, immediately after we stop controlling the flow, new cross-flow vortices begin to form, which is natural due to the presence of an inflectional instability. The nonlinear control, shown as the dash-dotted line in Figure 13, reduces the disturbance growth even further.

Case	Flow	Perturbation	Amp.	Control
1	A	TS wave		none
2	A	TS wave	0.0002	[75, 225]
3	A	TS wave	0.0002	[75, 225]
4	A	TS wave		none
5	A	TS wave	0.01	[75, 225]
6	A	TS wave	0.01	[75, 225]
7	В	Optimal		none
8	В	Optimal	0.00001	[75, 425]
9	В	Optimal	0.00001	[75, 425]
10	$^{\mathrm{C}}$	Cross-flow		none
11	$^{\mathrm{C}}$	Cross-flow	0.0002	[145, 295]
12	$^{\rm C}$	Cross-flow	0.0002	[145, 295]
т	T-1	D14:		D
Type	Flow	Resolution	-	Box
Α	Blasius	$576 \times 65 \times$	$4 - 500 \times$	$20 \times 12.83$

Type	Flow	Resolution	Box
A	Blasius	$576 \times 65 \times 4$	$500 \times 20 \times 12.83$
В	Blasius	$576 \times 65 \times 4$	$1128\times20\times12.83$
$^{\rm C}$	FSC	$576 \times 65 \times 24$	$500 \times 10 \times 25.14$

Table 1. Summary of different simulations. For all simulations the linear control parameter equals  $l^2=100$ . The non-linear control parameter equals  $\varepsilon=10^{-5}$ . The two different amplitudes for the TS wave simulations correspond to linear and weakly nonlinear disturbances.

When no control is used the objective function is 5.593 and with linear control on it reduces to 0.644. The nonlinear control then decreases it to 0.635 after two iterations.

As for the TS waves and optimal disturbances cases, transient effects linger in the flow until the very last part of the simulation. Therefore, the reduction in objective function is not as large as one might expect from the disturbance energy plot, which again is a snapshot at simulation end time.

### 7. Summary and conclusions

First we conclude that optimal control of transition appears to be possible to compute with the approximative discretized adjoint technique used in this work. This was also what the preliminary study by Högberg & Berggren (2000) suggested. In addition, the optimization problem was derived using the primitive variables, velocity and pressure, but solved using a velocity–vorticity formulation. This made it easy to implement a solver for the adjoint equations using

already developed codes as templates. The adjoint solver thus benefited from the efforts put into making the existing codes computationally efficient.

The optimization routine BFGS by Byrd *et al.* (1994) was found to perform well for the present optimization problems. No modification of the code was necessary.

The test cases for the boundary layer code provided confirmation that we can solve a nonlinear optimization problem. From the simple parametric study of control of oblique waves in channel flow we can draw the conclusions that the temporal extent of the control appears to be more important than the resolution. Also allowing a higher energy initially a lower energy at a later time can be the result. Furthermore it appears that there is enough control authority using blowing and suction on the wall to handle all the different stages of the oblique transition scenario. Finally, the choice of objective function in terms of time intervals is very important for the performance of the resulting control.

The simple flow cases studied to test the code can now be replaced with more complicated flows. In particular flows where non-linear effects are dominating are of interest, and so are flows with spatial variations in the mean flow profile.

Direct numerical simulations for three different flow cases have been performed without any control, with an optimal control obtained through a linear feedback loop, and with an optimal control computed from the full nonlinear Navier–Stokes equations in an iterative procedure. The nonlinear optimization problem is initiated with the linear control in order to speed up the convergence process. Some of the smaller simulations have also been initiated from zero control and they converged to the same control.

The results show that the nonlinear control improves the performance over the linear control markedly in cases where nonlinear effects are significant. Also for perturbations with a linear development there are differences, but a fine-tuning of the parameter l in the linear control problem could possibly reduce the difference.

The linear controller results are computed with the same tools as used in Högberg & Henningson (2002) and works well for the studied cases despite its limitations.

The nonlinear control has not been fully converged in any of the simulated cases indicating that one would expect small adjustments to the disturbance energy growth curves. However, the big changes in the control appear in the first few iterations.

Simulations with disturbance amplitudes high enough so that nonlinear effects are more pronounced, will be studied in future work, both for the optimal disturbances and the cross-flow vortices.

For nonlinear optimization simulations over larger time intervals and for larger domains, the checkpointing technique mentioned in section 2.1 needs to be applied.

Another important part of the nonlinear optimization problem, is the formulation of the optimization problem itself and the choice of inner products involved. This could have a large impact on the convergence rate of the iterative process and also on how well the "optimal control" will work (see e.g. Protas & Bewley (2002)).

For the linear optimization problem the next natural step is to attempt to reduce the amount of information necessary when computing the control by estimating the state of the flow based on realizable measurement data.

### Acknowledgment

The first author wish to thank Carlo Cossu for discussions and feedback on the work of the optimal initial conditions.

## Appendix A. Derivation of gradient for boundary layer

A.1. The governing equations

The domain where we solve the governing equations, given  $0 < T < +\infty$ , is

$$\Omega = (-x_l/2, x_l/2) \times (0, y_l) \times (-z_l/2, z_l/2),$$

$$Q = \Omega \times (0, T).$$
(68)

The boundary of  $\Omega$  is denoted  $\Gamma$ , and

$$\Gamma_l = \Gamma(y=0), \quad \Gamma_u = \Gamma(y=y_l),$$
(69)

and  $\Gamma_c \subset \Gamma_l$  represents the part of the lower boundary where control is applied. For temporal simulations  $\Gamma_c$  coincide with  $\Gamma_l$ .

The governing equations for boundary layer flow are the same as for the channel flow except for an extra term which is added to enforce periodicity of the physical flow in the streamwise direction. This is only needed for spatial simulations.

$$\begin{cases}
\frac{\partial u}{\partial t} + (u \cdot \nabla)u - \frac{1}{Re}\Delta u + \nabla \pi = \lambda(x)(U - u) & \text{in } Q, \\
\nabla \cdot u = 0 & \text{in } Q, \\
u|_{t=0} = u_0,
\end{cases}$$
(24)

with periodic boundary conditions in the horizontal directions, that is, the xand z-directions,

$$u|_{x=-x_{l}/2} = u|_{x=x_{l}/2},$$
  
 $u|_{z=-z_{l}/2} = u|_{z=z_{l}/2}.$ 
(25)

Left to be specified are the conditions in the free-stream and on the wall,

$$u|_{y=y_{\rm fst}} = U_{\infty}$$
 (which is approximated by  $\frac{\partial u}{\partial n}\Big|_{\Gamma_u} = 0$ ),  
 $u|_{\Gamma_c} = nv_c$ ,  
 $u|_{\Gamma_l \setminus \Gamma_c} = 0$ . (26)

In equation (24), U=U(x,y) is the velocity field that we force the solution towards in the fringe region. Pressure is denoted  $\pi$  and the Reynolds number Re is defined based on the free-stream velocity and the displacement thickness  $\delta^*$ . The scalar function  $\lambda=\lambda(x)$  is nonzero only in the fringe region and is defined as follows:

$$\lambda(x) = \lambda_{\text{max}} \left[ S \left( \frac{x - x_{\text{start}}}{\Delta_{\text{rise}}} \right) - S \left( \frac{x - x_{\text{end}}}{\Delta_{\text{fall}}} + 1 \right) \right],$$

where  $\lambda_{\text{max}}$ ,  $x_{\text{start}}$ ,  $x_{\text{end}}$ ,  $\Delta_{\text{rise}}$  and  $\Delta_{\text{fall}}$  are parameters used to specify the strength, extent and shape of the fringe forcing. The S-function is defined as,

$$S(r) = \begin{cases} 0 & r \le 0, \\ \frac{1}{1 + \exp(1/(1-r) + 1/r)} & 0 < r < 1, \\ 1 & r \ge 1. \end{cases}$$

As for the channel flow case we expand the control  $v_c$  in basis functions  $\psi_{l,m}$  with zero mass flux, and where  $\varphi_{l,m}$  are time dependent coefficients for the basis functions.

$$v_c(x, z, t) = \begin{cases} \varphi_l^T \psi_l = \sum_{m=1}^M \varphi_{l,m}(t)\psi_{l,m}(x, z) & \text{in } (T_1^c, T_2^c), \\ 0 & \text{otherwise.} \end{cases}$$
(27)

Where we have introduced the control vector  $\varphi_l$  defined as:

$$\varphi_l = (\varphi_{l,1}, \dots, \varphi_{l,M}).$$

### A.2. The objective function

We minimize the deviation energy from a given target velocity distribution  $u_T$  and add a regularization term including an  $\varepsilon > 0$ :

$$J(\varphi_l) = \frac{\varepsilon}{2} \int_{T_c^c}^{T_c^c} \int_{\Gamma_c} |v_c|^2 d\Gamma dt + \frac{1}{2} \int_{T_c^o}^{T_c^o} \int_{\Omega_o} |u - u_T|^2 dQ,$$
 (28)

where  $(T_1^c, T_2^c)$  is the control time period and  $(T_1^o, T_2^o)$  is the observation time period and  $\Omega_o$  is the part of the domain  $\Omega$  where the state of the flow is observed. The control problem can now be defined as:

Find 
$$\varphi^* \in \mathcal{U}_{ad}$$
 such that
$$J(\varphi^*) \le J(\varphi_l) \quad \forall \ v_c(\varphi_l) \in \mathcal{U}_{ad}, \tag{70}$$

where  $\varphi^*$  is the optimal control. The set of admissible controls is denoted  $\mathcal{U}_{ad}$  and is a subset of  $L^2((T_1^c, T_2^c); \mathbb{R}^M)$ .

A.3. Derivation of the objective function gradient

We begin by differentiating the objective function (28)

$$\delta J(\varphi_l) = \varepsilon \int_{T_1^c}^{T_2^c} \int_{\Gamma_c} \delta v_c \, v_c \, d\Gamma \, dt + \int_{T_1^o}^{T_2^o} \int_{\Omega_o} \delta u \cdot (u - u_T) \, dQ, \tag{71}$$

where the gradient of J is defined through the directional derivative of J in the  $\delta\varphi_l$ -direction as done in (4). The differentiated Navier–Stokes equations have the form

$$\begin{cases} \frac{\partial \delta u}{\partial t} + (\delta u \cdot \nabla)u + (u \cdot \nabla)\delta u - \frac{1}{Re}\Delta \delta u + \nabla \delta \pi = -\lambda(x)\delta u & \text{in } Q, \\ \nabla \cdot \delta u = 0 & \text{in } Q, \end{cases}$$

$$\delta u|_{t=0} = 0,$$

$$(72)$$

with the boundary conditions

$$\delta u|_{x=-x_l/2} = \delta u|_{x=x_l/2},$$

$$\delta u|_{z=-z_l/2} = \delta u|_{z=z_l/2},$$

$$\delta u|_{y=y_{\text{fst}}} = 0,$$

$$\delta u|_{\Gamma_c} = n\delta v_c,$$

$$\delta u|_{\Gamma_l \setminus \Gamma_c} = 0,$$
(73)

where

$$\delta v_c(x, z, t) = \begin{cases} \delta \varphi_l^T \psi_l = \sum_{m=1}^M \delta \varphi_{l,m}(t) \psi_{l,m}(x, z) & \text{in } (T_1^c, T_2^c), \\ 0 & \text{otherwise.} \end{cases}$$
(74)

Now, let us consider the adjoint variable p = p(x, y, z, t) and the adjoint pressure  $\sigma = \sigma(x, y, z, t)$  and require p to satisfy the boundary conditions:

$$p|_{x=-x_{l}/2} = p|_{x=x_{l}/2},$$

$$p|_{z=-z_{l}/2} = p|_{z=z_{l}/2},$$

$$p|_{\Gamma_{l}} = 0,$$

$$p|_{y=y_{\text{fst}}} = 0.$$
(75)

The boundary condition at  $y=y_{\rm fst}$  can be approximated with the artificial boundary condition

$$\left. \frac{\partial p}{\partial n} \right|_{\Gamma_u} = 0,$$

in the numerical simulations. With a sufficiently high box not only this condition will hold but also p and  $\sigma$  will approach zero.

By multiplying the first equation in (72) with p and then integrating over Q we obtain

$$\int_{Q} p \cdot \left( \underbrace{\frac{\partial \delta u}{\partial t}}_{1} + \underbrace{(\delta u \cdot \nabla)u}_{2} + \underbrace{(u \cdot \nabla)\delta u}_{3} \right) dQ = 0.$$

$$\underbrace{-\frac{1}{Re} \Delta \delta u + \nabla \delta \pi}_{4} + \underbrace{\lambda(x)\delta u}_{5} dQ = 0.$$
(76)

We apply integration by parts in space and time to move the derivatives from u to the adjoint variable p. For clarity we perform this step by step for each term. The first term gives

$$\int_{Q} p \cdot \frac{\partial \delta u}{\partial t} dQ = \int_{\Omega} (p(T) \cdot \delta u(T) - p(0) \cdot \delta u(0)) d\Omega$$

$$- \int_{Q} \frac{\partial p}{\partial t} \cdot \delta u dQ$$

$$= \int_{\Omega} p(T) \cdot \delta u(T) d\Omega - \int_{Q} \frac{\partial p}{\partial t} \cdot \delta u dQ,$$
(77)

where we have used the fact that  $\delta u(t=0)=0$ . Next, we consider the fourth term

$$-\frac{1}{Re} \int_{Q} p \cdot \Delta \delta u \, dQ + \int_{Q} p \cdot \nabla \delta \pi \, dQ$$

$$= -\frac{1}{Re} \int_{0}^{T} \left[ \int_{\Gamma} p \cdot \frac{\partial \delta u}{\partial n} \, d\Gamma + \int_{\Omega} \nabla p : \nabla \delta u \, d\Omega \right] \, dt$$

$$+ \int_{0}^{T} \left[ \int_{\Gamma} p \cdot n \, \delta \pi \, d\Gamma \, dt - \int_{\Omega} \nabla \cdot p \, \delta \pi \, d\Omega \right] \, dt$$

$$= \int_{0}^{T} p \cdot \left( n \, \delta \pi - \frac{1}{Re} \frac{\partial \delta u}{\partial n} \right) \, d\Gamma \, dt + \frac{1}{Re} \int_{0}^{T} \int_{\Gamma} \frac{\partial p}{\partial n} \cdot \delta u \, d\Gamma \, dt \qquad (78)$$

$$- \frac{1}{Re} \int_{Q} \Delta p \cdot \delta u \, dQ - \int_{Q} \nabla \cdot p \, \delta \pi \, dQ$$

$$= \frac{1}{Re} \int_{0}^{T} \int_{\Gamma_{u}} \frac{\partial p}{\partial n} \cdot \delta u \, d\Gamma \, dt + \frac{1}{Re} \int_{T_{1}^{c}}^{T_{2}} \left[ \delta \varphi_{l}^{T} \int_{\Gamma_{l}} \psi_{l} \nabla p_{2} \cdot n \, d\Gamma \right] \, dt$$

$$- \frac{1}{Re} \int_{Q} \Delta p \cdot \delta u \, dQ - \int_{Q} \nabla \cdot p \, \delta \pi \, dQ,$$

where  $p = (p_1, p_2, p_3)$ . In the second equality we used the boundary condition (30) for p at y = 0 and enforced symmetry. In the third equality the condition for  $\delta u$  at y = 0 in (73) was used. We also assumed that p goes to zero at the artificial boundary  $y = y_l$ . The : denotes a complete contraction defined as in (12).

The next term to rewrite, in relation (76), is the second term

$$\int_{Q} p \cdot (\delta u \cdot \nabla) u \, dQ = \int_{Q} (\nabla u)^{T} p \cdot \delta u \, dQ.$$
(79)

Finally, we rewrite the third term in (76)

$$\int_{Q} p \cdot (u \cdot \nabla) \delta u \, dQ$$

$$= \iint_{0}^{T} (p \cdot \delta u)(n \cdot u) \, d\Gamma \, dt$$

$$- \int_{Q} (p \cdot \delta u)(\nabla \cdot u) \, dQ - \int_{Q} (u \cdot \nabla) p \cdot \delta u \, dQ$$

$$= \iint_{0}^{T} (p \cdot \delta u)(n \cdot u) \, d\Gamma \, dt - \int_{Q} (u \cdot \nabla) p \cdot \delta u \, dQ,$$
(80)

where we have used the continuity condition on u and the boundary conditions (30) for p. The fifth term needs no rewriting.

Substituting (77), (78), (79) and (80) into (76) yields

$$\int_{\Omega} p(T) \cdot \delta u(T) \, d\Omega + \frac{1}{Re} \int_{T_{1}^{c}}^{T_{2}^{c}} \left[ \delta \varphi_{l}^{T} \int_{\Gamma_{l}} \psi_{l} \nabla p_{2} \cdot n \, d\Gamma \right] \, dt$$

$$+ \int_{Q} \delta u \cdot \left( -\frac{\partial p}{\partial t} + (\nabla u)^{T} p - (u \cdot \nabla) p - \frac{1}{Re} \Delta p + \lambda(x) p \right) \, dQ$$

$$- \int_{Q} \delta \pi \nabla \cdot p \, dQ + \frac{1}{Re} \int_{0}^{T} \int_{\Gamma_{u}} \frac{\partial p}{\partial n} \cdot \delta u \, d\Gamma \, dt$$

$$+ \int_{0}^{T} \int_{\Gamma_{u}} (n \cdot u) (p \cdot \delta u) \, d\Gamma \, dt = 0.$$
(81)

Now, require p to satisfy the adjoint equations:

Now, require 
$$p$$
 to satisfy the adjoint equations: 
$$\begin{cases} -\frac{\partial p}{\partial t} + (\nabla u)^T p - (u \cdot \nabla)p \\ -\frac{1}{Re} \Delta p + \lambda(x)p + \nabla \sigma = \begin{cases} u - u_T & \text{in } (T_1^o, T_2^o) \times \Omega_o \\ 0 & \text{otherwise} \end{cases} & \text{in } Q, \quad (29) \\ \nabla \cdot p = 0 & \text{in } Q, \\ p|_{t=T} = 0, \end{cases}$$

with the boundary conditions (30). With these assumptions equation (81) becomes

$$\int_{T_1^o \Omega_o}^{T_2^o} \delta u \cdot (u - u_T) \, dQ - \int_{Q} \delta u \cdot \nabla \sigma \, dQ 
+ \frac{1}{Re} \int_{0}^{T} \int_{\Gamma_u}^{T} \frac{\partial p}{\partial n} \cdot \delta u \, d\Gamma \, dt + \int_{0}^{T} \int_{\Gamma_u}^{T} (n \cdot u)(p \cdot \delta u) \, d\Gamma \, dt = 0,$$
(82)

since p and  $\partial p_2/\partial n$  is zero on the boundary y=0 due to the no-slip and continuity conditions. The second term in (82) can be rewritten

$$-\int_{Q} \delta u \cdot \nabla \sigma \, dQ = -\int_{0}^{T} \int_{\Gamma} \delta u \cdot n \, \sigma \, d\Gamma \, dt + \int_{Q} \nabla \cdot \delta u \, \sigma \, dQ$$

$$= -\int_{0}^{T} \int_{\Gamma} \delta u \cdot n \, \sigma \, d\Gamma \, dt,$$
(83)

since  $\nabla \cdot \delta u = 0$ . The final step is now to substitute the terms involving  $\delta u$ . When that is done the second term in the perturbed objective function (71) can be replaced with terms involving  $\delta \varphi$ . Since  $\delta u$  is known on parts of the boundary we can proceed as follows

$$-\int_{0}^{T} \int_{\Gamma} \delta u \cdot n \, \sigma \, d\Gamma \, dt$$

$$= -\int_{0}^{T} \int_{\Gamma_{u}} \delta u \cdot n \, \sigma \, d\Gamma \, dt + \int_{T_{1}^{c}}^{T_{2}^{c}} \left[ \delta \varphi_{l}^{T} \int_{\Gamma_{c}} \psi_{l} \sigma \, d\Gamma \right] dt.$$
(84)

Combining equation (83) and (84) and inserting that into (82) yield

$$\int_{T_{1}^{o}}^{T_{2}^{o}} \int_{\Omega_{o}} \delta u \cdot (u - u_{T}) dQ + \int_{0}^{T} \int_{\Gamma_{u}} \delta u \cdot \left( \frac{1}{Re} \frac{\partial p}{\partial n} - \sigma n + (n \cdot u)p \right) d\Gamma dt + \int_{T_{2}^{c}}^{T} \left[ \delta \varphi_{l}^{T} \int_{\Gamma_{c}} \psi_{l} \sigma d\Gamma \right] dt = 0.$$
(85)

Applying the fourth boundary condition (30) for p together with the assumption that also p = 0 and  $\sigma = 0$  (see the beginning of the section) at  $y = y_l$  we get

$$\int_{T_1^o}^{T_2^o} \int_{\Omega_o} \delta u \cdot (u - u_T) \, dQ = -\int_{T_1^c}^{T_2^c} \left[ \delta \varphi_l^T \int_{\Gamma_c} \psi_l \sigma \, d\Gamma \right] dt.$$
 (86)

Remains only to substitute (86) into (71) which yields

$$\delta J(\varphi_l) = \int_{T_1^c}^{T_2^c} \delta \varphi_l^T \int_{\Gamma_c} \psi_l \left( \varepsilon \varphi_l^T \psi_l - \sigma \right) d\Gamma dt$$
 (87)

where the gradient of the objective function can be identified as:

$$\frac{\partial J}{\partial \varphi_l} = \int_{\Gamma_c} \psi_l \left( \varepsilon \varphi_l^T \psi_l - \sigma \right) d\Gamma. \tag{31}$$

This is exactly the same expression for the gradient as for the channel flow case, equation (22) and (23), except that this gradient is restricted to information from  $\Gamma_c$ .

#### References

- Andersson, P., Berggren, M. & Henningson, D. S. 1999 Optimal disturbances and bypass transition in boundary layers. *Phys. Fluids* **11**, 134–150.
- Berggren, M. 1995 Optimal control of time evolution systems: Controllability investigations and numerical algorithms. PhD thesis, Rice University, Department of Computational and Applied Mathematics, Houston, Tx 77251-1892.
- Berggren, M. 1998 Numerical solution of a flow-control problem: vorticity reduction by dynamic boundary action. SIAM J. Sci. Comp. 19 (3), 829–860.
- Bewley, T. R. & Liu, S. 1998 Optimal and robust control and estimation of linear paths to transition. *J. Fluid Mech.* **365**, 305–349.
- Bewley, T. R., Moin, P. & Temam, R. 2001 DNS-based predictive control of turbulence: an optimal benchmark for feedback algorithms. *J. Fluid Mech.* 447, 179–225.
- Byrd, R. H., Peihuang, L., Nocedal, J. & Zhu, C. 1994 A limited memory algorithm for bound constrained optimization. Technical Report NAM-08. EECS Department, Northwestern University, http://www.netlib.org/toms/778.
- Canuto, C., Hussaini, M. Y., Quarteroni, A. & Zang, T. A. 1988 Spectral Methods in Fluids Dynamics. Springer.
- Cathalifaud, P. & Luchini, P. 2000 Algebraic Growth in Boundary Layers: Optimal Control by Blowing and Suction at the Wall. Eur. J. Mech. B Fluids  $\bf 19$ ,  $\bf 469-490$ .
- Chevalier, M., Högberg, M., Berggren, M. & Henningson, D. S. 2002 Linear and nonlinear optimal control in spatial boundary layers. *AIAA Paper* (2002–2755).
- Collis, S., Chang, Y., Kellogg, S. & Prabhu, R. D. 2000 Large eddy simulation and turbulence control. AIAA Paper 2000–2564.
- GLOWINSKI, R. & HE, J. 1998 On shape optimization and related issues. In *Computational Methods for Optimal Design and Control* (eds. J. Borggaard, J. Burns, E. Cliff & S. Schreck), pp. 151–179. Birkhäuser, Boston.
- GREGORY, N., STUART, J. T. & WALKER, W. S. 1955 On the stability of three

- dimensional boundary layers with application to the flow due to a rotating disk. *Phil. trans. R. Soc. Lond.* A 248, 155–199.
- Gunzburger, M. D., ed. 1995 Flow Control. Springer-Verlag.
- Gunzburger, M. D. 1998 Sensitivities in computational methods for optimal flow control. In *Computational Methods for Optimal Design and Control* (eds. J. Borggaard, J. Burns, E. Cliff & S. Schreck), pp. 197–236. Birkhäuser, Boston.
- HINZE, M. & KUNISH, K. 2000 Three Control Methods for Time Dependent Fluid Flow. Flow, Turbulence and Combustion 65 (3/4), 273–298.
- HÖGBERG, M. & BERGGREN, M. 2000 Numerical Investigation of Different Discretization Approaches for Optimal Control. Flow, Turbulence and Combustion 65 (3/4), 299–320.
- HÖGBERG, M. & BEWLEY, T. R. 2001 Spatially-localized convolution kernels for decentralized control and estimation of transition of plane channel flow. Automatica Submitted.
- HÖGBERG, M., CHEVALIER, M., BERGGREN, M. & HENNINGSON, D. S. 2001 Optimal control of wall bounded flows. Scientific Report FOI-R--0182--SE. Computational Aerodynamics Department, Aeronautics Division, FOI.
- HÖGBERG, M. & HENNINGSON, D. S. 1998 Secondary instability of cross-flow vortices in Falkner–Skan–Cooke boundary layers. J. Fluid Mech. 368, 339–357.
- HÖGBERG, M. & HENNINGSON, D. S. 2002 Linear optimal control applied to instabilities in spatially developing boundary layers. *J. Fluid Mech.* 470, 151–179.
- HÖGBERG, M., HENNINGSON, D. S. & BERGGREN, M. 2000 Optimal control of bypass transition. In *Advances in turbulence VIII* (ed. D. C.).
- Jameson, A. 1989 Computational aerodynamics for aircraft design. Science 245, 361–371.
- Joshi, S. S., Speyer, J. L. & Kim, J. 1997 A systems theory approach to the feedback stabilization of infinitesimal and finite-amplitude disturbances in plane Poiseuille flow. *J. Fluid Mech.* **332**, 157–184.
- Joslin, R. D., Gunzburger, M. D., Nicolaides, R. A., Erlebacher, G. & Hussaini, M. Y. 1997 A Self-contained, Automated Methodology for Optimal Flow Control Validated for Transition Delay. *AIAA Journal* **35** (5), 816–824.
- KAWAKAMI, M., KOHAMA, Y. & OKUTSU, M. 1999 Stability characteristic of stationary crossflow vortices in three-dimensional boundary layer. AIAA Paper 99–0811.
- Kim, J. & Lim, J. 2000 A linear process in wall-bounded turbulent shear flows. *Phys. Fluids* **12** (8), 1885–1888.
- LERCHE, T. 1997 Experimentelle Untersuchung nichtlinearen Strukturbildung im Transitionsprozeß einer instabilen Grenzschicht. Fortscrittberichte, VDI, Reihe 7: Strömungstechnik Nr. 310.
- Luchini, P. 2000 Reynolds-number-independent instability of the boundary layer over a flat surface: optimal perturbations. *J. Fluid Mech.* **404**, 289–309.
- Lundbladh, A., Berlin, S., Skote, M., Hildings, C., Choi, J., Kim, J. & Henningson, D. S. 1999 An Efficient Spectral Method for Simulations of Incompressible Flow over a Flat Plate. Technical Report TRITA-MEK 1999:11. Department of Mechanics, Royal Institute of Technology, KTH.
- LUNDBLADH, A., HENNINGSON, D. S. & JOHANSSON, A. 1992 An Efficient Spectral Integration Method for the Solution of the Navier–Stokes Equations. Technical Report FFA TN 1992-28. The Aeronautical Research Institute of Sweden, FFA.

- Malik, M. R., Li, F., Choudhari, M. M. & Chang, C.-L. 1999 Secondary instability of crossflow vortices and swept-wing boundary layer transition. *J. Fluid Mech.* 399, 86–115.
- METCALFE, R. W. 1994 Boundary layer control: A brief review. In *Computational Fluid Dynamics '94*, *Invited Lectures of the Second European CFD Conference* (eds. S. Wagner, J. Periaux & E. Hirschel), pp. 52–60. Stuttgart, Germany: John Wiley & Sons.
- MORKOVIN, M. V. 1969 The many faces of transition. In *Viscous Drag Reduction* (ed. C. S. Wells). Plenum Press.
- NORDSTRÖM, J., NORDIN, N. & HENNINGSON, D. S. 1999 The fringe region technique and the Fourier method used in the direct numerical simulation of spatially evolving viscous flows. SIAM J. Sci. Comp. 20 (4), 1365–1393.
- PROTAS, B. & BEWLEY, T. R. 2002 Regularization opportunities in the adjoint analysis of multiscale systems. In *Advances in Turbulence IX* (eds. I. P. Castro, P. E. Hancock & T. G. Thomas). Proceedings of the Ninth European Turbulence Conference
- REDDY, S. C., SCHMID, P. J., BAGGETT, J. S. & HENNINGSON, D. S. 1998 On stability of streamwise streaks and transition thresholds in plane channel flows. *J. Fluid Mech.* **365**, 269–303.
- SRITHARAN, S. S., ed. 1998 Optimal control of viscous flows. SIAM.
- Thomas, A. S. W. 1990 Active wave control of boundary-layer transition. In *Viscous Drag Reduction in Boundary Layers* (eds. D. M. Bushnell & J. N. Hefner), *Progress in Astronautics and Aeronautics*, vol. 123. Washington, D.C: American Institute of Aeronautics and Astronautics.